The effect of the adherends' thickness on static ultrasonic welding of thermoplastic composites

MSc. Thesis by

Natalia Sofía Guevara Sotelo

TU Delft

The effect of the adherends' thickness on static ultrasonic welding of thermoplastic composites

by

Natalia Sofía Guevara Sotelo

to obtain the degree of Master of Science Aerospace Engineering
at Delft University of Technology,
to be defended publicly on Tuesday May 24, 2022 at 10:00.

Student number:	5272572	
Project duration:	September 1, 2021 – May 24, 2022	
Thesis committee:	Dr. I. F. Villegas,	TU Delft, Chair & Supervisor
	Dr. D. M. J. Peeters,	TU Delft, Examiner
	Dr. J. J. E. Teuwen,	TU Delft, Examiner
	C. B. G. Brito,	TU Delft, Additional

An electronic version of this thesis is available at `http://repository.tudelft.nl/`.

TU Delft

Acknowledgements

I would like to express my most sincere gratitude to all the people who contributed to the making of this thesis.

To Dr. Irene Fernandez Villegas for her guidance and support. Thank you for sharing you knowledge with me, for your patience throughout this process, and the enthusiasm towards my research. Also, I appreciate the freedom you gave me by allowing me to manage my own time.

To my parents Javier and Luz Marina and to the rest of my family in Colombia who are constantly rooting for me.

To Dr. Julie Teuwen, Dr. Daniël Peeters, and Camila Brito for taking the time to revise my work and agreeing to be on my thesis committee.

To the members of the Composite Welding Group for our interesting meetings and feedback. Special thanks to Camila, Bhanu, and Bram.

To Victor, Fred, Durga, Dave, Alexander, and all the members from the DASML laboratory who supported me with kindness and patience.

To my little family in The Netherlands: Alejandra, Tatiana M., Camilo, Andrés, and Tatiana G. Thank you for making me feel at home.

To my professors from Universidad de Los Andes, especially Dr. Juan Pablo Casas Rodríguez and Dr. Álvaro Pinilla Sepúlveda.

To Dr. Sofia Teixeira de Freitas and Dr. Daniël Peeters for giving me the opportunity to be part of the MoM team. The nice lectures and instructions helped clearing out my mind in times of chaos.

Finally, to all my friends. Special thanks to Juan Camilo, Angie, Nicolás, Johann, Santiago, and Sofía.

Executive summary

Fiber-reinforced polymer composites have gained relevance in the aerospace industry due to their great potential for weight reduction. This, thanks to their outstanding specific properties and ability to be tailored to different applications. Developing efficient composite joining techniques is a challenge that requires great attention as it is key to a more sustainable industry. Thermoplastic composites present the great advantage that they can be joined via fusion bonding, a joining technique in which the interface is virtually erased and is generally faster than other available techniques such as mechanical fastening and adhesion bonding. A fusion bonding technology that stands out for its short processing times and cost-efficiency is ultrasonic welding, a process in which the joint is developed via low-amplitude and high-frequency mechanical vibrations that heat up the interface. Although the effect of different parameters is well known, the particular effect of the part -commonly referred to as adherend- thickness is yet not fully understood.

This thesis investigated the effect of the adherends' thickness on the process response and weld evolution on static ultrasonic welding of CF/LMPAEK thermoplastic composites. Different characterization techniques were used to assess the latter, such as the output from the welding equipment (power and displacement), temperature readings, microscopy analysis, high-speed camera recordings, and numerical models. The results showed that increasing only the top adherend's thickness gradually increases the heating in this adherend up to a point where significant fiber squeeze-out is observed at early stages of the process. This overheating was associated with hammering and the differences in compliance when increasing the thickness. It is hypothesized that this hammering may contribute to overheating. Welding with a higher force significantly decreased the overheating in the top adherend as hammering is reduced, whereas changing the amplitude did not show to be as influential. In contrast, increasing only the bottom adherend's thickness did not have as much effect on the process. The dissipated power and cooling rate were the two variables that showed to be most affected, and both were associated with more bulk viscoelastic dissipation as the thickness increases. Finally, changing from fabric to UD reinforcement and welding only different top adherend's thicknesses resulted in less hammering and fewer differences in the process response and weld evolution between thin and thick adherends, which was associated with the variation in compliance.

The findings of this study indeed contribute to the understanding of the effect of the adherends' thickness. However, more research is required to fully grasp this effect on ultrasonic welding of thermoplastic composites. For example, developing a process envelope that quantifies the thickness limitations for different process parameters and investigating the effect of the thickness in continuous ultrasonic welding are some of the next steps towards a more robust and well-understood joining technology for thermoplastic composites.

Contents

Nomenclature vi

1 Introduction 1
- 1.1 Background & motivation . . . 1
- 1.2 Literature study . . . 1
  - 1.2.1 Thermoplastic composites and welding techniques . . . 2
  - 1.2.2 Ultrasonic welding . . . 3
  - 1.2.3 Part thickness in ultrasonic welding . . . 6
- 1.3 Conclusions from the literature study . . . 8
- 1.4 Research questions . . . 9
- 1.5 Research methodology . . . 9
- 1.6 Report outline . . . 10

2 Materials, setup & analysis methods 11
- 2.1 Materials . . . 11
  - 2.1.1 Adherends . . . 11
  - 2.1.2 Energy directors . . . 12
- 2.2 Experimental setup . . . 12
- 2.3 Analysis methods . . . 14
  - 2.3.1 High speed camera . . . 14
  - 2.3.2 Cross-sectional microscopy . . . 14
  - 2.3.3 Speed of sound measurements . . . 14
  - 2.3.4 COMSOL Multiphysics 5.6 models . . . 15

3 Results 18
- 3.1 Effect of changing the top adherend's thickness . . . 18
  - 3.1.1 Power and displacement . . . 18
  - 3.1.2 Amplitude . . . 19
  - 3.1.3 High-speed camera snapshots . . . 20
  - 3.1.4 Microscopy . . . 20
  - 3.1.5 Temperature readings . . . 21
  - 3.1.6 COMSOL wave propagation model . . . 22
- 3.2 Effect of changing the bottom adherend's thickness . . . 23
  - 3.2.1 Power and displacement . . . 23
  - 3.2.2 Amplitude . . . 23
  - 3.2.3 High-speed camera snapshots . . . 25
  - 3.2.4 Temperature readings . . . 25
  - 3.2.5 COMSOL heat transfer model . . . 26
  - 3.2.6 COMSOL wave propagation model . . . 27
- 3.3 Effect of changing the process parameters . . . 28
  - 3.3.1 Power and displacement . . . 28
  - 3.3.2 Amplitude . . . 28
  - 3.3.3 High-speed camera snapshots . . . 30
  - 3.3.4 Microscopy . . . 32
  - 3.3.5 Temperature readings . . . 32

3.4 Effect of changing to UD reinforcement . . . 34
3.4.1 Power and displacement . . . 34
3.4.2 Amplitude . . . 35
3.4.3 High-speed camera snapshots . . . 36
3.4.4 Microscopy . . . 37

4 Discussion 39
4.1 Effect of changing the top adherend's thickness . . . 39
4.2 Effect of changing the bottom adherend's thickness . . . 45
4.3 Effect of changing the process parameters . . . 48
4.4 Effect of changing to UD reinforcement . . . 50

5 Conclusions and recommendations 53
5.1 Conclusions . . . 53
5.2 Final comments and recommendations . . . 54

A Power and displacement curves 56
A.1 Effect of changing the top adherend's thickness . . . 56
A.2 Effect of changing the bottom adherend's thickness . . . 57

B Amplitude curves 59
B.1 Effect of changing the top adherend's thickness . . . 59
B.2 Effect of changing the bottom adherend's thickness . . . 60
B.3 Effect of changing the process parameters . . . 61
B.3.1 Low force-low amplitude (500 N, 60 um) . . . 61
B.3.2 High force-High amplitude (1500 N, 80 um) . . . 62
B.3.3 High force-Low amplitude (1500 N, 60 um) . . . 62
B.4 Effect of changing to UD reinforcement . . . 63
B.4.1 Reference case: low force-high amplitude (500 N, 80 um) . . . 63
B.4.2 Low force-low amplitude (500 N, 60 um) . . . 64
B.4.3 High force-high amplitude (1500 N, 80 um) . . . 64
B.4.4 High force-low amplitude (1500 N, 60 um) . . . 64

C High-speed camera results 65
C.1 Effect of changing the top adherend's thickness . . . 65
C.2 Effect of changing the bottom adherend's thickness . . . 66
C.3 Effect of changing the process parameters . . . 68
C.3.1 Low force-low amplitude (500 N, 60 um) . . . 68
C.3.2 High force-high amplitude (1500 N, 80 um) . . . 69
C.3.3 High force-low amplitude (1500 N, 60 um) . . . 70
C.4 Effect of changing to UD reinforcement . . . 71
C.4.1 Reference case: low force-high amplitude (500 N, 80 um) . . . 72
C.4.2 Low force-low amplitude (500 N, 60 um) . . . 73
C.4.3 High force-high amplitude (1500 N, 80 um) . . . 74
C.4.4 High force-low amplitude (1500 N, 60 um) . . . 75

D Microscopy 76
D.1 Effect of changing the top adherend's thickness . . . 76
D.2 Effect of changing the process parameters . . . 77
D.2.1 Low force-low amplitude (500 N, 60 um) . . . 77
D.2.2 High force-high amplitude (1500 N, 80 um) . . . 78
D.2.3 High force-low amplitude (1500 N, 60 um) . . . 80
D.3 Effect of changing to UD reinforcement . . . 80
D.3.1 High force-high amplitude (1500 N, 80 um) . . . 81
D.3.2 High force-low amplitude (1500 N, 60 um) . . . 82

E Temperature readings **83**
E.1 Effect of changing the top adherend's thickness . . . 83
E.2 Effect of changing the bottom adherend's thickness . . . 84

F COMSOL wave propagation model **86**
F.1 Evaluation of the model . . . 86
F.2 Effect of changing the top adherend's thickness . . . 89
F.3 Effect of changing the bottom adherend's thickness . . . 93

G COMSOL heat transfer model **97**

H Speed of sound measurements **100**

I The thermocouples effect **102**

Bibliography **104**

Nomenclature

B	Bottom adherend's thickness
CF	Carbon fiber
CUW	Continuous ultrasonic welding
ED	Energy director
HAZ	Heat-affected zone
HSC	High-speed camera
HT	Heat transfer
LSS	Lap shear strength
T	Top adherend's thickness
TC	Thermocouple
TP	Thermoplastic
TPC	Thermoplastic composite
TTH	Through-the-thickness heating
UD	Uni-directional
USW	Ultrasonic welding
VEH	Viscoelastic heating
WP	Wave propagation

1
Introduction

1.1. Background & motivation

Reducing structural weight by means of optimizing the joint design is crucial for developing more sustainable solutions for the ongoing problem of fuel consumption in the aerospace industry. Fiber reinforced polymer composites have shown great potential in weight reduction, owing it to their excellent stiffness and strength-to-weight ratios, and the ability to tailor these properties to specific applications. Therefore, in order to exploit these material to their fullest potential, it is essential to properly understand their behavior and limitations.

The use of thermoplastic composites (TPCs) in the aerospace industry has been accelerating as a result of the advantages that they present when compared to more mature available composite technologies such as fiber reinforced thermosets. This can be attributed to their increased toughness, increased service temperature, fast processing cycles, reprocessability, and recyclability [1]. Overcoming barriers such as development of affordable and fast automated processes and efficient joining techniques will allow more applications of TPCs in the aerospace industry [2]. For example, the new developments and research have enabled the use of TPCs in aircraft, like in the main wing leading edges of the Airbus A340 and A380, and the Gulfstream Aerospace G650's rudder and elevators [2]. This industrial application is expected to increase in the following years through the implementation of different programs which aim to increase the technology readiness level.

Due to their polymeric nature that consists of entangled chains, TPCs have the advantage that they can be welded, a process in which the interface is virtually erased and eliminates the need for discontinuities such as holes. There are multiple welding techniques available which have been traditionally used for thermoplastics (TPs) welding, and have evolved into the TPCs field [3]. Among these techniques, ultrasonic welding (USW) stands out for its fast processing times and increased cost efficiency compared to traditional joining methods [4]. USW consists on pressurizing the parts -or adherends- together and subjecting them to mechanical vibrations. The temperature rise is achieved by friction and viscoelastic heating, and energy can be concentrated at the interface by implementing asperities known as energy directors (EDs) [5]. In order to upscale this technique, more understanding of the key parameters involved in the process and the overall limitations is required. It has been proven that several parameters such as the frequency, amplitude, thickness and geometry of the ED, and geometrical misalignments influence the process [6–9]. However, to the knowledge of the author, the effect of the adherends' thickness is yet to be explored and therefore creates a gap on the knowledge of the process.

Thus, the motivation for this Master's thesis to contribute to the understanding of the role that the adherends' thickness plays in the USW process, which therefore represents a step towards developing a more robust technique for joining TPC structures.

1.2. Literature study

The following chapter summarizes the findings of a detailed literature study executed before the research activities.

1.2.1. Thermoplastic composites and welding techniques

Thermoplastics (TPs) are polymers that become liquid upon application of heat and can be remoulded into different shapes [10]. In a molecular level, they consist of multiple chains that are entangled and interact with each other via secondary bonds. TPs can be categorized, based on the arrangement of the chains, into semi-crystalline and amorphous, were semi-crystalline TPs are those whose chains are arranged in an organized fashion and form crystals.

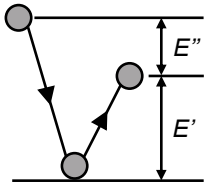

Figure 1.1: Storage ($E^{'}$) vs. loss ($E^{''}$) moduli. [11].

TPc will experience a viscoelastic behavior, meaning that they behave elastically when subjected to low temperatures and high strain rates, and viscous when applying small strain rates at elevated temperatures [10]. The example of a bouncing ball is often used to explain this behavior. The storage modulus ($E^{'}$) is a measure of how elastic the material is and -ideally- is equivalent to the Young's modulus (E)[1]. It can be related to the energy that the ball gives back (how high it bounces) [12] in Figure 1.1. On the other hand, the loss modulus ($E^{''}$) relates to the viscous response and the energy lost to friction and internal motions, represented as the height that is lost after the ball bounces [12, 13]. The ratio between the loss and the storage moduli is referred as the loss tangent $\tan(\delta) = \frac{E^{''}}{E^{'}}$ and is a measure of the energy dissipation potential of the material [10].

Because of this entanglement nature, TPs can be joined via fusion bonding, which is an alternative to more mature joining techniques such as mechanical fastening and adhesion bonding. Fusion bonding can be defined as the joining of two polymer parts by the fusion and consolidation of their interface, and the process can be described with the following steps [5]: surface preparation, heating, pressure, diffusion, and cooling. This technique eliminates some of the disadvantages of the other techniques such as short processing times, reduced surface preparation, and absence of foreign material at the interface [5].

Diffusion during fusion bonding can be better described with Figure 1.2. Intimate contact between the two parts is achieved by means of heat and pressure, where the asperities are flattened and wetting of the surfaces occurs. Upon achieving this contact, the barrier is eliminated and the polymer chains can move and diffuse with each other, a process than is referred as autohesion. After cooling down under pressure, the two parts have consolidated, where the mechanical strength of the joint develops and the interface itself is erased [14]. Heating can occur in bulk or in a localized fashion. The latter can be achieved by different welding techniques that are categorized based on their heating mechanism [15]: thermal, electromagnetic, and friction. Thermal welding occurs in two steps: heat applied to the individual surfaces which are then pressurized together [14–16]. In electromagnetic welding, the heating mechanism occurs via an electromagnetic field or electric current that melts the polymer at the interface and allows further diffusion [15]. Finally, friction welding uses frictional work as a heating mechanism while applying pressure to join the parts together.

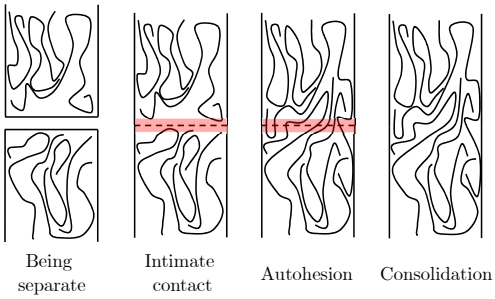

Figure 1.2: Fusion of two thermoplastic interfaces. Adapted from [14].

Because TPCs consist of embedded fibers in a TP matrix, they can also be welded by means of the techniques mentioned previously. However, the presence of the fibers can change the heating dynamics. For example, if the matrix is reinforced with carbon fibers (CFs), their high thermal and electrical conductivity may cause uneven heating, delamination, and geometrical distortion of the parts [5]. Nonetheless, there are promising welding techniques for fiber reinforced TPs such as resistance, induction, and ultrasonic welding [14–16]. Resistance and induction welding are part of the electromagnetic welding techniques, while ultrasonic welding (USW) is part of the friction welding techniques. From these three promising techniques, USW stands out for being fast and energy efficient [17] and therefore has the potential to be up-scaled in the future.

[1] In reality it is not because of the differences between both tests and methods used to calculate E and $E^{'}$ [12]

1.2.2. Ultrasonic welding

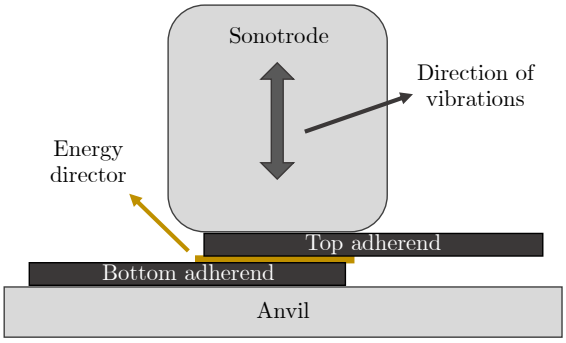

Figure 1.3: Principle of USW of TPCs.

USW is one of the most widely used welding techniques for thermoplastics joining [18]. It uses high frequency (≈ 20 - 50 kHz) and low amplitude (≈ 10 - 250 μm) sinusoidal mechanical vibrations [19, 20]. Figure 1.3 shows the principle of ultrasonic welding. The adherends to be joined are kept together against a flat surface (known as the anvil) by means of force imposed by the equipment. The mechanical vibrations are transferred via the sonotrode and can be applied transverse (plastic USW) or parallel (metal USW) to the interface. For TPCs, plastic USW is generally used [19]. In order to concentrate the vibrational energy at the interface, artificial asperities called energy directors (EDs) are placed between the two adherends [5]. These EDs are resin-rich features that are typically made of the same material as the polymer matrix. After this vibration phase, the adherends are allowed to cool down during the consolidation phase, where only pressure is applied. According to Benatar and Gutowski [3] USW is a process made up of five sub-processes, namely: (1) mechanics and vibrations of the parts, (2) viscoelastic heating of the TP, (3) heat transfer, (4) flow and wetting, and (5) intermolecular diffusion.

Figure 1.4 shows the diagram of a typical USW equipment. The energy is transformed to mechanical vibrations with a fixed frequency by the piezoelectric transducer, and are then transferred to the adherends by the sonotrode (or horn). The sonotrode is placed perpendicular to the welding interface, and the ratio of amplification will be determined by its shape. Because the sonotrode has a fixed amplification, a booster is placed in between. The product of the amplification ratios of the booster and the sonotrode will determine the overall amplification ratio. Finally, the force is applied by a pneumatic piston that is attached to the system. [21]. One of the ways in which USW can be classified is as spot, static, or continuous. Spot welding, as its name suggests, consists of relatively small spot welds - typically circular- that are used for joining parts. These spots can be analogous to mechanical fasteners, and both have been compared in literature [22–25]. The principle of static USW has been described previously, and its main difference with spot welding is that in the latter the welded area is smaller than the overlap [19]. Both spot and static welding can be sequential, meaning that the joint is composed of successive independent welds. Finally, continuous USW (CUW) is where the sonotrode is translated through the weldline, allowing high welding speeds [19]. Studies by Jongbloed et al. have greatly contributed to the understanding and development of this process [8, 26–29]. Because this thesis work will not deal with CUW, the further literature review will focus on static USW.

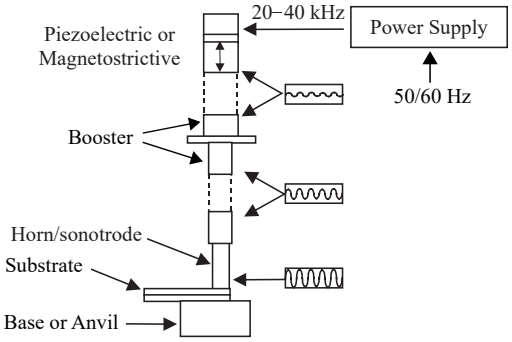

Figure 1.4: Setup of an USW equipment. Diagram adapted from [15].

Heating mechanism and the role of the energy director

The heating mechanism in USW comes from a combination of surface friction and viscoelastic heating [30]. Initially, when temperatures are below the the glass transition temperature (T_g) of the matrix, the process is dominated by interfacial friction heating which will be affected by the welding force and relative displacement between the ED and adherends [6, 31]. The force applied will increase contact between the surfaces, which has been shown to decrease the weld time [3]. The relative displacement will affect the vibration amplitude, which converts the transverse vibration to parallel displacement to the weldline by means of cyclic deformation of the ED [6]. Interfacial friction heating combined with thermal conduction will give the initial temperature rise at the interface to the T_g [32]. After this, the process is dominated by viscoelastic heating which, combined with thermal conduction of both the resin and fibers, will heat the interface above the T_g and spread the heat-affected zone. As suggested by its name, viscoelastic heating is possible in TPCs because the matrix will exhibit both elastic and viscous behaviours (as mentioned in Section 1.2.1). The material can

therefore be represented with a spring and damper in parallel, according to the Voigt-Kelvin model [33]. The viscoelastic heating rate ($\dot{Q}_v$) is given by:

$$\dot{Q}_v = \frac{\omega \cdot \varepsilon_0^2 \cdot E''}{2} \quad (1.1) \qquad \dot{Q}_v = e\frac{\omega \cdot \varepsilon_0^2 \cdot E''}{2} \quad (1.2)$$

This rate will be affected by the cyclic strain on the ED (ε_0), the loss modulus of the resin (E'') (which is dependent on the temperature and frequency, and the vibration frequency (ω in rad/s, f in Hz), as shown in Equation 1.1 [6]. This equation can be modified to account for the loss of contact between the sonotrode and the top adherend by including a term called the hammering efficiency (e) [30], as seen in Equation 1.2. This hammering efficiency is described as the ratio between the actual heat generation and the ideal heat generation (when no contact is lost) [30].

EDs therefore have the purpose of concentrating the heat generation at the interface, and both the relative movement between the ED and at least one of the adherends (surface friction), and a lower stiffness of the ED (viscoelastic heating) will ensure this heat generation [19]. The most recent geometries of EDs that have been studied are flat films [6, 7, 34, 35], woven or expanded meshes [8, 36], integration via fused deposition [37], and placing no ED at all [31, 38]. From all these energy directing options, the woven or expanded polymer mesh stands out. Jongbloed et al. [8] studied the weld uniformity in static and CUW by using a woven PPS mesh and comparing the results with a flat film. The mesh ED has a much higher compliance than the flat ED, which was believed to improve the weld uniformity and quality. It was found that the LSS increased (33.7 ± 2.4 MPa vs. 18.8 ± 6.2 MPa) and that there was more contact between the adherends and the ED. This contact is achieved by flattening of the mesh during the weld process, which does not occur when using flat films.

Parameters affecting USW

From a processing point of view, USW will be governed by the welding force (F_w), vibration amplitude (A), and vibration time (t) [19], which will therefore define the welding energy (E_w) as seen in Equation 1.3 [4, 39]. Wang et al. [39] concluded that the bonding efficiency and weld area increase with an increase in E_w until a threshold is reached. However, with a further increase of energy, the bonding efficiency will decrease due to material degradation as pores develop [39]. F_w and A will determine the rate at which heat is generated [19]; higher values will yield fast heat generation, and vice-versa. The vibration amplitude is related to viscoelastic heating via Equation 1.1, while the force relates to friction heating via Equation 1.4 [19] which defines the normal stresses (N) at each location of the welding interface. These can be divided into a static (N_s) and dynamic (N_d) component, which depend on F_w, the welding area (S_w), and the dynamic normal stress (σ_n) generated by the vibration applied during welding. Equation 1.5 [19] shows the lower limit for σ_n found by considering a vertical uniform sinusoidal deformation equal to the amplitude of the vibration divided by the thickness of the welding stack (t_w), where E'_w corresponds to the elastic modulus of the stack [19]. In USW the dynamic normal stresses are higher than the static ones [40], which would imply that the amplitude will have more effect on the welding time than the force. However, because the hammering effect is highly sensitive to different factors like the compliance and the welding force, studies have observed that the force plays a more influential role in the welding time than the amplitude since an increase of the force decreases the hammering effect [19, 35]. Therefore, a higher force causes more intimate contact between the adherends and ED [41] and increases the transmission of vibrations from the sonotrode the to the welding stack [19, 41]. Finally, the third factor affecting the welding energy is the welding time, which is one of the ways in which the process can be controlled for a given combination of amplitude and force. However, USW can be also be controlled by the dissipated energy or the sonotrode vertical displacement [19] and it has been found that controlling the process by either one of these parameters gives more quality results than controlling it by the time itself. In this case, the sonotrode displacement refers to the vertical travel from the initial point where the sonotrode touches the welding stack with a given force. Zhao et al. [22] found that a displacement-controlled approach was more robust for sequential spot welding, since it is less sensitive to external boundary conditions such as the welding jigs.

$$E_w = F_w \cdot f \cdot A \cdot t \quad (1.3) \qquad N = N_s + N_d = \frac{F_w}{S_w} + \sigma_n \quad (1.4) \qquad \sigma_n > \frac{A \cdot E'_w}{t_w} \quad (1.5)$$

Other parameters have shown to affect both the process response and weld quality, such as the consolidation time [42], misalignment of the adherends [9], crystallinity of the resin [11, 43, 44], and orientation of

the fibers for the case of unidirectional (UD) TPCs [45].

Process monitoring and weld quality

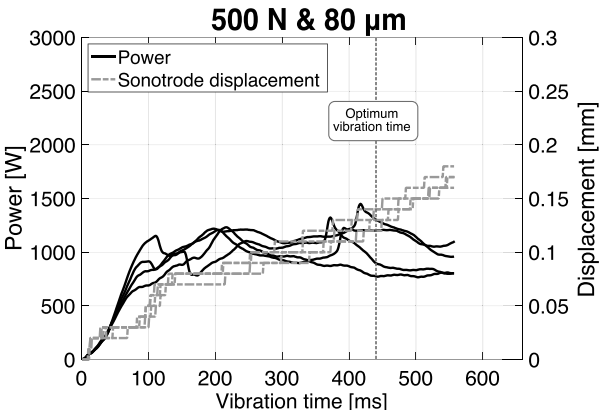

Figure 1.5: Typical power and displacement curves during USW with mesh EDs [28].

An advantage of USW is the easiness to perform in situ monitoring of the process, described as real-time and non-intrusive monitoring of one or more processing parameters [19]. The availability of welders with integrated micro-processors has facilitated the monitoring of the USW process and the different phenomena occurring by allowing the measurement of the dissipated power and displacement of the sonotrode. An example of this is Figure 1.5, which corresponds to the power and relative sonotrode displacement during USW of CF/PPS composites with 0.20 mm-thick woven mesh EDs [28]. In this figure, it can be seen the "optimum vibration time" is shown at around 450 ms. Different methodologies can be used to determine the optimum point of a weld for a given force and amplitude. Villegas [6, 35] followed a methodology that consists of stopping the process at different stages and analyzing the welds in terms of strength, fracture surface, and cross sectional microscopy in order to link the process response to the occurring physical phenomena during the weld. The author concluded that, for CF/PEI composites with flat EDs, the optimum point (best weld quality and higher LSS) occurs at the stage in which local melting of the adherends starts and the ED has squeezed so much that the weldline virtually disappears. Jongbloed et al. [28] used a similar methodology to determine the optimal vibration time in Figure 1.5. The author stopped at different times and defined an interval with high LSS values. The optimum time was then defined as the minimum time in this interval for which there were no non-welded areas as observed from the fractography analysis. For this case, and for other studies where mesh EDs were used [42, 46], the optimum vibration time was found to occur after the displacement plateau, therefore showing the potential of in-situ monitoring for obtaining quality welds. It is important to highlight that the value of the LSS alone should be combined with knowledge of other aspects (such as fracture analysis and cross sectional microscopy) in order for the results to be valuable [47].

Through-the-thickness heating

Through-the-thickness heating (TTH) refers to heating of the adherends during the ultrasonic welding process. This phenomena can lead to damage such as fiber and resin squeeze out and porosity, which may lead to a lower structural integrity of the weld [29]. Jongbloed et al. [29] suggested that a higher TTH may be the result of thermal conduction to the adherends caused by an increased interface temperature. In this study, the authors measured the temperature evolution at the interface and within the adherends using thermocouples, and compared the experimental results with a heat transfer (HT) model as can be seen in Figure 1.6. In this figure, there is a rapid temperature increase during the vibration phase in the experimental results, while the temperature increase occurs during the consolidation phase in the model. The discrepancy between the experimental results and the model was explained by the authors with the existence of an extra heating mechanism: bulk viscoelastic heating, which may occur because the ED loses its ability to concentrate the energy at the interface only once it has flatten and has a lower compliance [29]. Another important finding of this study is that the top adherend considerably heats more than the bottom adherend, which relates to the fact that the top adherend absorbs more vibrational

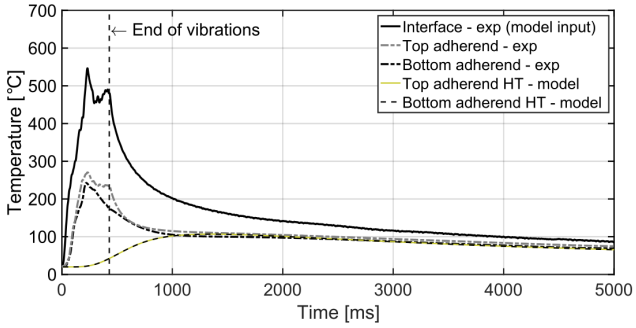

Figure 1.6: Temperature evolution during static USW of CF/PPS adherends and mesh EDs (500 N, 80 μm, 430 ms) [29].

energy than the bottom adherend, and therefore experiences more viscoelastic heating. Finally, reducing the energy input during the process -for example, by reducing the amplitude- showed to reduce the TTH.

1.2.3. Part thickness in ultrasonic welding

Near and far-field welding

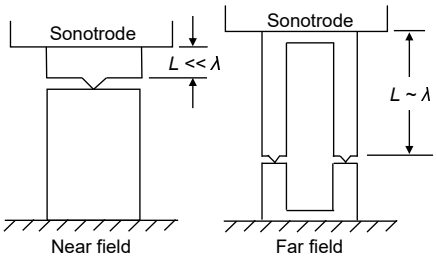

Figure 1.7: Accepted definition of near and far-field. Diagram adapted from [48].

An accepted industry standard is to divide USW into near and far-field, as shown in Figure 1.7. According to Benatar [48], in near-field welding the distance from the tip of the sonotrode to the interface L (therefore the thickness of the top adherend) is much lower than the wavelength (λ) in the adherends at 20 kHz, while in far-field this distance is of the same order as the wavelength. This will have an effect on the amplitude of the vibrations that reach the interface: during near-field the vibrations at this point are close to the amplitude of the vibrations that the sonotrode exerts, while during far-field this amplitude will depend on the wave propagation through the material [48]. The value of $L = 6$ mm has been defined as the distance that separates near and far-field USW for plastics which have a wavelength between 6 and 13 cm at 20 kHz [11, 48]. To the knowledge of the author, near and far-field USW have not been properly defined nor explored for TPCs.

Studies [41, 49, 50] have shown that it is more challenging to weld TPs in the far-field than in the near-field, especially for semi-crystalline TPs since they will internally absorb a percentage of the vibrations and it becomes harder to transmit the energy to the interface [4]. It was often found that during far-field welding the TP will melt at the sonotrode/adherend interface rather than at the welding interface due to the vibrational energy being too low to reach the ED and getting concentrated at the sonotrode contact instead. The authors also noticed that increasing the welding force is particularly important during far-field welding since it transmits more energy to the interface, and therefore stronger welds were obtained [49].

A more detailed explanation of near and far-field USW was not found in literature. Two main issues with this definition were identified. The first point of question is the definition itself. It sounds reasonable to divide the process according to how much of the vibrational amplitude reaches the interface, as it could give an indication of how feasible the process is for different thickness values. However, certain discrepancies were found in the reasoning behind choosing 6 mm as the turning point between near and far-field welding and the inconsistencies in some studies. The longitudinal wave speed for common thermoplastics ranges from approximately 1000 m/s to 2900 m/s [51]. At the operational 20 kHz frequency of the majority of the ultrasonic welders that are used in literature, the wavelength will indeed be in the order of 5 to 15 cm. If far-field welding occurs when the distance L is of the same order as the wavelength, then the minimum flipping point should also be in the order of [cm]. This is however not the case as the value for L is reported (and accepted in industry) as 6 mm, which is one order of magnitude less than the minimum wavelength in thermoplastics. In different studies on far-field ultrasonic welding of thermoplastics, this results on sample thicknesses that are nowhere near the wavelength of the material. For example, in the studies by Benatar and Cheng [49] and Liu et al. [50] the sample thickness was 30 mm and the material was HDPE (high density polyethylene), which has a wavelength of around 120 mm[2]. To the date, this reasoning (distance L of the same order as the wavelength in far-field welding) is still reported in literature [53].

The second point of question has to do with the origin of the definition of near and far-field ultrasonic welding. Even though Benatar [48] explained the reasoning behind this categorization, this author was not the first one to introduce the terms near and far-field ultrasonic welding. In fact, the earliest available literature[3] on ultrasonic welding of thermoplastics from the 1960s [54–56] already distinguished these two regions. Other terms found in literature to refer to near and far-field are "local" and "remote", and "direct" and "indirect" ultrasonic welding. A more in depth definition of these terms, aside from the distance from the sonotrode to the joint equal to 6 mm or 1/4 in, was not given in these articles. A common denominator,

[2] Speed of sound 2400 m/s [52] over the frequency of the equipment 20 kHz
[3] That the author was able to acquire

however, is that the weldability of multiple thermoplastics is given for both regions and in a qualitative and fairly subjective manner. For example, by using terms like "Poor" or "Fair-Good" to define whether a certain thermoplastic is suitable for welding in the near or far-field based on how efficiently they transmit the vibrations. The fact that this weldability was already defined is an indicator that even earlier studies were already dealing with this classification, however these may have not been published or are very challenging to find as the journals have not been -and most likely will not get- digitalized.

If the first point of question is ignored, the lack of more information on what defines the welds that are produced in a near-field configuration vs. a far-field configuration raises a gap in knowledge. Few indications were found in the available literature as presented earlier. Other authors have proposed other forms of determining the weldability of thermoplastics in these regions. Potente [57] proposed two indexes: the damping efficiency (measure of the reduction in amplitude when the distance between the sonotrode and the interface is one wavelength) and the energy factor (indicates how much energy will be required for the welding process) [57]. The author stated that thermoplastics with a high damping efficiency and energy index -therefore having an increased crystallinity- are then not suited for far-field welding.

When it comes to thermoplastic composites, even less information was found by the author on near and far-field welding or on the limitations of the top adherend's thickness. One thing can be taken for granted however: the presence of fibers affects the weldability of the materials. New effects are now relevant in fiber-reinforced composites, like complex wave reflection/refraction in the fiber-matrix or ply interfaces [58], anisotropy in the wave propagation [58], and thermal conductivity of the fibers. For example, material properties that are key during ultrasonic welding such as the loss modulus (affecting the viscoelastic heating rate) and loss tangent (affecting the wave attenuation) will be altered, as seen in Figure 1.8 where the DMA results for PEEK and CF/PEEK are presented. Even though there have been important efforts in understanding the propagation of the vibrations during the process [59–61], a complete comprehension of the effect of the fibers is not yet fully developed [53].

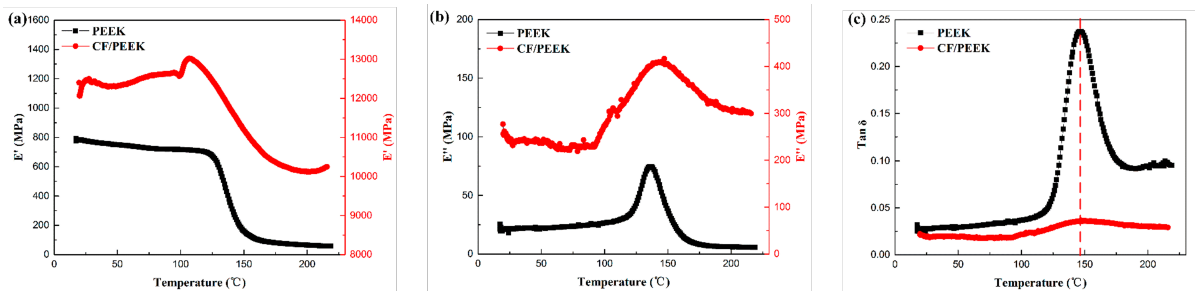

Figure 1.8: DMA results of PEEK and woven CF/PEEK composites. **(a)** Storage modulus (E') vs. temperature **(b)** Loss modulus vs. temperature (E'') **(c)** $\tan\delta$ vs. temperature. Image taken from [62].

Through-the-thickness wave propagation

During plastic USW, the waves transmitted to the parts are longitudinal and are generated by a sinusoidal displacement of the sonotrode with a peak-to-peak amplitude (A) and frequency (f). These waves will propagate through the welding stack, where the wavelength λ will be defined by Equation 1.6 [63] and depends on both the frequency and the speed of sound in a given material (c).

$$\lambda = \frac{c}{f} \tag{1.6}$$

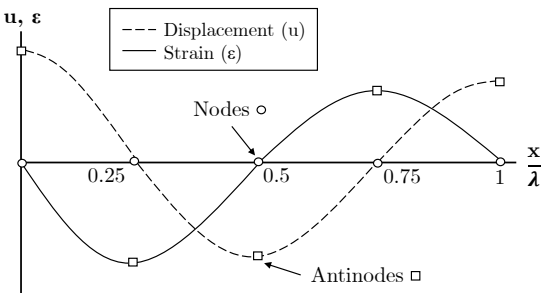

Figure 1.9: Typical displacement and strain in one wavelength (λ) of a linear viscoelastic material where x is the distance from the source of the wave. Diagram based on [49].

In linear viscoelastic materials, the longitudinal ultrasonic waves will propagate through the material and create displacement (u) and strain (ε) fields like seen in Figure 1.9. Because of the viscoelastic nature of TPs, the strain will lag with respect to the displacement, which can be considered as a damping process resulting

in the sinusoidal response of both u and ε being out of phase with respect to each other [10]. Some authors [49, 64–66] have suggested that for far-field welding where triangular EDs are present, the interface should be at a displacement antinode for maximum heating at the ED. Experimental tests have supported this theory, where stronger welds were obtained when positioning the interface at these points [49]. Furthermore, it has also been theorized that, for parts that are being welded with EDs, a very low percentage of the waves will be transmitted through the interface due to a low impedance [49]. From Figure 1.9 it can also be seen that the displacement and strain amplitudes decrease as x/λ increases. This behavior is referred as attenuation and it can be explained in linear viscoelastic materials by solving the time and distance-dependent harmonic 1-D wave equation that considers the material properties. According to literature [67], this attenuation depends on the time and distance from the sonotrode and is given by:

$$u(x,t) = u_0 \exp(-ax + i\omega(t - x/c)) \qquad (1.7) \qquad\qquad a = \frac{\omega \tan\delta}{c} \qquad (1.8)$$

Where u is the amplitude of vibration in the material, u_o is the amplitude exerted by the sonotrode, a is the damping coefficient, ω is the vibration frequency, c is the wavespeed in the material, and $\tan\delta$ is the loss tangent. This attenuation will be significant while welding in the far-field [48]. In contrast, it will not be relevant during near-field welding, where wave propagation can be neglected and the problem can be modelled using lumped masses with Voigt-Kelvin elements [41, 48].

Besides the simplified model of Benatar and Cheng [49] for wave propagation, other authors have also aimed to model this wave transmission during USW. One example is the study by Li et al. [59], where the purpose was to predict the weld quality during USW of CF composites without EDs by linking the wave transmission with the equipment output (power and displacement), the force, and the amplitude. The model considers the wave transmission and reflection when travelling from one media to another, and low errors when validating the model were obtained when a good contact condition is achieved during the experimental process.

Thickness in previous studies

Bhudolia et al. [4] commented on the feasibility to weld thick parts due to the difficulty for the vibrations to penetrate enough in order to achieve a quality weld [68]. The authors also mentioned that, according to Wagner et al. [69], the current thickness limitation -due to the power of the equipment- is around 3 mm. However, when corroborating this information from the article of Wagner et al. [69], it was noted that this limitation was established for metal USW and not plastic USW, even though the article of Bhudolia et al. [4] specifically regarded USW of TPCs.

In a study by Villegas [35] it was stated that when changing the welding configuration, the optimum welding energy would have to be redefined, but the optimum travel will be relatively insensitive to those changes. This, because the travel is related to the physical changes that occur at the interface and is therefore independent of the energy dissipated to the surroundings [35]. This was validated by doubling the thickness of the original CF/PEI adherends (1.92 mm to 3.84 mm) and comparing both the strength and welder output when applying 300 N of force and 86.2 μm of amplitude while using flat EDs. Both adherends had an optimal weld at the same stage (40% travel) and experienced the same type of failure. The main differences were found to be the dissipated energy and the LSS, where both values increased for the 3.84 mm adherends. In composite laminates, the bending stiffness is known to increase if the thickness increases [70], which will therefore reduce the bending moments at the edges of the joint [35] and can explain the increase in LSS. On the other hand, the difference in energy between the two samples indicates that the processing parameters required to obtain optimal welds would need be changed if an energy-controlled process had been used.

1.3. Conclusions from the literature study

USW is a fusion bonding technique that shows great potential for joining TPCs structures by creating strong and high quality joints [3, 6, 28, 35]. This process uses ultrasonic waves to heat up the interface while concentrating the vibrational energy at the interface by implementing EDs. The geometry of these EDs will greatly impact the strength and quality of the weld. The most recent studies have shown that using mesh EDs increases the weld uniformity and strength of the joint [8, 36]. The process can be monitored with the output of the equipment (power and displacement) and it can be linked to the physical phenomena occurring and the

strength of the joint, where the optimum point can be determined [6, 28, 35]. The effect of the processing parameters, consolidation time, thickness and geometry of the EDs, manufacturing misalignments, crystallinity of the materials and joint, and fiber orientation for UD reinforcement has been investigated in previous studies [6, 8, 9, 11, 28, 34, 35, 42, 44, 45]. However, limited literature was found on the effect of the adherends' thickness for USW of TPCs. For TPs, an accepted division of the process according to the thickness of the top adherend is near and far-field. Far-field USW refers to the type of welding in which the thickness of the top adherend is such that the wave propagation and attenuation through the material will play a relevant role, and is therefore more challenging to achieve. However, no literature was found on the meaning of near and far-field welding for TPCs. Because of this gap of knowledge in the topic, a thesis that investigates the effect of the adherends' thickness was done, with the ultimate goal of gaining understanding on the role that this thickness plays for TPCs.

1.4. Research questions

Based on the conclusions from the literature study, the main research question is:

What is the effect of the adherends' thickness on the process response and weld evolution under different process parameters during static ultrasonic welding of thermoplastic composites with fabric and UD reinforcement?

This main research question can be divided into the following specific questions and sub-questions:

1) What are the effect and limitations of the top adherend's thickness?
- **a**) What defines the thickness limitation of the top adherend?
- **b**) How sensitive are the process response and weld evolution to the thickness change of the top adherend?
- **c**) How does changing the thickness of the top adherend affect the wave propagation through the welding stack?

2) What are the effect and limitations of the bottom adherend's thickness?
- **a**) Do the results obtained when welding different thicknesses suggest that there will be a maximum thickness limitation for the bottom adherend?
- **b**) How sensitive are the process response and weld evolution to the thickness change of the bottom adherend?
- **c**) How does changing the thickness of the bottom adherend affect the wave propagation through the welding stack?

3) How will the effect of the thickness change for different force and amplitude values?

4) How applicable is the accepted industrial definition of near and far-field ultrasonic welding to thermoplastic composites?
- **a**) What quantitative and qualitative data could define the change from near to far-field welding of thermoplastic composites?
- **b**) Will the near and far-field regions be the same for all force and amplitude combinations or is it dependent on the processing parameters?

5) Will changing the fiber architecture (from fabric to UD) influence the effect and limitations of the adherends' thickness?

1.5. Research methodology

As can be seen from the research questions, the effect of the bottom and top adherends' thickness on the process response (behaviour of the process variables during welding) and weld evolution (physical changes occurring at the adherends or ED) were investigated separately. This was executed by keeping the thickness constant for one adherend while varying the other adherend's thickness with an initial set of force and amplitude values. The research subquestions were posed under the hypothesis that the top adherend will have a thickness limitation (based on the findings of the literature study), while it was unsure whether the bottom adherend's thickness will be limited or not. Considering the initial results, the process parameters were

changed for specific thickness values and the process response and weld evolution were analyzed again. A detailed explanation of the methods used for this analysis will be given in Chapter 2. The previous activities were performed with adherends having a fabric reinforcement and, based on the knowledge gained during this stage, specific thicknesses and process parameters were then chosen for the investigation of the thickness effect for adherends with UD reinforcement. This final stage is considerably less extensive as it aims to give an initial understanding of the differences of the thickness effect between fabric and UD adherends.

1.6. Report outline

Chapter 2 presents the materials, experimental setup, and different analysis methods that were used for this research. In Chapter 3 the results are presented following an order that is congruent with the research questions presented previously: effect of the bottom adherend, effect of the top adherend, process response when changing the parameters, and comparison between the effect of the thickness when using adherends with fabric and UD reinforcement. Once the results have been presented, a discussion will take place in Chapter 4 following also a storyline related to the research questions. Finally, Chapter 5 summarizes the findings while answering the research questions and gives some recommendations for future work on the effect of the adherend's thickness during USW of TPCs.

2

Materials, setup & analysis methods

All the equipment used for the manufacturing of the materials, the experimental activities, and the analysis methods are located in the Delft Aerospace Structures and Materials Laboratory (DASML) at Delft University of Technology (Delft, The Netherlands).

2.1. Materials

2.1.1. Adherends

The material used for the adherends was Toray TC1225 CF/LMPAEK (carbon fiber reinforced low-melt polyaryletherketone) provided by Toray Advanced Composites in The Netherlands. CF/LMPAEK was used for this research because of its low melting temperature (T_m) and because many of the current projects within the Composites Welding Group from TU Delft use CF/LMPAEK. For the fabric adherends, the reinforcement was a 5 harness satin fabric, while the UD adherends had a uni-directional reinforcement. Some properties of both materials are shown in Table 2.1.

Table 2.1: General properties of TC1225 CF/LMPAEK. Information provided by Toray.

Property	**Value fabric**	**Value UD**
Fiber	T300JB carbon	T700 carbon
Fiber areal weight [g/m^2]	277	194
Resin content [%]	42	34
Density [g/cm^3]	1.532	1.587
Consolidated ply thickness [mm]	0.31 ± 0.02	0.185 ± 0.016
Glass transition temperature [°C]	147	
Melting temperature [°C]	305	
Processing temperature [°C]	340 - 385	

The thicknesses and stacking sequences for the different adherends can be seen in Table 2.2. For the fabric-reinforced adherends, 0° is the direction of the warp yarns and 90° is the direction of the weft yarns, meaning that the apparent main orientation of fibers was kept parallel to the longitudinal direction of the adherends. For the UD-reinforced adherends, the 90° was kept adjacent to the weldline. This decision was made based on the results by Köhler et al. [45], were it was found that this configuration provides a more uniform heat distribution during USW and reduces the edge defects.

The impregnated rolls were cut in a GERBER cutting machine with a knife cutter. For the fabric laminates, the roll was cut into 580 mm × 580 mm plies, while for the UD laminates it was cut into 580 mm × 290 mm plies that were then joined to make 580 mm × 580 mm plies. These were then stacked and tacked with a spot welder to avoid movement during consolidation, and the edges were covered in aluminum foil to prevent leakage of the matrix into the press. The stacked plies were sandwiched between two stainless steel plates which were previously cleaned with a degreasing agent (Hyso QD) and Marbocote 227CEE release agent, and then sandwiched again between two isolated graphite plates to provide a uniform heat distribution over the

entire laminate during consolidation. The fabric-reinforced laminates were consolidated in a hot platen Joos press at 365°C and 10 bar for 30 min, and the UD-reinforced laminates were consolidated at 370°C and 10 bar for 50 min. The heating and cooling rates for both cycles was 7 °C/min. For the cases of higher thicknesses, thermocouples were placed at the edges and at the symmetry line of the stacked plies in order to check if the required temperatures were reached at these points.

Table 2.2: Thicknesses used for the adherends.

Reinforcement	Nominal thickness [mm]	Layup	Number of plies
Fabric	1.17	$[(0/90)_2]_S$	4
	1.83	$[(0/90)_3]_S$	6
	2.37	$[(0/90)_4]_S$	8
	3.55	$[(0/90)_6]_S$	12
	4.72	$[(0/90)_8]_S$	16
	5.79	$[(0/90)_{10}]_S$	20
UD	1.10	$[90/0/90]_S$	6
	1.85	$[90/(0/90)_2]_S$	10
	3.67	$[(90/0)_{10}]_S$	20

The quality of the 580 mm × 580 mm consolidated laminates was evaluated by means of a C-scan. Finally, the laminates were cut in a water-cooled Proth grinding machine with a diamond blade into single lap-shear adherends with dimensions of 25.4 mm × 101.6 mm. The final cut adherends can be seen in Figure 2.1.

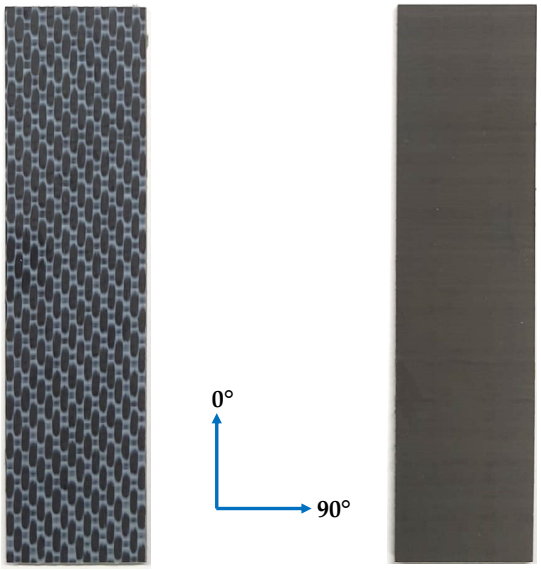

Figure 2.1: Adherends. Fabric 1.83 mm-thick (left) and UD 1.85 mm-thick (right).

2.1.2. Energy directors

Considering the conclusions from Section 1.3, a plain-woven LMPAEK 500 μm mesh provided by Victrex was used for the EDs. These were cut into rectangles with dimensions slightly larger than the overlap (25.4 mm × 12.7 mm). Before welding, both the adherends and EDs were cleaned with a degreasing agent Hyso QD.

2.2. Experimental setup

A VE20 Slimline dialog 6200 welder from Herrmann Ultrasonics with a frequency of 20 kHz was used for ultrasonic welding, as can be seen in Figure 2.2a. The rectangular sonotrode has a contact area of 15 mm × 30 mm and a gain of 1:1.7, and the booster has a gain of 1:2. The equipment can provide a peak-to-peak amplitude of 86.2 μm and a force between 130 and 2500 N. Thanks to the microprocessor, the power can be adjusted to keep the amplitude constant during the vibration phase, and can also provide in-situ data such as the sonotrode displacement, power, and consumed energy within time intervals of 1 ms. The evolution of the

process parameters (namely force, amplitude, and frequency) during vibration is also an output of the equipment. In particular, the power, displacement, and amplitude curves will be shown in the Results section. The equipment gives the option to control the process by displacement, time, or energy. Both displacement and time control were used for this study.

The jig, identified by the name Z-51414S, used for welding can be seen in Figure 2.2b. This jig is designed for welding of single lap-shear adherends. These adherends have dimensions of 25.4 mm × 101.6 mm and an overlapped joint of 25.4 mm × 12.7 mm. The alignment of adherends and clamps is ensured by placing pins, which locate the center of the overlap at the center of the sonotrode. The clamps are tightened with a torque of 14 N·m and the distance between the center of the overlap and the middle of the clamps (55 mm) is kept constant for all experiments unless indicated otherwise. To ensure parallelism between the bottom and top adherends, a dummy adherend (with a thickness equal to the bottom adherend) and ED are placed below the top adherend. Finally, in order to avoid bending of the clamps, aluminum supports are placed below the clamps at both ends.

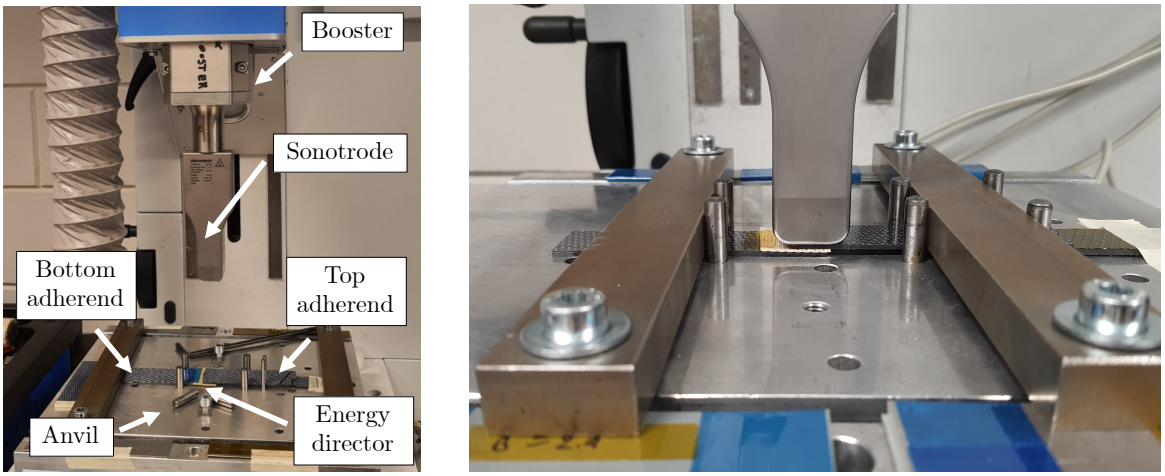

(a) Ultrasonic welding equipment.

(b) Ultrasonic welding setup.

Figure 2.2: Setup and equipment.

K-type thermocouples (GG220-2K-0, product number 2-2200-0004 provided by Tempco B.V., Bodegraven, the Netherlands) were used to obtain the evolution of the temperature during the welding process. These thermocouples (TCs) have an outer diameter of 0.70 mm and a wire diameter of 0.10 mm. They were placed at the adherends (for which holes needed to be drilled at the edges) and at the interface. The holes drilled for the adherend thermocouples had the dimensions shown in Figure 2.3a, while the interface thermocouples were placed at the center of the overlap, as shown in Figure 2.3b. The thermocouples were connected to an analog amplifier and the readings were sampled at a frequency of 1 kHz. The temperature measurements were either done with the three thermocouples at the time (bottom adherend, interface, and top adherend) or only with interface thermocouples. The original data was filtered in Matlab using a moving average filter with a window size of 20 points.

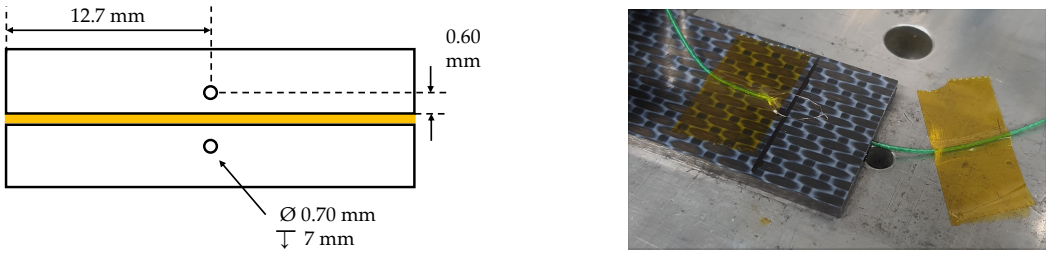

(a) Position of the TCs in the adherends.

(b) TCs at the interface and bottom adherend.

Figure 2.3: Thermocouples (TCs) setup.

2.3. Analysis methods

Besides the power, displacement, and amplitude data obtained from the welder and the temperature readings from the thermocouples, different methods were used to analyze the results.

2.3.1. High speed camera

A Photron FASTCAM NOVA S Series high speed camera was use to record the welds in slow motion. A rate of 1000 frames per second and a shutter speed of 0.1 μs was shown to be sufficient to capture the required phenomena occurring during vibration. Because it is not possible to show the media in this report, images at different times during vibration will be shown.

2.3.2. Cross-sectional microscopy

The welded specimens were cut with a diamond blade in a Struers Secotom-10 cutting machine in the orientation as shown in Figure 2.4. These specimens were not consolidated as the purpose is to only see the phenomena occurring during the vibration phase. This orientation was chosen from the high-speed camera recordings, which will be shown in the results section. The location of the cut was chosen based on where the damage occurred. If no damage was visible, then the cuts were made in the center of the overlap. In the micrographs, the left edge corresponds to the edge that is on front in the configuration shown by Figure 2.2. The cut specimens were then embedded in a clear resin-hardener "EpoFix" mixture, with a weight resin-to-hardener ratio of 175:21, and set to cure for over 12 hours. In order to remove entrapped air in the resin, the pouring of the mixed resin was made in a Struers Citovac vacuum. Once cured, they were ground and polished in a Struers Tegramin 20 Polishing machine. The grinding and polishing cycle was the following:

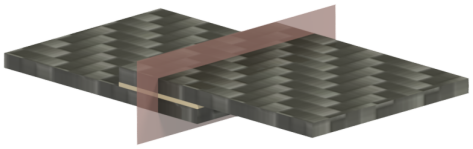

Figure 2.4: Cross section used for microscopy analysis

1. SiC grinding paper with 320 grit for 1 minute
2. SiC grinding paper with 1000 grit for 1 minute
3. SiC grinding paper with 2000 grit for 1 minute
4. Polishing in a diamond suspension with particle size of 3 μm with a colloidal silica suspension (OP-S NonDry) for 4 minutes.
5. Polishing in a diamond suspension with particle size of 1 μm with a colloidal silica suspension (OP-S NonDry) for 3 minutes.

Once the samples were prepared, they were inspected in a Keyence VK-X1000 3D laser scanning confocal microscope and a 10-times magnification.

2.3.3. Speed of sound measurements

In order to relate the wavelength in the material to the thickness of the adherends, the speed of sound was measured. This was done with an ultrasonic testing equipment Olympus Omniscan MX with a phased array technology. The method used for this was a pulse-echo, for which the principle can be seen in Figure 2.5. The sample is placed on top of a smooth plain surface and a probe (which acts as both the transmitter and receiver) is positioned on top with the required amount of coupling gel. First, it generates ultrasonic waves (represented as the pulse) at a frequency of 5 MHz that travel through the thickness of the sample. When these waves reach the sample/table interface, a portion of them will get reflected (represented as the echo) and the signal will be received by the probe. The speed of sound (c) can be calculated as the thickness of the sample over the time-of-flight of the wave, and the wavelength at 20 kHz can be calculated using Equation 1.6.

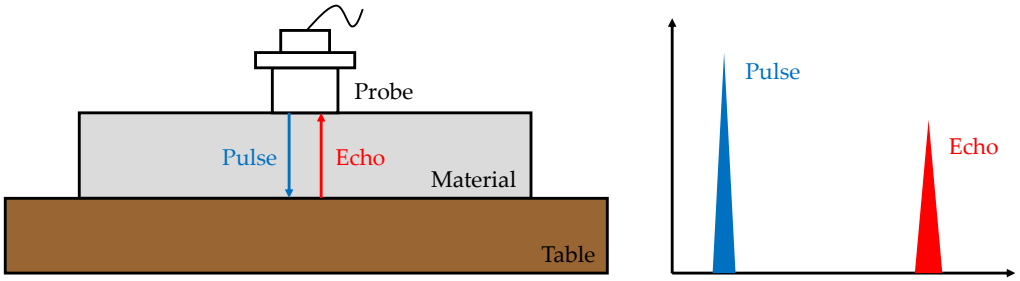

Figure 2.5: Schematic of the pulse-echo method.

2.3.4. COMSOL Multiphysics 5.6 models

In order to gain more understanding on the role of the thickness, simple models in COMSOL Multiphysics 5.6 were built to further understand the role of the thickness in the process. Figure 2.6 shows the parts that were considered for these models.

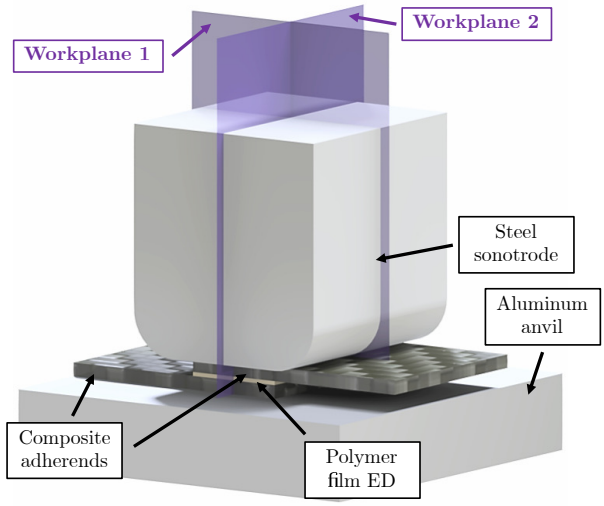

Figure 2.6: 2D views used for the COMSOL models.

Heat transfer model

A 2D heat transfer model was built to examine the effect of the bottom adherend only from a heat conduction point of view. The reasoning behind only choosing the bottom adherend will be explained in Chapter 4. Workplane 2 from Figure 2.6 was used since the position of the thermocouples in the experimental setup corresponds to this cross section. The model was built as in the study on through-the-thickness heating in CUW by Jongbloed et al. [29], in which a 2D transient heat transfer model was used based on the heat transfer equation:

$$\rho C_p \frac{\partial T}{\partial t} = k\nabla^2 T \tag{2.1}$$

Where $\rho, C_p, k, T,$ and t are density, heat capacity, conductivity, temperature, and time. Because the thickness of the ED is very thin compared to the adherends, it is neglected in the model. The geometry and boundary conditions can be seen in Figure 2.7. The different domains (sonotrode, top adherend, bottom adherend, and anvil) are made into a union, in which they are connected and share boundaries with the neighbouring domains. The input temperature comes from experimental measurements when placing thermocouples at the interface, and a thermal contact is applied at the sonotrode/adherend and anvil/adherend interfaces in order to evaluate the joint conductance at two surfaces in contact. For the definition of this thermal contact, the following values were assumed: 1.6 MPa of pressure, surface roughness average height of 1 μm, surface roughness average slope of 0.2, and Brinell hardness of 3 GPa. The remaining parameters were set as the default values [71, 72]. Finally, the other boundaries are thermally insulated, which could exaggerate the heat

transfer to the adherends since there is no heat dissipation to the environment [29]. In order to determine the temperature evolution, probes are located at the same distance as the experimental thermocouples (0.6 mm from the interface) at both the top and bottom adherends. The properties of the materials can be seen in Table 2.3.

The values for steel and aluminum were obtained from the COMSOL database for steel 1040 and aluminum 5083. The values for the CF/LMPAEK adherends were obtained from the provider's datasheet [73], and are given as a function of the temperature. Therefore, the properties are given to the model as an interpolation function. The conductivity of the composites corresponds to that of the thickness direction.

Table 2.3: Material properties used for the heat transfer model.

	Density (ρ) [kg/m^3]	**Heat capacity** (C_p) [J/kg · K]	**Thermal conductivity** (k) [W/m · K]
Steel sonotrode	7860	480	52
Aluminum anvil	2665	955	120
CF/LMPAEK adherends	Figure 2.8	Figure 2.8	0.74 @ 20°C 0.91 @ 200°C

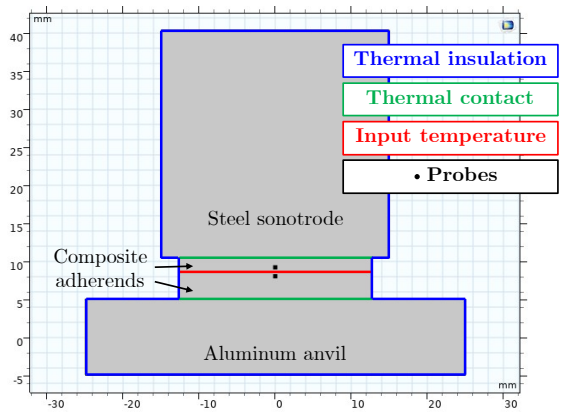

Figure 2.7: Geometry and boundary conditions for the COMSOL heat transfer model.

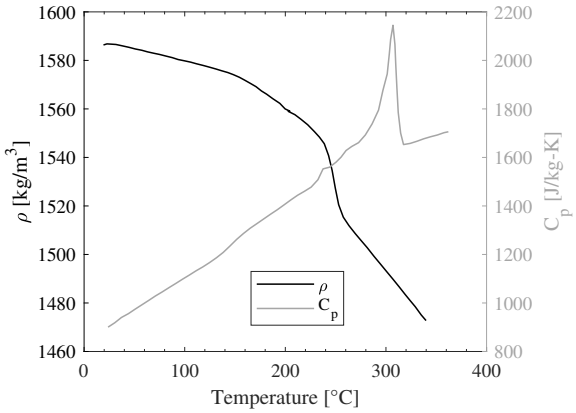

Figure 2.8: Density and heat capacity of the CF/LMPAEK adherends [73].

Wave propagation model

A 3D wave propagation model was built to visualize the effect of the thickness on the ultrasonic wave propagation though the welding stack. The solid mechanics module was used for this model as similar approaches for modelling wave propagation were found in literature [74–76]. The model is based on the following solid mechanics equation [77]:

$$\rho \frac{\partial^2 \mathbf{u}}{\partial t^2} = \nabla_X (FS) + \mathbf{F}_V \tag{2.2}$$

Where ρ, u, t, F, S, and F_V correspond to the density, displacement, time, deformation gradient, stress tensor, and body force. A plane-strain approximation was considered for this model. Figure 2.9 shows the geometry and boundary conditions as seen from the front in a 2D view. Because the purpose of the simplified model is to visualize the wave propagation through the welding stack, no contact was assumed between the sonotrode, adherends, ED, and anvil. This means that the model does not account for slippage and friction. Therefore, these domains were made into a union as in the heat transfer model. The clamps were modelled as fixed supports under the idealization that no horizontal or vertical movement at the clamp occurs. The distance between these supports to the center of the sonotrode is the same as the experimental setup (55 mm as was mentioned in Section 2.2). The lower edge of the anvil is also modelled as a fixed support. The sonotrode exerts half a sinusoidal displacement (only compression) as shown in Figure 2.9.

The properties of the materials can be seen in Table 2.4. The properties of the sonotrode, anvil, and film ED were obtained from the COMSOL database for steel 1040, aluminum 5083, and AvaSpire AV-621 low-melt flow PAEK. To simplify the model, the CF/LMPAEK adherends were considered isotropic with a Young's modulus equal to the transverse modulus as the adherends are loaded transversely in compression. This simplification has been done before in literature [78, 79]. The transverse modulus (E_{comp}) was calculated like in the study of Levy et al., where a rule of mixtures proposed by Jacquet et al. [80] is used:

$$E_{\text{comp}} = \frac{E_f E_m}{E_m + E_f\left(1 - \sqrt{V_f}/\sqrt{V_f}\right)} + \left(1 - \sqrt{V_f}\right)E_m \tag{2.3}$$

Where E_f is the modulus of the fibers (taken as 230 GPa [81]), E_m is the modulus of the LMPAEK resin (see Table 2.4), and V_f is the fiber volume content (taken as 0.58). The Poisson's ratio was taken as 0.4 [78].

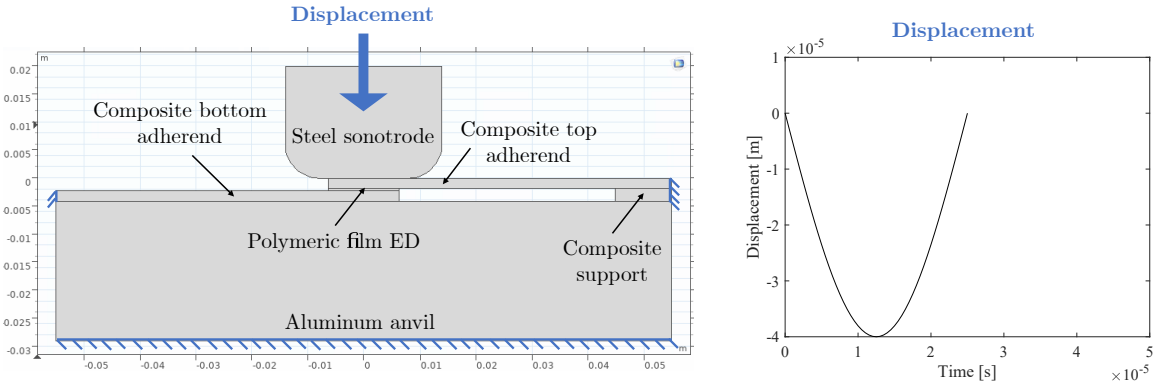

Figure 2.9: Geometry and boundary conditions for the COMSOL wave propagation model.

Table 2.4: Material properties used for the wave propagation model.

	Density (ρ) [kg/m^3]	**Young's modulus (E) [GPa]**	**Poisson's ratio (ν) [-]**
Steel sonotrode	7860	205	0.28
Aluminum anvil	2665	69	0.33
CF/LMPAEK adherends	1532	13.3	0.40
LMPAEK film	1290	3.1	0.39

The mesh was built with triangular elements. A minimum size (h_{min}) of 12 elements per wavelength, and a maximum size (h_{max}) of 6 elements per wavelength was taken [82]. The value of the wavelength was calculated using Equation 1.6, where the wave speed (c) corresponds to the minimum value of the pressure (c_p) and shear (c_s) wave speeds across all domains [77]:

$$c_p = \sqrt{\frac{E(1-\nu)}{\rho(1+\nu)(1-2\nu)}} \tag{2.4}$$

$$c_s = \sqrt{\frac{E}{2\rho(1+\nu)}} \tag{2.5}$$

Where E, ν, and ρ are the Young's modulus, Poisson's ratio, and density. The time stepping (Δt) is recommended to be T/60 [83], where T is the period of the wave. If the mesh size and the time steps follow the aforementioned rules, the Courant-Friedrichs-Lewy (CFL) relation show in Equation 2.6 is around 0.1, which gives near optimal results [83].

$$CFL = \frac{c_{\text{max}}\Delta t}{h_{\text{max}}} \tag{2.6}$$

Because of all the assumptions made to built this model (isotropic and elastic composites, solid ED, only elastic analysis, and no friction), the results will be analyzed qualitatively as they do not represent what the actual experimental welding is. The model is meant to give more understating of the role of the thickness on wave propagation. Therefore, the sonotrode does not exert the static force but only the sinusoidal displacement at 20 kHz and 80 μm of peak-to-peak amplitude.

3

Results

The results in this chapter are presented according to the order of the research questions: effect of changing the top adherend's thickness (Section 3.1), effect of changing the bottom adherend's thickness (Section 3.2), effect of changing the process parameters (Section 3.3), and effect of the thickness when changing from fabric to UD reinforcement (Section 3.4). How these results contribute to answering the research questions will be discussed in Chapter 4. Throughout this chapter, the top adherend's thickness is presented with the letter "T", and the bottom adherend's thickness is presented with the letter "B".

3.1. Effect of changing the top adherend's thickness

The adherends used for this part of the research have a fabric reinforcement (see Table 2.2). An initial set of force and amplitude values (500 N, 80 μm), and the bottom adherend's thickness (B = 1.83 mm) were kept constant so that only the effect of changing the top adherend's thickness was evaluated.

3.1.1. Power and displacement

Figure 3.1 shows representative power and displacement curves for each thickness of the top adherend. The individual power and displacement curves for multiple samples with the same thickness can be seen in Appendix A (Figure A.1). The adherends were welded until the displacement of the sonotrode was equal to the thickness of the ED (referred to as a 100% displacement).

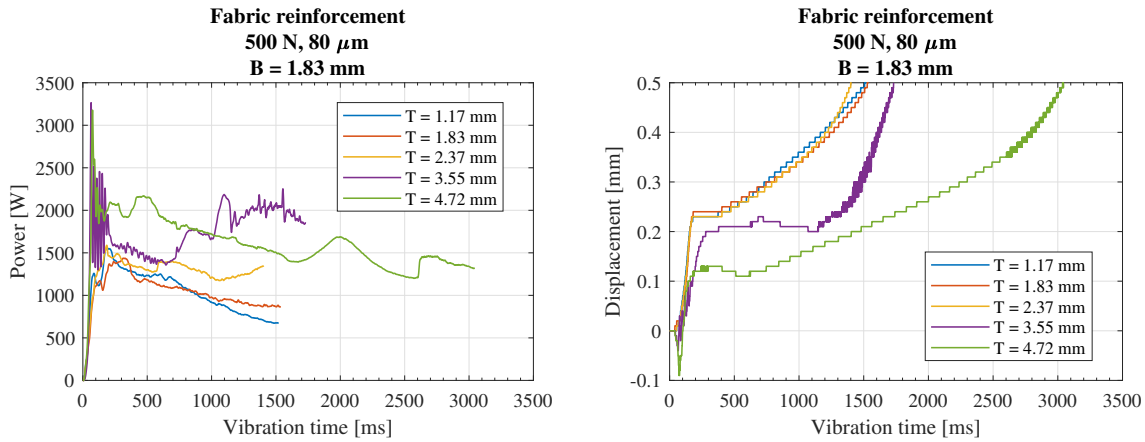

(a) Power curves

(b) Displacement curves

Figure 3.1: Representative power and displacement curves for different thickness of the top adherend at 100 % displacement (travel of the sonotrode equal to the thickness of the ED).

A quick examination of these curves reveals that both the power and displacement follow a same trend for thinner adherends (1.17 mm, 1.83 mm, and 2.37 mm), whereas the behaviour changes abruptly for the thicker ones (3.55 mm and 4.72 mm). To show how unstable the process is with the thicker values when compared

to the thin ones, multiple curves for the thicknesses of 2.37 mm, 3.55 mm and 4.72 mm are presented in Figure 3.2. Only two welds were possible for a thickness of 4.72 mm as, in some occasions, the equipment was not able to vibrate.

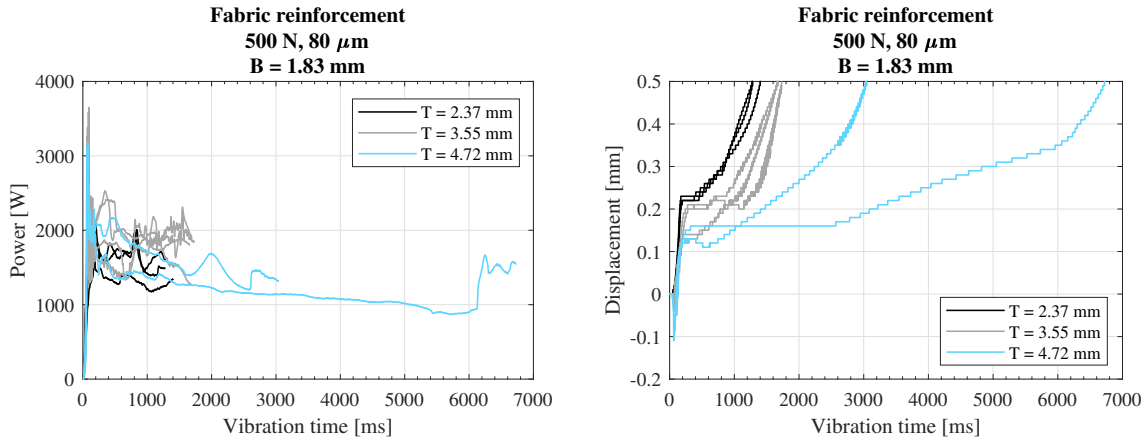

(a) Power **(b)** Displacement

Figure 3.2: Multiple power and displacement curves for top adherend thicknesses of 2.37 mm, 3.55 mm, and 4.72 mm at 100% displacement (travel of the sonotrode equal to the thickness of the ED).

From Figure 3.1b it can be seen that there are three distinctive regions: an initial increase of the displacement, a displacement plateau, and a final increase in displacement. This behaviour is characteristic for static USW with mesh EDs as seen in literature [8, 28, 84], where the optimum time is found somewhere after the displacement plateau when welding CF/PPS adherends. An example portraying this behaviour was already shown in the literature study (Figure 1.5 in Section 1.2). The explanation of the relationship between the physical phenomena with the power and displacement curves will be given in Chapter 4. However, addressing these stages is relevant for further results regarding the weld evolution.

3.1.2. Amplitude

Figure 3.3 shows representative amplitude and displacement curves for top adherend thicknesses of 1.17 mm, 2.37 mm, and 3.55 mm and 100% displacement. Multiple amplitude curves for all the thicknesses presented previously can be found in Appendix B (Figure B.1).

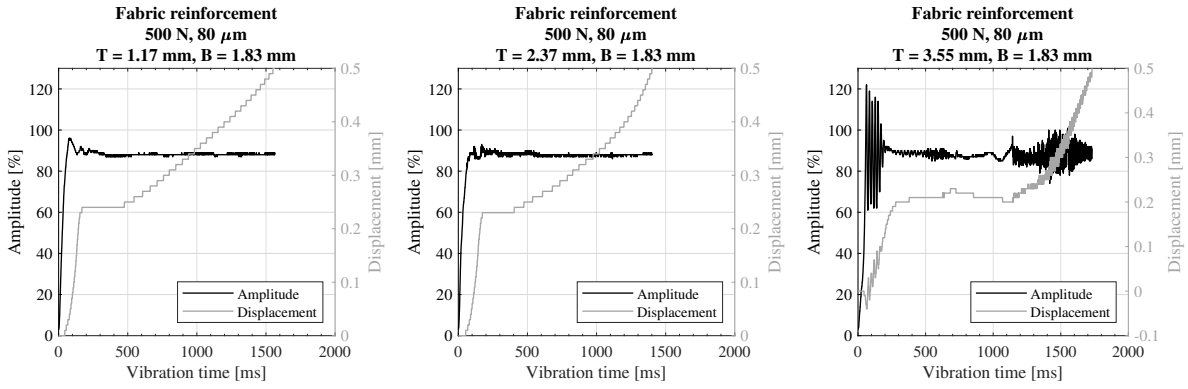

(a) T = 1.17 mm **(b)** T = 2.37 mm **(c)** T = 3.55 mm

Figure 3.3: Amplitude and displacement curves for different thicknesses of the top adherend. The nominal amplitude was 80 μm (88% of the maximum amplitude the equipment can provide).

It is clear that the process response is greatly affected by the change of the top adherend's thickness. In order to evaluate the weld evolution and visualize the changes between the thin and thick adherends, some 100% welds were recorded with the high-speed camera (HSC) and are presented in the following section.

3.1.3. High-speed camera snapshots

The evolution of the weld at different moments of the displacement curve was evaluated for top adherends with thicknesses of 1.17 mm, 2.37 mm, and 3.55 mm. The reason for choosing these values is to compare the evolution of two thin adherends (and check if a similar behaviour is followed), and see what changes occur for the thickness value at which the behaviour is different. Because sometimes the equipment could not vibrate for the 4.72 mm thickness, no video was recorded for this adherend. The detailed evolution at different points for each thickness is shown in Appendix C (Figure C.1 and Figure C.2). From these images it can be seen that for the thin adherends (1.17 mm and 2.37 mm), the physical changes happen at the same points of the displacement curve: flattening of the ED, squeeze-out of the ED, and fiber squeeze-out. However, a new phenomena occurs for the 3.55 mm thickness: squeeze-out of the top adherend at early stages of the process. Figure 3.4 shows the comparison between 2.37 mm and 3.55 mm, where this squeeze-out is pointed with red arrows.

This phenomena occurred during every weld of the 3.55 mm thickness and at different points in the displacement curve as shown in Figure 3.5. Again, the red arrows indicate the squeeze-out. In some cases, this squeeze-out is seen only as a white spot since the camera records in a gray-scale and therefore the spark that results of the resin squeeze-out is not fully captured. To evaluate this evolution in more detail, the welded specimens were analyzed by looking the cross-sectional micrographs at different points as shown in the following section.

3.1.4. Microscopy

The evolution of the weld was evaluated in different points: after the beginning of the plateau, during the plateau, after the end of the plateau, and at the end of the displacement curve. The micrographs showing this full evolution for adherends with a top thickness of 1.17 mm and 3.55 mm can be seen in Appendix D (Figure D.1 and Figure D.2). The reason for choosing these two thicknesses will be explained in Section 3.3. To visualize the extent of heating and damage during the vibration phase, the samples were not subjected to consolidation after vibration.

From looking at these images from Appendix D it is noticed that top adherend squeeze-out happens at an early stage for the 3.55 mm-thick adherend. A side-by-side comparison after the beginning of the plateau is shown in Figure 3.6.

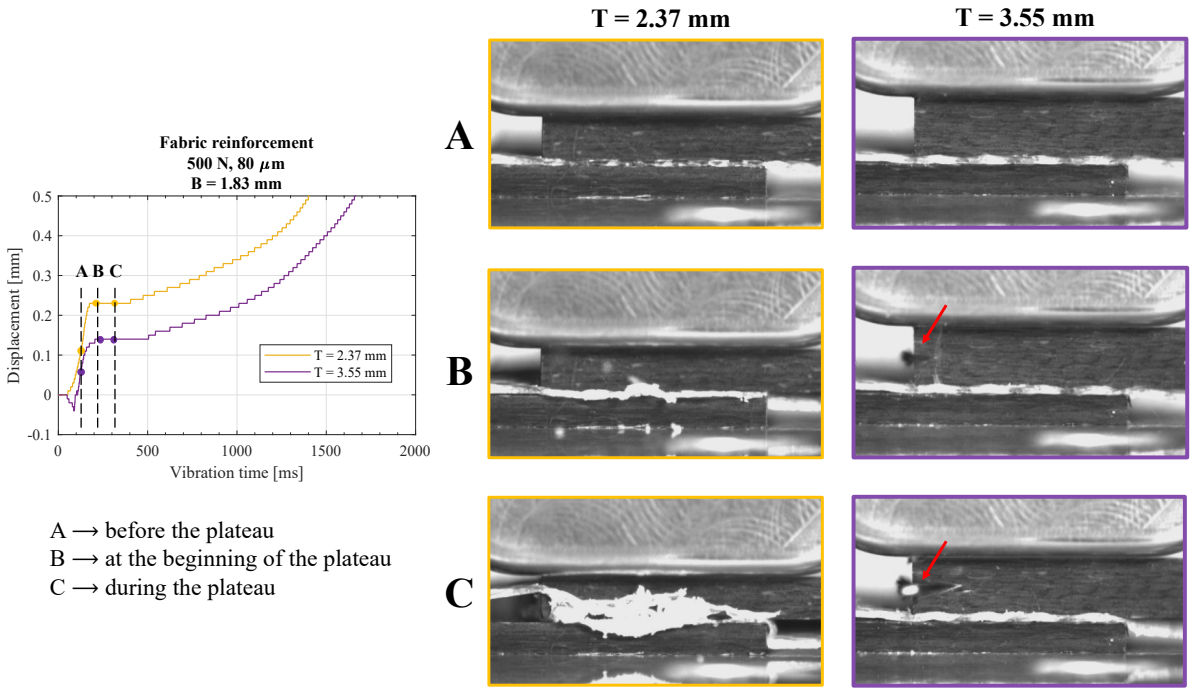

Figure 3.4: HSC snapshots at different points of the displacement curve for top adherend thicknesses of 2.37 mm and 3.55 mm. The red arrows indicate fiber squeeze-out.

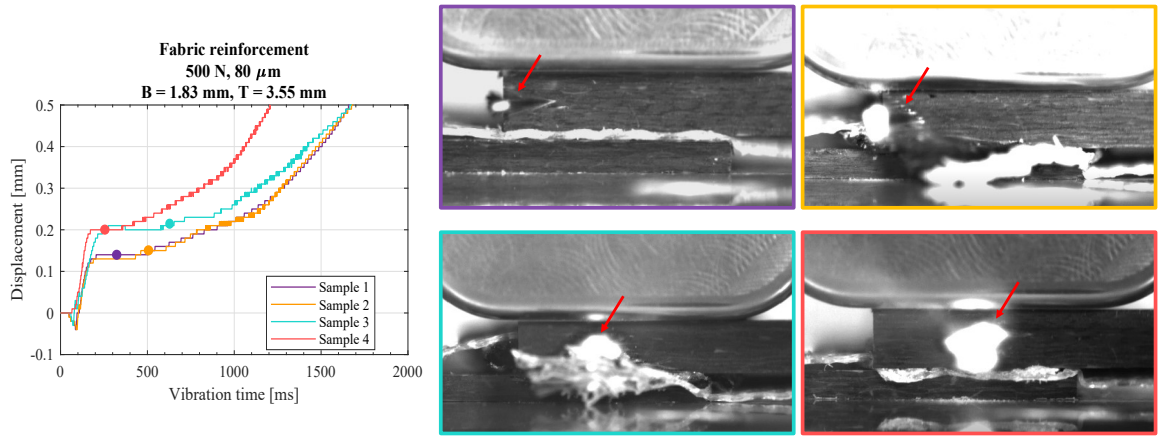

Figure 3.5: HSC snapshots at different points in the displacement curve where the damage in the top adherend was first observed for 4 different samples with a thickness of 3.55 mm. The red arrows indicate fiber squeeze-out.

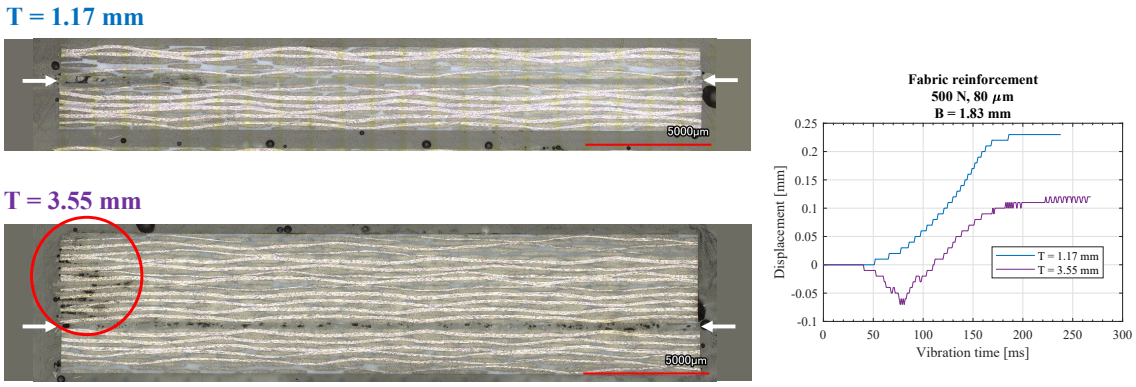

Figure 3.6: Comparison of the micrographs at the beginning of the plateau for top adherends with thicknesses of 1.17 mm and 3.55 mm. The samples were not consolidated. The white arrows indicate the weldline and the damage (deconsolidation, voids, and fiber squeeze-out) is circled in red.

3.1.5. Temperature readings

Figure 3.7 shows representative temperature curves at the interface, bottom adherend, and top adherend for different thicknesses of the top adherend. The consolidation time was set to 4000 ms. The individual curves for each thickness can be seen in Appendix E (Figure E.1).

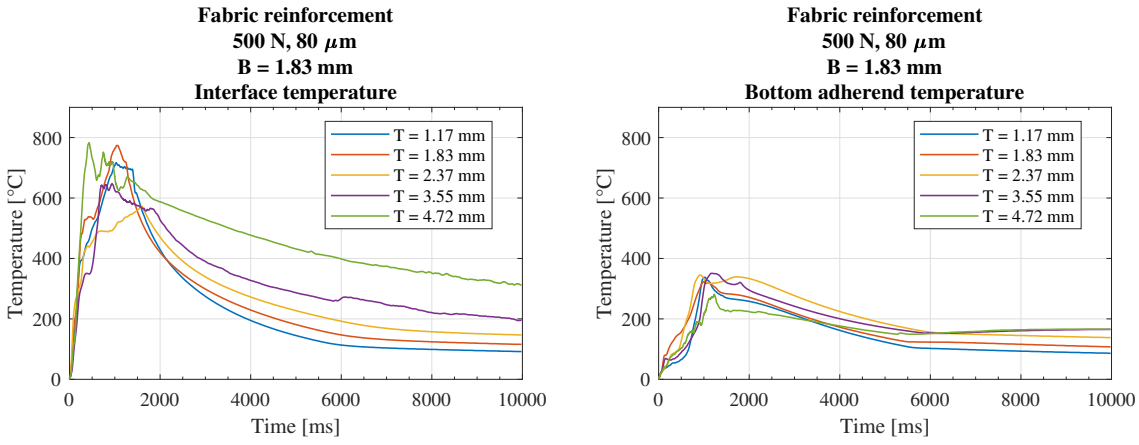

(a) Interface temperature

(b) Bottom adherend temperature

Figure 3.7: Representative temperature curves for different thicknesses of the top adherend. The thermocouples in the adherends were located 0.60 mm away from the interface.

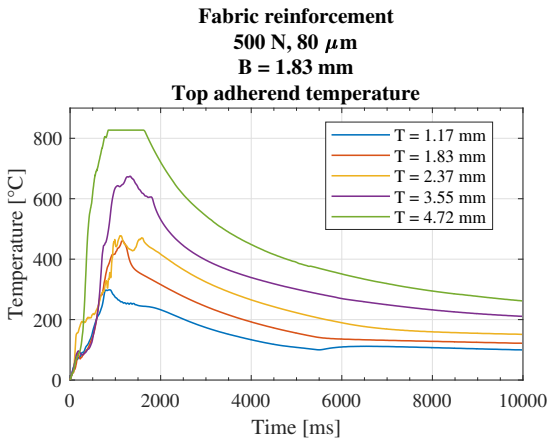

(c) Top adherend temperature

Figure 3.7: (continued) Representative temperature curves for different thicknesses of the top adherend. The thermocouples in the adherends were located 0.60 mm away from the interface.

3.1.6. COMSOL wave propagation model

Figure 3.8 shows the results from the wave propagation model when assuming the top adherend's thickness as 1.17 mm and 4.72 mm. The sonotrode was hidden for clarity. The propagation of the ultrasonic wave is visualized with the total displacement magnitude in the geometry. The time at which this displacement is maximum (see Figure 2.9) is 1.25 $\times 10^{-5}$ s. To emphasise on the wave propagation in the thickness direction, the results on a 2D plane (workplane 1 from Figure 2.6) are shown in Figure 3.9. The complete evolution can be seen in Appendix F (Figure F.5 to Figure F.8). Furthermore, Figure 3.10 shows the comparison of the displacement magnitude in the through-the-thickness direction in the middle of the overlap for both thickness values.

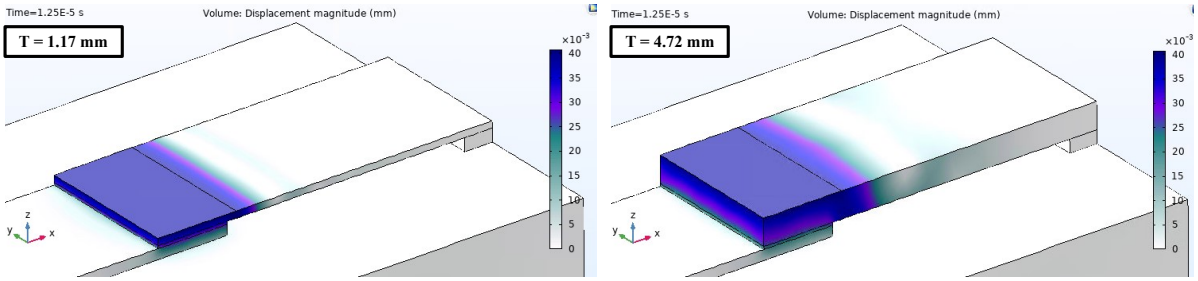

(a) Time = 1.25 $\times 10^{-5}$ s

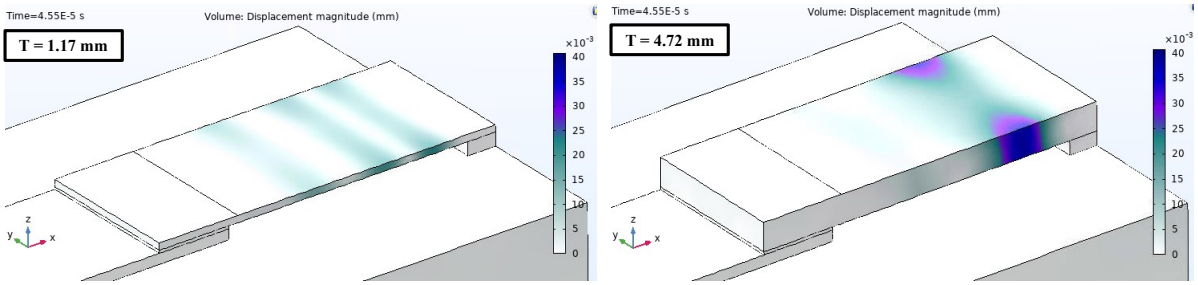

(b) Time = 3.65 $\times 10^{-5}$ s

Figure 3.8: COMSOL wave propagation model results (total displacement magnitude in mm]) for a top adherend's thickness of 1.17 mm and 4.72 mm.

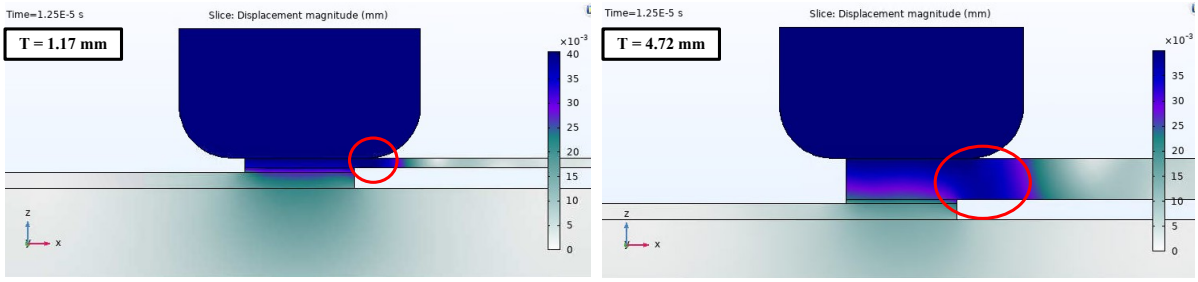

Figure 3.9: COMSOL wave propagation model results (total displacement magnitude in mm) for a top adherend's thickness of 1.17 mm and 4.72 mm at the point of maximum displacement. Results in the sliced workplane 1 from Figure 2.6. The area under the right edge of the sonotrode is circled in red.

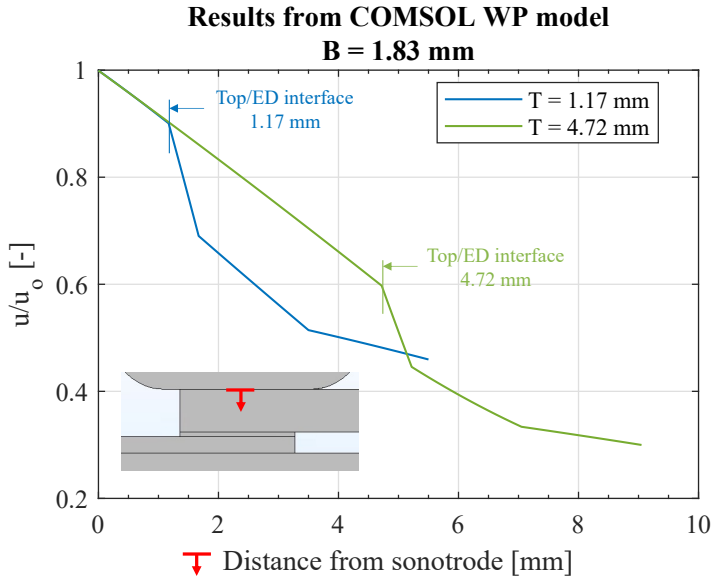

Figure 3.10: Through-the-thickness ratio of the total displacement magnitude (u) over the displacement imposed by the sonotrode (u_o) at 1.25 $\times 10^{-5}$ s in the middle of the overlap. The vertical lines indicate the top adherend/ED interface.

3.2. Effect of changing the bottom adherend's thickness

The adherends used for this part of the research have a fabric reinforcement (see Table 2.2). The force and amplitude values (500 N, 80 μm), and the top adherend's thickness (T = 1.83 mm) were kept constant so that only the effect of changing the bottom adherend's thickness was evaluated.

3.2.1. Power and displacement

Figure 3.11 shows representative power and displacement curves for each thickness of the bottom adherend. The individual power and displacement curves for multiple samples with the same thickness can be seen in Appendix A (Figure A.2). The adherends were welded until the displacement of the sonotrode was equal to the thickness of the ED (referred to as a 100% displacement).

As opposed to the curves when the top adherend's thickness changes, the power and -particularly- the displacement are clearly less sensitive to the change of the bottom adherend's thickness. To emphasize on the similarities, multiple curves are shown for 1.17 mm and 5.79 mm-thick adherends in Figure 3.12.

3.2.2. Amplitude

Figure 3.13 shows representative amplitude and displacement curves for bottom adherend thicknesses of 1.17 mm, 3.55 mm, and 5.79 mm and 100% displacement. Multiple amplitude curves for the different thicknesses presented previously can be found in Appendix B (Figure B.2).

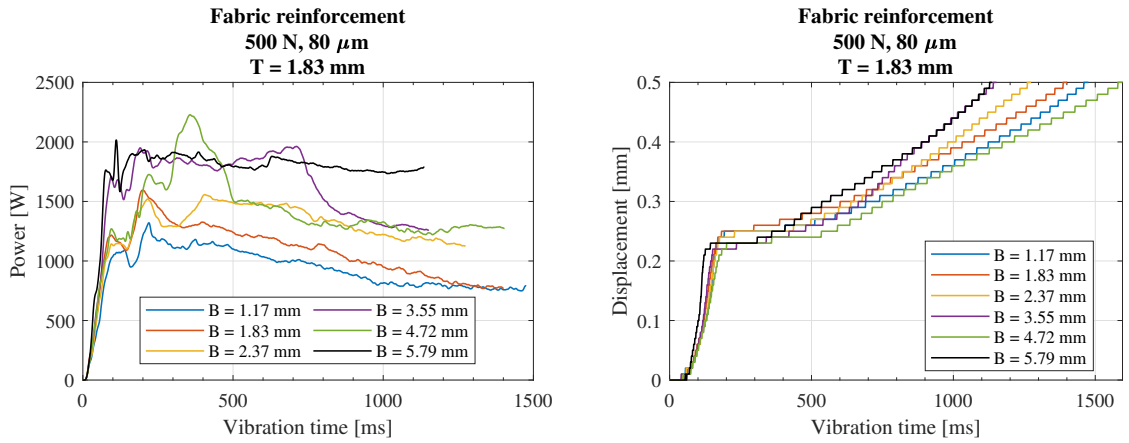

(a) Power curves **(b)** Displacement curves

Figure 3.11: Representative power and displacement curves for different thickness of the bottom adherend at 100 % displacement (travel of the sonotrode equal to the thickness of the ED).

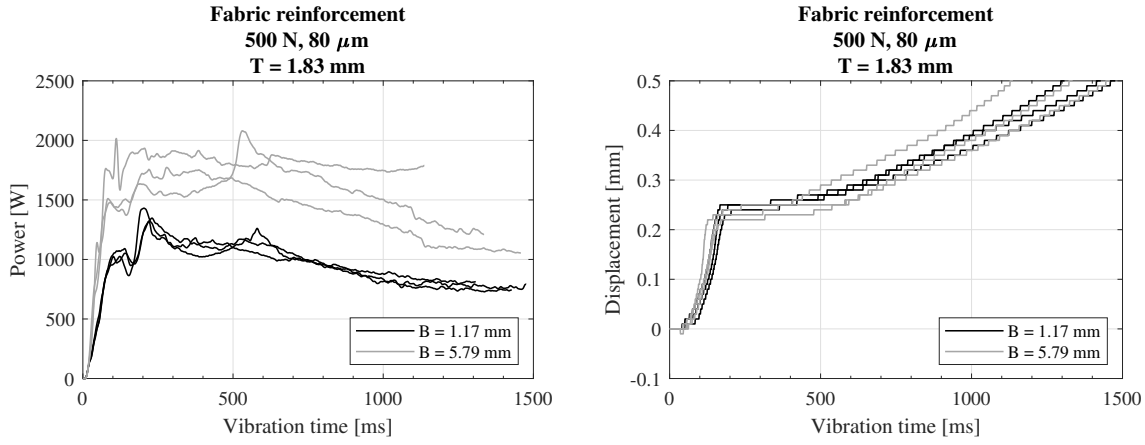

(a) Power curves **(b)** Displacement curves

Figure 3.12: Multiple power and displacement curves for bottom adherend thicknesses of 1.17 mm and 5.79 mm at 100% displacement (travel of the sonotrode equal to the thickness of the ED).

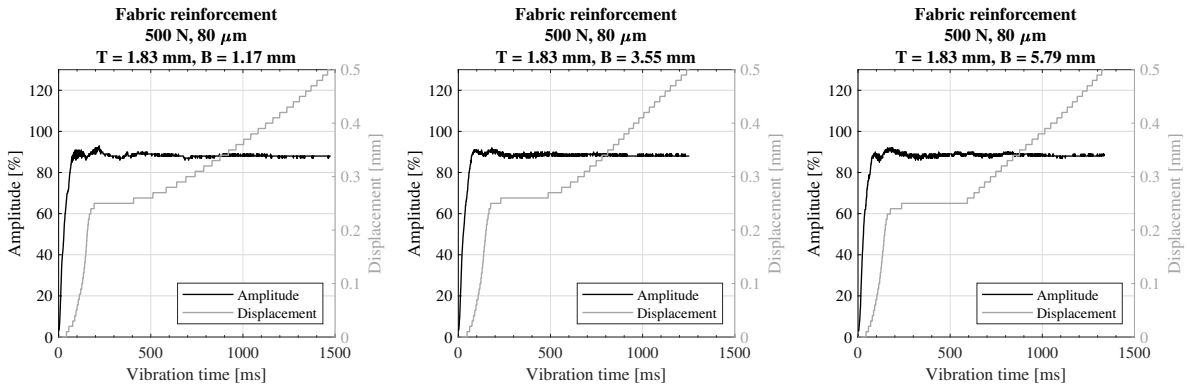

(a) B = 1.17 mm **(b)** B = 3.55 mm **(c)** B = 5.79 mm

Figure 3.13: Amplitude and displacement curves for different thicknesses of the bottom adherend. The nominal amplitude was 80 μm (88% of the maximum amplitude the equipment can provide).

3.2.3. High-speed camera snapshots

To visualize the difference in the weld evolution when changing the thickness of the bottom adherend, the two extreme cases (1.17 mm and 5.79 mm) were recorded with a HSC. The complete evolution at different points can be seen in Appendix C (Figure C.3 and Figure C.4). The comparison at three different points in the displacement curve (before the plateau, during the plateau, and well after the plateau) are shown in Figure 3.14.

3.2.4. Temperature readings

Figure 3.15 shows representative temperature curves at the interface, bottom adherend, and top adherend for different bottom adherend thicknesses. The consolidation time was set to 4000 ms. The individual curves for each thickness can be seen in Appendix E (Figure E.2). The 3.55 mm thickness is not shown because this thickness was added later in the study, when the decision to focus on the effect of changing the top adherend's thickness was already made. To focus on the differences between the extreme cases, three curves for the 1.17 mm and 5.79 mm-thick adherends are shown in Figure 3.15d. In this case, only interface TCs were present to avoid the effect of placing TCs in the adherends (see Appendix I).

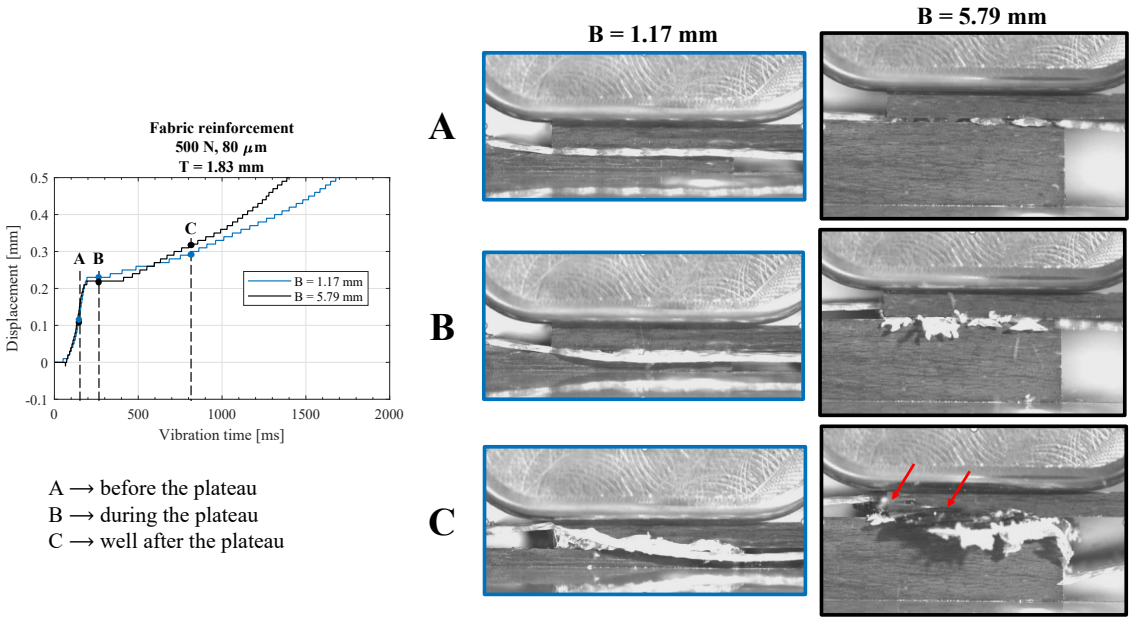

Figure 3.14: HSC snapshots at different points of the displacement curve for bottom adherend thicknesses of 1.17 mm and 5.79 mm. The red arrows indicate fiber squeeze-out.

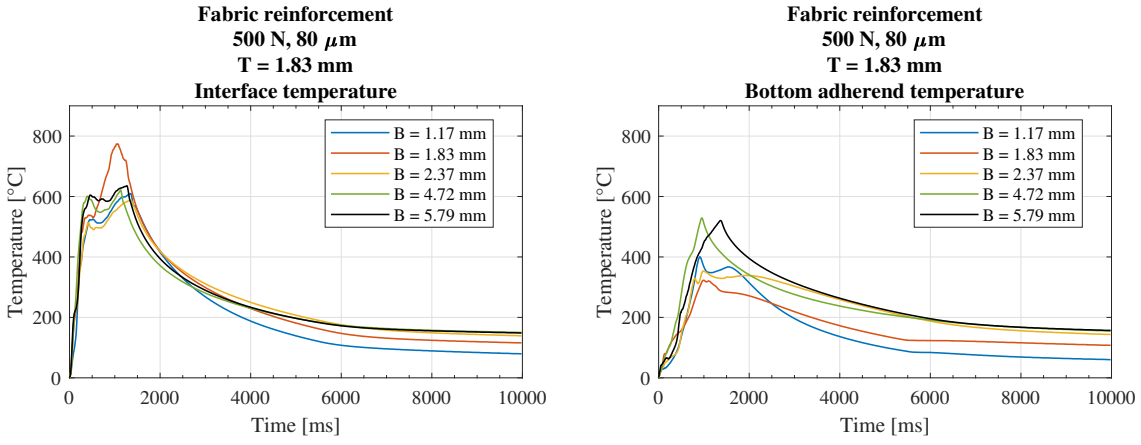

(a) Interface temperature

(b) Bottom adherend temperature

Figure 3.15: Representative temperature curves for different thicknesses of the bottom adherend. The thermocouples in the adherends were located 0.60 mm away from the interface.

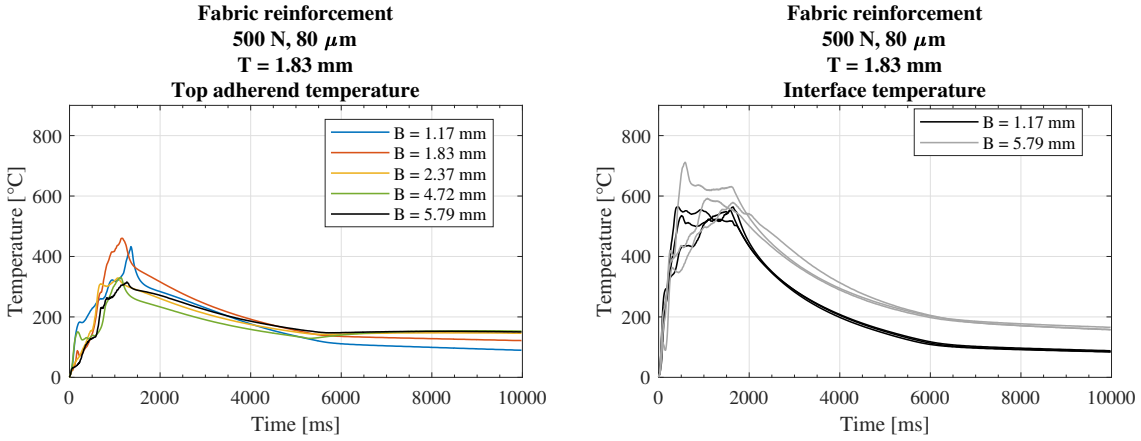

(c) Top adherend temperature

(d) Interface temperature (only interface TCs present)

Figure 3.15: (continued) Representative temperature curves for different thicknesses of the bottom adherend. The thermocouples in the adherends were located 0.60 mm away from the interface.

3.2.5. COMSOL heat transfer model

Figure 3.16 shows the results from the COMSOL heat transfer (HT) model (see Section 2.3.4). The experimental input temperature was obtained from an interface thermocouple (TC) reading. Because the response of changing the thickness of the bottom adherend on the heat transfer is to be evaluated, the same experimental temperature was used for all thicknesses. The top and bottom probes correspond to the position of the experimental TCs, which are located 0.60 mm away from the interface. To emphasize on the differences for different thicknesses, a close-up is presented. The images of the evolution at different times for different thickness values are shown in Appendix G (Figure G.1 to Figure G.3).

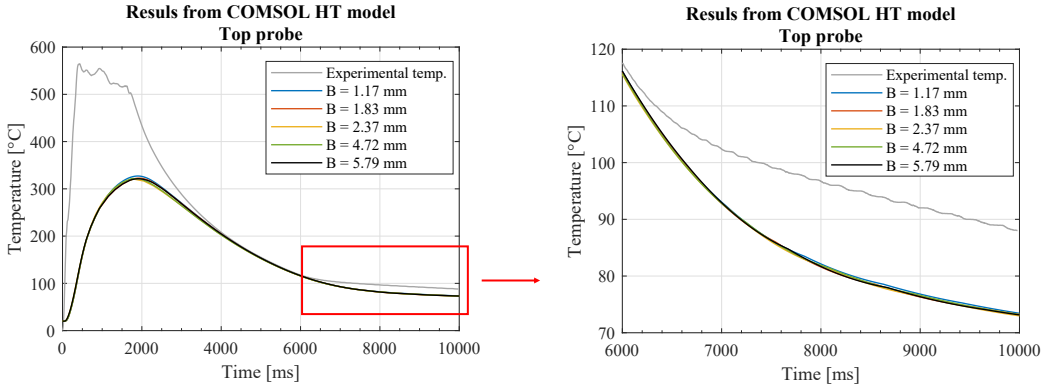

(a) Top probe

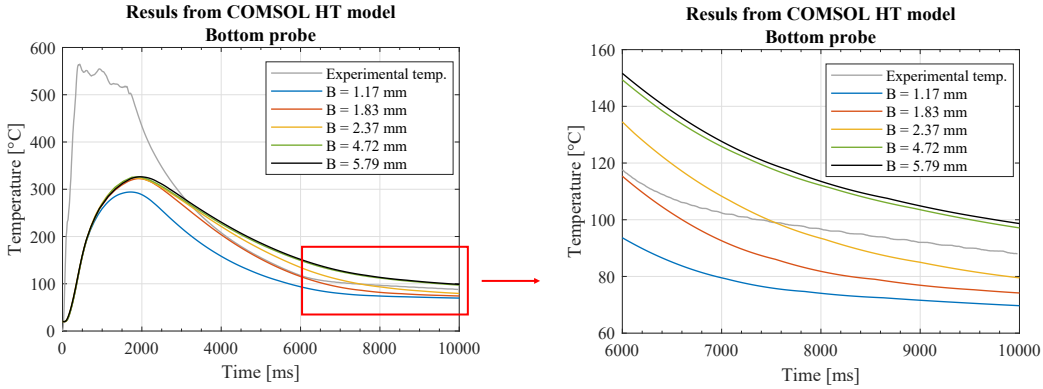

(b) Bottom probe

Figure 3.16: Results of the COMSOL heat transfer model. The experimental input temperature is the interface temperature for one of the experiments.

3.2.6. COMSOL wave propagation model

Figure 3.17 shows the results from the wave propagation model when assuming the bottom adherend's thickness as 1.17 mm and 5.79 mm. The sonotrode was hidden for clarity. The propagation of the ultrasonic wave is visualized with the total displacement magnitude in the geometry. The time at which this displacement is maximum (see Figure 2.9) is 1.25 $\times 10^{-5}$ s. To emphasise on the wave propagation in the thickness direction, the results on a 2D plane (workplane 1 from Figure 2.6) are shown in Figure 3.9. The complete evolution can be seen in Appendix F (Figure F.9 to Figure F.12). Furthermore, Figure 3.19 shows the comparison of the displacement magnitude in the through-the-thickness direction in the middle of the overlap.

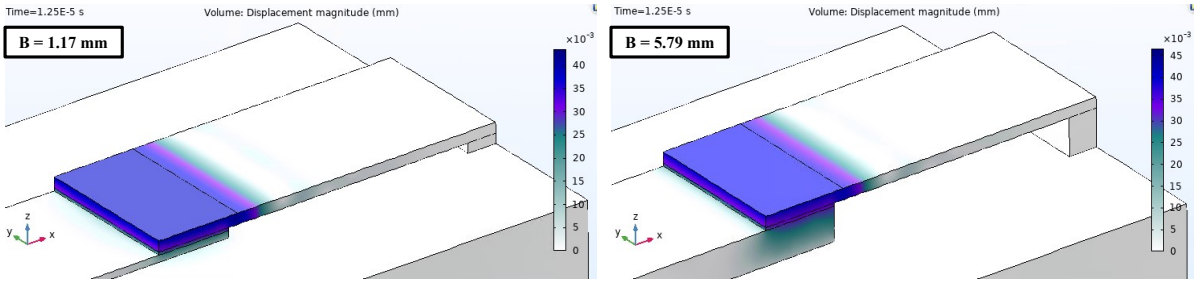

(a) Time = 1.25 $\times 10^{-5}$ s

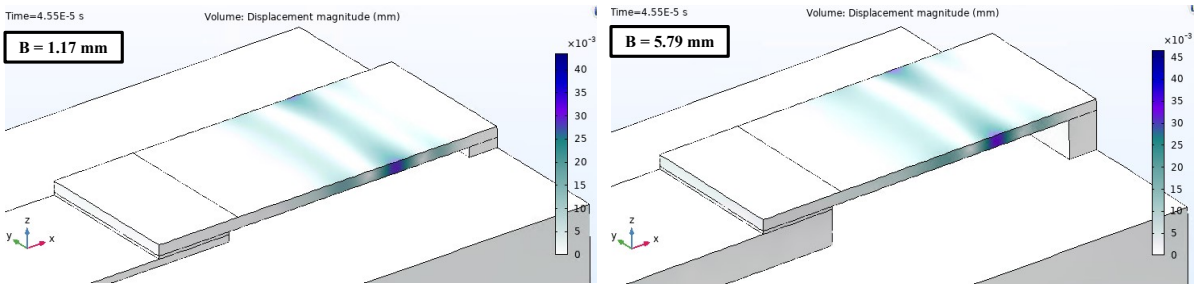

(b) Time = 3.65 $\times 10^{-5}$ s

Figure 3.17: COMSOL wave propagation model results (total displacement magnitude in mm]) for a bottom adherend's thickness of 1.17 mm and 5.79 mm.

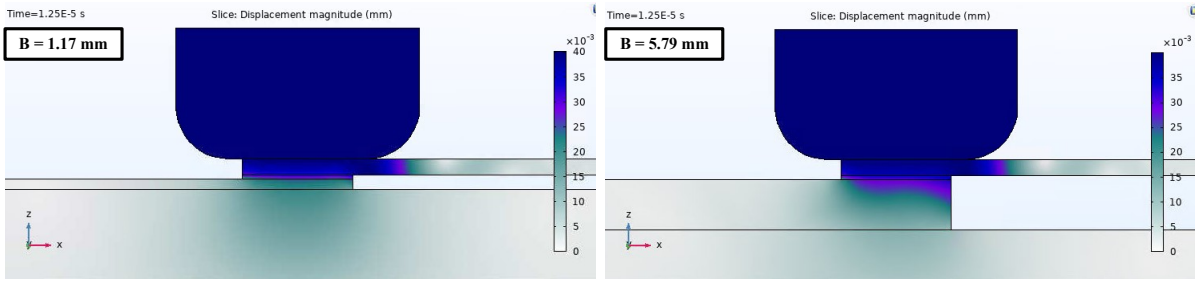

Figure 3.18: COMSOL wave propagation model results (total displacement magnitude in mm) for a bottom adherend's thickness of 1.17 mm and 5.79 mm at the point of maximum displacement. Results in the sliced workplane 1 from Figure 2.6.

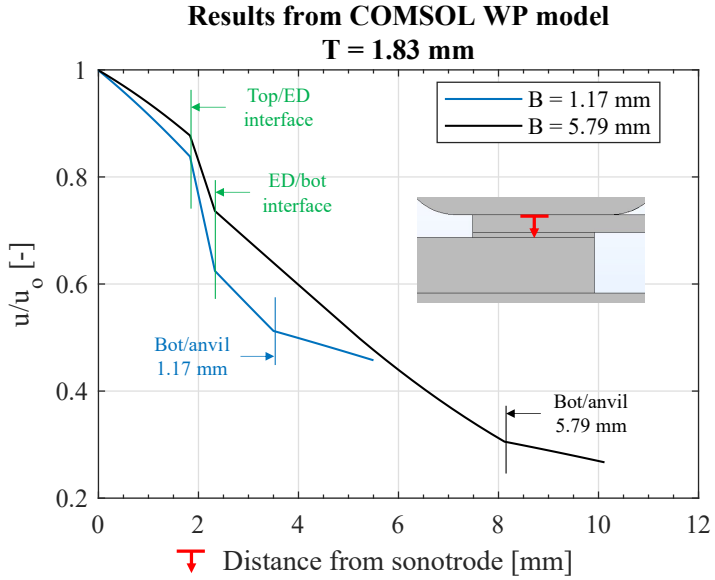

Figure 3.19: Through-the-thickness ratio of the total displacement magnitude (u) over the displacement imposed by the sonotrode (u_o) at 1.25 $\times 10^{-5}$ s in the middle of the overlap. The vertical lines indicate the different interfaces (top adherend/ED, ED/bottom adherend, and bottom adherend/anvil.

A cross-sectional microscopy analysis was not executed for different thicknesses of the bottom adherend. This, because the effect of changing the top adherend's thickness was found to be much more relevant and therefore the research was focused on the effect of the top adherend's thickness.

3.3. Effect of changing the process parameters

From the previous results it is evident that the process response and weld evolution are more sensitive to the change of the top adherend's thickness than the bottom adherend's thickness. Therefore, for the remaining of the research (changing process parameters and changing to UD reinforcement) only the top adherend was studied. Three combinations of parameters were chosen aside from the low force-high amplitude reference case (500 N, 80 μm): low force-low amplitude (500 N, 60 μm), high force-high amplitude (1500 N, 80 μm), and high force-low amplitude (1500 N, 60 μm). Initially, only two adherend thicknesses were chosen: 1.17 mm and 3.55 mm. The reason for choosing these two values is because the purpose is to compare how changing the process parameters affects thin and thick adherends. The 3.55 mm-thick adherend showed to be the turning point for the reference case, and therefore it was evaluated. The 1.17 mm-thick adherend was selected instead of the 2.37 mm-thick in case that the turning point when changing the process parameters was 2.37 mm rather than 3.55 mm. The adherends used for this part of the study had a fabric reinforcement.

3.3.1. Power and displacement

Figure 3.20 and Figure 3.21 show the power and displacement curves for the previously mentioned combinations of process parameters and 100% displacement. A quick evaluation of the displacement graphs makes it clear that increasing the force minimizes the differences between the thin and thick adherends. Therefore, the next thick adherend (4.72 mm) was also evaluated for the high force cases. However, the equipment was sometimes not able to vibrate after a certain point, which explains why some curves do not end at a 0.50 mm displacement.

3.3.2. Amplitude

The amplitude between thin and thick adherends for the low force-low amplitude case showed to have a similar response as the reference case and can be seen in Appendix B (Figure B.3). However, it significantly changed for the high force cases. Figure 3.22 shows representative amplitude and displacement curves for the high force-high amplitude case and 100% displacement. Multiple curves for both high force cases can be seen in Appendix B (Figure B.4 and Figure B.5).

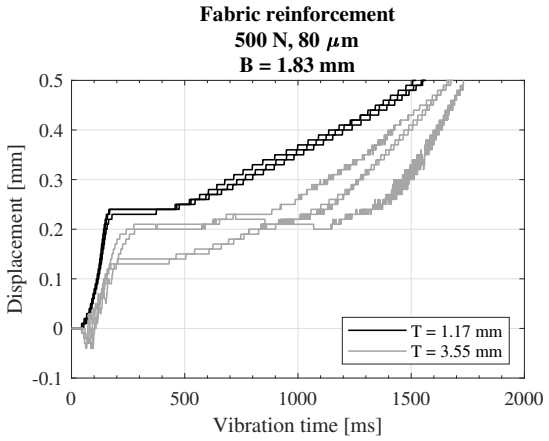

(a) 500 N, 80 μm (reference case).

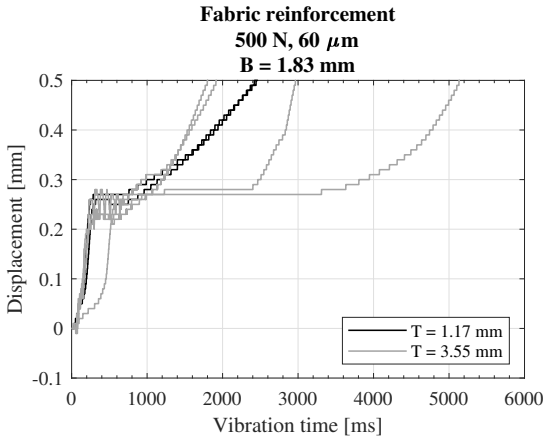

(b) 500 N, 60 μm.

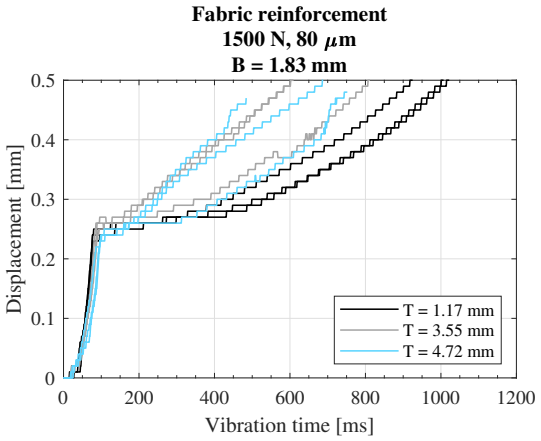

(c) 1500 N, 80 μm.

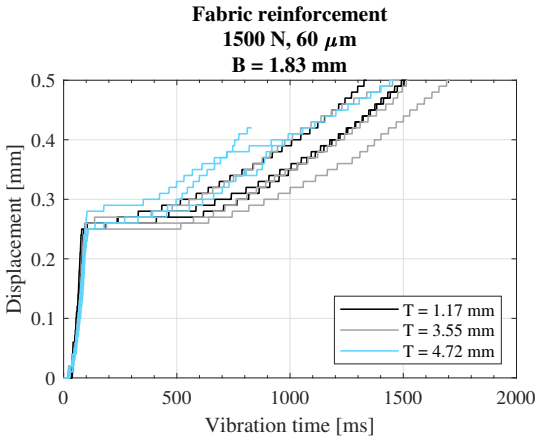

(d) 1500 N, 60 μm.

Figure 3.20: Displacement curves for different thicknesses of the top adherend and under different process parameters at 100 % displacement (travel of the sonotrode equal to the thickness of the ED).

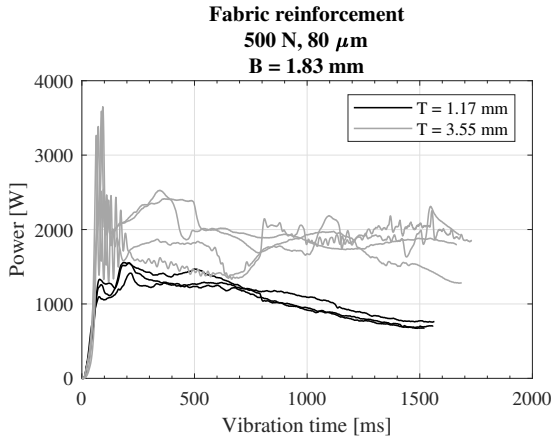

(a) 500 N, 80 μm (reference case).

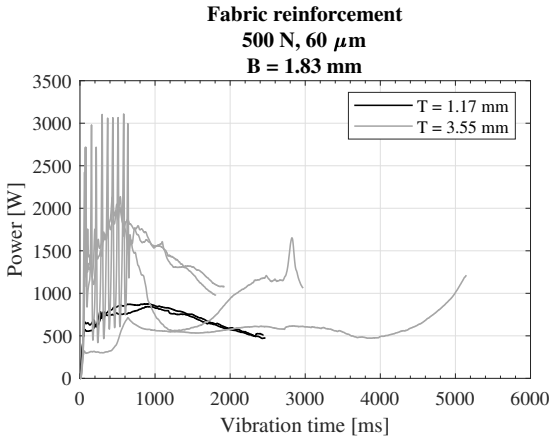

(b) 500 N, 60 μm.

Figure 3.21: Power curves for different thicknesses of the top adherend and under different process parameters at 100 % displacement (travel of the sonotrode equal to the thickness of the ED).

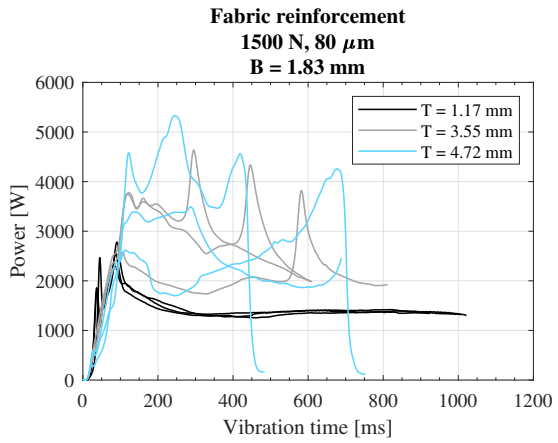

(c) 1500 N, 80 μm.

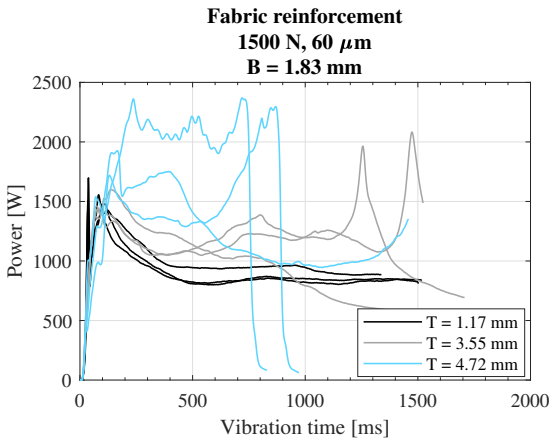

(d) 1500 N, 60 μm.

Figure 3.21: (continued) Power curves for different thicknesses of the top adherend and under different process parameters at 100 % displacement (travel of the sonotrode equal to the thickness of the ED).

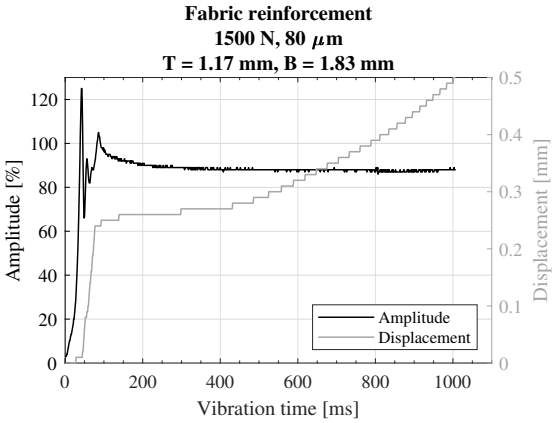

(a) T = 1.17 mm

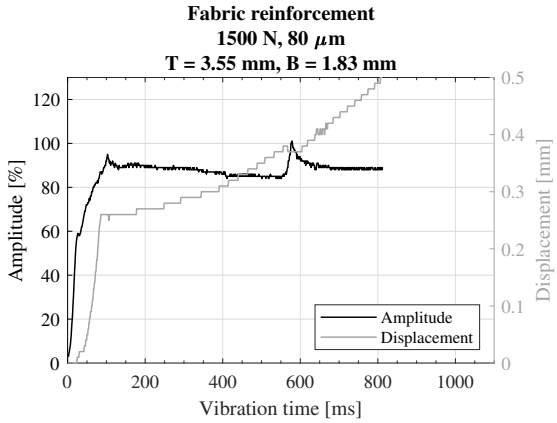

(b) T = 3.55 mm

Figure 3.22: Amplitude and displacement curves for 1.17 mm and 3.55 mm-thick top adherends with force and nominal amplitude values of 1500 N and 80 μm (88% of the maximum amplitude the equipment can provide).

3.3.3. High-speed camera snapshots

The HSC snapshots for the reference case (500 N, 80 μm) were already presented in Section 3.1.3 (Figure 3.4). The complete evolution at different points of the displacement curves for the different thickness values and under the new combinations of process parameters are shown in Appendix C (Figure C.5 to Figure C.10).

Decreasing the amplitude while keeping the force constant (500 N, 60 μm) gives a similar response as the reference case, where squeeze-out of the top adherend during the plateau is observed. However, a different evolution is found for the thicker adherends when increasing the force. Figure 3.23 and Figure 3.24 show the comparison at different points of the displacement plateau between the thin adherend (1.17 mm) and a thick one (3.55 mm or 4.72 mm) when welding with a high force (1500 N).

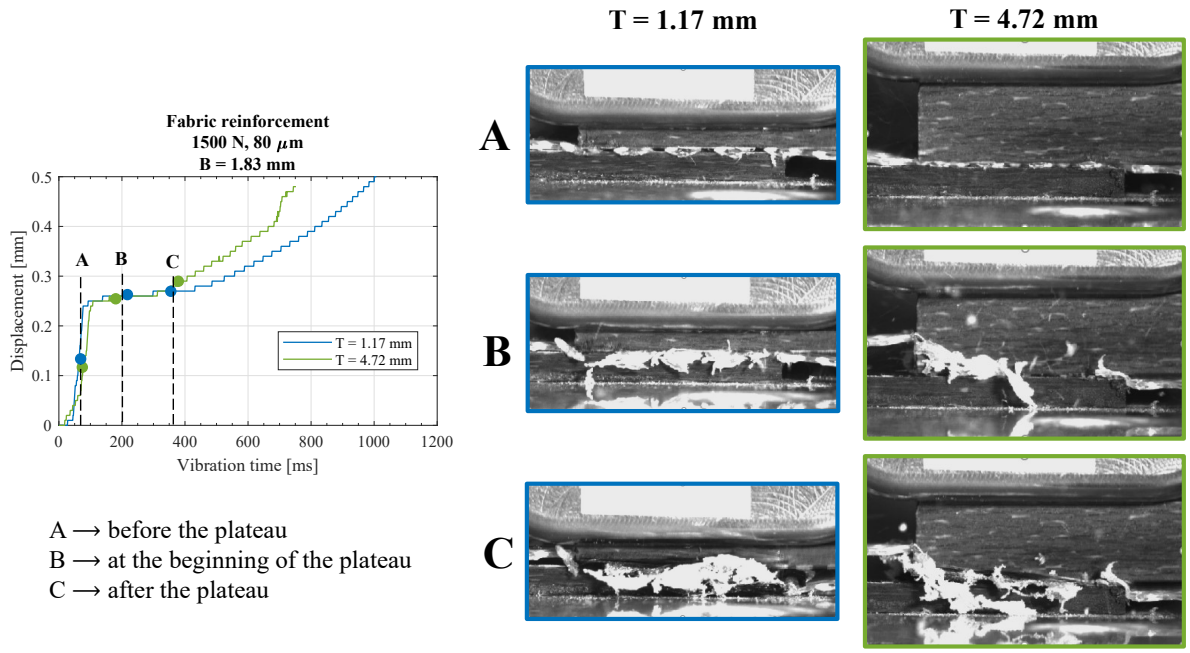

Figure 3.23: HSC snapshots at different points of the displacement curve for top adherend thicknesses of 1.17 mm and 4.72 mm with force and amplitude values of 1500 N, 80 μm.

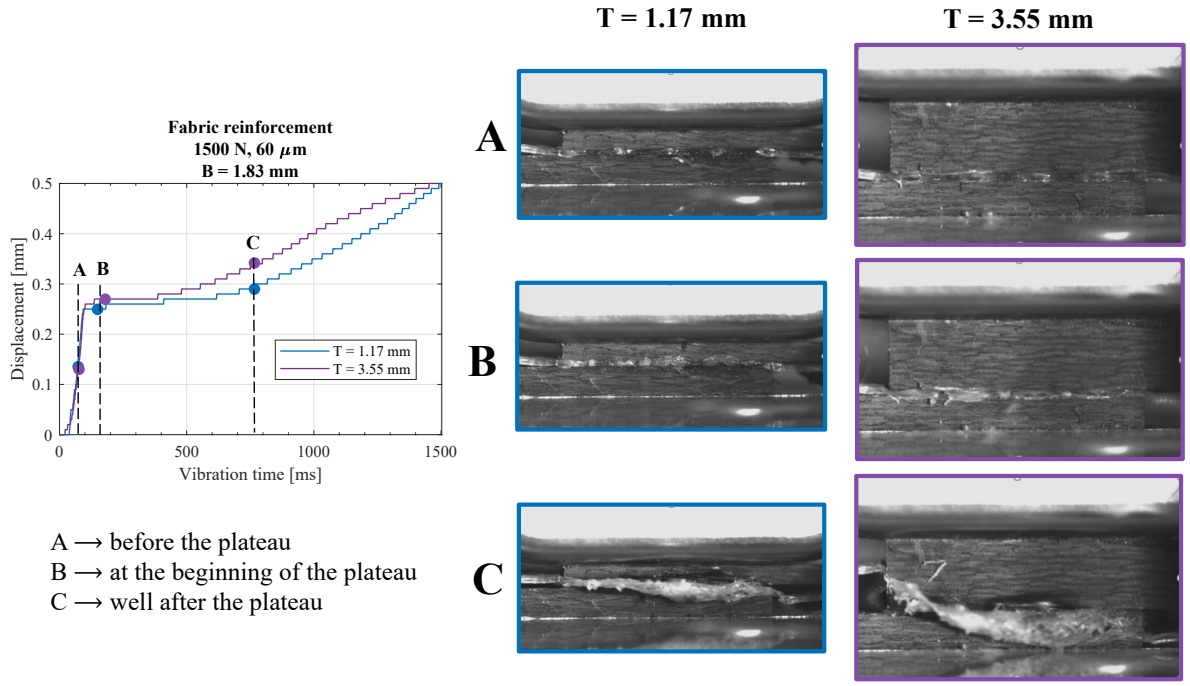

Figure 3.24: HSC snapshots at different points of the displacement curve for top adherend thicknesses of 1.17 mm and 3.55 mm with force and amplitude values of 1500 N, 60 μm.

Although no obvious differences in the weld evolution are seen in the previous figures, the differences between displacement curves of the thin and thick adherends indicate that there is a change in the physical phenomena that cannot be detected with the HSC videos only. Therefore, the weld evolution was evaluated again at different point of the displacement curve.

3.3.4. Microscopy

The complete evolution for the new combinations of process parameters at the beginning of the plateau, during the plateau, after the plateau, and at the end of the curve can be seen in Appendix D (Figure D.3 to Figure D.9). As expected from the HSC videos, the low force-low amplitude thick adherends also present damage at early stages of the process. However, this is not what occurs for the high force cases. Figure 3.25 and Figure 3.26 show the comparison of the micrographs between the thin and thick adherends when welded after the end of the displacement plateau. Again, there was no consolidation after vibration. The individual displacement curves for each weld are included for better comparison.

3.3.5. Temperature readings

In order to avoid the effects of placing thermocouples (TCs) at the adherends (see Appendix I), temperature readings were obtained with TCs only at the interface for the the different process parameters. Figure 3.27 presents the temperature curves for the thicknesses of 1.17 mm and 3.55 mm, where two readings per thickness are shown as some thermocouples malfunctioned during the vibration phase. The consolidation time was set to 4000 ms.

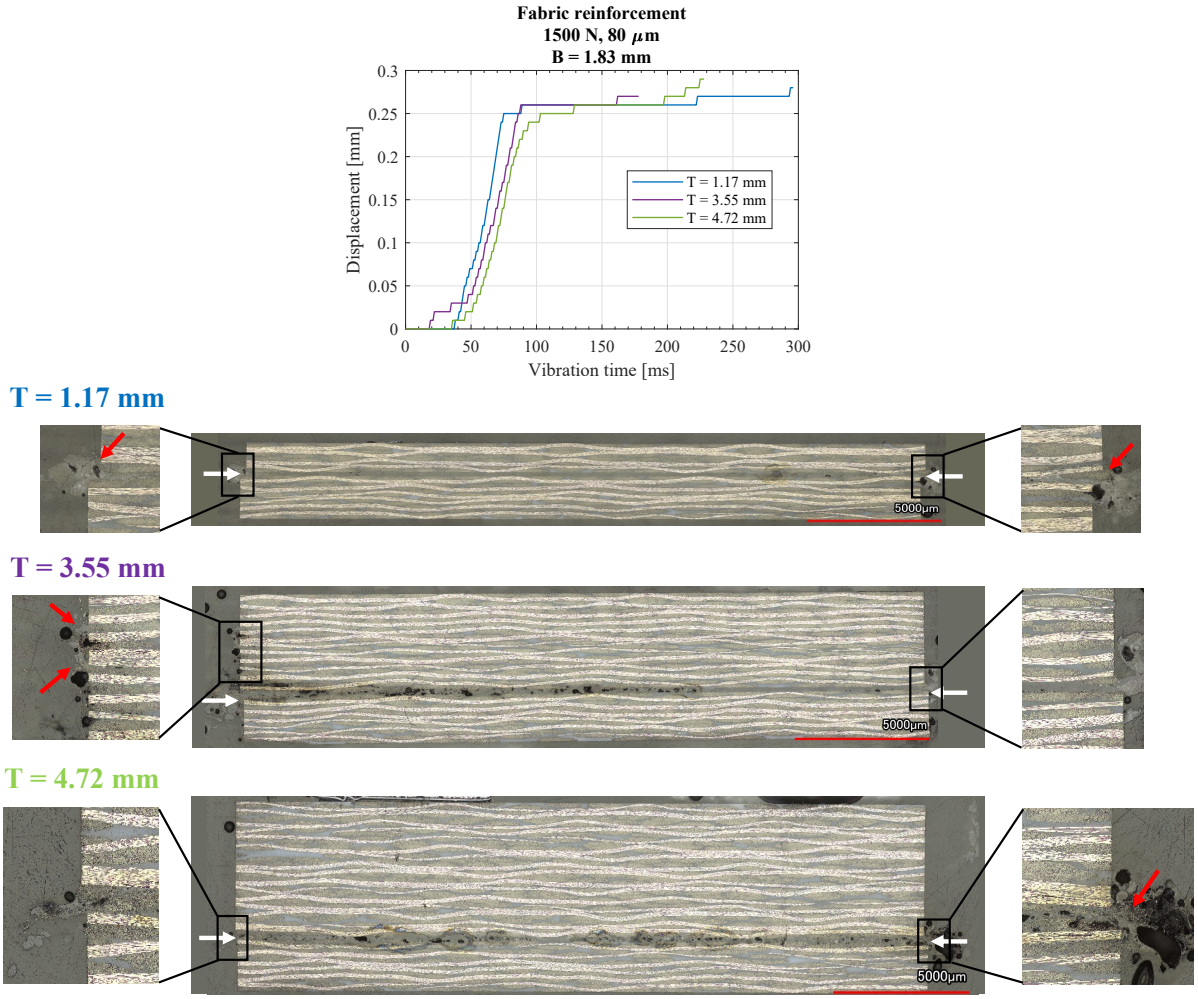

Figure 3.25: Micrographs for top adherend thicknesses of 1.17 mm, 3.55 mm, and 4.72 mm after the displacement plateau with force and amplitude values of 1500 N, 80 μm. The white and red arrows indicate the weldline and fiber squeeze-out.

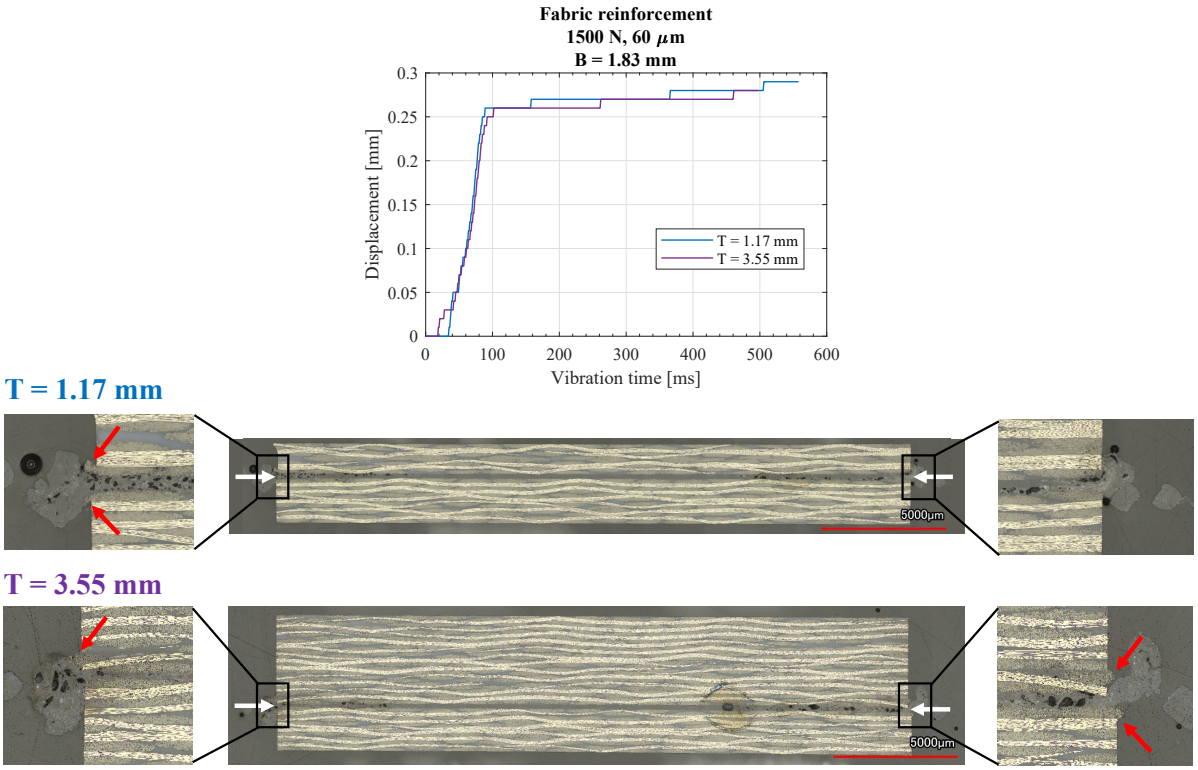

Figure 3.26: Micrographs for top adherend thicknesses of 1.17 mm and 3.55 mm after the displacement plateau with force and amplitude values of 1500 N, 60 μm. The white and red arrows indicate the weldline and fiber squeeze-out.

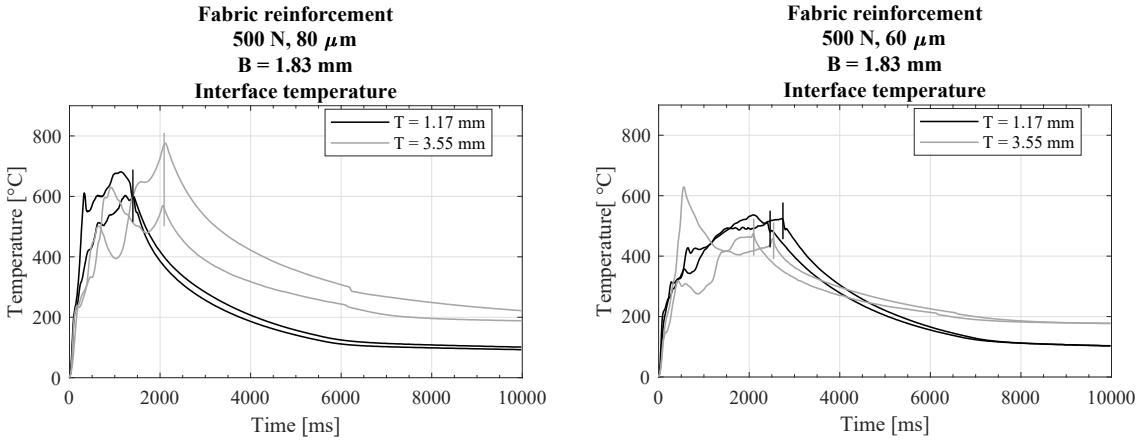

(a) 500 N, 80 μm

(b) 500 N, 60 μm

Figure 3.27: Temperature curves for different force and amplitude values and top adherend thicknesses of 1.17 mm and 3.55 mm. Only interface TCs were placed. The vertical lines indicate the end of vibrations.

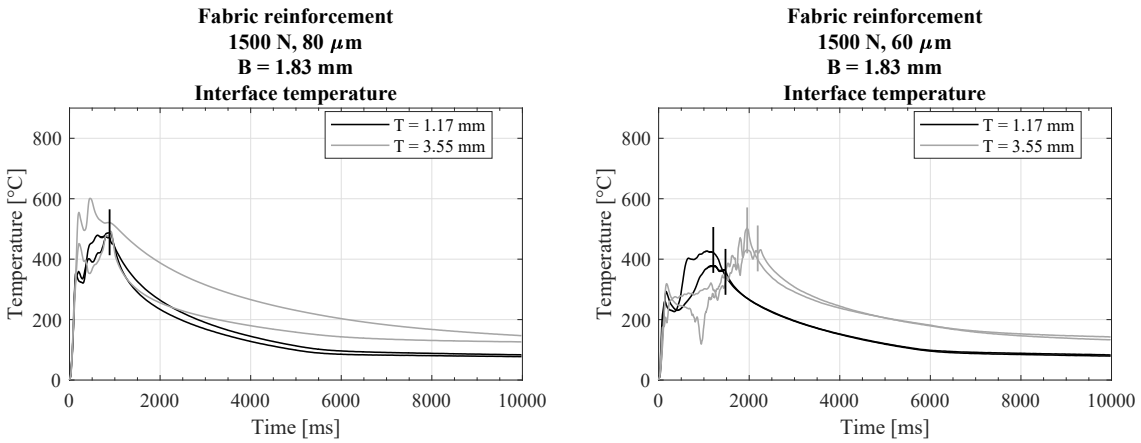

(c) 1500 N, 80 μm **(d)** 1500 N, 60 μm

Figure 3.27: (continued) Temperature curves for different force and amplitude values and top adherend thicknesses of 1.17 mm and 3.55 mm. Only interface TCs were placed. The vertical lines indicate the end of vibrations.

3.4. Effect of changing to UD reinforcement

The final part of the study consisted on changing the adherend's reinforcement from fabric to UD. Because this part is meant to be less extensive as the previous ones, only selected thicknesses were chosen as well as process parameters for microscopy analysis. Thickness values close to 1.17 mm and 3.55 mm were chosen for the same reasons as explained before, plus a value close to 1.83 mm for the thickness of the bottom adherend. Because the individual thickness is different for the fabric and UD semipreg plies, the exact thicknesses could not be matched. The thickness values used for the UD-reinforced adherends can be seen in Table 2.2.

3.4.1. Power and displacement

Figure 3.29 and Figure 3.28 show the power and displacement curves for the different combinations of process parameters. The adherends were welded until the displacement of the sonotrode was equal to the thickness of the ED (referred to as a 100% displacement). For the high force-high amplitude case, the sonotrode could not vibrate for a top adherend's thickness of 1.10 mm and therefore the 1.85 mm-thick adherends were used as the thin adherend.

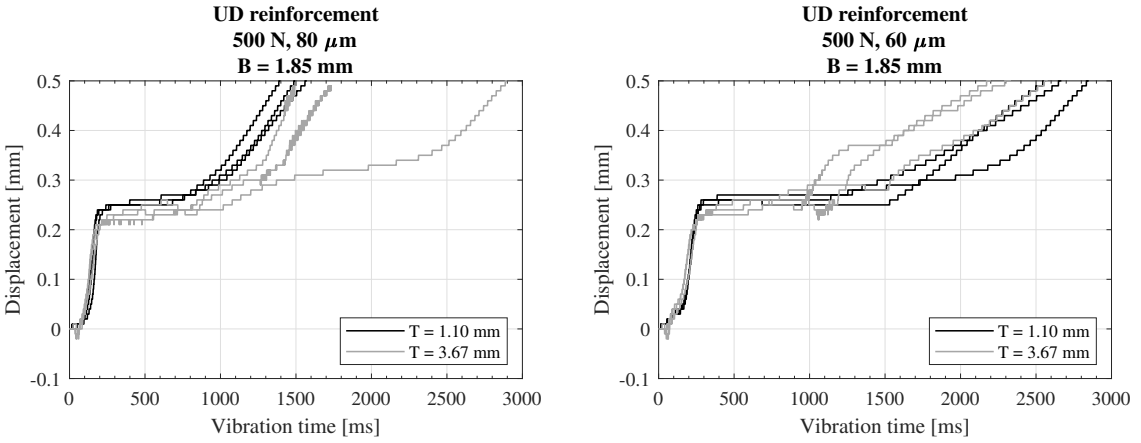

(a) 500 N, 80 μm. **(b)** 500 N, 60 μm.

Figure 3.28: Displacement curves for different thicknesses of the top adherend and under different process parameters at 100 % displacement (travel of the sonotrode equal to the thickness of the ED). Adherends with UD reinforcement.

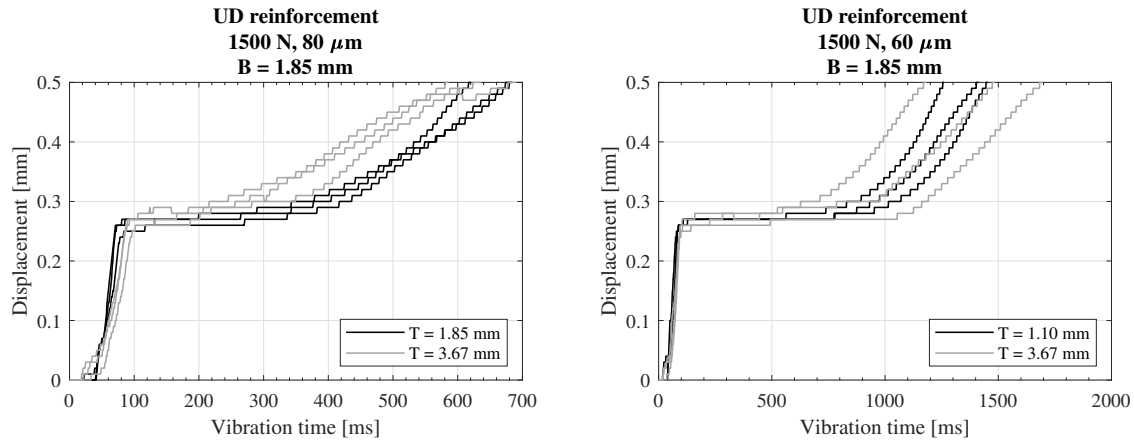

(c) 1500 N, 80 μm. **(d)** 1500 N, 60 μm.

Figure 3.28: (continued) Displacement curves for different thicknesses of the top adherend and under different process parameters at 100 % displacement (travel of the sonotrode equal to the thickness of the ED). Adherends with UD reinforcement.

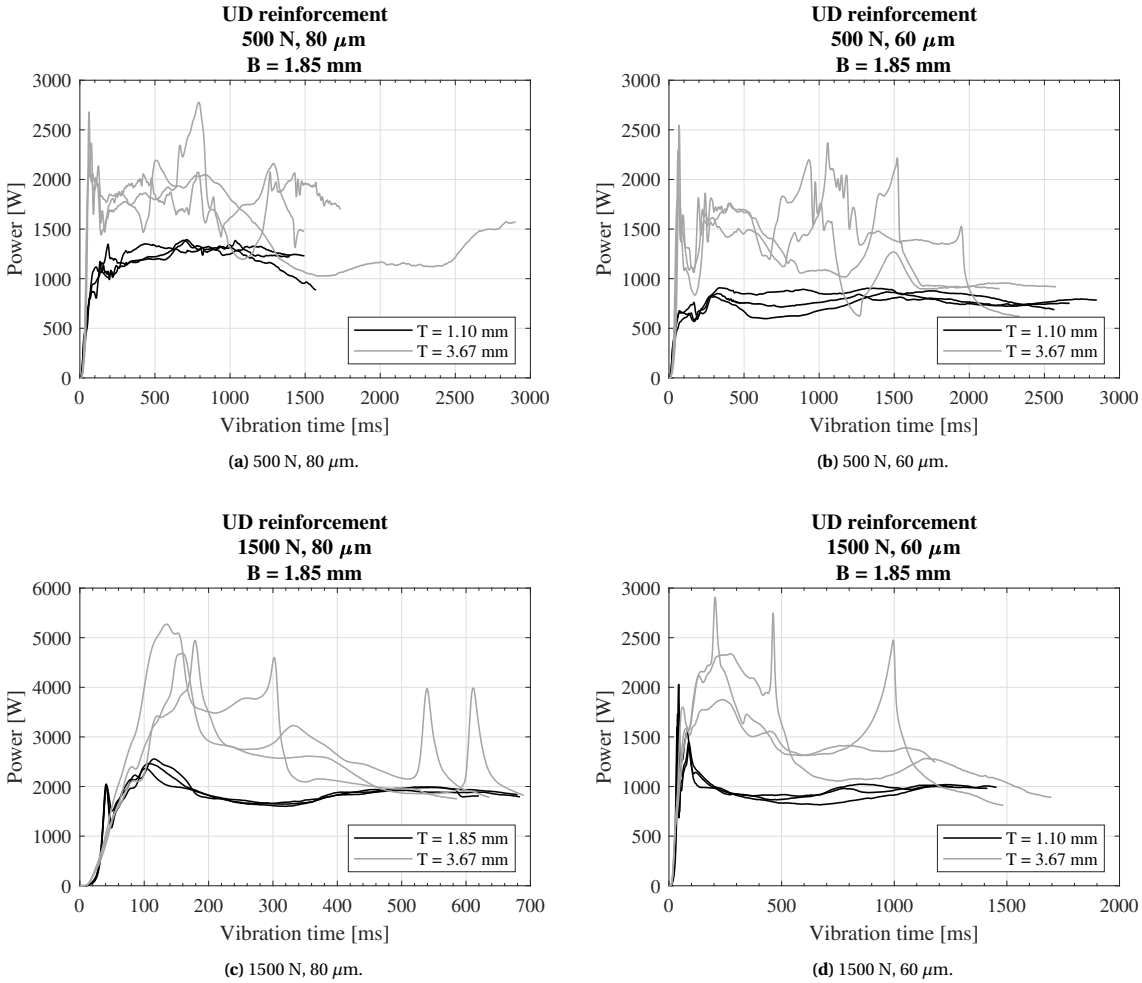

(a) 500 N, 80 μm. **(b)** 500 N, 60 μm.

(c) 1500 N, 80 μm. **(d)** 1500 N, 60 μm.

Figure 3.29: Power curves for different thicknesses of the top adherend and under different process parameters at 100 % displacement (travel of the sonotrode equal to the thickness of the ED). Adherends with UD reinforcement.

3.4.2. Amplitude

Figure 3.30 shows representative amplitude and displacement curves for the reference low force-high amplitude case. Multiple curves for the different process parameters are shown in Appendix B (Figure B.6 to

Figure B.9).

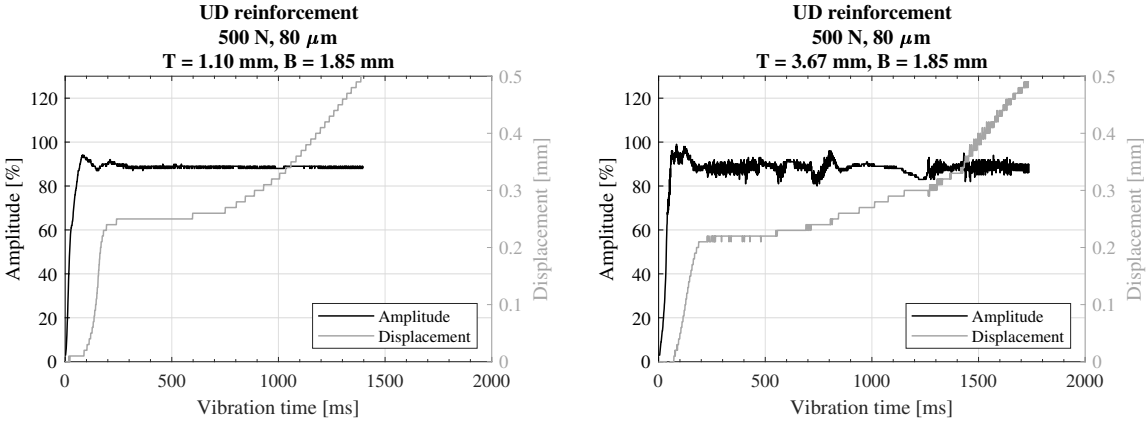

(a) T = 1.17 mm **(b)** T = 3.55 mm

Figure 3.30: Amplitude and displacement vs. time for 1.10 mm and 3.67 mm-thick top adherends with force and nominal amplitude values of 500 N and 80 μm (88% of the maximum amplitude the equipment can provide). Adherends with UD reinforcement.

3.4.3. High-speed camera snapshots

The welds were again recorded for all the combinations of force and amplitude values. The complete weld evolution can be seen in Appendix C (Figure C.11 to Figure C.18). For the low force cases, when welding the thick adherend there is again squeeze-out of the top adherend at early stages of the process. However, there is also squeeze out of the bottom adherend at early stages of the process when welding the thin top adherend. This can be seen in Figure 3.31 where the red arrows indicate the squeeze-out. For the high force cases there is also squeeze-out of the bottom adherend when welding thinner adherends. However, when welding thicker adherends, the squeeze-out of the top adherend also occurs in the right corner of the sonotrode/adherend interface very early in the process. This is shown in Figure 3.32. The squeeze-out at this corner was also noticed in the fabric adherends, but towards the end of the displacement curve.

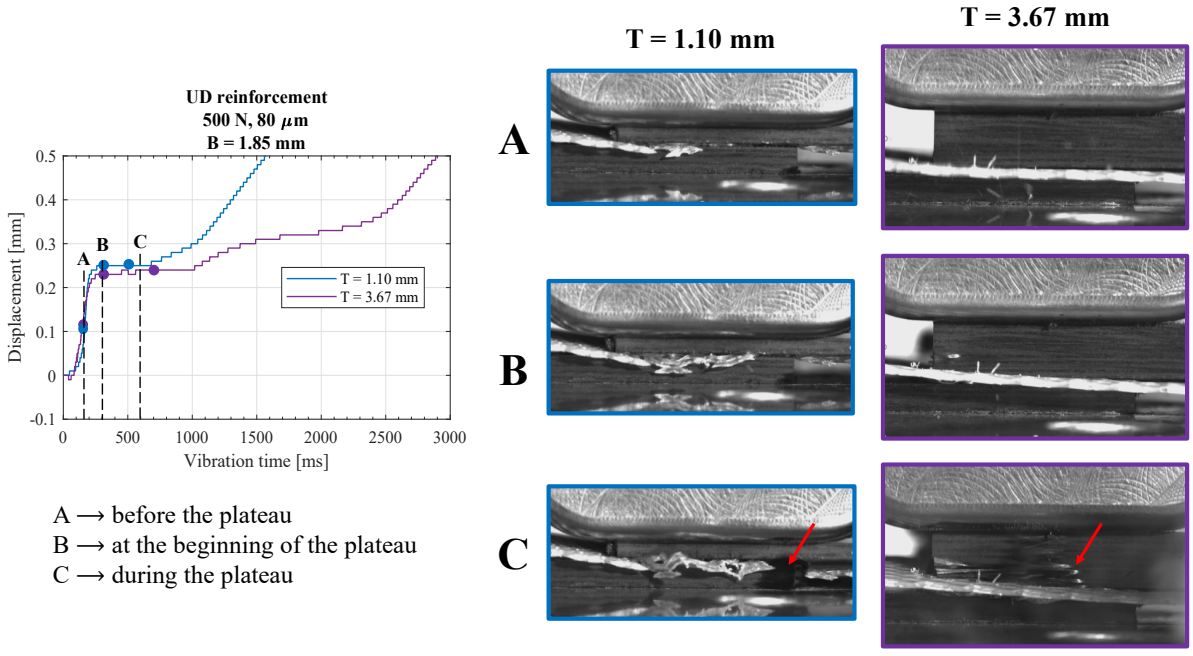

Figure 3.31: HSC snapshots at different points of the displacement curve for top adherend thicknesses of 1.10 mm and 3.67 mm and force and amplitude values of 500 N, 80 μm. The red arrows indicate fiber squeeze-out. Adherends with UD reinforcement.

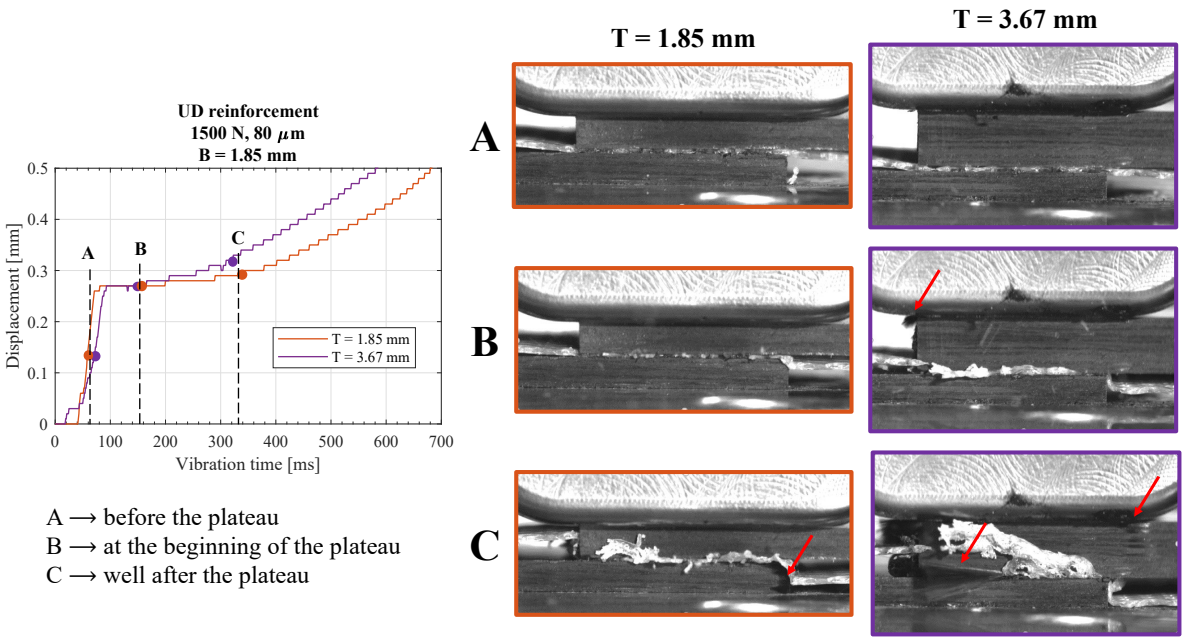

Figure 3.32: HSC snapshots at different points of the displacement curve for top adherend thicknesses of 1.85 mm and 3.67 mm and force and amplitude values of 1500 N, 80 μm. The red arrows indicate fiber squeeze-out. Adherends with UD reinforcement.

3.4.4. Microscopy

The complete evolution at the different points of the displacement curve can be seen in Appendix D (Figure D.10 to Figure D.13). Only the high force cases were chosen for microscopy as the low force cases already showed poor results (squeeze-out of the top adherend at early stages of the process) for the thicker adherends with the fabric reinforcement, and the same is expected from the UD adherends as seen from the HSC snapshots.

Figure 3.33 shows the micrographs for the 1.85 mm and 3.67 mm-thick adherends after the end of the plateau with high force-high amplitude, and Figure 3.34 shows the micrographs during the plateau (for the 1.10 mm-thick adherend) and after the end of the plateau (for the 3.67 mm-thick adherend) with high force-low amplitude.

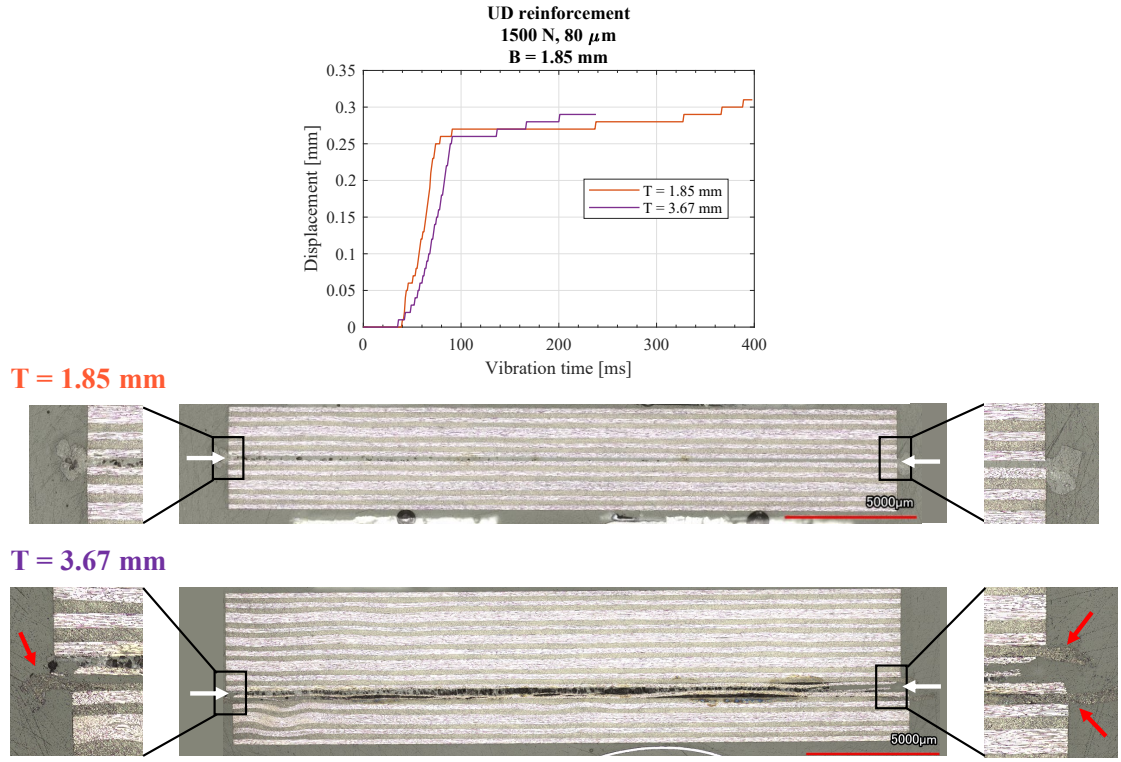

Figure 3.33: Micrographs for top adherend thicknesses of 1.85 mm and 3.67 mm after the displacement plateau with force and amplitude values of 1500 N, 80 μm. The white and red arrows indicate the weldline and fiber squeeze-out. Adherends with UD reinforcement.

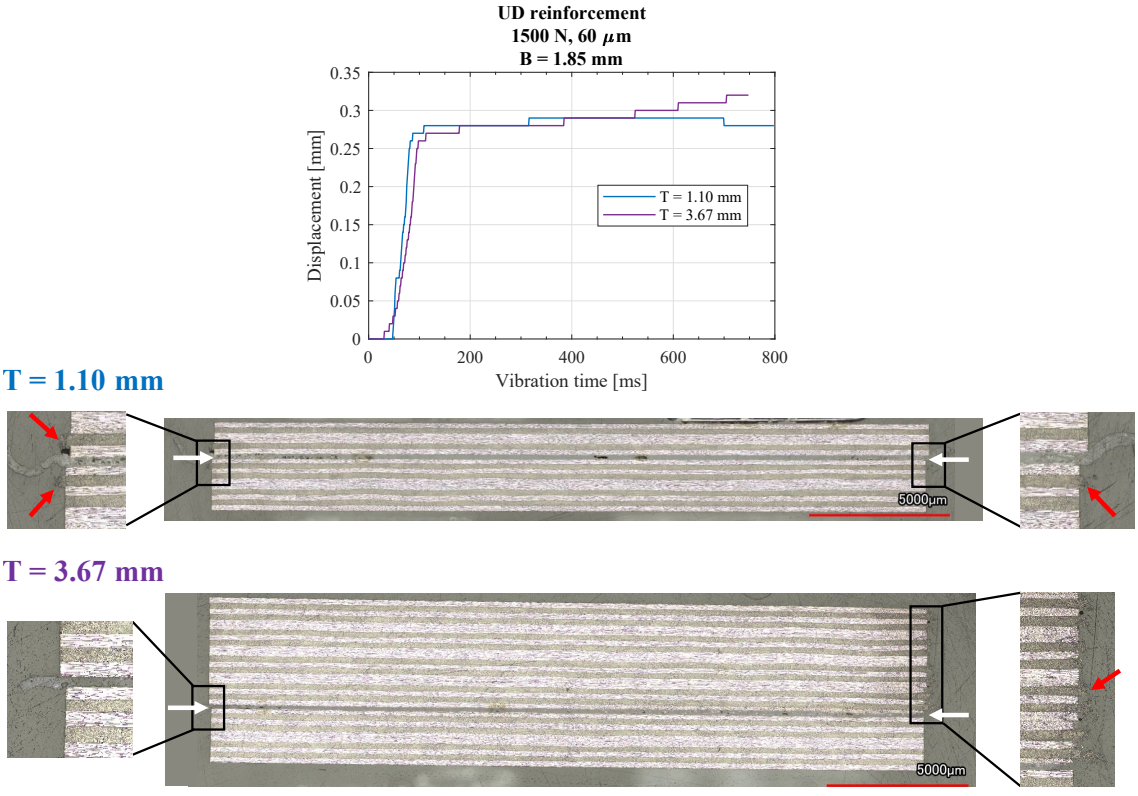

Figure 3.34: Micrographs for top adherend thicknesses of 1.10 mm and 3.67 mm the different points in the displacement curve with force and amplitude values of 1500 N, 60 μm. The white and red arrows indicate the weldline and fiber squeeze-out. Adherends with UD reinforcement.

4

Discussion

The aim of this study was to answer the following research question: **what is the effect of the adherends' thickness on the process response and weld evolution under different process parameters during static ultrasonic welding of thermoplastic composites with fabric and UD reinforcement?** This main question was broken down into specific questions that were presented in Section 1.4 which are divided into the following topics: effect of changing the top adherend's thickness (including near and far-field ultrasonic welding in thermoplastic composites), effect of changing the bottom adherend's thickness, effect of changing the process parameters, and effect of the thickness when changing to UD reinforcement.

It is important to acknowledge that this study was intended to give an initial understanding on the role that the thicknesses of the top and bottom adherends play rather than developing an envelope that defines the thickness limitations for USW or finding optimal conditions for given thicknesses. This is the reason why no lap-shear strength and fractography analyses were performed as testing samples with different thicknesses gives odd stress states, and changing the thickness of the top and bottom adherends at the same time does not agree with the scope of the research questions.

4.1. Effect of changing the top adherend's thickness

From the displacement curves (Figure 3.1b) it is seen that the behaviour does not change for the thin adherends (1.17 mm, 1.83 mm, and 2.37 mm). This, plus the fact that the high-speed camera (HSC) snapshots at different points in the displacement curves (Figure C.2) show a similar evolution, indicates that the physical changes occurring at the interface are insensitive to the thickness increase within this range, which was already discussed in the study by Villegas [35]. For such thickness values, the explanation of these changes can be complemented with information found in literature for ultrasonic welding with mesh EDs [8]. As was mentioned in Section 3.1.1, there are three distinctive regions in the displacement curves: an initial increase of the displacement, a displacement plateau, and a final increase in displacement. From the start of the vibrations until the beginning of the plateau, the ED is flattened as the filaments of the mesh are starting to fill up the open spaces. During the plateau, these filaments widen as the ED is melting and the open spaces are gradually filled until the end of such plateau. All the open spaces have been filled after the end of the plateau and the thickness of the weldline is practically zero [8].

The behaviour of the power can also be linked to these changes at the interface. The evolution of the power-interface temperature, the power-displacement, and the power-amplitude for a thin top adherend (1.83 mm) is shown in Figure 4.1. There is an initial power rise that occurs before the beginning of the displacement plateau and at temperatures below the T_g as seen from Figure 4.1a. This rapid increase in power can be explained by the behaviour of the amplitude at such point (Figure 4.1c), where it is seen that it overshoots as the sonotrode is adjusting to the sudden vibrations and the ED is relatively cool. After passing the T_g, there is a small decrease in power since the amorphous regions of the ED start flowing and viscoelastic heating becomes dominant as the loss modulus of the resin peaks. Because heat is already being transferred to the cooler adherends, these amorphous regions of the ED re-solidify which can explain why the power increases again. The power peaks at T_m when the filaments of the ED start flowing and filling up the empty

spaces, which occurs at the beginning of the displacement plateau as seen from Figure 4.1b. In literature, this increase of power when the ED starts flowing is attributed to the increase in mechanical impedance as the melt fronts meet [3]. For the case with mesh EDs, this may be a result of the meeting of the melt fronts from adjacent filaments as they fill the open spaces. Once the ED starts melting, the power remains somewhat constant until the end of the displacement plateau. After the end of the plateau, the power starts dropping as the uppermost layers of the adherends start locally melting, which causes a downwards displacement of the sonotrode as there is squeeze flow from both the adherends and ED.

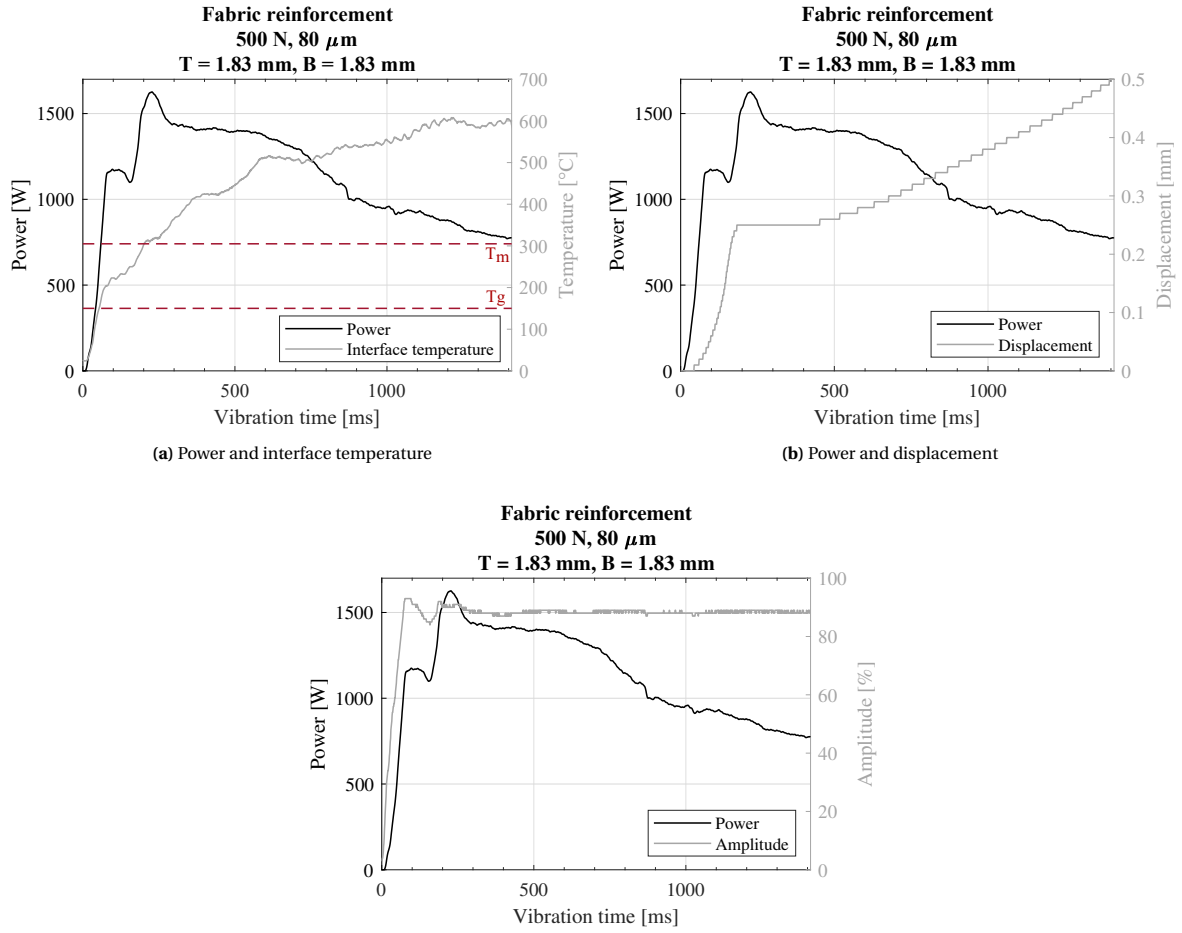

(a) Power and interface temperature

(b) Power and displacement

(c) Power and amplitude. The amplitude (80 μm) corresponds to 88% of the maximum amplitude the equipment can provide.

Figure 4.1: Representative power-interface temperature, power-displacement, and power-amplitude curves for a 1.83 mm-thick top adherend welded at 100% displacement (travel of the sonotrode equal to the thickness of the ED).

A different story is observed from the curves in Figure 3.1b for the thicker adherends (3.55 mm and 4.72 mm), for which the displacement follows a very different behaviour. This happens because the physical changes are no longer occurring only at the interface, but also in the top adherend as was seen from the HSC snapshots and microscopy (Figure 3.4 and Figure 3.6). The overheating in the top adherend causes fiber squeeze-out in a rather unpredictable way, which explains why the displacement curves for the same thickness of the top adherend (as shown in Figure 3.5) each follow a different behaviour.

The COMSOL model results (Section 3.1.6) show what the effect of the thickness is solely based on the wave propagation through the welding stack, which is originated from the vertical oscillation of the sonotrode only (80 μm at 20 kHz). As mentioned in Section 2.3.4, the assumptions made to built the model make it not suitable for a quantitative analysis or for direct comparison with the experimental results, and therefore the findings should be analyzed qualitatively. For example, by not including the fibers in the adherend, the complex reflection or refraction at the fiber-matrix or ply interfaces [58] is not considered. The comparison between the 1.17 mm-thick and 4.72 mm-thick top adherends shows that the increase in thickness will have an

effect on the wave attenuation as it passes through the top adherend, which therefore reduces the amplitude of the vibrations that reach the interface as seen in Figure 3.10. Considering such behaviour, then the vibrational energy originated from the sonotrode (quantified by the amplitude) attenuates in the top adherend rather than being concentrated at the interface. Hence, the friction between the molecules causes viscoelastic heating in the top adherend, which could explain why its temperature increases as it becomes thicker (Figure 3.7c). This would therefore imply that the friction and viscoelastic heating rates (which both depend on the cyclic strain on the ED) would be reduced as the thickness of the top adherend increases, potentially explaining the differences in behavior for thin and thick adherends. Because the vibrations that are transmitted to the interface are limited by this thickness increase, therefore the vibrations that reach the bottom adherend should also get reduced. The previous explanation would be valid if not for the temperature curves at the interface and bottom adherend for each thickness of the top adherend (Figure 3.7a and Figure 3.7b). If indeed increasing the thickness of the top adherend limits the vibrations that reach the interface -therefore reducing the cyclic strain-, then it should be expected that both temperatures would significantly reduce as the thickness of the top adherend increases. This is however not the case as seen from such figures. This therefore indicates that the wave attenuation is not as significant as estimated from the COMSOL model and that the assumptions made to build such model do not give an accurate representation. It is recommended that, for future numerical analyses on wave propagation during ultrasonic welding of thermoplastic composites, the composite is modelled as a viscoelastic material and that the presence of a fiber reinforcement is considered.

If the problem is analyzed from a static point of view and reduced to a series of springs where only the part of the adherends under the overlap is considered [85] as shown in Figure 4.2, the relationship between the strain at the ED and the thickness of the top adherend can also be determined. The strain on the adherends and ED (considering that the ED does not cover the whole overlap area) is given by:

$$\varepsilon_{\text{adh}} = \frac{\Delta L}{L_{\text{ED}} \frac{E_{\text{comp}} A_{\text{comp}}}{E_{\text{ED}} A_{\text{ED}}} + T + B} \tag{4.1}$$

$$\varepsilon_{\text{ED}} = \frac{\Delta L}{L_{\text{ED}} + \frac{E_{\text{ED}} A_{\text{ED}}}{E_{\text{comp}} A_{\text{comp}}} (T + B)} \tag{4.2}$$

Where ΔL is the deformation resulting from the amplitude of the vibrations (in this case 40 μm), T is the thickness of the top adherend, L_{ED} is the thickness of the ED (0.50 mm), B is the thickness of the bottom adherend (1.83 mm), E_{ED} is the modulus of the ED (3.1 GPa as assumed in the COMSOL model), E_{comp} is the modulus of the composite adherends (13.3 GPa as assumed in the COMSOL model from Equation 2.3), A_{ED} is the area covered by the ED (estimated as 235.8 mm^2 with ImageJ for an undeformed ED), and A_{comp} is the overlap area (12.7 × 25.4 mm^2). Because the top and bottom adherends have the same modulus, the strain at both is the same.

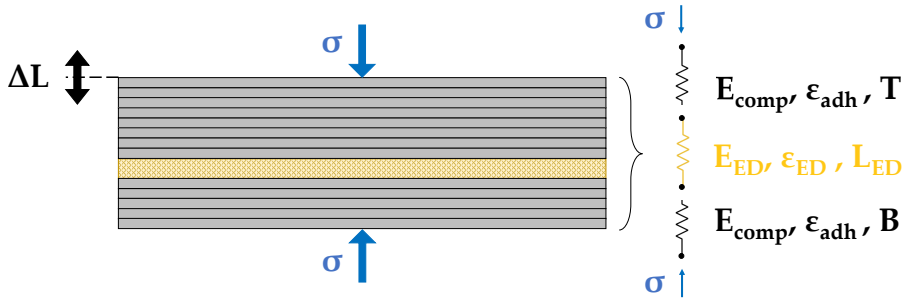

Figure 4.2: Static simplification of the ultrasonic welding process. Diagram adapted from [85]. σ is the stress applied to the welding stack, ε is the strain in the different components, ΔL is the total deformation, T and B are the thicknesses of the top and bottom adherend, L_{ED} is the thickness of the ED, and E_{ED} and E_{comp} are the moduli of the ED and adherends.

Figure 4.3 shows the strain on the adherends (Equation 4.1) and ED (Equation 4.2) for different thicknesses of the top adherend. It is observed that the strain on the adherends is not significantly affected by the increase in thickness, which would contradict the fact that there was overheating in the thicker adherends.

This, because a higher cyclic strain would account for more viscoelastic dissipation and, hence, more heating in the adherend as it becomes thicker. On the other hand, it is also observed that the strain on the ED is much more affected by such increase in thickness. The gap between the strain on the ED and the adherends seems to reduce as the thickness increases, which would indicate that the ED is no longer as effective at concentrating energy at the interface. However, the ratio $\varepsilon_{ED}/\varepsilon_{adh}$ indicates otherwise and therefore does not support the obtained results.

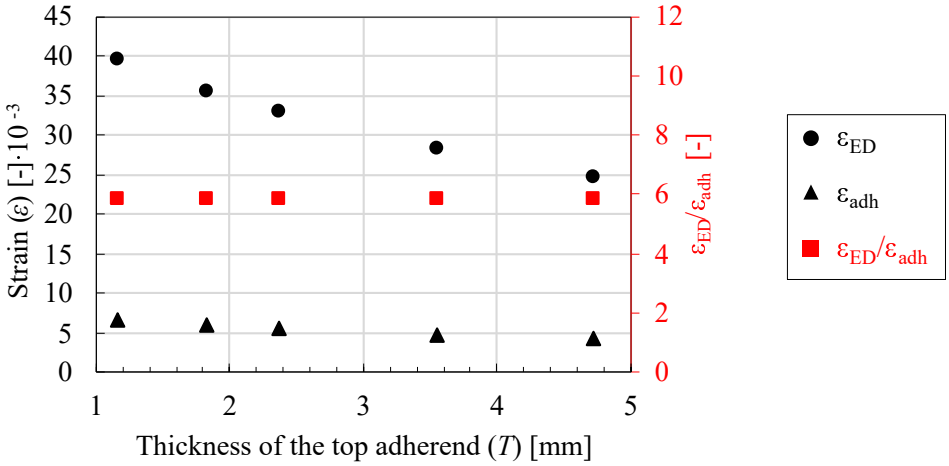

Figure 4.3: Strain on the energy director (ε_{ED}), strain on the adherends (ε_{adh}), and ratio $\varepsilon_{ED}/\varepsilon_{adh}$ for different thicknesses of the top adherend.

According to literature, and mentioned in the Literature study, the concentration of heat generation at the interface partially relies on the fact that the stiffness (reciprocal of compliance) of the ED is lower than the adherends [19]. If this were not the case, then the ED does not have the role of concentrating energy anymore [86]. The compliance (C) of the ED [8] and top adherend (simplifying it as an isotropic material with a modulus equal to the transverse modulus 13.3 GPa) is given by:

$$C_{ED} = \frac{L_{ED}}{E_{ED} A_{ED}} \tag{4.3}$$

$$C_{adh} = \frac{T}{E_{comp} A_{comp}} \tag{4.4}$$

If the compliance for different thicknesses of the top adherend is compared to the compliance of the ED (Figure 4.4), then it is noted that for the thicker adherends (3.55 mm and 4.72 mm) such values are larger than for the ED. Considering only this compliance, then the fact that C_{adh} is larger than C_{ED} for such thicknesses should explain the overheating in the top adherend, as the vibrational energy is no longer being concentrated at the interface, but rather dissipated in the top adherend. However, the viscoelastic heating rate is dependent on the cyclic strain (see Equation 1.1) and not the compliance, and Figure 4.3 indicates that this ratio of the strain on the ED and adherends does not change with thickness. This therefore suggests that the statements indicated in literature, and mentioned previously, should be revised.

The previous analysis points to the fact that the effect of the thickness on the cyclic strain due to the vertical oscillation of the sonotrode is not the culprit of the overheating, and therefore this overheating must come from another effect. A possible candidate for such behaviour is hammering. Hammering is an inherent effect during ultrasonic welding as there is loss of contact between the sonotrode and the top adherend [30] as depicted in Figure 4.5 where the displacement imposed by the sonotrode and the actual displacement in the top adherend are shown. Although it does not give a direct quantification, the evolution of the amplitude can give valuable information about hammering and how it is affected by the increase in thickness. Figure 3.3 shows the evolution of the amplitude and displacement during the vibration phase for top adherend thicknesses of 1.17 mm, 2.37 mm, and 3.55 mm. In these figures, the set peak-to-peak amplitude was 80 μm, which corresponds to 88% of the maximum amplitude that the equipment can deliver. From the beginning of the process

until before the beginning of the displacement plateau the sonotrode is adjusting to the vibrations and therefore the amplitude is not immediately set to its nominal value, which sometimes causes an overshoot. After this, the amplitude oscillates around 88% until the end of vibrations. The oscillations have a larger amplitude as the thickness increases, which therefore is an indication that hammering also increases. For the 3.55 mm-thick case, the amplitude of these oscillations around the nominal value is quite exaggerated, even reaching values above the maximum input amplitude of the equipment. This increase in hammering could contribute to the overheating in the top adherend by including an excitation to the welding stack every time it impacts the top adherend after losing contact with it. If the frequency of such impact is close to a natural frequency of the system, then it could cause an oscillatory excitation which would contribute to viscoelastic heating as there is more cyclic strain. A confirmation of such statement would be possible by performing a modal analysis of the system under the displacement imposed by the sonotrode while accounting for such hammering.

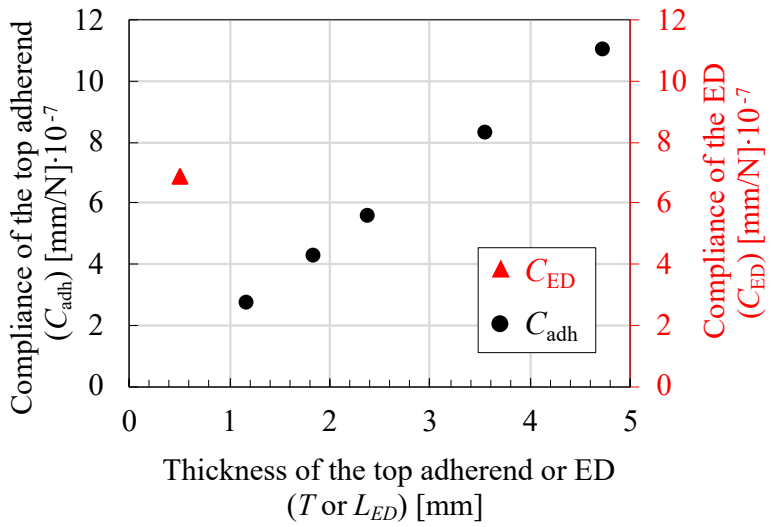

Figure 4.4: Compliance of the top adherend (C_{adh}) vs. its thickness (T). The compliance of the ED (C_{ED}) is shown at L_{ED} = 0.50 mm (thickness of the ED).

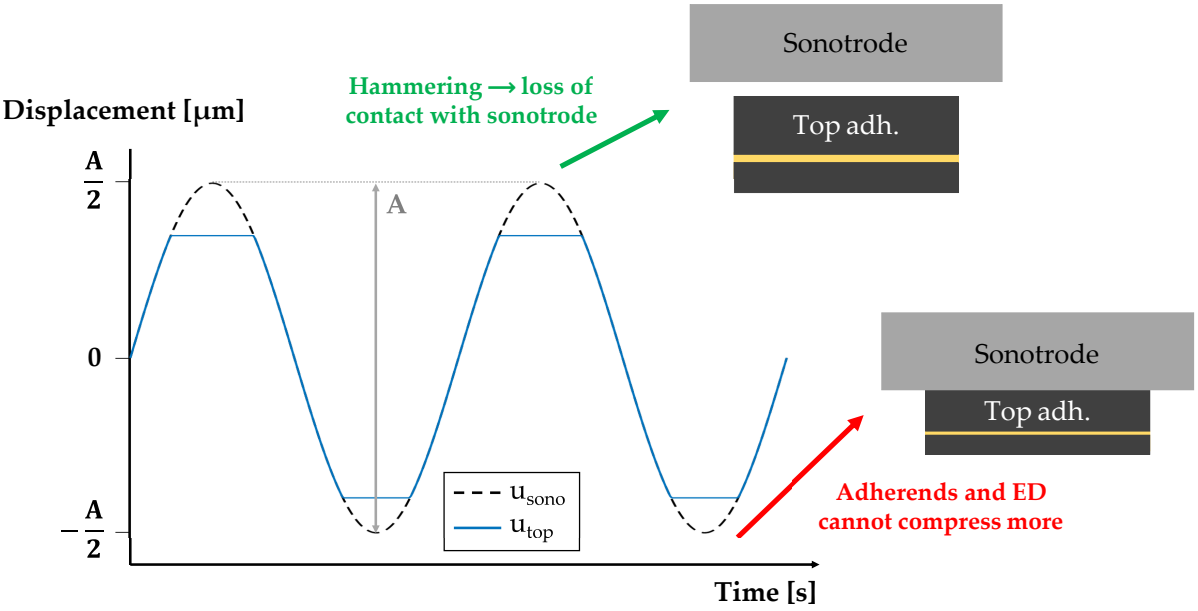

Figure 4.5: Displacement imposed by the sonotrode (u_{sono}) and displacement at the top adherend (u_{top}), where A is the peak-to-peak vibration amplitude. The upper and lower cuts in the displacement are caused by hammering (loss of contact between sonotrode and top adherend) and the limited compressibility of the adherends and ED, respectively.

The fact that these oscillations in the amplitude curves occur for thicker adherends also contradicts the results from the static problem (Figure 4.3) and suggests that the behaviour is not defined by the static response, but rather the dynamic one. This, because such oscillations indicate that indeed there is more cyclic strain as the thickness increases, which again would account for the overheating in the top adherend. The cause of this direct relationship between hammering and thickness is however not clear as thicker adherends are more compliant and therefore capable of deforming more under a given compressive load, which should then cause less hammering. This is also depicted in Figure 4.5 in the lower cut of the displacement. It is important to note that such cut depends on how much can the adherend compress under the static and dynamic loads, and may not even occur for certain cases, like when welding with a much lower force or amplitude. A possible cause for such behaviour could be the fact that when the sonotrode is retracting, the more compliant adherends expand more and therefore impose a displacement on the sonotrode in the opposite direction. In fact, this is the explanation that Nonhof and Luiten [67] give for such hammering during ultrasonic welding of thermoplastics (that the adherends bounce between the sonotrode and the anvil). Nonetheless, the authors also indicated that this hammering should also decrease for thicker -and therefore more compliant- adherends, which is in disagreement with the findings of this study.

As was mentioned earlier, the results from the static problem are not in agreement with the experimental findings. Benatar and Gutowski [3] suggested that analyzing the problem by acknowledging the effects associated with squeeze flow and discriminating the behaviour of the ED under the static and dynamic loads provides a better understanding of the ultrasonic welding process. Based on the dimensionless numbers for the fluid ED (Reynolds, Mach, Deborah, and Weissenberg) that would give an indication of the inertia, compressibility, and elasticity, the authors estimated the behaviour of the triangular EDs at different stages of the process and under the static and dynamic loads. The analysis showed that the molten ED does not behave equally under static and dynamic conditions. For example, early in the process and under the static loading it behaves like a soft spring in parallel with a soft damper, whereas dynamically it behaves like a hard spring [3]. Although in such study this analysis was not performed for the composite adherends since their viscoelastic heating is neglected as their thickness was such that the welding configuration is in the near-field, a similar analysis could help explain why there is this relationship with thickness and hammering. If the same is occurring at the beginning of the welding process for the adherends (static behaviour like a soft spring in parallel with a damper, but dynamic behaviour like a hard spring), then the fact that more compliant adherends are causing increased hammering could be explained. Furthermore, this could also help explain why the evolution of the amplitude for the 3.55 mm-thick top adherend (Figure 3.3c) varies during the welding process and seems to coincide with the different stages of the displacement curve.

The thickness of the top adherend is also related to the classification of near and far-field welding, as was mentioned in the Literature study (Section 1.2.3), where the two issues found with this definition were discussed. If the discrimination between near and far-field is considered from a purely qualitative point of view and the 6 mm turning point is neglected (as discussed in the literature study), then the results from this study would suggest that the "near"-field region comprises the top adherend thicknesses of 1.17 mm, 1.83 mm, and 2.37 mm whereas the "far"-field occurs for thicknesses of 3.55 mm, 4.72 mm and, most likely, higher thickness values. This, based on the differences in the weld evolution (efficiently identified by the displacement curves) and the fact that overheating and damage of the top adherend was inevitable for the thicker samples. This however would be for the reference case of low force-high amplitude (500 N, 80 μm) results that were shown in Section 3.1. Yet, as was shown in Section 3.3, changing the force and amplitude alters the behaviour of the process and the weld evolution for the same top adherend thickness values. Furthermore, if the wavelength of the samples used in this study is considered (146 mm as seen from Appendix H), then the fact that "far"-field occurrences (for example, difficulty to weld and melting of the top adherend/sonotrode interface) happened in samples with a thickness of 3.55 mm is unexpected. Besides, as shown previously in this section, wave attenuation through the top adherend was not responsible for the poor quality of the welds for thicker adherends. The latter suggests that for thermoplastic composites, it would be more valuable to develop an index or envelope that considers other domains that are relevant during ultrasonic welding, such as material properties, process parameters, and geometric conditions, rather than adopting the -not so elaborated- near and far-field ultrasonic welding definition from thermoplastics to address the top adherend thickness matters. This, because the turning thickness point that limits the process will not be the same under different conditions. For example, Villegas [35] was capable of welding 3.84 mm-thick CF/PEI adherends and obtain the same weld evolution as 1.92 mm-thick ones, whereas in this study with CF/LMPAEK adherends a thick-

ness of 3.55 mm showed may differences with respect to thinner samples. This may be attributed to the fact that PEI is an amorphous polymer and therefore the behaviour under the wave propagation is different than for the semi-crystalline material [11] in this study (LMPAEK).

The experimental findings therefore suggest that the limitation of the top adherend's thickness is more related to the overheating of the adherend rather than the loss in amplitude at the interface due to wave attenuation. For the conditions in this part of the study, such limitation was found to be 3.55 mm as overheating of the top adherend was imminent and there was a poor repeatability of the experiments. Furthermore, the results also suggest that there is a direct relationship between the compliance of the top adherend and hammering, based on the amplitude curves. It is also theorized that hammering may even contribute to more overheating as it creates a new impact in the top surface due to the loss of contact with it. Multiple new questions are raised from the analysis of these findings and therefore more research is encouraged to further understand the role of the top adherend's thickness.

4.2. Effect of changing the bottom adherend's thickness

The process response and weld evolution were much less sensitive to the change of the bottom adherend's thickness. Unlike the case in which when the thickness of the top adherend is increased, Figure 3.11b shows that the displacement curves are similar for all the different thicknesses of the bottom adherend, even when comparing multiple welds for the thickness extremes (1.17 mm and 5.79 mm) as shown in Figure 3.12b. As was discussed previously, the fact that the displacement behaviour is alike indicates that similar physical changes are occurring at the welding interface. Furthermore, from the amplitude curves for different thicknesses (Figure 3.13 and Figure B.2) the same is also observed.

The power showed to be one of the main variables affected by the change in the bottom adherend's thickness, as shown in Figure 3.11 and Figure 3.12 where it is seen that it gradually increases with thickness. As was mentioned in the Literature study, the power output from the equipment does not only consists of the power required to create the weld, but also the dissipated power to the surroundings. Increasing the amount of viscoelastic material (by increasing the thickness of the adherend) therefore causes more bulk viscoelastic dissipation related to the viscous behaviour of the polymeric matrix [87], thus requiring more power from the equipment. Li et al. [88] indicated the following relationship: $P \propto x^{1.5}$, where P is the welding power [W] and x is the plate thickness [mm]. This however is for the case in which both adherends have the same thickness. If the maximum power is also assumed to be dependent on the bottom adherend's thickness raised to a power (shown in Figure 4.6), a relationship between these two variables $P \propto B^{0.23}$ is obtained. The relationship between maximum power and thickness could be explained by the dependency of the power on the friction and viscoelastic heating rates and is therefore a result of the variables in such heating rates that will depend on the thickness of the bottom adherend. According to literature [9, 78], the power at any moment during the welding process is described as:

$$P = \dot{Q}_{\text{fric}} + \dot{Q}_{\text{visc}} = \chi\alpha\omega\frac{\mu E^{'}}{\pi\nu}\varepsilon_o^2 V_{ED} \; + \; \chi\alpha\frac{\omega E^{''}\varepsilon_o^2}{2}V_{ED} \tag{4.5}$$

Where $\dot{Q}_{\text{fric}}$ and $\dot{Q}_{\text{visc}}$ are the interfacial friction and viscoelastic heating rates that are dependent on the efficiency of the process χ, hammering coefficient α, vibration frequency ω, friction coefficient μ, storage modulus $E^{'}$, Poisson's ratio ν, loss modulus $E^{''}$, cyclic strain in the ED ε_o^2, and volume of the ED V_{ED} [9]. For the conditions in this study, the power peak was found to occur around T_m (as shown in Figure 4.1a) and therefore the storage and loss moduli at such temperature should be used to determine the maximum value. Nonetheless, this equation does not account for friction and viscoelastic heating in the adherends, which was found to significantly contribute to the power as indicated by Figure 4.6. The expression for friction heating (first term in Equation 4.5) would not be appropriate to determine such heating rate in the adherends, as the mechanism is no longer interfacial friction but intermolecular friction. However, the expression for viscoelastic heating rate (second term in Equation 4.5) should still be valid as it relies on the cyclic strain at the bottom adherend. Assuming this cyclic strain is not significantly dependent on the thickness of the adherend, then perhaps a linear regression is more coherent as the volume of the adherend is linearly dependent on its thickness. Regardless of whether a linear relationship is an appropriate regression or not, it is relevant to highlight the importance of understanding the underlying cause of an obtained behaviour rather than assuming the response that adjusts better to a certain regression.

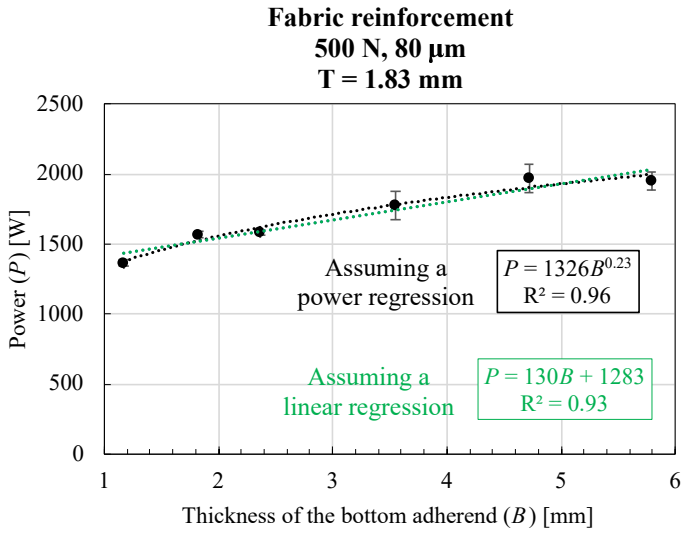

Figure 4.6: Maximum output power vs. thickness of the bottom adherend (n = 3). Both power and linear regressions are shown.

Another noticeable effect of increasing the thickness (applicable for both the top and bottom adherends) is the cooling rate as can be seen from Figure 3.15 where it is evidenced that the temperature at both the interface and adherends decreases more rapidly for thinner adherends than for thicker ones. In order to support these results, the COMSOL heat transfer model was built to evaluate what the effect of increasing the thickness is solely based on heat transfer. These results are not suitable for direct comparison with the experimental data since there is also viscoelastic heating in the bottom adherend, as was discussed in the study of Jongbloed et al. [29]. The COMSOL results (Figure 3.16) show a similar trend as the experimental results, where it is seen that the 1.17 mm-thick adherend cools down much faster and, as the thickness increases, cooling of the adherends becomes slower. Something that can be noticed from both the numerical and experimental results is that the temperature values seem to converge towards the end of the curves for the 4.72 mm and 5.79 mm-thick bottom adherends. In order to check if the same is to be expected from a much thicker case, a 10.00 mm-thick adherend was modelled as can be seen in Figure 4.7, where only the results in the bottom probe are shown as the top probe temperature (Figure 3.16a) showed to be much less sensitive to the change in the bottom adherend thickness. In this plot with the added thickness, the curve for the 5.79 mm-thick adherend is not visible as it overlaps with the 10.00 mm-thick adherend.

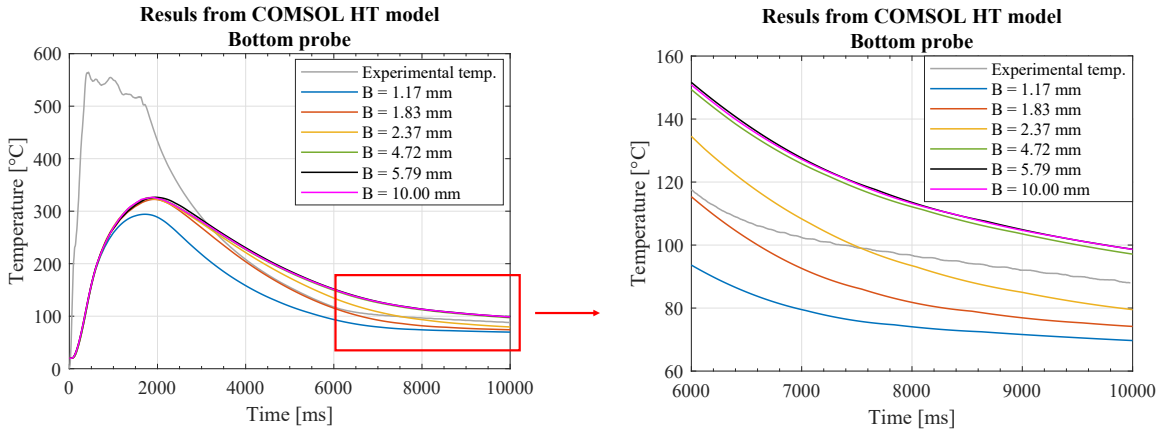

Figure 4.7: Results of the COMSOL heat transfer model with an additional thickness B = 10.00 mm. The experimental input temperature is the interface temperature for one of the experiments.

The reasoning behind this behaviour in the COMSOL results can be explained by the fact that, as the thickness of the bottom adherend increases, the heat source (interface) is further away from the much more conductive aluminum anvil. This is supported by Figure 4.8 where the through-the-thickness temperature in

the bottom adherend is shown at 2500 ms and 7500 ms for four thickness values (same thickness values that are presented in Appendix G). The 5.79 mm-thick curve at 2500 ms overlaps with the 10.00 mm-thick one and therefore is not properly seen. The curves show that there is a temperature decrease for all the thicknesses as the position in the bottom adherend is closer to the anvil. This trend is seen clearly when comparing the behaviour of the 2.37 mm and 10.00 mm-thick adherends at 2500 ms. Although this may also contribute to the changes in cooling for the different thicknesses of the bottom adherend in the experimental results, the slower cooling for thicker adherends can also be attributed to bulk viscoelastic heating resulting from more dissipation when the thickness increases, as was mentioned previously. This can also be partially supported by the temperature in the bottom adherend (Figure 3.15b) where it is seen that the thicker adherends reach higher temperatures. These readings, however, may present scattering and the maximum values obtained are not as trustworthy as the overall followed trends. The slower cooling for the thicker adherends can therefore be explained by the fact that more material is being heated during the vibration phase. Although the temperature in the bottom adherend for thicknesses of 4.72 mm and 5.79 mm (Figure 3.15b) followed a similar behaviour, it is unknown whether for higher thicknesses (B > 5.79 mm) the same will occur. The possibility that fiber squeeze-out from the bottom adherend occurs for even thicker adherends (as in the case for thick top adherends) is not ruled out, and therefore it is not possible to determine a thickness limitation based on the temperature readings.

The differences in the cooling may have an effect on the crystallinity at the interface. A previous study [89] on CF/PPS adherends showed that indeed there is an inversely proportional dependency of the crystallinity on the cooling rate. This, because the polymer chains are allowed to arrange in crystalline domains if subjected to a lower cooling rate [89]. Although the crystallization kinetics of PPS and LMPAEK may not be directly comparable, a similar trend could be expected from the material in this study and therefore a higher crystallinity at the interface is expected when welding thicker adherends. According to the provider of the material (see Section 2.1) [73], the highest crystallization rate for the neat LMPAEK polymer (quantified by the time to reach 50% of the relative crystallinity at such temperature) is obtained at 220° C. If the cooling rates at this point are calculated for the extreme thickness cases of the bottom adherend (as shown in Figure 4.9), it is then seen that the cooling rate for the thicker adherend is close to half the cooling rate for the thinner one. Furthermore, the provider also indicates that the crystallinity can be increased by extending the time spent above 220° C [73] and below the melting temperature (T_m). This window time between the indicated temperature values was also calculated and is presented in Figure 4.9, where it is seen that the duration is considerably higher for the 5.79 mm-thick adherend. The extent of these effects (cooling rate and duration of the window between T_m and 220° C) on the crystallinity at the interface was not quantified in this study and therefore the specific effect of the bottom adherend's thickness on the degree of crystallinity remains unknown.

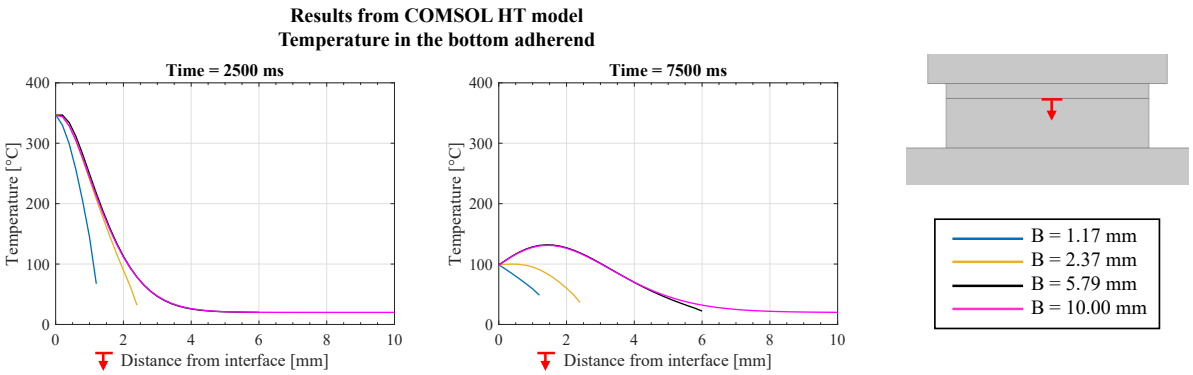

Figure 4.8: Though-the-thickness temperature profile in the bottom adherend and the middle of the overlap at 2500 ms and 7500 ms for thicknesses of 1.17 mm, 2.37 mm, 5.79 mm, and 10.00 mm.

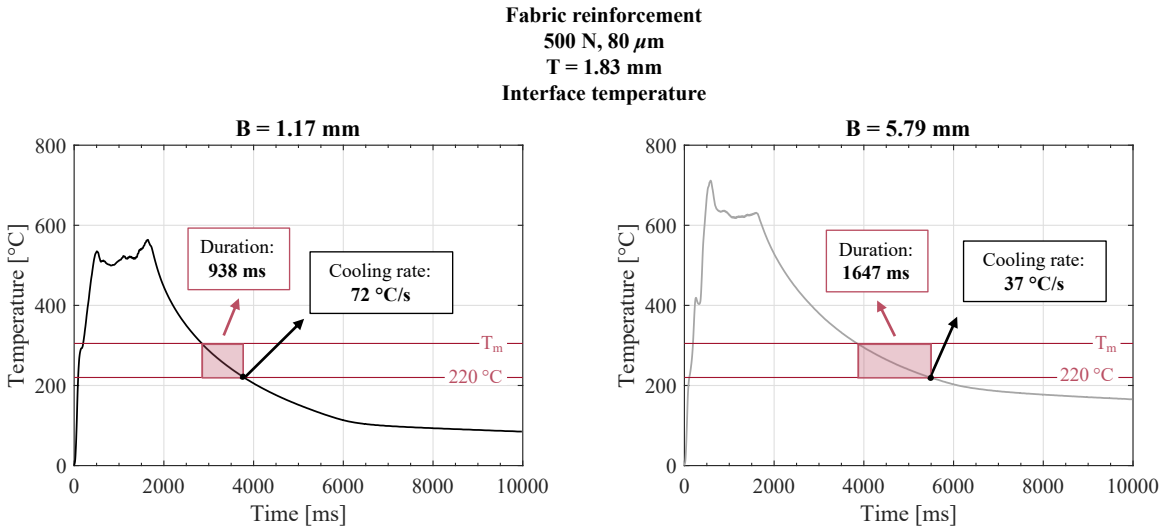

Figure 4.9: Interface temperature for bottom adherend thicknesses of 1.17 mm and 5.79 mm. The duration of the window in which the temperature is between 220°C and 305°C (T_m) and the cooling rate at 220°C are indicated in the graphs.

The effect of the thickness solely based on wave propagation through the welding stack was also evaluated with the COMSOL model (Section 3.2.6). The results show that increasing the bottom adherend's thickness will have an effect on the amplitude reaching the bottom adherend/anvil interface as the wave gets attenuated thought the bottom adherend, therefore affecting the wave reflection at such interface. This effect is evidenced in Figure 3.19, where it can be seen that this reflection affects the amplitude at the top adherend/ED interface by introducing a displacement in the opposite direction as the one imposed by the sonotrode, hence causing a lower total displacement for the 1.17 mm-thick adherend. The effect of this behaviour in the experimental results -particularly in temperature readings- was however not clearly seen. Figure 3.15a and Figure 3.15d show that, in general, similar peak interface temperatures were obtained for the different thicknesses of the bottom adherend with the exception of two curves (B = 1.83 mm in Figure 3.15a and a curve of B = 5.79 mm in Figure 3.15d) that reach higher values, which is attributed to scattering. On the other hand, Figure 3.14 shows that, for the same position in the displacement curve, there is visible fiber squeeze-out from the 5.79 mm-thick adherend but not from the 1.17 mm-thick one. This response can create the misconception that there is overheating in the adherends as the thickness increases. However, it may be an indicator that, at this point, the welding stage is not the same for both thicknesses, and therefore different phenomena are occurring at the welding interface at such time. Furthermore, it is not possible to blindly assume that there is no fiber squeeze-out from the adherends in the 1.17 mm case as the visibility from the high-speed camera is limited. For this, a microscopy analysis would be required.

The experimental results therefore indicate that the two major effects of increasing the bottom adherend's thickness are on the dissipated power and cooling rate. From these results it is not possible to determine the thickness limitation of the bottom adherend. To determine this limitation, more research is required on the effect of the thickness on the weld quality (microscopy, lap-shear strength, and fractography) as this was not investigated in the current study.

4.3. Effect of changing the process parameters

Changing the process parameters showed to have a major effect on the differences in the process response and weld evolution for thin and thick adherends with respect to the low force-high amplitude reference case. The effect of the force and amplitude on the power and vibration time is as expected from the results found in literature [6, 35]. A lower amplitude will affect the viscoelastic heating rate (Equation 1.1) since the cyclic strain is reduced, which will therefore increase the vibration time for a given travel (in this case, 100% displacement) and decrease the dissipated power. This behaviour is observed in the power and displacement curves (Figure 3.20 and Figure 3.21). Decreasing the amplitude also resulted on overall lower temperatures at the interface as seen in Figure 3.27, again caused by a decreased heating rate.

Increasing the force has the opposite effect as decreasing the amplitude, as the vibration time is reduced and a higher power is required. As was mentioned in the Literature study, interfacial friction is the initial heating mechanism until the T_g is reached. Therefore, when the force is increased, the intimate contact between the ED and adherends also increases resulting on a higher number of initiation sites (nucleation and growth of hot spots) resulting from this friction [6], and thus faster cycles are obtained and more is power required as the interfacial heating rate increases. This rapid heating when having higher force and amplitude values has also shown to affect the heat-affected zone (HAZ) in the adherends. This can be observed in the micrographs for the 1.17 mm-thick top adherend at 500 N, 60 μm and 1500 N, 80 μm (Figure D.3 and Figure D.5). The faster heating rate obtained for the high force-high amplitude case results in a smaller HAZ, which is identified by the presence of voids caused by deconsolidation.

Increasing the force has also shown to significantly decrease the hammering effect as there is more contact between the sonotrode and the top adherend [19]. As it was mentioned in Section 4.1, this increase in hammering when welding thick adherends potentially contributes to the overheating in the top adherend leading to considerable fiber squeeze-out in early stages of the process. When looking at the amplitude evolution for a top adherend thickness of 3.55 mm at 1500 N, 80 μm (Figure 3.22b) and comparing it to the figure introduced before for the reference case (Figure 3.3c) it is quite evident that the amplitude of the oscillations around 88% decreases significantly, indicating that less hammering occurs. Furthermore, when comparing the HSC snapshots of the reference case (Figure 3.4) and the high force-high amplitude case (Figure 3.23) it is evident that less overheating in the thick top adherend occurs, therefore supporting such relation between hammering and heating of the top adherend. As hammering decreases, the transmission of energy from the sonotrode to the welding stack is also improved. Despite this, the fact that similar temperature values during vibration were obtained for the 1.17 mm and 3.55 mm-thick adherends and under the different combinations of process parameters (Figure 3.27) again confirms that wave attenuation does not play a significant role in the overheating of the top adherend. The changes when increasing the force are even visible when looking at the top adherend surface as seen in Figure 4.10. Here, the comparison between the low force-high amplitude and high force-high amplitude cases with and without consolidation (4000 ms with the same force used during vibration) is shown. For the 500 N, 80 μm case, the overheating of the top adherend is such that it even causes visible damage in the top adherend's surface with and without consolidation. In contrast, the high force case shows only a small deconsolidated area when the sonotrode is removed immediately after vibration and no visible damage in the surface when consolidating.

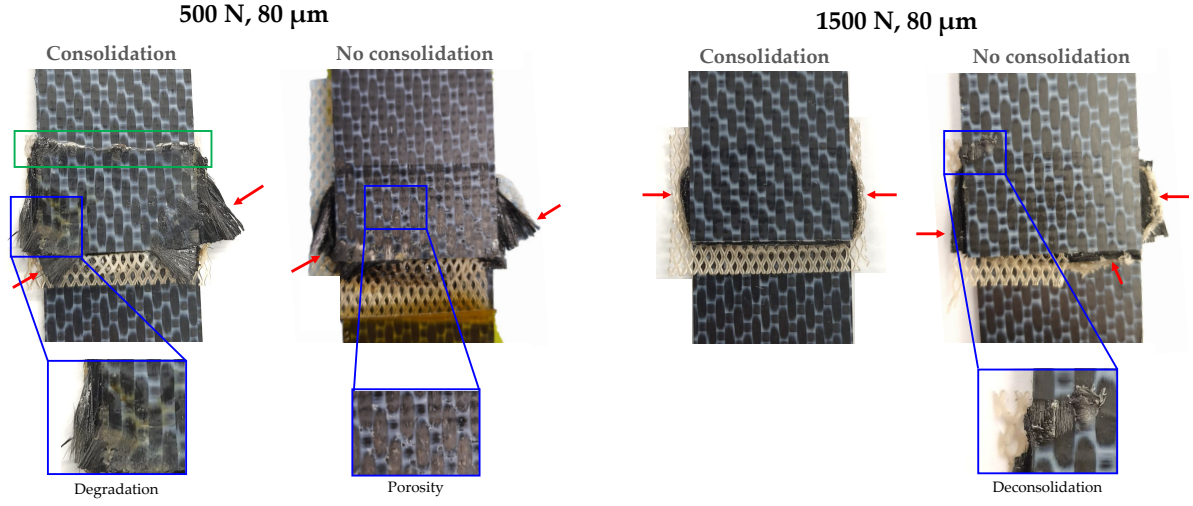

Figure 4.10: Comparison of the top adherend surface for different force and amplitude values with and without consolidation (4000 ms with the same force used during vibration). The thickness of the top adherend was 3.55 mm. The red arrows indicate fiber squeeze-out, the blue squares zoom-in parts of the images, and the green square shows wrinkling.

Figure 3.22 shows the amplitude evolution during the vibration phase for the high force-high amplitude case. It is noticed that there is a significant overshoot at the beginning of the vibrations for the 1.17 mm-thick adherend, whereas this does not occur for the 3.55 mm-thick one nor in the reference case (Figure 3.3a). The same behaviour is observed for the high force-low amplitude case (Figure B.5). This is a result of the lower

compliance of the thinner adherend causing a lower compressibility, as was mentioned in Section 4.1. As the downwards compression increases (either by increasing the force or amplitude), the thinner adherend is less capable of deforming and therefore causes this overshoot in amplitude since the equipment needs to overcome this resistance. Because the power is adjusted to keep the amplitude constant, Figure 3.21c and Figure 3.21d also show this change in behavior between the different thicknesses of the top adherend. It can also be noticed from these power curves for the thicker adherends in the high force cases that there is a second peak towards the end of the curve. This may be an indication that the dynamic response of either the composite adherends or ED change or that there is squeeze flow at this stage, therefore explaining this sharp rise in power. However, it is not possible to confirm this statement as no micrographs were obtained at these points.

Although the overheating of the top adherend was significantly reduced, there was still fiber squeeze-out as seen in Figure 3.25 in the 3.55 mm-thick adherend. It is however very interesting that the 4.72 mm-thick one only shows squeeze-out from the layers adjacent to the interface, which also occurs mildly in the thin sample and can be attributed to the high force exerted by the sonotrode. This again indicates how unpredictable the fiber squeeze-out can be when welding thicker samples and why there are still differences between the displacement curves, although much less when compared to the low force cases. The high force-low amplitude case shows a different story between the thin and thick adherends. The displacement curves (Figure 3.20d) are much more similar between the 1.17 mm and 3.55 mm-thick adherends, which also gets reflected in the micrographs shown in Figure 3.26 where only minor fiber squeeze-out for both thicknesses is seen in the plies adjacent to the interface. In this case, both increasing the force and decreasing the amplitude contribute to lower hammering and viscoelastic heating in the top adherend, hence resulting in less overheating and fewer differences in the process response and weld evolution for thin and thick adherends.

It is not possible to indicate whether an acceptable weld (in terms of the expected lap-shear strength values and failure modes) would be obtained for the thicker adherends when welding with the force and amplitude values that showed the best results in this study (1500 N, 60 μm). However, the findings suggest that the reduction in hammering -and overheating in the top adherend- resulting from such combination of parameters is most likely to yield better welds, and is therefore suggested as a starting point for applications where a top thick adherend is present.

4.4. Effect of changing to UD reinforcement

The final part of this study was to evaluate the changes in the process response and weld evolution between thin and thick adherends with unidirectional (UD) instead of fabric reinforcement. One of the most obvious differences is that there is much more squeeze-out and much less deconsolidation when comparing to the results with a fabric reinforcement, especially from the high-speed camera snapshots and micrographs. For example, Figure 4.11 compares the micrographs of two thick top adherends at a 100% displacement, under the same process parameters and without consolidation after vibration.

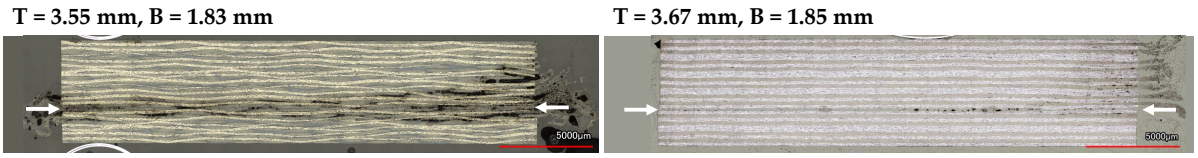

Figure 4.11: Micrographs for fabric (left) and UD (right) adherends welded at a 100% displacement with force and amplitude values of 1500 N, 60 μm and no consolidation after vibration. The white arrows indicate the weldline.

The higher squeeze-out can be explained by the nature of both composites. The architecture itself of the adherends with a fabric reinforcement makes the fibers more constrained as the bundles are interlocked with each other, whereas this is not the case for UD-reinforced adherends since each ply contains only one fiber direction. The micrographs (Figure D.10 to Figure D.13) also show fiber squeeze-out of the fibers in the 0° direction and at earlier stages in the process. The reasoning behind this behaviour was discussed in the study by Köhler et al. [45], where the authors attributed it to the polymer squeeze-flow for different fiber orientations and the fact that, once the resin is molten and the fibers can flow, motion is restricted in the 0°direction because the cooler parts of the adherends that are far away from the interface are still in a solid state. The

much less deconsolidation observed from the UD adherends is also a result of the interlocking of the fibers in the fabric architecture. Because the bundles are arranged in a woven configuration, when first consolidated in the hot-platen press they are significantly compressed. Therefore, when re-heated during the welding process this elastic energy that was stored previously is released (analogous to what happens when releasing a compressed spring) and therefore causes much more deconsolidation. This however will be counteracted during the consolidation phase, which was omitted in this study.

In particular, the significant squeeze-out from the 0° direction showed to be problematic, even when welding thin adherends. Figure 4.12 shows fiber squeeze-out from both the top and bottom UD-reinforced adherends in locations where no damage was noticed previously for fabric adherends that early in the welding process. The thicker adherends show squeeze-out at the right edge of the sonotrode, after the end of the overlap (green circles in Figure 4.12). Because the contact area of the sonotrode is larger than the overlap, the vibrations generated at this point will not get transmitted to the rest of the welding stack, but will rather get concentrated in this area of the top adherend. This behaviour was also noticed in the COMSOL wave propagation results (see Figure 3.9) where it can be seen that the amplitude at such area of the top adherend (circled in red) is larger than its surroundings. This occurs regardless of the type of reinforcement, but the squeeze-out resulting from it is much more prominent in the UD adherends, therefore occurring much earlier in the process and to a higher extent. Another noticeable effect that was not seen in the fabric adherends is squeeze-out from the bottom adherend early in the process. This can be seen on the edges in Figure 4.12, and on the transverse direction in the micrographs (Figure 3.33 and Figure 3.34).

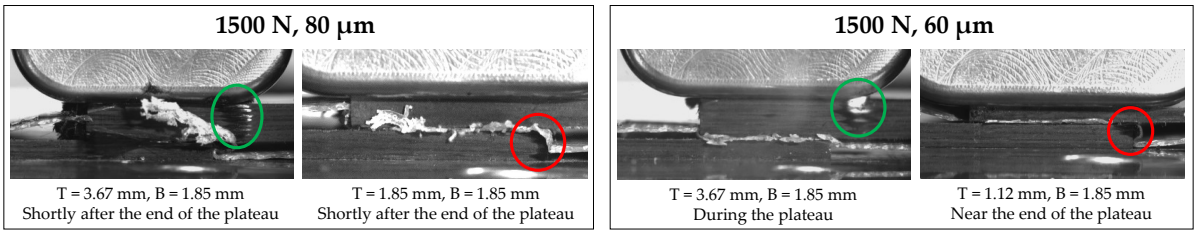

Figure 4.12: HSC snapshots for the high force cases with both thin and thick adherends with UD reinforcement. Squeeze-out under the right edge of the sonotrode is circled in green, and squeeze-out in the bottom adherend in circled in red.

From the power and displacement curves (Figure 3.28 and Figure 3.29) it is seen that the effect of changing the process parameters on the behaviour of such curves is similar to what was observed for adherends with a fabric reinforcement. However, when comparing such curves for a similar thickness of the top adherend (Figure 4.13) it is noticed that there are significant differences between the behaviour between two types of reinforcement. In the study by Köhler et al. [45] it was shown that by only changing the orientation of the fibers adjacent to the weldline (0° or 90° configuration) in UD adherends, the power and displacement curves were fairly affected. This was attributed to the the different heating dynamics for both configurations, and was supported with temperature measurements at the interface. The differences in Figure 4.13 will certainly be caused by the effects of the fiber architecture adjacent to the weldline on the heating dynamics, in combination with the other factors that change between the two types of reinforced adherends, such as the resin content. The research on the differences in the behaviour of the process between adherends with a fabric and UD reinforcement is, however, not part of this study, as only the effect of the thickness is to be addressed. Therefore, such investigation is suggested for future research.

There is a significantly increased similarity in the displacement curves between thin and thick adherends for a given set of process parameters for UD-reinforced adherends as compared to fabric ones. An example of this is the comparison between Figure 3.20b and Figure 3.28b, considering that the UD adherends were thicker (3.67 mm) than the fabric ones (3.55 mm). The amplitude curves for thick adherends (Figure 3.30b) also show fewer oscillations around the nominal amplitude when compared to the fabric case (Figure 3.3c), indicating that less hammering occurred. This again points the relationship between compliance of the adherends and hammering, as the UD-reinforced adherends will have a lower compliance. This, because of the reduced resin content (see Table 2.1 for the comparison of the values) and the interlocking of the fiber bundles in a woven configuration. The fact that the displacement curves in Figure 3.28b (which give an indication of the weld evolution) are more similar between thin and thick adherends, and that less fiber squeeze-out from the adherends was observed (Figure D.11 and Figure D.13) therefore indicates that there was less overheating

from the top adherend as compared to the fabric case, which also supports the hypothesis that hammering may contribute to the overheating of the top adherend.

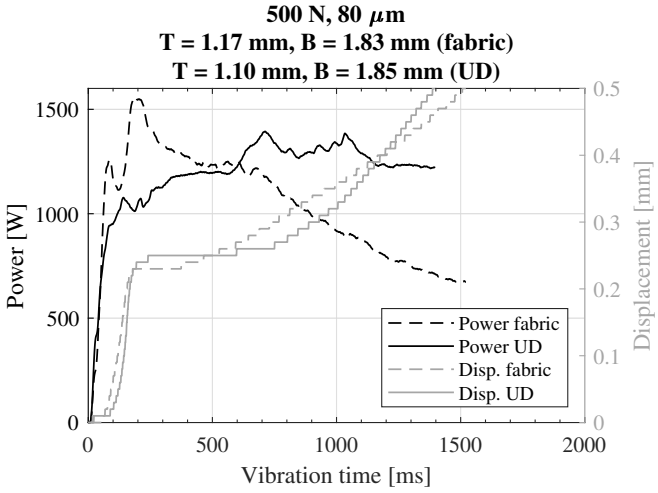

Figure 4.13: Comparison between the power and displacement curves for adherends with a fabric (- -) and UD (-) reinforcement.

5

Conclusions and recommendations

This chapter summarizes the main findings of the study while answering the research questions and gives recommendations for future research.

5.1. Conclusions

The main research question of this study was the following: **what is the effect of the adherends' thickness on the process response and weld evolution under different process parameters during static ultrasonic welding of thermoplastic composites with fabric and UD reinforcement?**.

The research was divided into four different stages as presented in the results and discussion: effect of the top adherend, effect of the bottom adherend, effect of the thickness when changing the process parameters, and differences on the effect of the thickness between fabric and UD-reinforced adherends. The main conclusions are therefore given as short answers to the research questions presented in Section 1.4.

1) What are the effect and limitations of the top adherend's thickness?

Increasing the thickness will cause overheating in the top adherend, resulting in significant fiber squeeze-out for thicker adherends. This was shown not to be related to wave attenuation when the thickness increases, as the temperature readings indicate otherwise. The static analysis is also in disagreement with the obtained results, as the ratio of cyclic strain of the energy director to the cyclic strain of the adherends was shown not to change for the thickness of the top adhered. Therefore, the effectiveness of the energy director on concentrating the energy at the interface is not affected by the increase in thickness. The amplitude curves indicated that there is a relationship between the compliance of the top adherend -which increases with thickness- and hammering, as more hammering occurred for the thicker adherends. It is hypothesized that this hammering may contribute to overheating of the top adherend by introducing an impact load every time there is loss of contact between the sonotrode and the top adherend. The reason for increased hammering on more compliant adherends is yet not clear, but it is theorized that it is related to both their compressibility plus the behaviour at different stages of the process under the static and dynamic loads.

2) What are the effect and limitations of the bottom adherend's thickness?

The process response and weld evolution showed to be much less sensitive to the change of the bottom adherend's thickness, which was evidenced in the behaviour of the displacement and amplitude curves. Two main effects of increasing the thickness were identified. The first one, which also applies for the top adherend, is that the cooling rate decreases as the thickness increases. Considering the information found in literature and from the provider's datasheet, this may affect the crystallinity at the interface as the polymer chains have more time to arrange into crystals for slower cooling rates. The second effect was on the dissipated power. As more material is added by increasing the thickness, more bulk viscoelastic dissipation related to the viscous behaviour of the polymeric matrix is experienced. Although the COMSOL wave propagation results showed that there will also be an effect of the thickness on the

wave reflection at the bottom adherend/anvil interface, this effect was not clearly evidenced in the experimental results. In order to determine the specific thickness limitation of the bottom adherend, more research on the effect on the weld quality is required. Nonetheless, considering the findings from this study, the thickness limitation of the bottom adherend is expected to be much higher than for the top adherend.

3) How will the effect of the thickness change for different force and amplitude values?

The effects of changing the force and amplitude on the overall process response were consistent with what can be found in literature. However, increasing the force showed to have a major effect on the overheating of the top adherend for thick samples. This can be attributed to the significant reduction in hammering that was shown to contribute to this overheating. Even though there was still damage in some cases when welding thick adherends -hence portraying the poor repeatability of the experiments- the extent of the damage is much less severe and therefore indicates that the thickness limitation will he higher when the force is increased. On the other hand, reducing the amplitude was not as influential even though hammering is also reduced for a lower amplitude. The combination of force and amplitude values for which there is fewer hammering (1500 N, 60 μm) resulted on the less amount of overheating of the top adherend.

4) How applicable is the accepted industrial definition of near and far-field ultrasonic welding to thermoplastic composites?

Two issues were identified on the definition of near and far-field ultrasonic welding. The first one is the inconsistency between the definition -that far-field occurs when the distance from the sonotrode to the interface is close to the wavelength in the material- and the actual wavelength range for thermoplastics at the operational frequency. If this definition is considered, then it would not be applicable for the adherends used in this study as the wavelength at 20 kHz was found to be one order of magnitude larger than the distance for which far-field welding starts, according to literature. The second one is the lack of available information on the implications of near and far-field welding and the origin of this definition. Few "symptoms" of far-field welding were identified in literature; for example, damage in the surface of the top adherend and impossibility to weld. Again, this occurred for adherends with a thickness of a 3.55 mm, which is nowhere close to the wavelength of the composite. Because the presence of fibers in the thermoplastic will create new effects such as fiber-matrix and/or ply reflection, then the definition found in literature may not be a proper fit for thermoplastic composites. Based on the results from this study and those found in literature, it would be more valuable to develop indices or envelopes that quantify the thickness limitations, as they will depend on other conditions such as the matrix material and process parameters.

5) Will changing the fiber architecture (from fabric to UD) influence the effect and limitations of the adherends' thickness?

Changing to a UD reinforcement showed to have an effect on the deconsolidation and, most importantly, the extent of fiber squeeze-out, especially in the 0° direction. This squeeze-out was now identified even at early stages of the process and in the bottom adherend, presenting a new challenge when compared to the fabric adherends. However, the displacement curves (which are an effective tool to assess the weld evolution) are considerably less different between thin and thick adherends when compared to those obtained with fabric adherends. Less hammering was observed from the thicker adherends as indicated by the amplitude curves. This supports the relationship between hammering and compliance, as UD adherends will have a lower compliance resulting from a decreased resin content and the absence of fiber interlocking as in the case for the woven fabric. The fact that the thick UD adherends also had less overheating (as seen from the micrographs) also supports the hypothesis that hammering contributes to such overheating.

5.2. Final comments and recommendations

As was mentioned in the discussion, the aim of this research was to develop an understanding of the effect of the adherends' thickness on the process response and weld evolution. Although this was indeed achieved,

more research is required on the topic as these findings serve as a baseline for future studies that will ultimately increase the technology readiness level of ultrasonic welding of thermoplastic composites.

There are still many aspects around the effect of the thickness that still need to be studied to ultimately develop welding envelopes that are useful in industry. The following can be commented and recommended for such future studies:

- Since the cooling rate was shown to decrease for thicker top and bottom adherends, then it is possible that the consolidation parameters (namely time and pressure) will have to be adjusted for different thickness values.
- The effect of changing the thickness of the adherends was not evaluated by means of lap-shear strength or fractography analyses since this would require both adherends to have the same thickness. As an assessment of these two criteria is crucial for developing quality welds, further research on this is required.
- The thickness limitation of the top adherend during continuous ultrasonic welding (CUW) of thermoplastic composites is expected lo be lower than for static ultrasonic welding. This, since during CUW there is another cyclic strain added by the movement of the sonotrode which would contribute even more to the overheating of the top adherend.
- A proper quantification of how hammering contributes to overheating and why it occurs more as the thickness of the top adherend increases would help gain a better understanding. Perhaps adopting a methodology such as the one by Palardy et al. [30] or doing a modal analysis would add valuable information to the effect of the top adherend's thickness.
- As was mentioned in the conclusions and seen from the results, a microscopy analysis was not done for different thicknesses of the bottom adherend. This was mainly because of time constrains as the effect of changing the top adherend's thickness showed to be more relevant. Therefore, although this study provided some understanding of its effect, more research is still recommended.
- Increasing the force showed to be an effective strategy to mitigate the overheating in the top adherend. Therefore, if welding of thick adherends is required, an initial approach would be to increase the force as much it is allowed by the equipment limitations.
- Ultrasonic welding of unidirectional-reinforced composites is still at its early stages. Although some information on the differences between fabric and UD-reinforcement was acquired during this study, a more detailed comparison between these two types of reinforcement would be useful to further development of this technology. This, since in an industrial level UD composites are most likely to become more significant due to the easiness of automation and higher strength.
- Placing thermocouples in the adherends showed to have a relevant effect on the process, especially when welding thick top adherends. If such temperature readings are imminent, then avoiding drilling holes on the adherends could give more reliable readings. One way of achieving this could be by embedding the thermocouples during consolidation of the laminates.

A

Power and displacement curves

A.1. Effect of changing the top adherend's thickness

The figures shown in this section are a complement of the results shown in Section 3.1.1 where the top adherend's thickness was changed while keeping the process parameters (500 N, 80 μm) and bottom adherend's thickness (B = 1.83 mm) constant. The individual power and displacement curves for a 100% displacement (travel of the sonotrode equal to the thickness of the ED) for the different thicknesses of the top adherend are shown in Figure A.1.

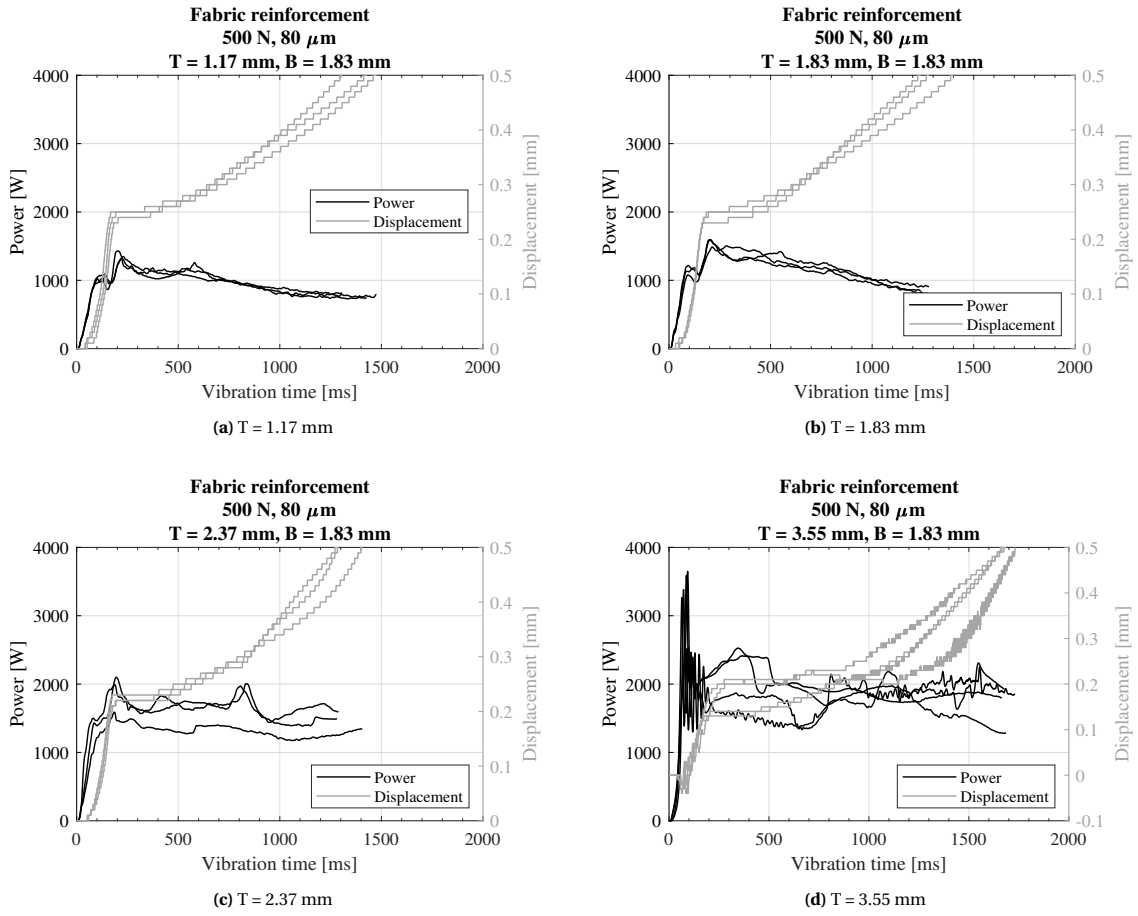

(a) T = 1.17 mm

(b) T = 1.83 mm

(c) T = 2.37 mm

(d) T = 3.55 mm

Figure A.1: Power and displacement curves for different thicknesses of the top adherend at 100 % displacement (travel of the sonotrode equal to the thickness of the ED).

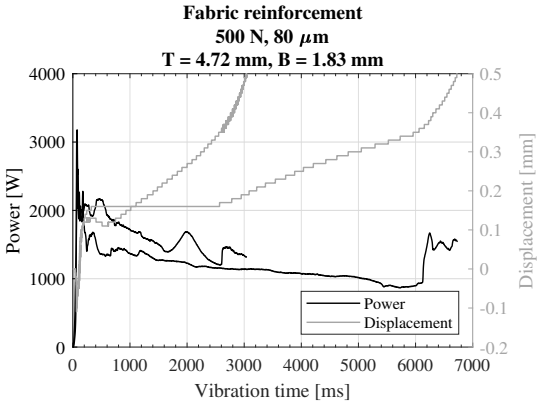

(e) T = 4.72 mm

Figure A.1: (continued) Power and displacement curves for different thicknesses of the top adherend at 100 % displacement (travel of the sonotrode equal to the thickness of the ED).

A.2. Effect of changing the bottom adherend's thickness

The figures shown in this section are a complement of the results shown in Section 3.2.1 where the bottom adherend's thickness was changed while keeping the process parameters (500 N, 80 μm) and top adherend's thickness (T = 1.83 mm) constant. The individual power and displacement curves for a 100% displacement (travel of the sonotrode equal to the thickness of the ED) for the different thicknesses of the bottom adherend are shown in Figure A.2.

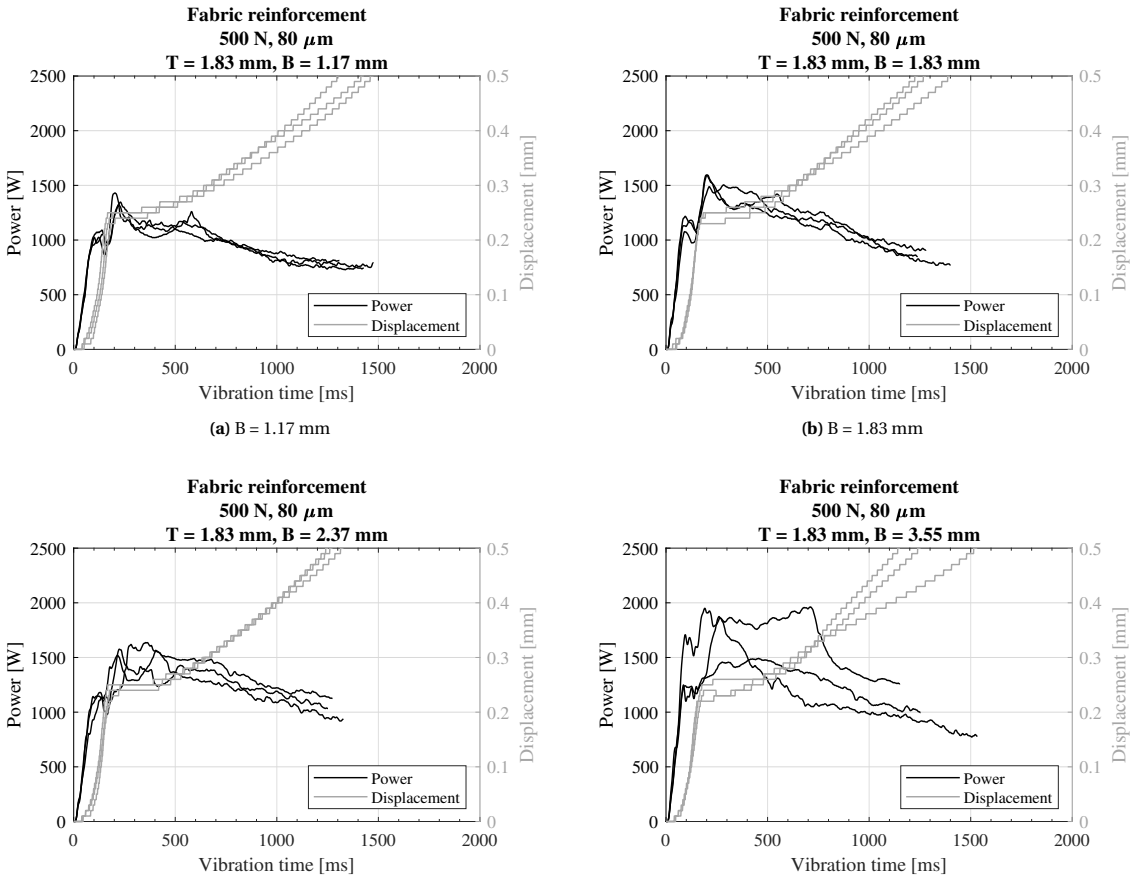

(a) B = 1.17 mm

(b) B = 1.83 mm

(c) B = 2.37 mm

(d) B = 3.55 mm

Figure A.2: Power and displacement curves for different thicknesses of the bottom adherend at 100 % displacement (travel of the sonotrode equal to the thickness of the ED).

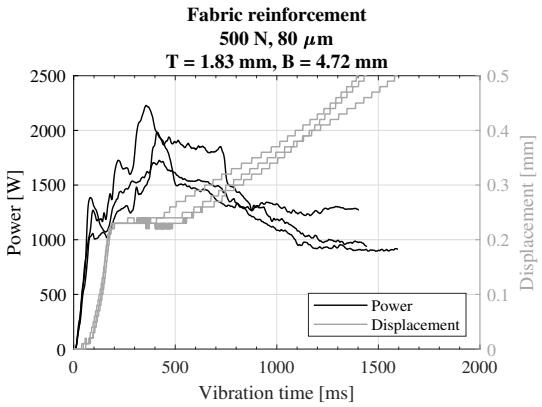

(e) B = 4.72 mm

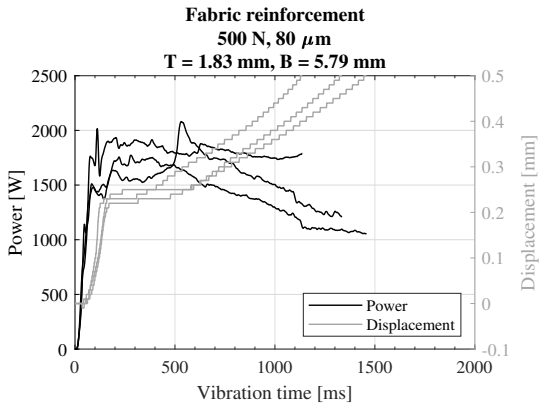

(f) B = 5.79 mm

Figure A.2: (continued) Power and displacement curves for different thicknesses of the bottom adherend at 100 % displacement (travel of the sonotrode equal to the thickness of the ED).

B

Amplitude curves

B.1. Effect of changing the top adherend's thickness

The figures shown in this section are a complement of the results shown in Section 3.1.2 where the top adherend's thickness was changed while keeping the process parameters (500 N, 80 μm) and bottom adherend's thickness (B = 1.83 mm) constant.

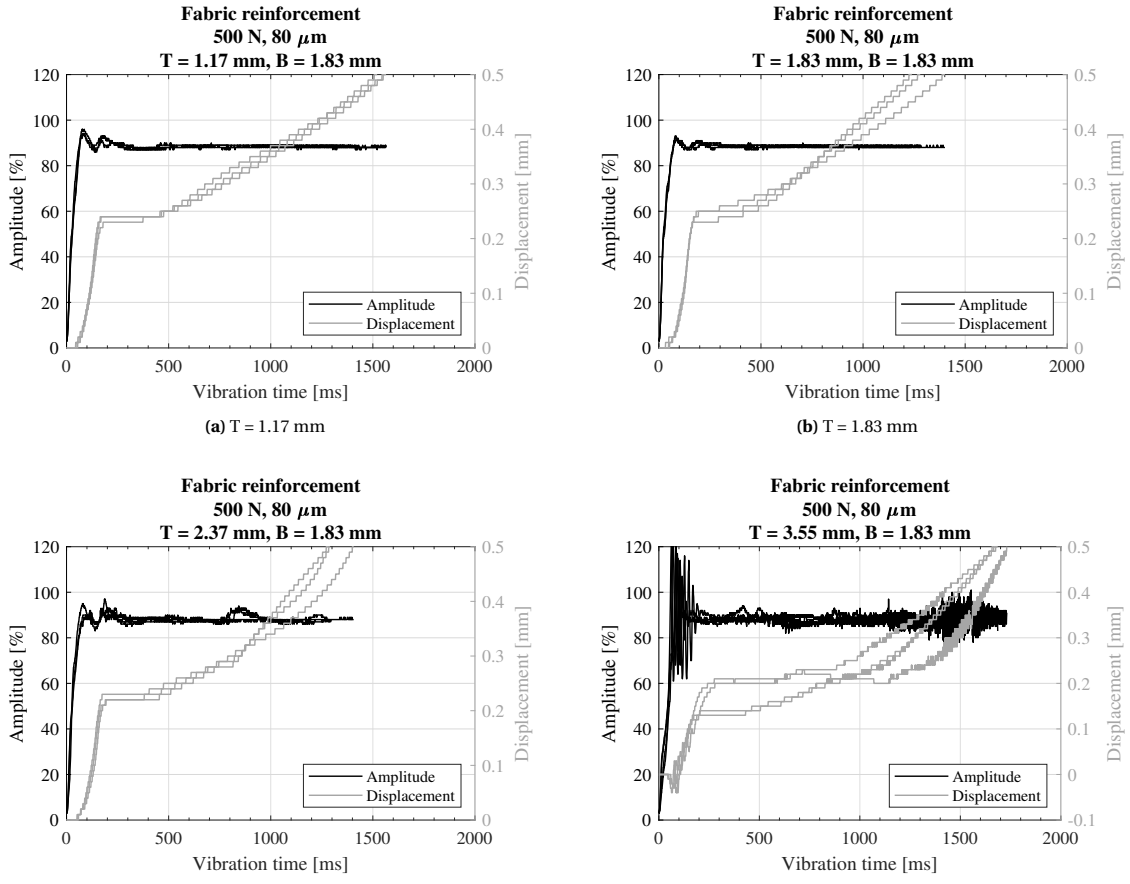

(a) T = 1.17 mm **(b)** T = 1.83 mm **(c)** T = 2.37 mm **(d)** T = 3.55 mm

Figure B.1: Amplitude and displacement curves for different thicknesses of the top adherend at 100 % displacement (travel of the sonotrode equal to the thickness of the ED). The nominal amplitude was 80 μm (88% of the maximum amplitude the equipment can provide).

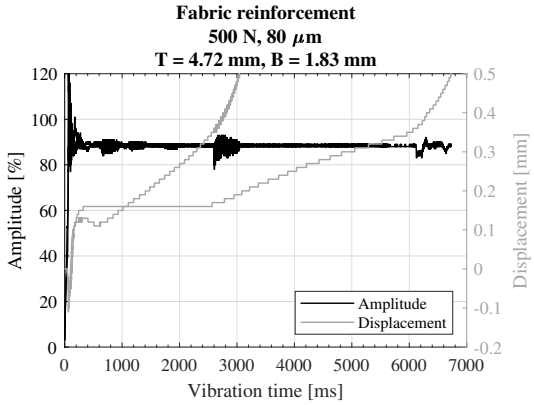

(e) T = 4.72 mm

Figure B.1: (continued) Amplitude and displacement curves for different thicknesses of the top adherend at 100 % displacement (travel of the sonotrode equal to the thickness of the ED). The nominal amplitude was 80 μm (88% of the maximum amplitude the equipment can provide).

B.2. Effect of changing the bottom adherend's thickness

The figures shown in this section are a complement of the results shown in Section 3.2.2 where the bottom adherend's thickness was changed while keeping the process parameters (500 N, 80 μm) and top adherend's thickness (T = 1.83 mm) constant.

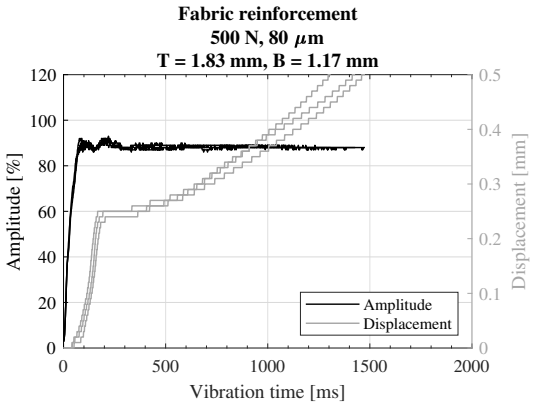

(a) B = 1.17 mm

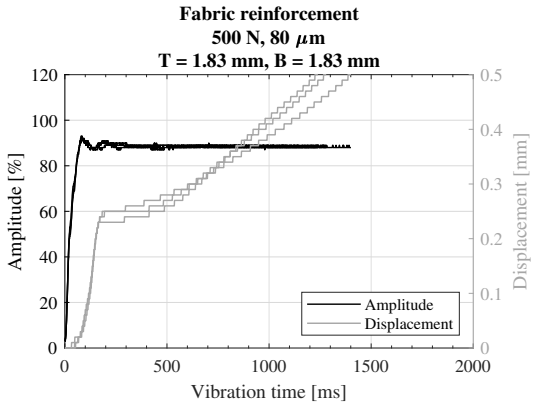

(b) B = 1.83 mm

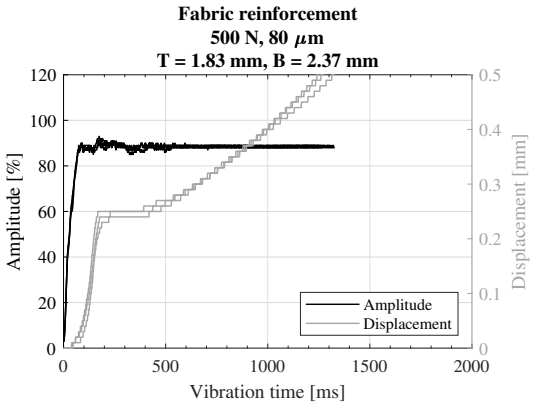

(c) B = 2.37 mm

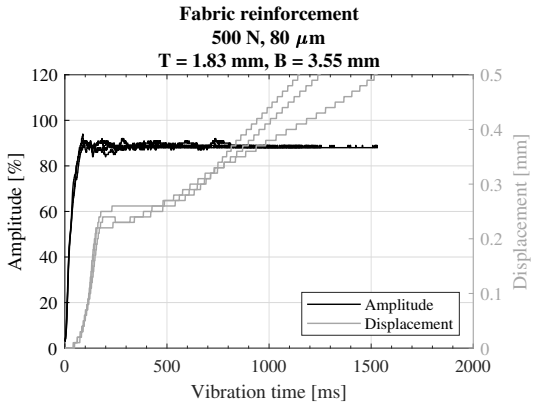

(d) B = 3.55 mm

Figure B.2: Amplitude and displacement curves for different thicknesses of the bottom adherend at 100 % displacement (travel of the sonotrode equal to the thickness of the ED). The nominal amplitude was 80 μm (88% of the maximum amplitude the equipment can provide).

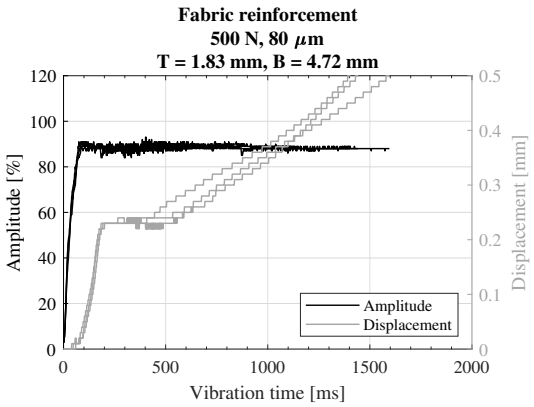

(e) B = 4.72 mm

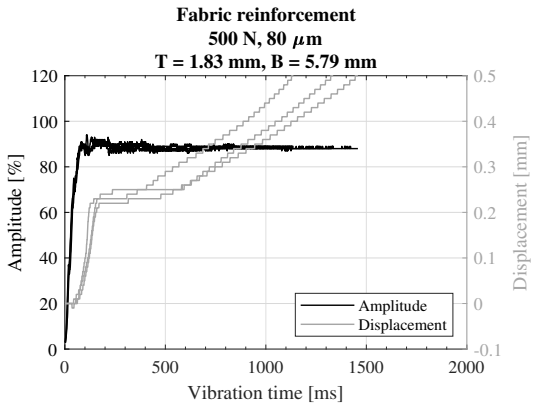

(f) B = 5.79 mm

Figure B.2: (continued) Amplitude and displacement curves for different thicknesses of the bottom adherend at 100 % displacement (travel of the sonotrode equal to the thickness of the ED). The nominal amplitude was 80 μm (88% of the maximum amplitude the equipment can provide).

B.3. Effect of changing the process parameters

The figures shown in this section are a complement of the results shown in Section 3.3.2 where the process parameters were changed and different thicknesses of the top adherend were evaluated (the bottom adherend's thickness B = 1.83 mm remained constant). The snapshots for the reference case of low force-high amplitude (500 N, 80 μm) were already shown in the previous section. The adherends used had a fabric reinforcement.

B.3.1. Low force-low amplitude (500 N, 60 um)

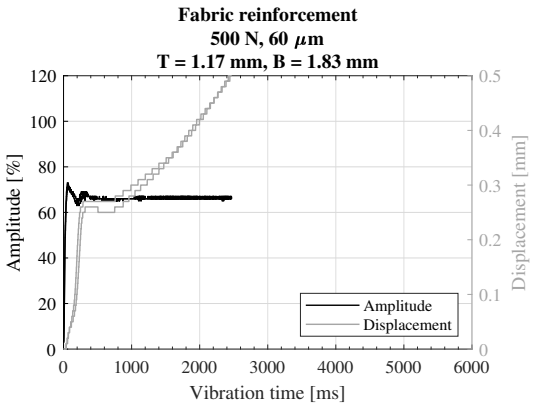

(a) T = 1.17 mm

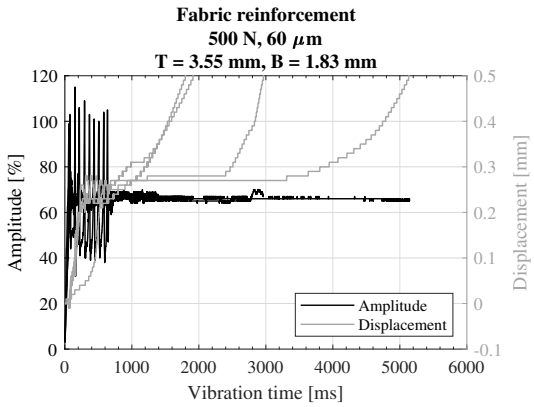

(b) T = 3.55 mm

Figure B.3: Amplitude and displacement curves for different thicknesses of the top adherend at 100 % displacement (travel of the sonotrode equal to the thickness of the ED) and force and amplitude values of 500 N and 60 μm (66% of the maximum amplitude the equipment can provide).

B.3.2. High force-High amplitude (1500 N, 80 um)

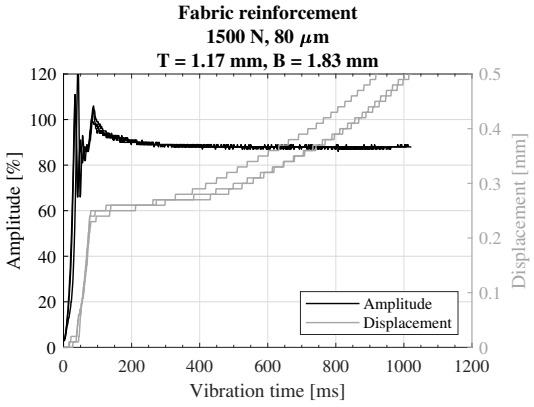

(a) T = 1.17 mm

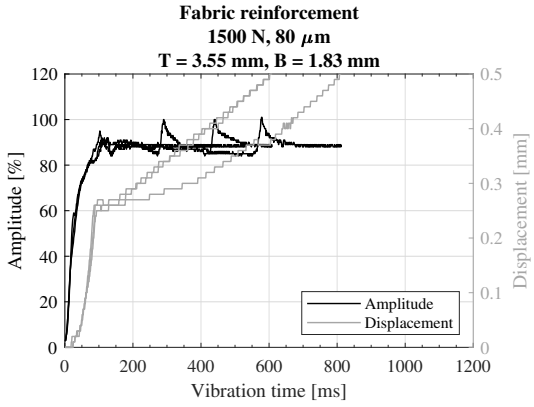

(b) T = 3.55 mm

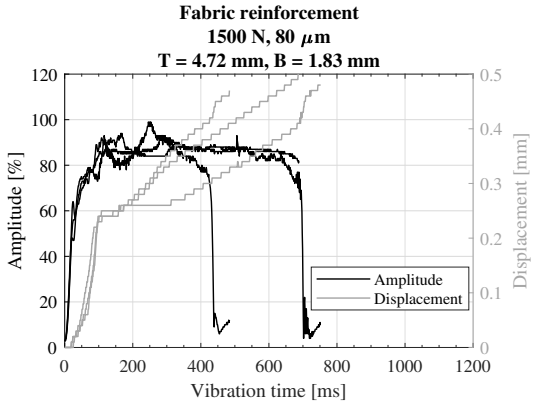

(c) T = 4.72 mm

Figure B.4: Amplitude and displacement curves for different thicknesses of the top adherend at 100 % displacement (travel of the sonotrode equal to the thickness of the ED) and force and amplitude values of 1500 N and 80 μm (88% of the maximum amplitude the equipment can provide).

B.3.3. High force-Low amplitude (1500 N, 60 um)

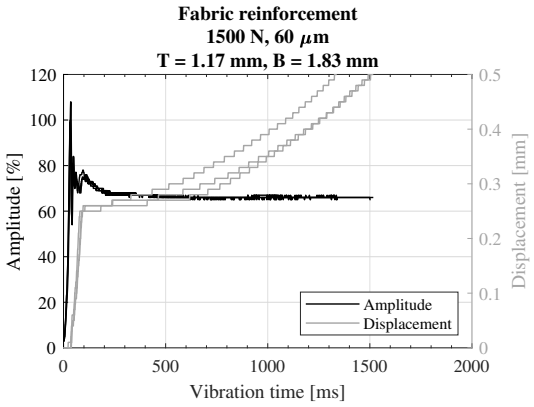

(a) T = 1.17 mm

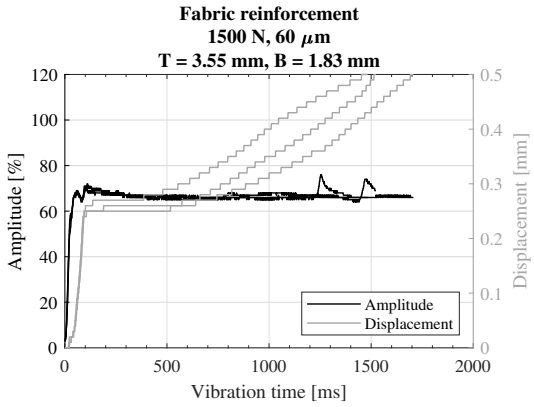

(b) T = 3.55 mm

Figure B.5: Amplitude and displacement curves for different thicknesses of the top adherend at 100 % displacement (travel of the sonotrode equal to the thickness of the ED) and force and amplitude values of 1500 N and 60 μm (66% of the maximum amplitude the equipment can provide).

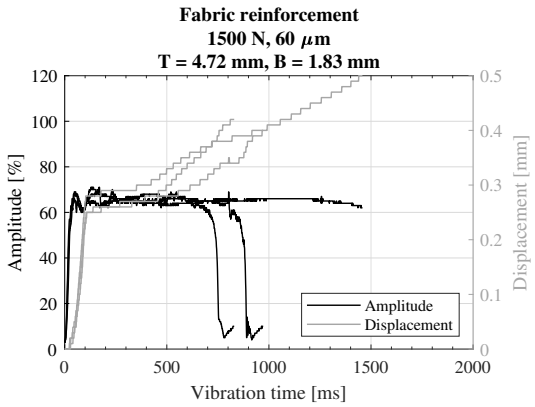

(c) T = 4.72 mm

Figure B.5: Amplitude and displacement curves for different thicknesses of the top adherend at 100 % displacement (travel of the sonotrode equal to the thickness of the ED) and force and amplitude values of 1500 N and 60 μm (66% of the maximum amplitude the equipment can provide).

B.4. Effect of changing to UD reinforcement

The reinforcement of the adherends was changed to UD. The figures shown in this section are a complement of the results shown in Section 3.4.2 where the process parameters were changed and different thicknesses of the top adherend were evaluated (the bottom adherend's thickness B = 1.85 mm remained constant).

B.4.1. Reference case: low force-high amplitude (500 N, 80 um)

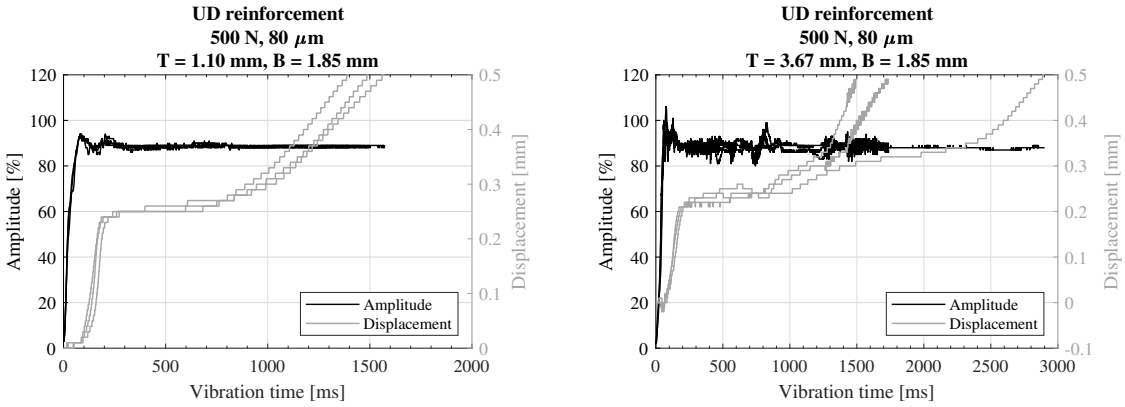

(a) T = 1.10 mm

(b) T = 3.67 mm

Figure B.6: Amplitude and displacement curves for different thicknesses of the top adherend at 100 % displacement (travel of the sonotrode equal to the thickness of the ED) and force and amplitude values of 500 N and 80 μm (88% of the maximum amplitude the equipment can provide). Adherends with UD reinforcement.

B.4.2. Low force-low amplitude (500 N, 60 um)

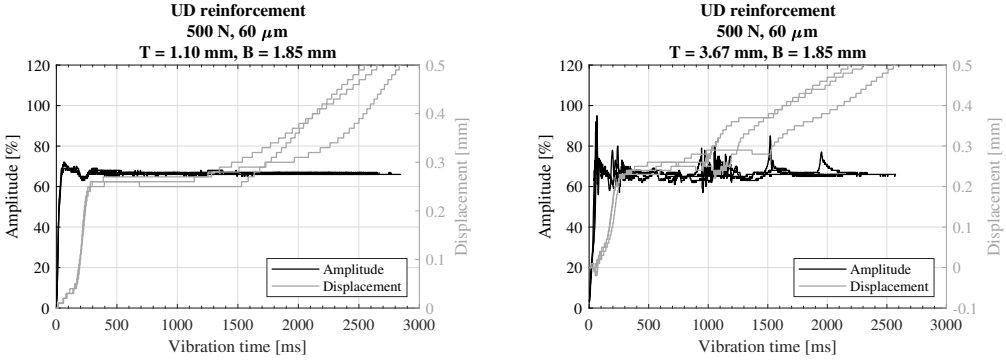

(a) T = 1.17 mm **(b)** T = 3.55 mm

Figure B.7: Amplitude and displacement curves for different thicknesses of the top adherend at 100 % displacement (travel of the sonotrode equal to the thickness of the ED) and force and amplitude values of 500 N and 60 μm (66% of the maximum amplitude the equipment can provide). Adherends with UD reinforcement.

B.4.3. High force-high amplitude (1500 N, 80 um)

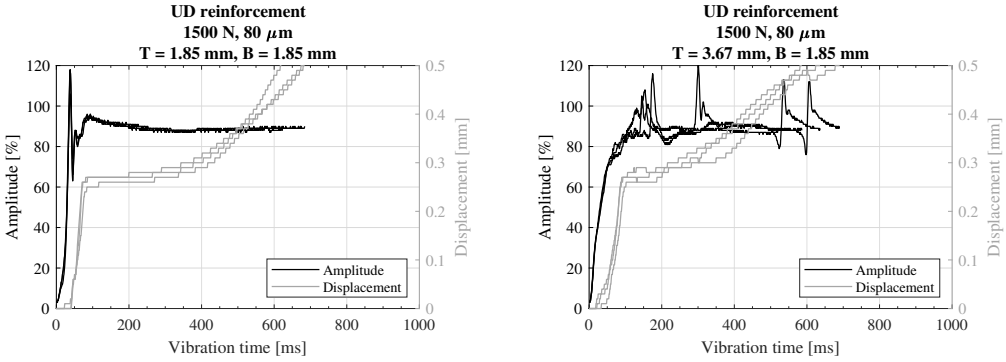

(a) T = 1.85 mm **(b)** T = 3.67 mm

Figure B.8: Amplitude and displacement curves for different thicknesses of the top adherend at 100 % displacement (travel of the sonotrode equal to the thickness of the ED) and force and amplitude values of 1500 N and 80 μm (88% of the maximum amplitude the equipment can provide). Adherends with UD reinforcement.

B.4.4. High force-low amplitude (1500 N, 60 um)

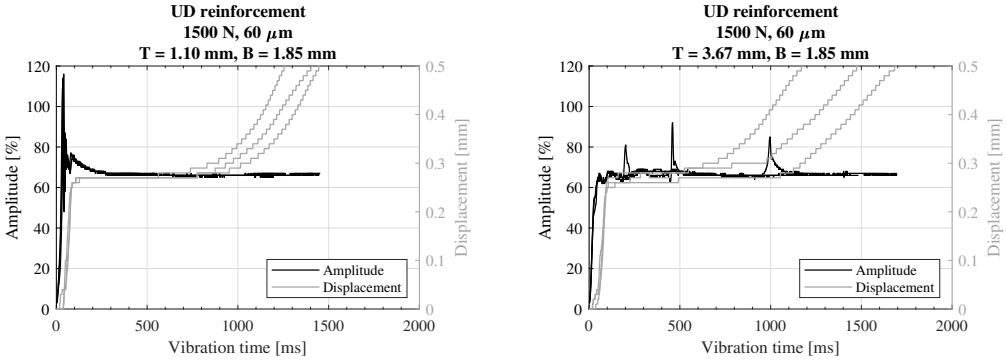

(a) T = 1.10 mm **(b)** T = 3.67 mm

Figure B.9: Amplitude and displacement curves for different thicknesses of the top adherend at 100 % displacement (travel of the sonotrode equal to the thickness of the ED) and force and amplitude values of 1500 N and 860 μm (66% of the maximum amplitude the equipment can provide). Adherends with UD reinforcement.

C

High-speed camera results

This appendix shows the detailed evolution of the weld as captured high the high-speed camera (HSC). Some images have already been presented in Chapter 3. A figure is shown first with the displacement curves for each thickness where the points indicate the different times at which the snapshots are shown. After showing this figure, the snapshots for each thickness are presented and the time is indicated.

C.1. Effect of changing the top adherend's thickness

The figures shown in this section are a complement of the results shown in Section 3.1.3 where the top adherend's thickness was changed while keeping the process parameters (500 N, 80 μm) and bottom adherend's thickness (B = 1.83 mm) constant. The adherends used had a fabric reinforcement. The white spots shown in the snapshots of Figure C.2a were part of an attempt to track the displacement in the adherends.

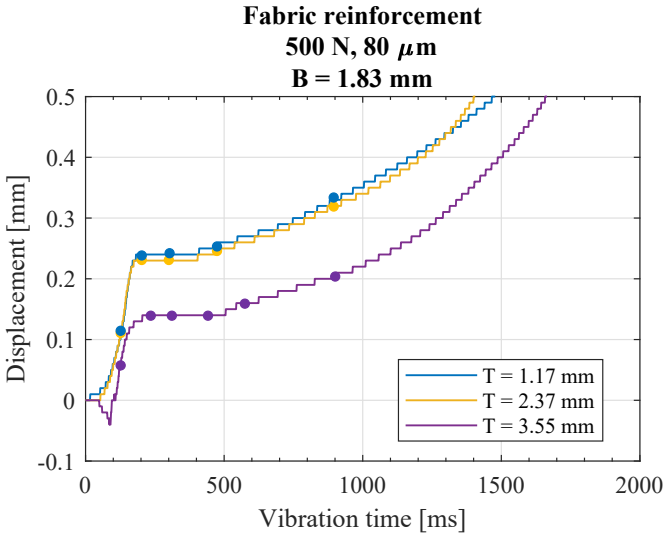

Figure C.1: Displacement curves of the HSC snapshots shown in Figure C.2.

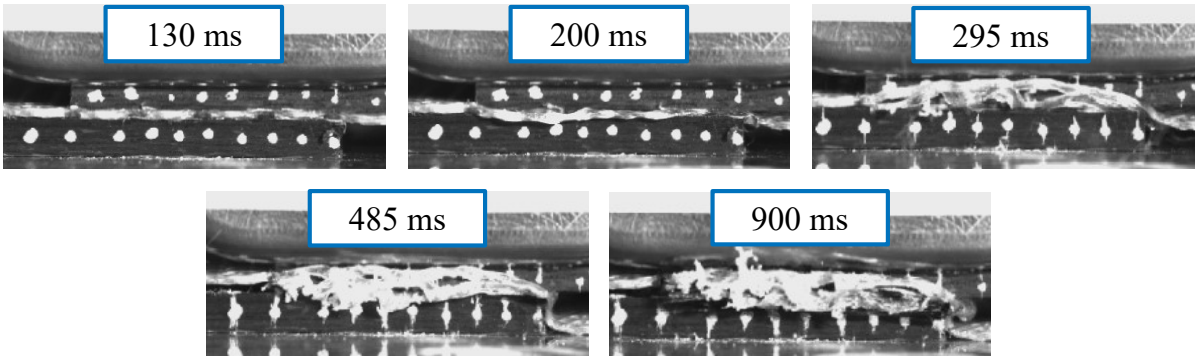

(a) T = 1.17 mm

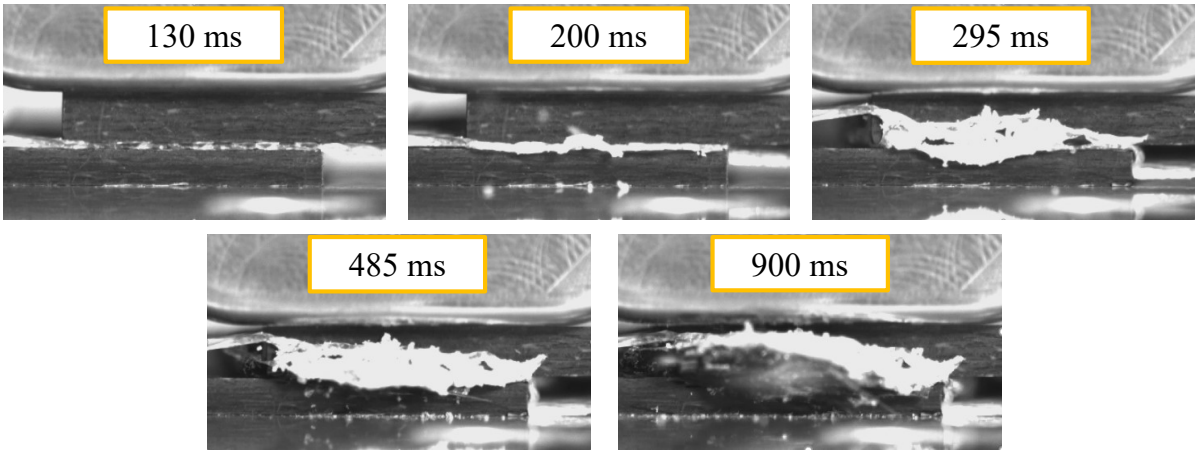

(b) T = 2.37 mm

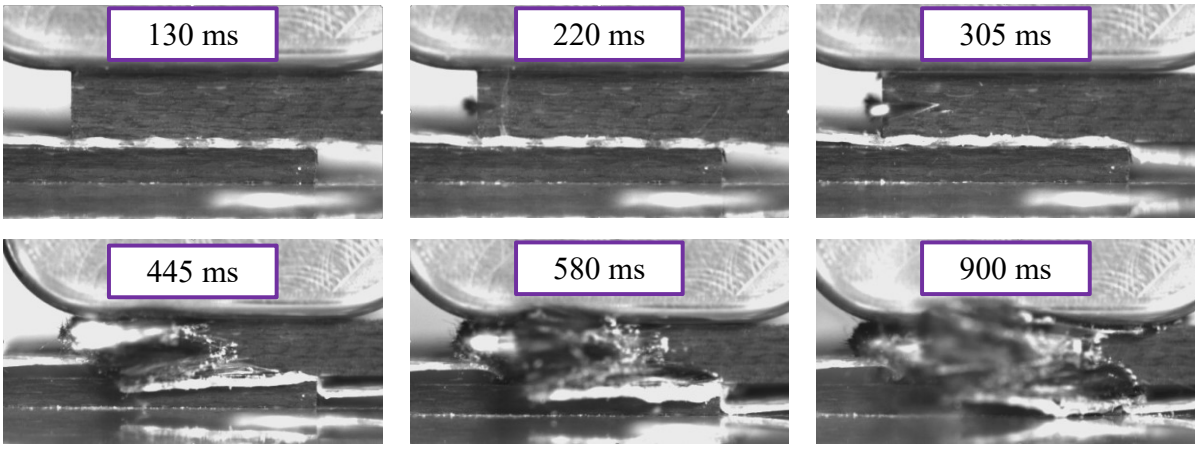

(c) T = 3.55 mm

Figure C.2: HSC snapshots at different points of the displacement curves shown in Figure C.1

C.2. Effect of changing the bottom adherend's thickness

The figures shown in this section are a complement of the results shown in Section 3.2.3 where the bottom adherend's thickness was changed while keeping the process parameters (500 N, 80 μm) and top adherend's thickness (T = 1.83 mm) constant. The adherends used had a fabric reinforcement.

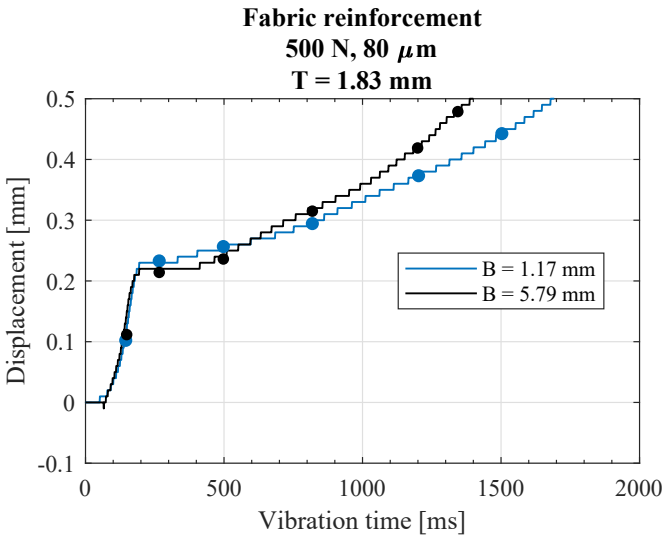

Figure C.3: Displacement curves of the HSC snapshots shown in Figure C.4.

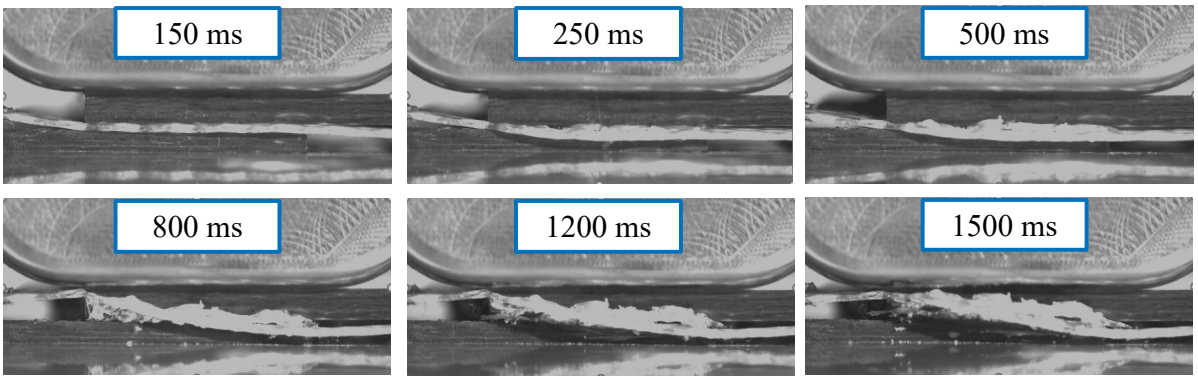

(a) B = 1.17 mm

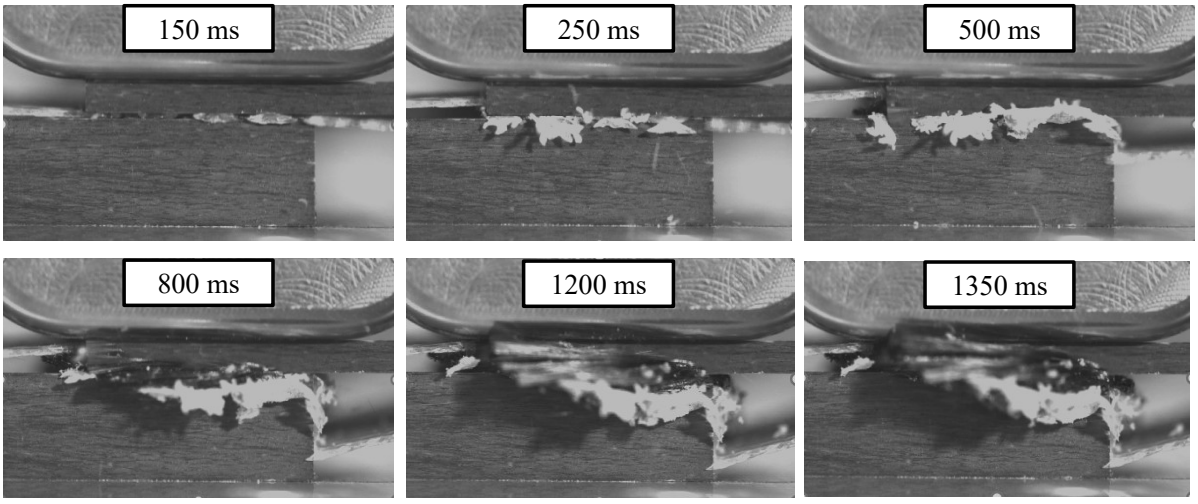

(b) B = 5.79 mm

Figure C.4: HSC snapshots at different points of the displacement curves shown in Figure C.3.

C.3. Effect of changing the process parameters

The figures shown in this section are a complement of the results shown in Section 3.3.3 where the process parameters were changed and different thicknesses of the top adherend were evaluated (the bottom adherend's thickness B = 1.83 mm remained constant). The snapshots for the reference case of low force-high amplitude (500 N, 80 μm) were already shown in Section C.1. The adherends used had a fabric reinforcement.

C.3.1. Low force-low amplitude (500 N, 60 um)

The white spots shown in the snapshots of Figure C.6 were part of an attempt to track the displacement in the adherends. The thicker adherend (3.55 mm) also showed squeeze-out at early stages of the process (during the displacement plateau).

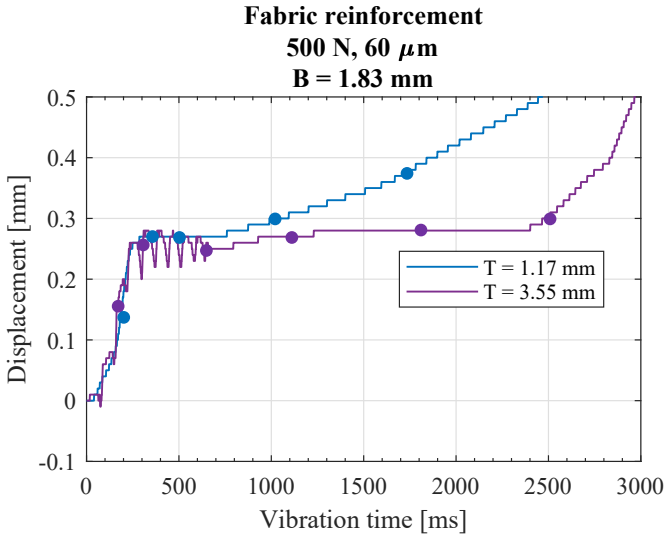

Figure C.5: Displacement curves of the HSC snapshots shown in Figure C.6. 500 N, 60 μm.

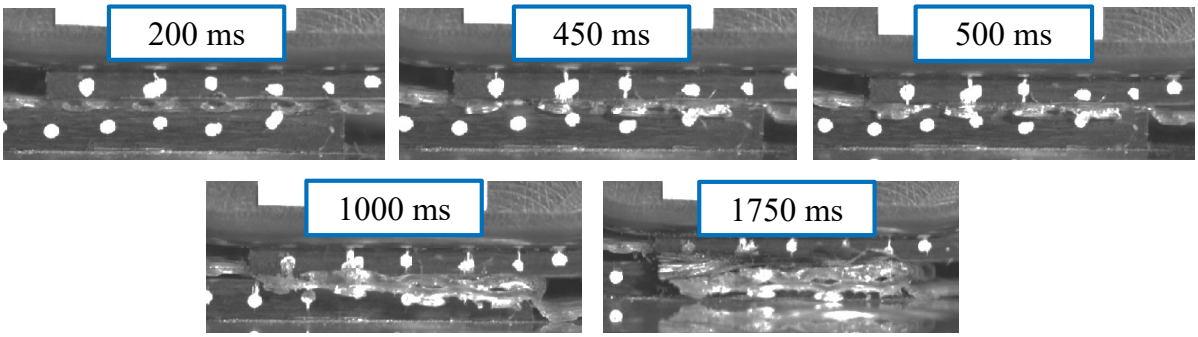

(a) T = 1.17 mm

Figure C.6: HSC snapshots at different points of the displacement curves shown in Figure C.5. 500 N, 60 μm.

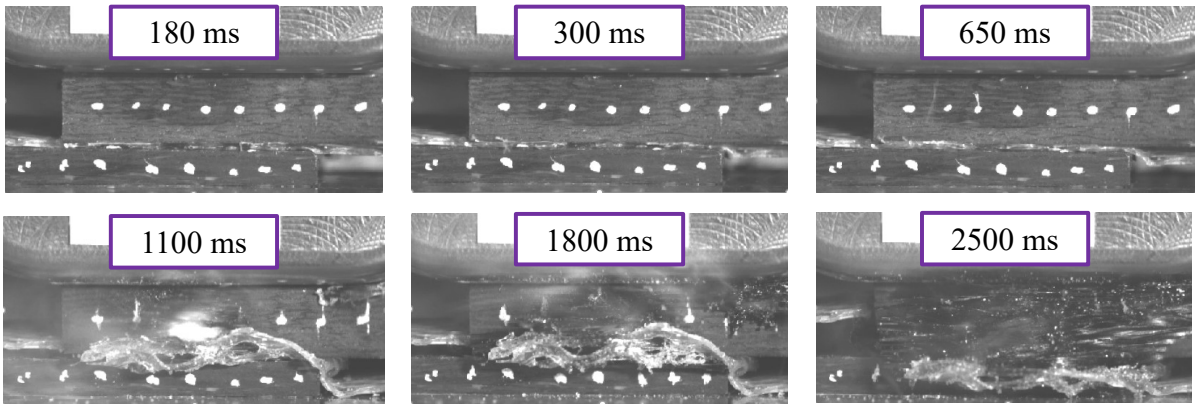

(b) T = 3.55 mm

Figure C.6: (continued) HSC snapshots at different points of the displacement curves shown in Figure C.5. 500 N, 60 μm.

C.3.2. High force-high amplitude (1500 N, 80 um)

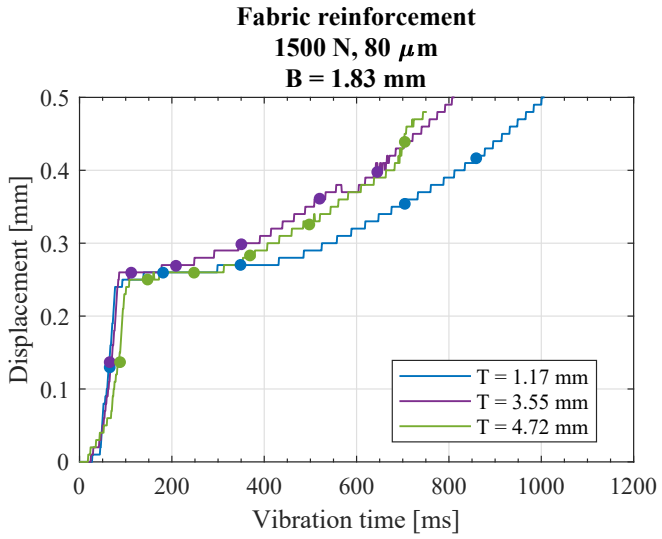

Figure C.7: Displacement curves of the HSC snapshots shown in Figure C.8. 1500 N, 80 μm.

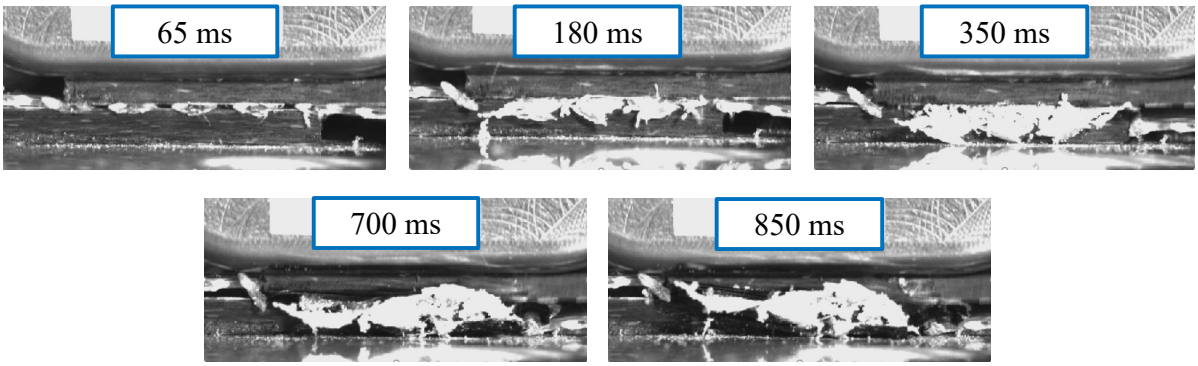

(a) T = 1.17 mm

Figure C.8: HSC snapshots at different points of the displacement curves shown in Figure C.7. 1500 N, 80 μm.

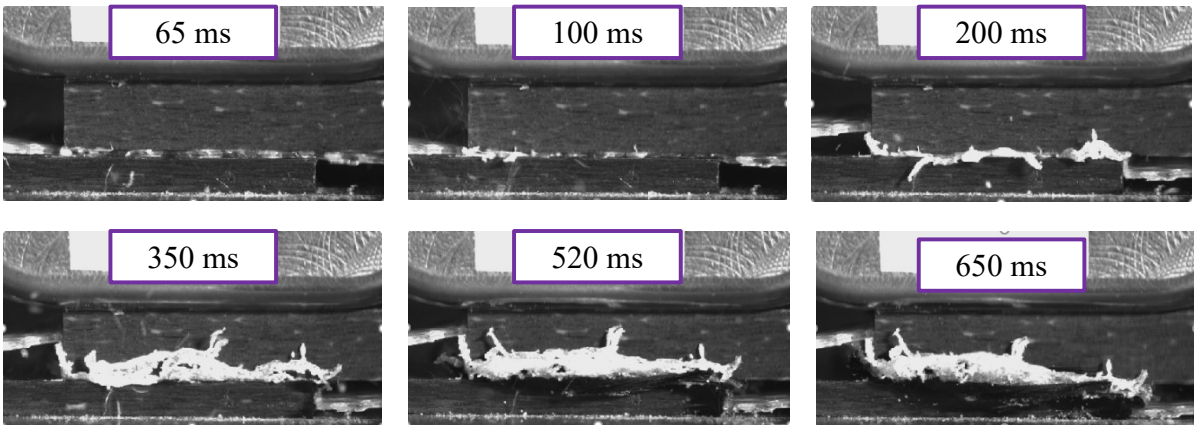

(b) T = 3.55 mm

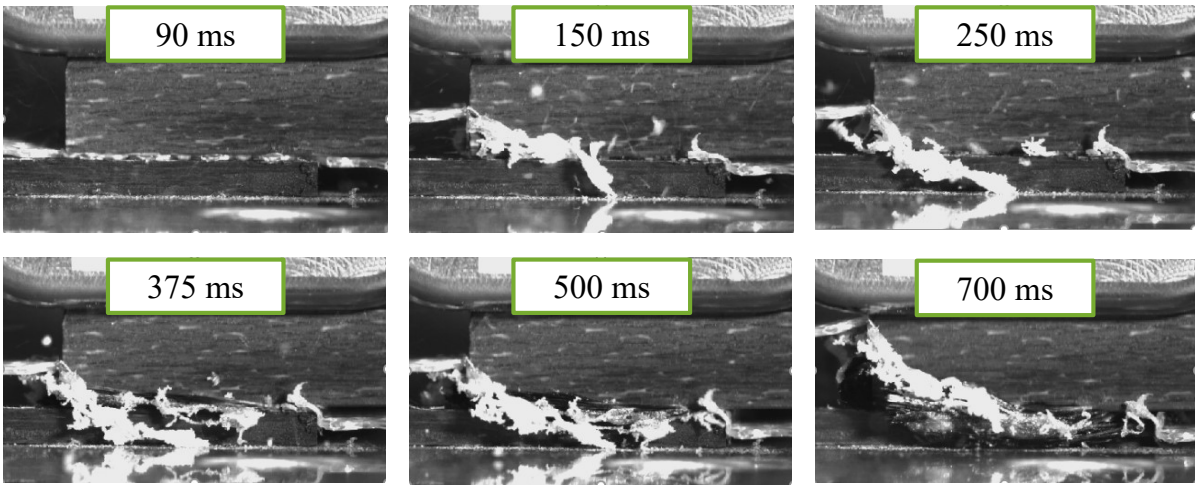

(c) T = 4.72 mm

Figure C.8: (continued) HSC snapshots at different points of the displacement curves shown in Figure C.7. 1500 N, 80 μm.

C.3.3. High force-low amplitude (1500 N, 60 um)

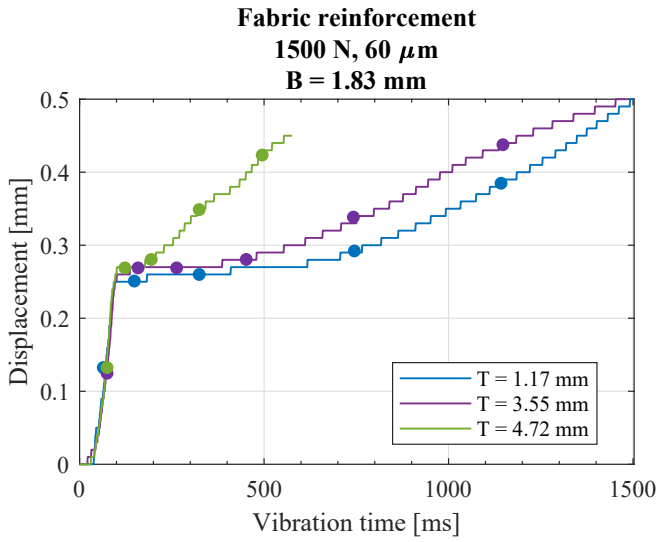

Figure C.9: Displacement curves of the HSC snapshots shown in Figure C.10. 1500 N, 60 μm.

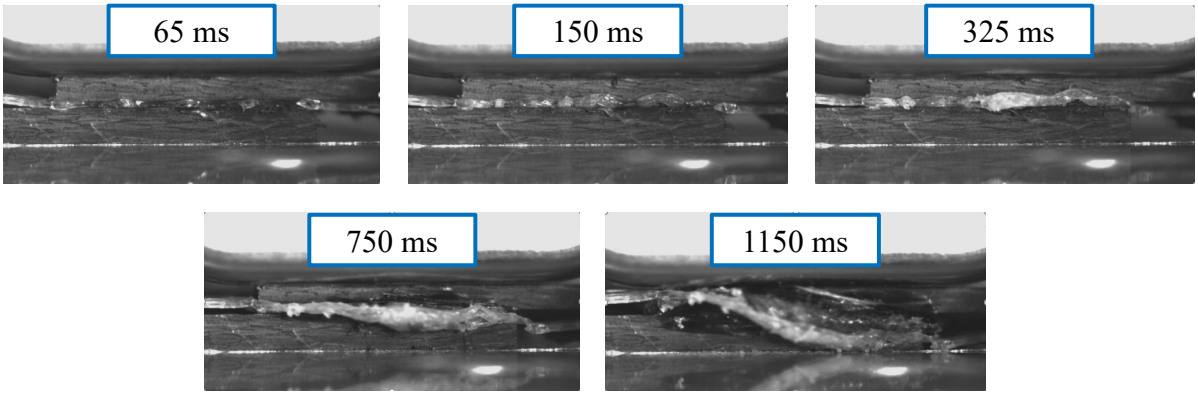

(a) T = 1.17 mm

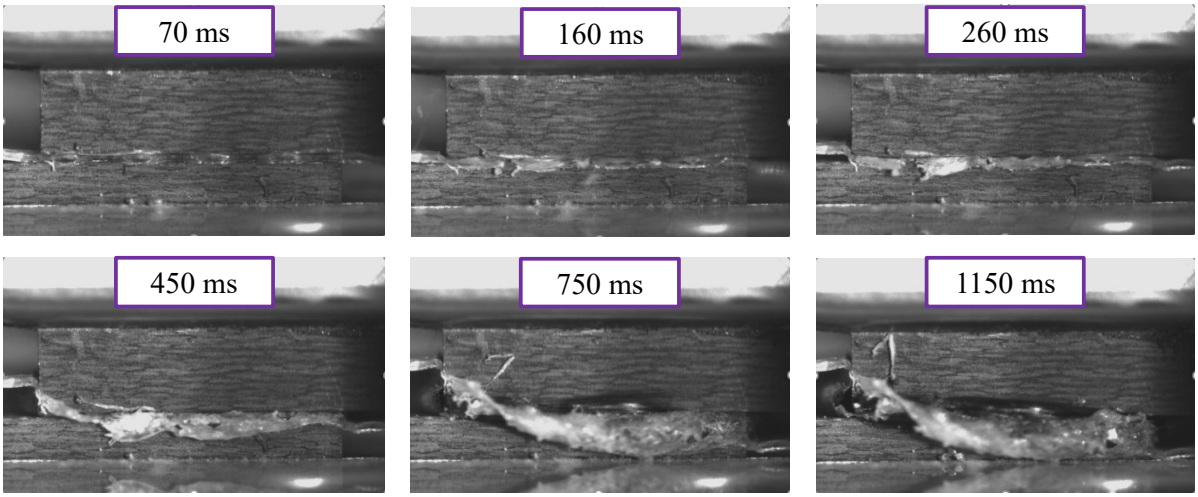

(b) T = 3.55 mm

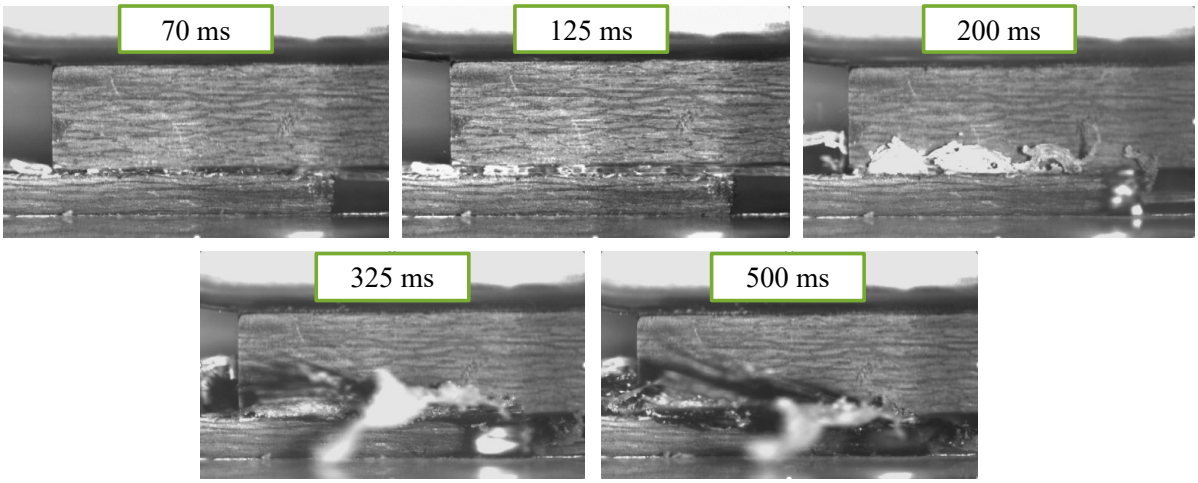

(c) T = 4.72 mm

Figure C.10: HSC snapshots at different points of the displacement curves shown in Figure C.9. 1500 N, 60 μm.

C.4. Effect of changing to UD reinforcement

The reinforcement of the adherends was changed to UD. The figures shown in this section are a complement of the results shown in Section 3.4.3 where the process parameters were changed and different thicknesses of the top adherend were evaluated (the bottom adherend's thickness B = 1.85 mm remained constant).

C.4.1. Reference case: low force-high amplitude (500 N, 80 um)

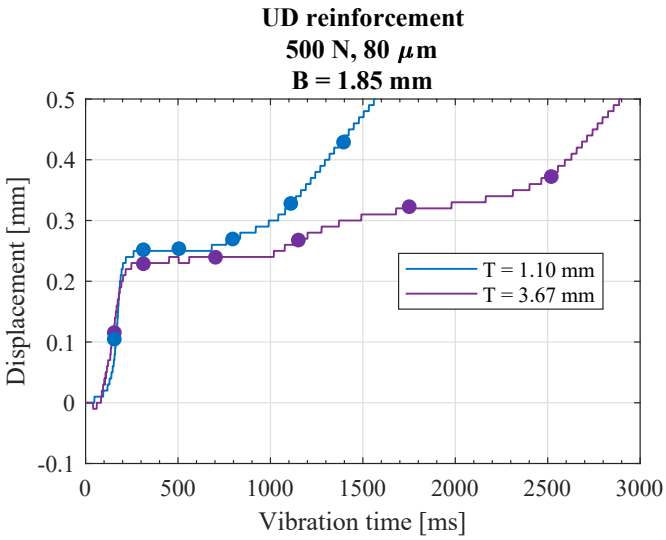

Figure C.11: Displacement curves of the HSC snapshots shown in Figure C.12. 500 N, 80 μm. UD reinforcement.

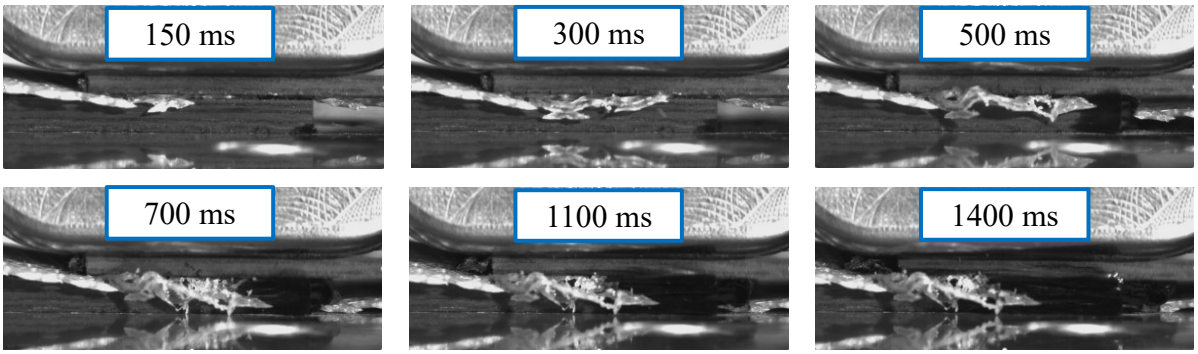

(a) T = 1.10 mm

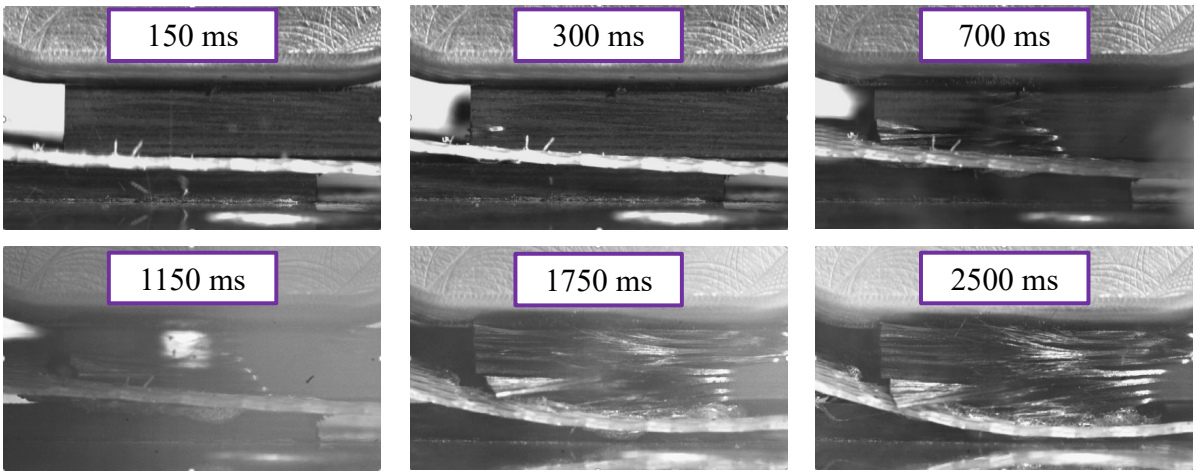

(b) T = 3.67 mm

Figure C.12: HSC snapshots at different points of the displacement curves shown in Figure C.11. 500 N, 80 μm. UD reinforcement.

C.4.2. Low force-low amplitude (500 N, 60 um)

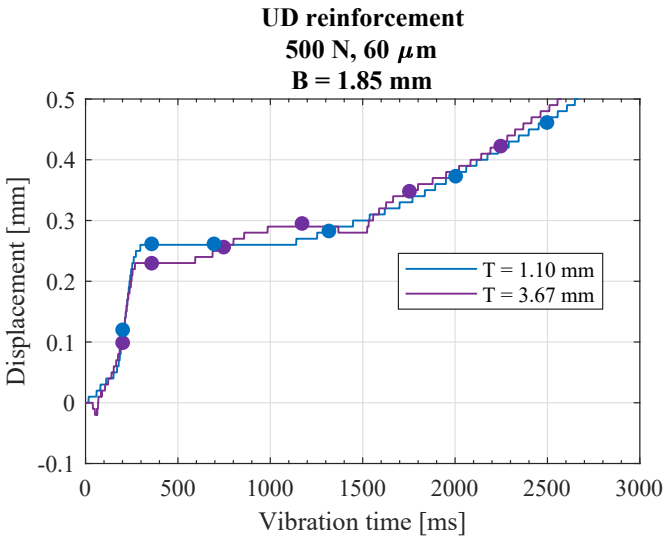

Figure C.13: Displacement curves of the HSC snapshots shown in Figure C.14. 500 N, 60 μm. UD reinforcement.

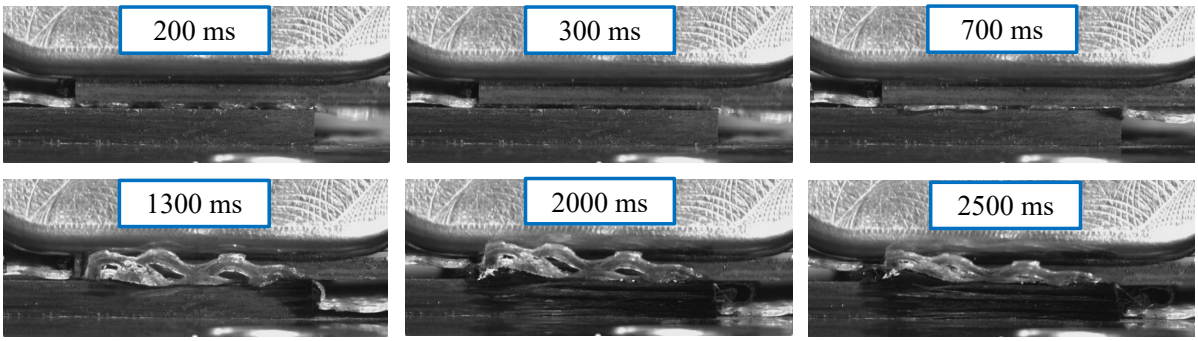

(a) T = 1.10 mm

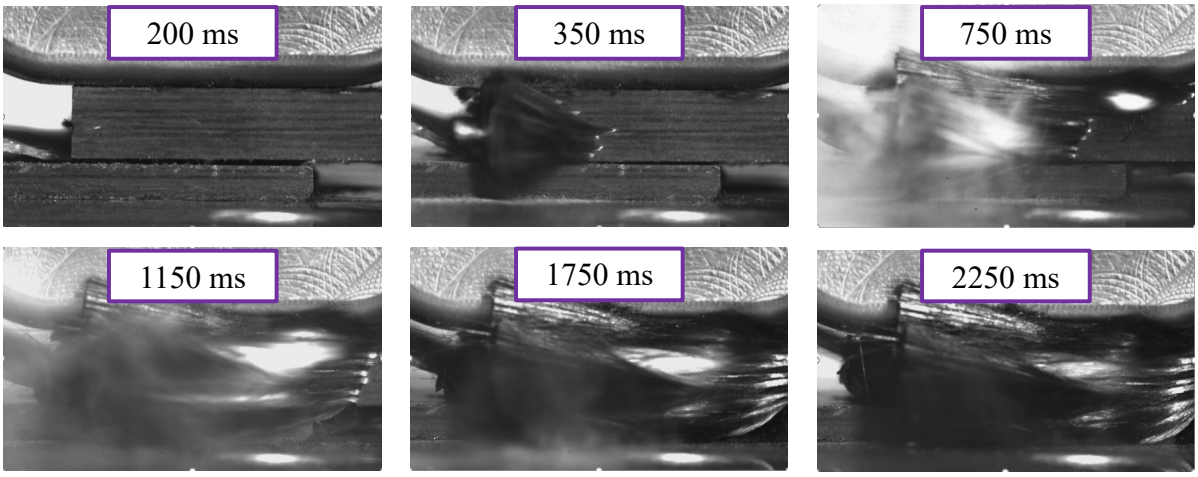

(b) T = 3.67 mm

Figure C.14: HSC snapshots at different points of the displacement curves shown in Figure C.13. 500 N, 60 μm. UD reinforcement.

C.4.3. High force-high amplitude (1500 N, 80 um)

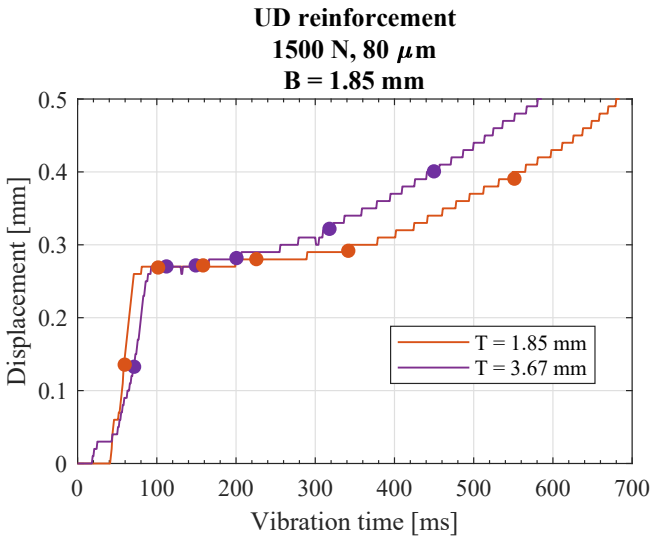

Figure C.15: Displacement curves of the HSC snapshots shown in Figure C.16. 1500 N, 80 μm. UD reinforcement.

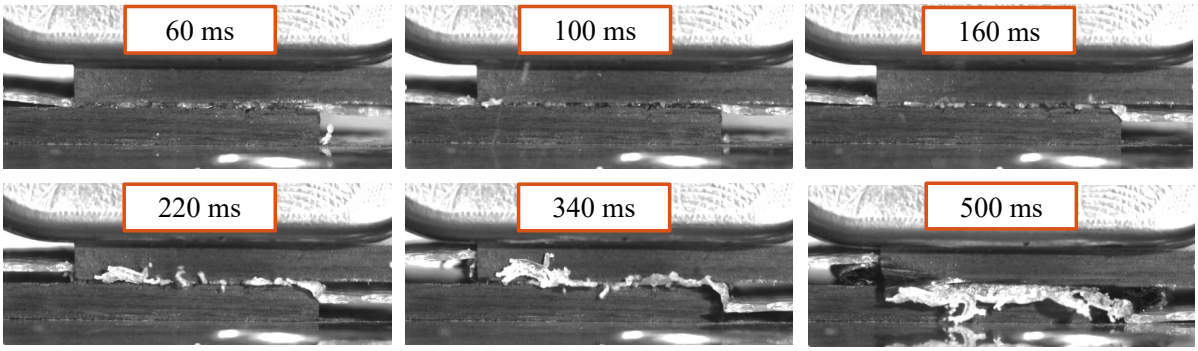

(a) T = 1.85 mm

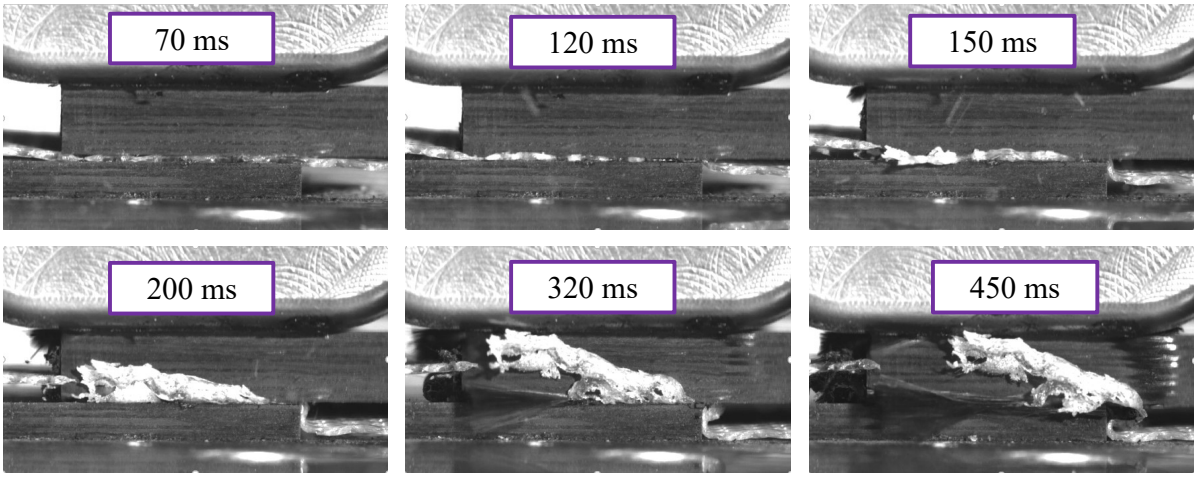

(b) T = 3.67 mm

Figure C.16: HSC snapshots at different points of the displacement curves shown in Figure C.15. 1500 N, 80 μm. UD reinforcement.

C.4.4. High force-low amplitude (1500 N, 60 um)

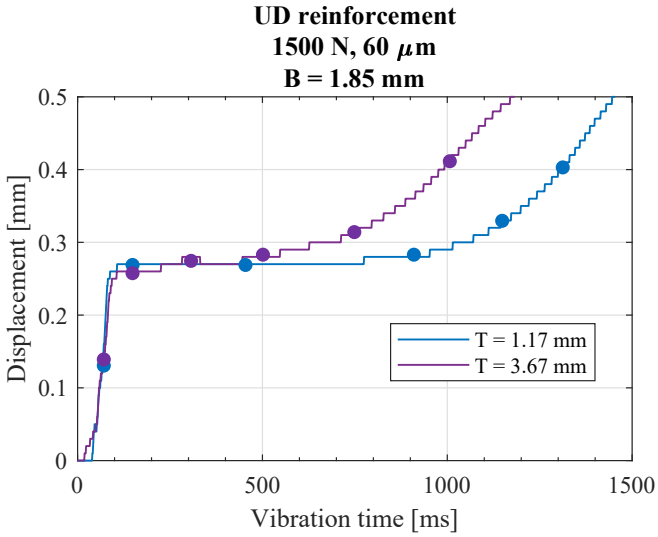

Figure C.17: Displacement curves of the HSC snapshots shown in Figure C.18. 1500 N, 60 μm. UD reinforcement.

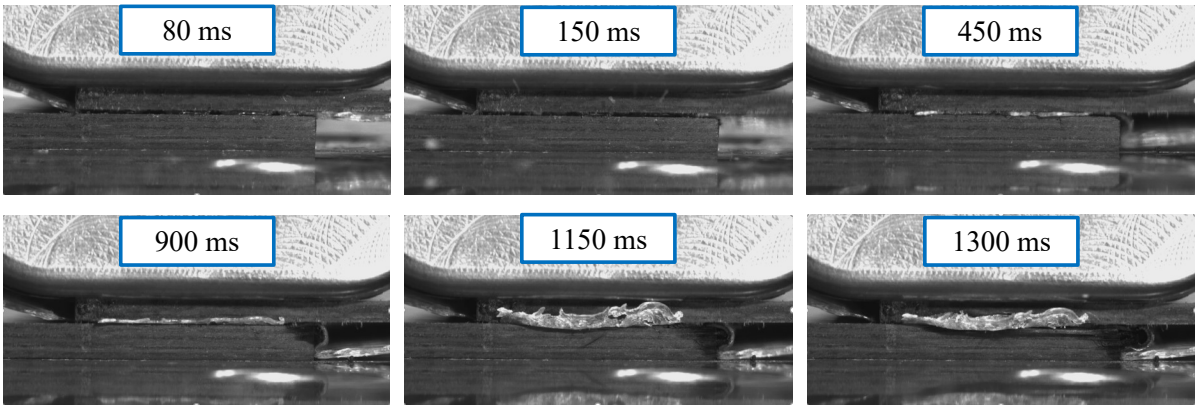

(a) T = 1.10 mm

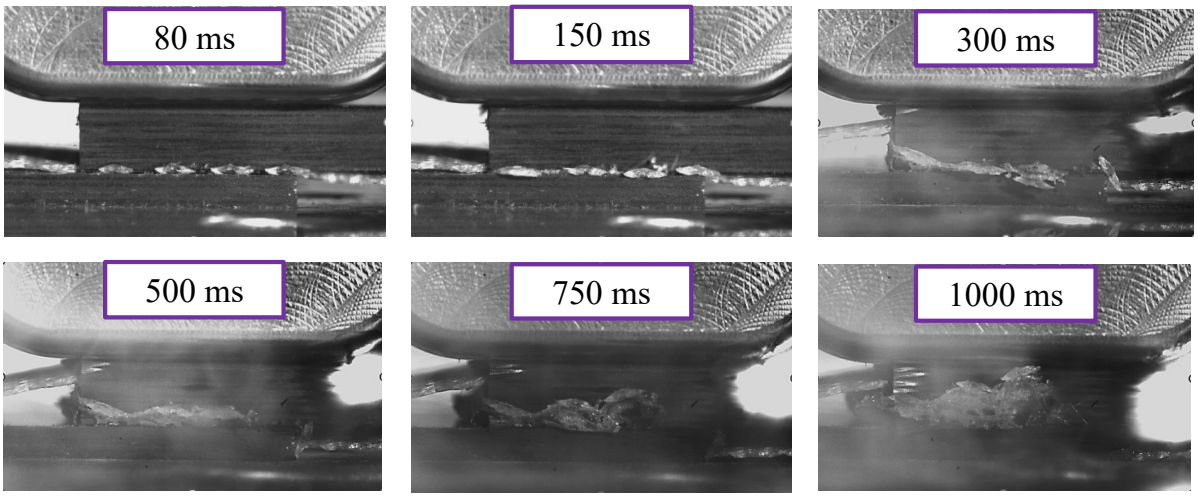

(b) T = 3.67 mm

Figure C.18: HSC snapshots at different points of the displacement curves shown in Figure C.17. 1500 N, 60 μm. UD reinforcement.

D

Microscopy

This appendix shows the detailed evolution of the weld with micrographs at different points of the displacement curves: beginning of the plateau, during the plateau, after the plateau, and at the end of the displacement curve. The white arrows indicate the weldline. Some images have already been presented in Section 3. Note that only the curve for the micrograph at the 100% displacement is shown as each cross-section corresponds to a single displacement curve. Particularly in the thick samples, the position in the displacement curve will not occur at the same time for different samples, therefore each micrograph is labeled with displacement rather than time as in the results from Appendix C. Because only the effect of the welding stage is to be visualized, the samples were not consolidated after vibration.

D.1. Effect of changing the top adherend's thickness

The figures shown in this section are a complement of the results shown in Section 3.1.4 where the top adherend's thickness was changed while keeping the process parameters (500 N, 80 μm) and bottom adherend's thickness (B = 1.83 mm) constant. The adherends used had a fabric reinforcement.

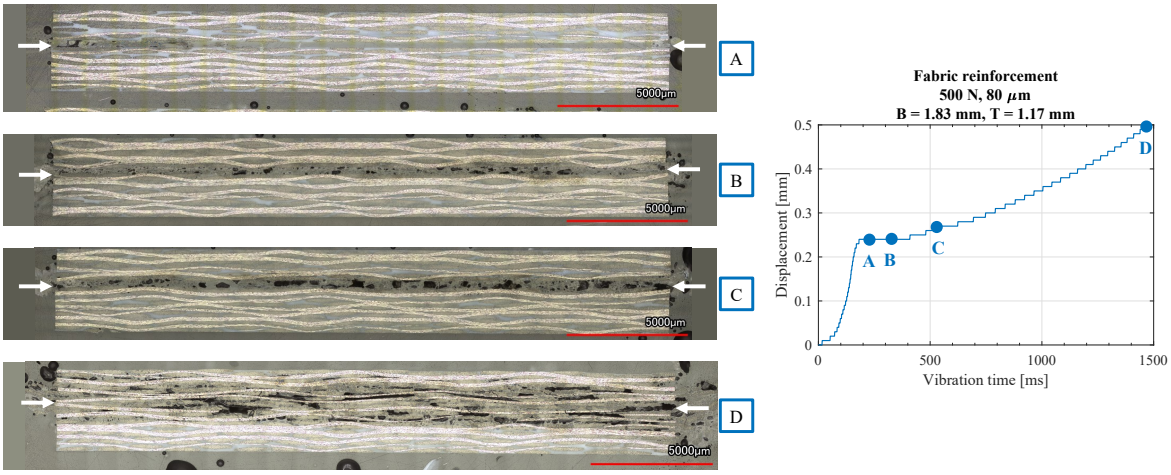

Figure D.1: Cross sectional micrographs for T = 1.12 mm at different points of the displacement curve. 500 N, 80 μm and no consolidation.

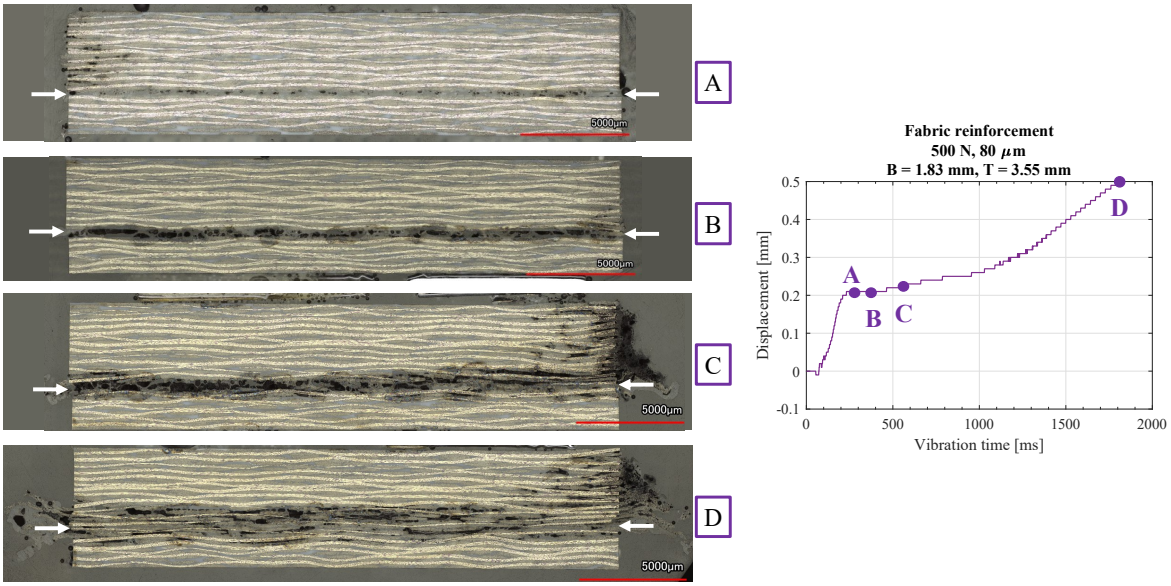

Figure D.2: Cross sectional micrographs for T = 3.55 mm at different points of the displacement curve. 500 N, 80 μm and no consolidation.

D.2. Effect of changing the process parameters

The figures shown in this section are a complement of the results shown in Section 3.3.4 where the process parameters were changed and different thicknesses of the top adherend were evaluated (the bottom adherend's thickness B = 1.83 mm remained constant). The snapshots for the reference case of low force-high amplitude (500 N, 80 μm) were already shown in the previous section. The adherends used had a fabric reinforcement.

D.2.1. Low force-low amplitude (500 N, 60 um)

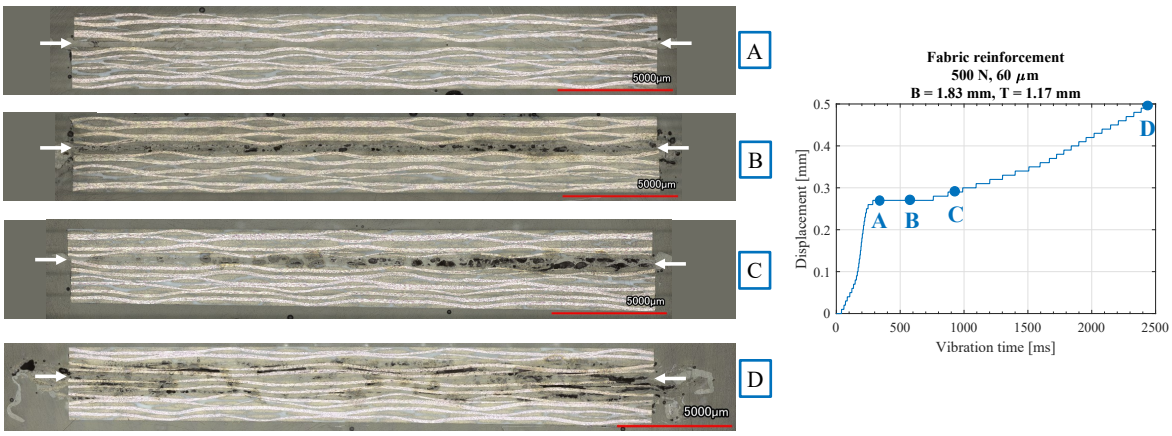

Figure D.3: Cross sectional micrographs for T = 1.17 mm at different points of the displacement curve. 500 N, 60 μm and no consolidation.

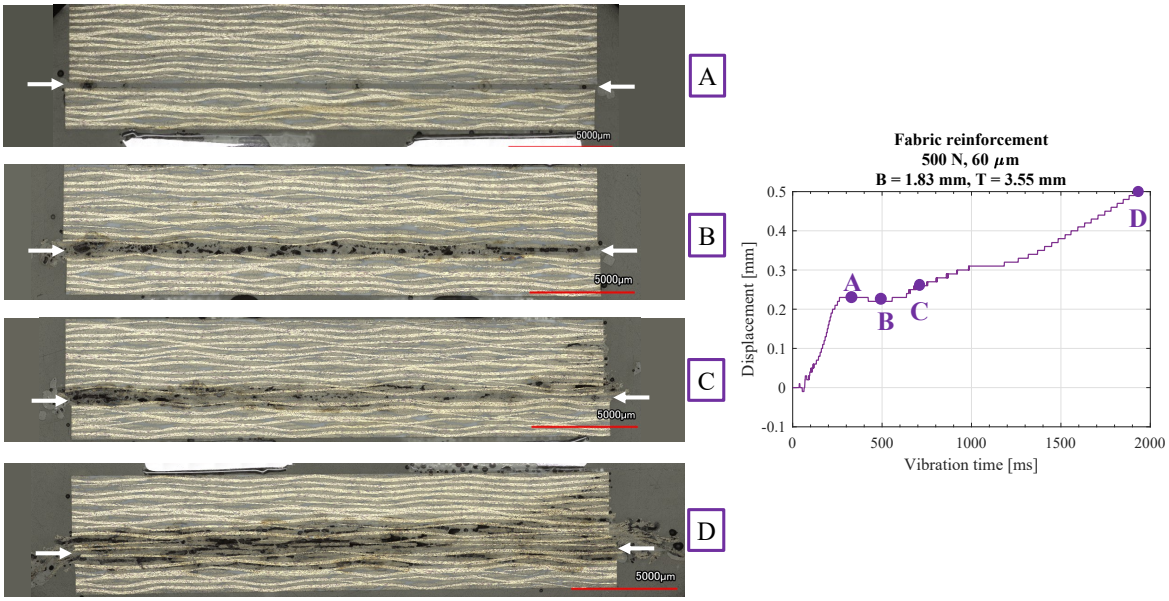

Figure D.4: Cross sectional micrographs for T = 3.55 mm at different points of the displacement curve. 500 N, 60 μm and no consolidation.

D.2.2. High force-high amplitude (1500 N, 80 um)

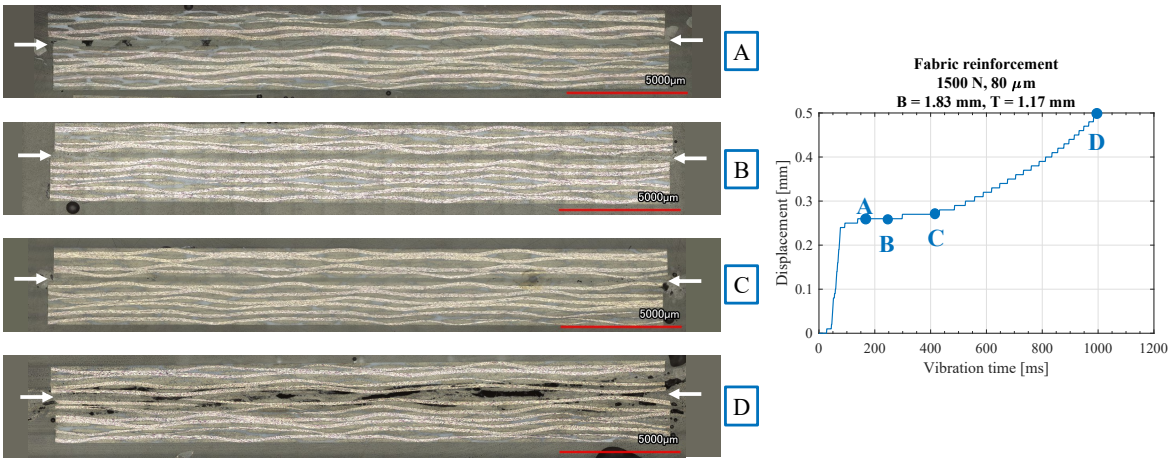

Figure D.5: Cross sectional micrographs for T = 1.17 mm at different points of the displacement curve. 1500 N, 80 μm and no consolidation.

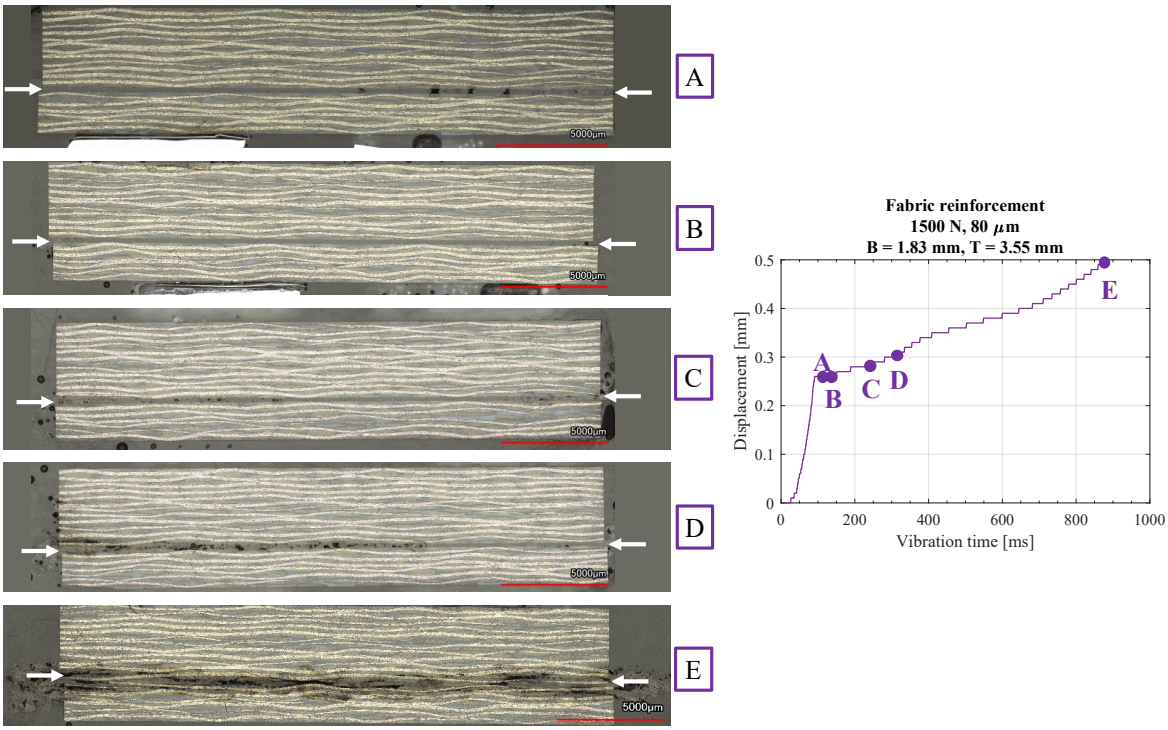

Figure D.6: Cross sectional micrographs for T = 3.55 mm at different points of the displacement curve. 1500 N, 80 μm and no consolidation.

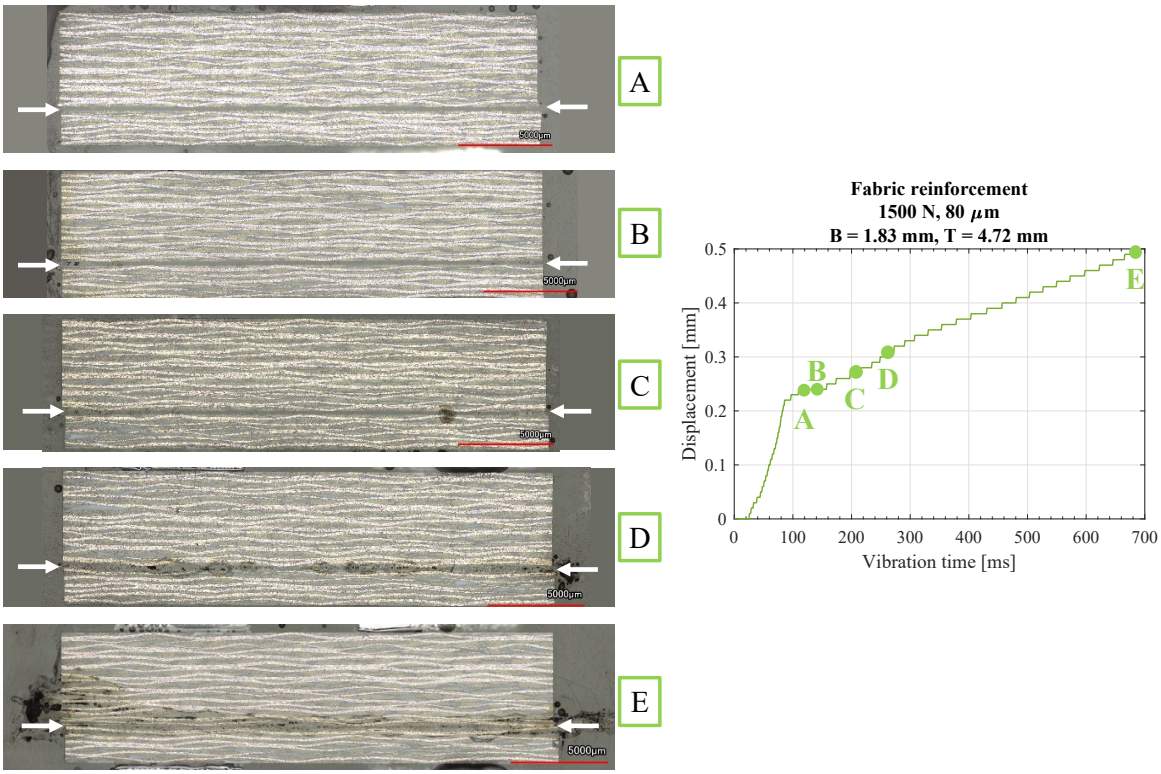

Figure D.7: Cross sectional micrographs for T = 4.72 mm at different points of the displacement curve. 1500 N, 80 μm and no consolidation.

D.2.3. High force-low amplitude (1500 N, 60 um)

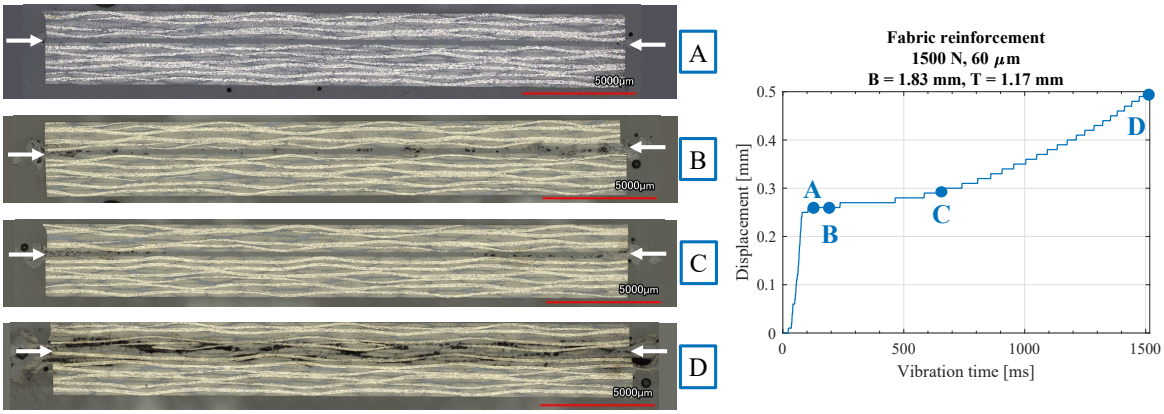

Figure D.8: Cross sectional micrographs for T = 1.17 mm at different points of the displacement curve. 1500 N, 60 μm and no consolidation.

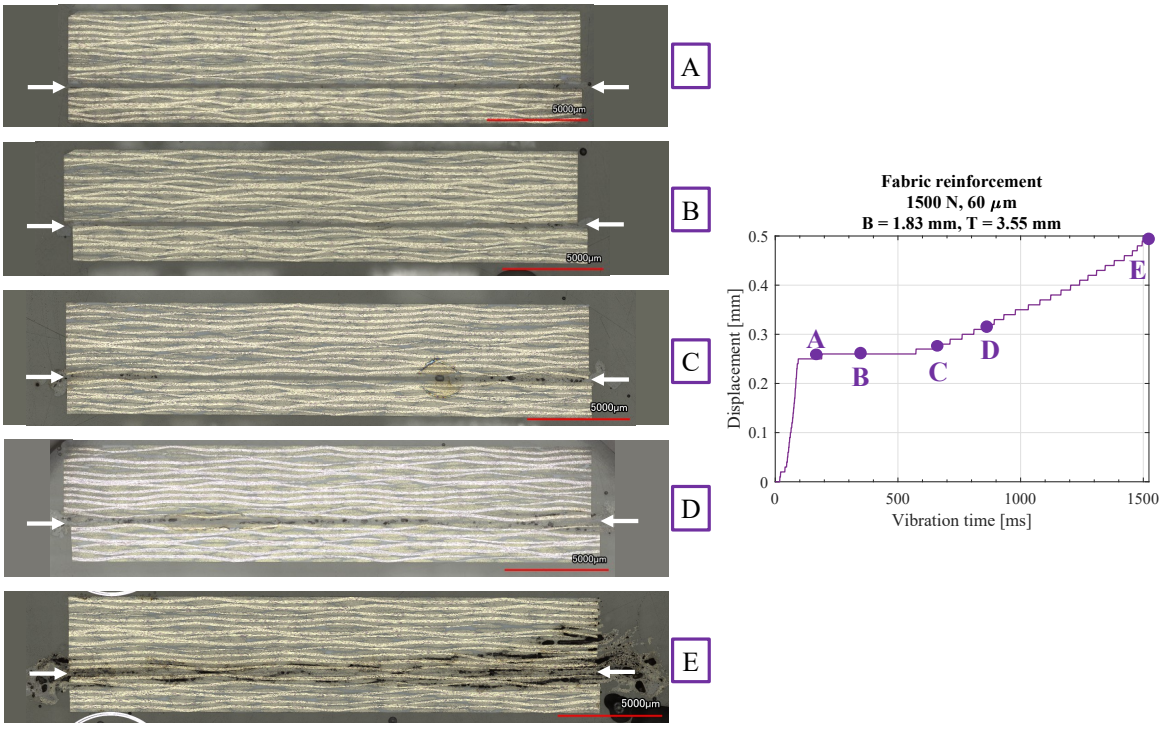

Figure D.9: Cross sectional micrographs for T = 3.55 mm at different points of the displacement curve. 1500 N, 60 μm and no consolidation.

D.3. Effect of changing to UD reinforcement

The reinforcement of the adherends was changed to UD. The figures shown in this section are a complement of the results shown in Section 3.4.4 where the process parameters were changed and different thicknesses of the top adherend were evaluated (the bottom adherend's thickness B = 1.85 mm remained constant). Only the micrographs for the high force cases were obtained as the low force cases would present damage such as squeeze-out from the top adherend as was seen from the high-speed camera snapshots.

D.3.1. High force-high amplitude (1500 N, 80 um)

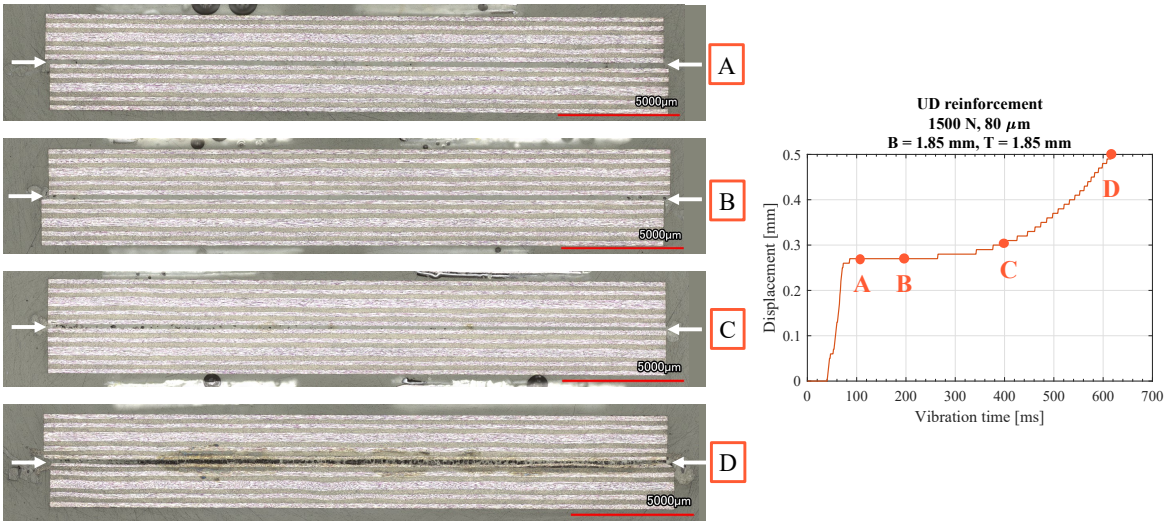

Figure D.10: Cross sectional micrographs for T = 1.85 mm at different points of the displacement curve. 1500 N, 80 μm and no consolidation. UD reinforcement.

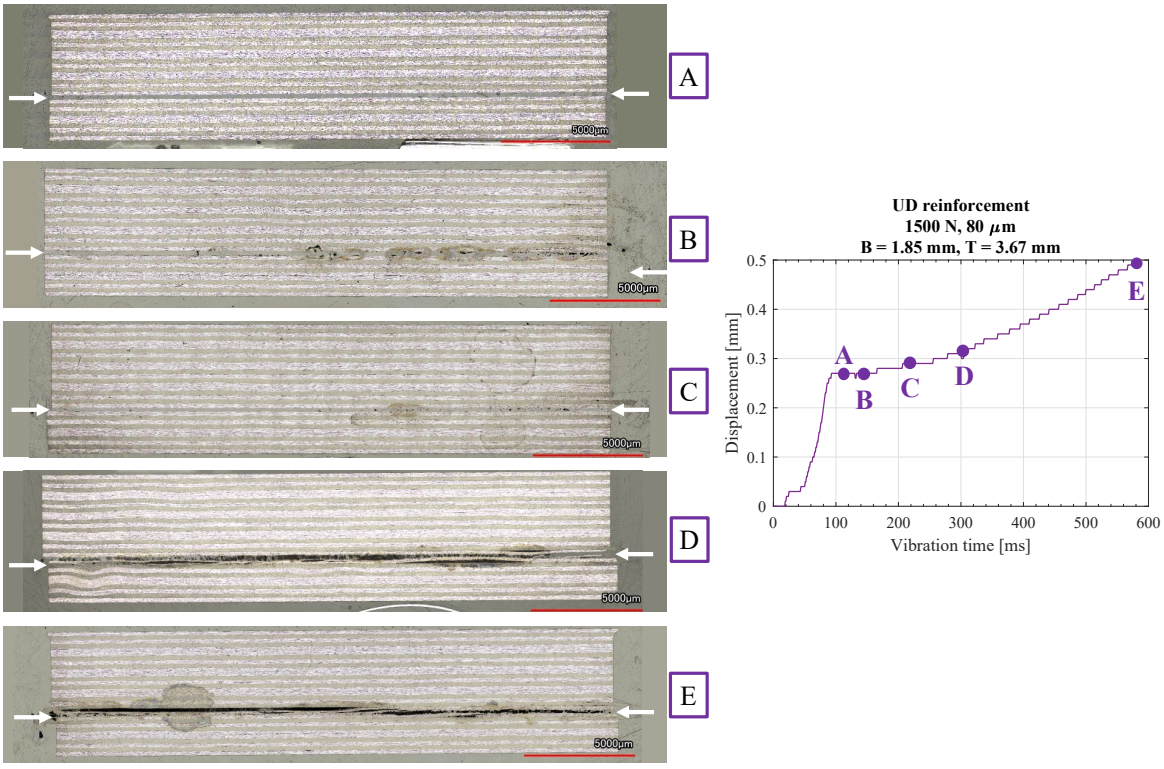

Figure D.11: Cross sectional micrographs for T = 3.67 mm at different points of the displacement curve. 1500 N, 80 μm and no consolidation. UD reinforcement.

D.3.2. High force-low amplitude (1500 N, 60 um)

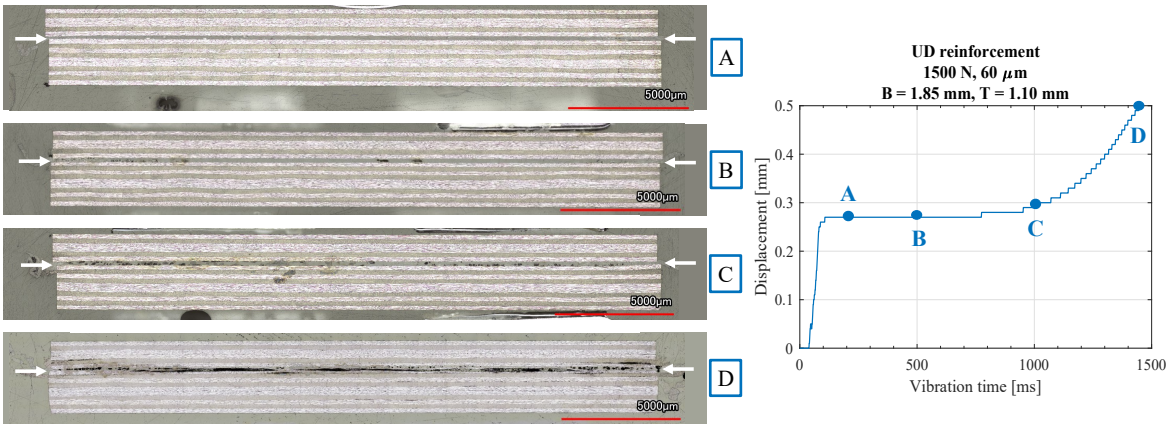

Figure D.12: Cross sectional micrographs for T = 1.10 mm at different points of the displacement curve. 1500 N, 60 μm and no consolidation. UD reinforcement.

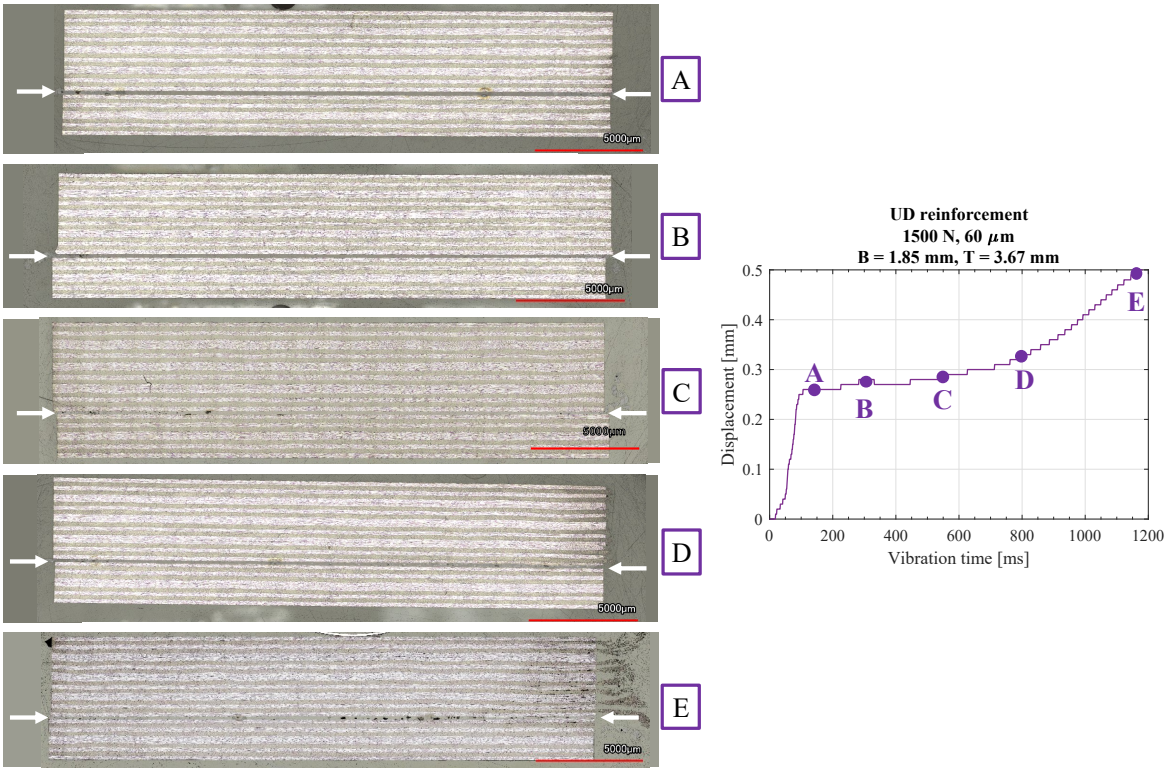

Figure D.13: Cross sectional micrographs for T = 3.67 mm at different points of the displacement curve. 1500 N, 60 μm and no consolidation. UD reinforcement.

E

Temperature readings

This appendix shows the individual temperature readings for each thickness of the top and bottom adherend. In multiple cases, the thermocouples would not survive and therefore only one reading is presented. The dashed line shows the end of vibrations and the consolidation time was set to 4000 ms. When multiple readings are presented, this value corresponds to an average.

E.1. Effect of changing the top adherend's thickness

The figures shown in this section are a complement of the results shown in Section 3.1.5 where the top adherend's thickness was changed while keeping the process parameters (500 N, 80 μm) and bottom adherend's thickness (B = 1.83 mm) constant. The adherends used had a fabric reinforcement.

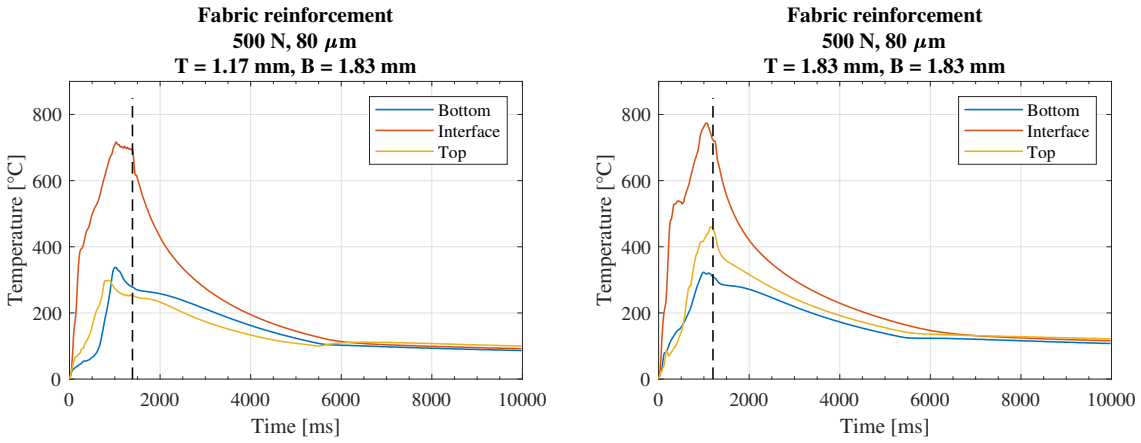

(a) T = 1.17 mm

(b) T = 1.83 mm

Figure E.1: Temperature curves for different thicknesses of the top adherend where all TCs were present. 500 N, 80 μm. The dashed line represents the end of vibrations.

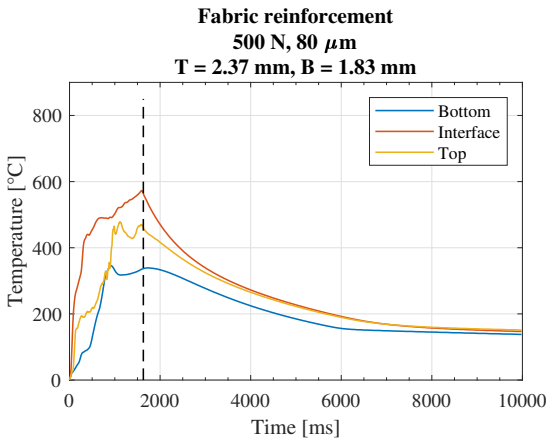

(c) B = 2.37 mm

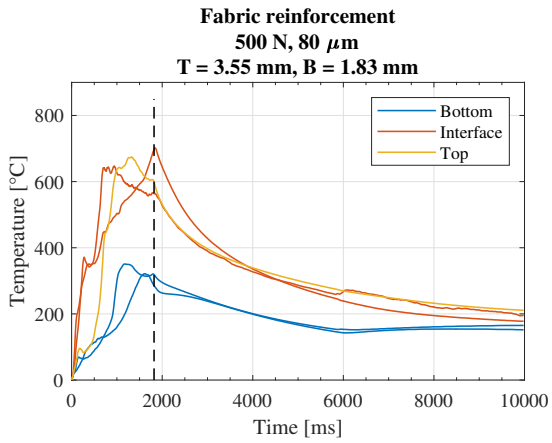

(d) T = 3.55 mm

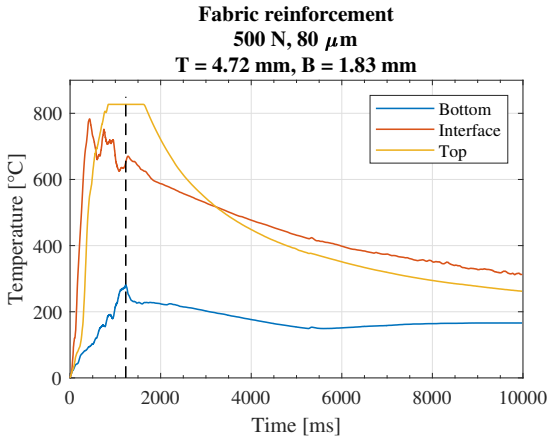

(e) T = 4.72 mm

Figure E.1: (continued) Temperature curves for different thicknesses of the top adherend where all TCs were present. 500 N, 80 μm. The dashed line represents the end of vibrations.

E.2. Effect of changing the bottom adherend's thickness

The figures shown in this section are a complement of the results shown in Section 3.2.4 where the bottom adherend's thickness was changed while keeping the process parameters (500 N, 80 μm) and top adherend's thickness (B = 1.83 mm) constant. The adherends used had a fabric reinforcement.

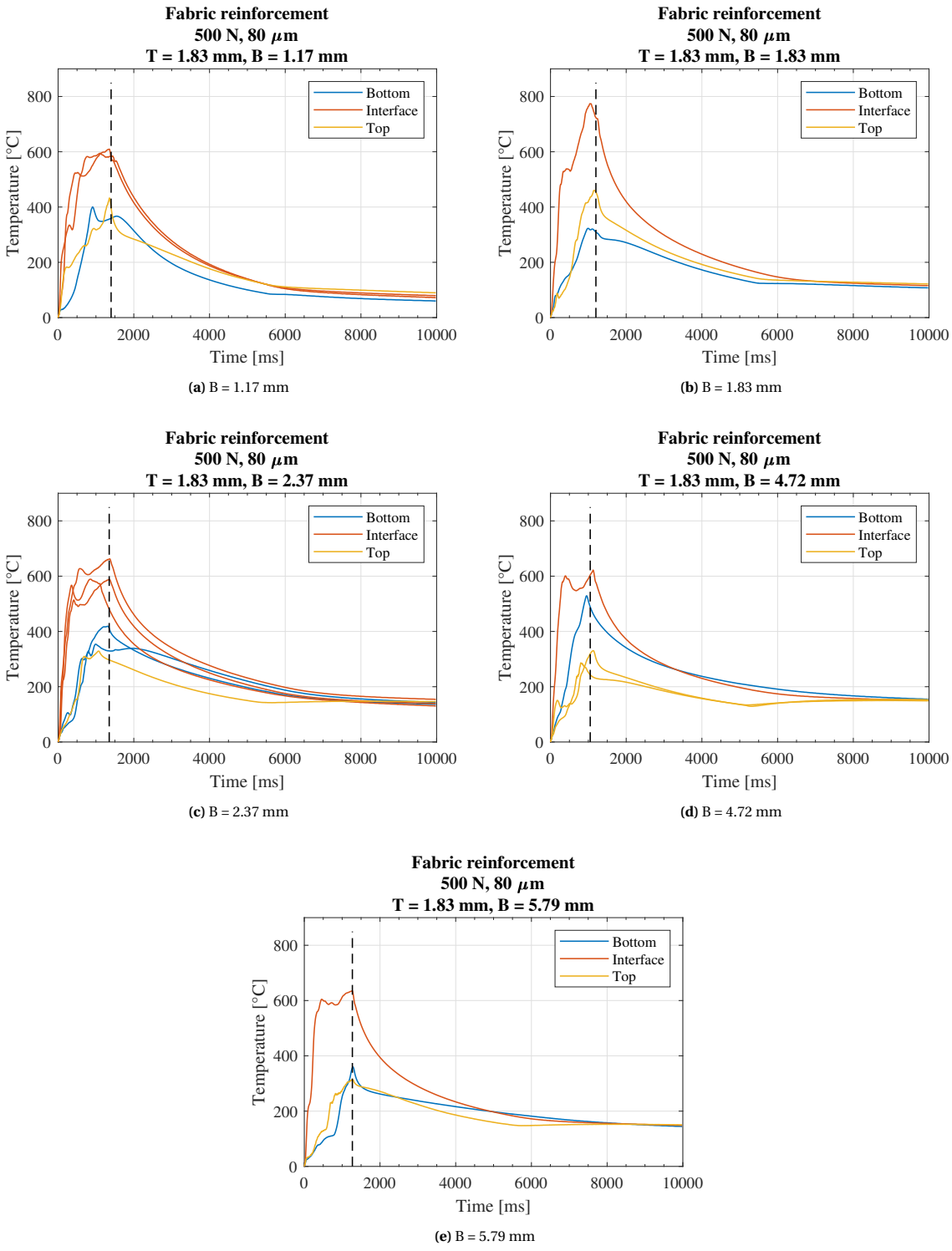

(a) B = 1.17 mm

(b) B = 1.83 mm

(c) B = 2.37 mm

(d) B = 4.72 mm

(e) B = 5.79 mm

Figure E.2: Temperature curves for different thicknesses of the bottom adherend where all TCs were present. 500 N, 80 μm. The dashed line represents the end of vibrations.

F

COMSOL wave propagation model

This appendix shows a more in detail evolution from the COMSOL wave propagation model (see Section 2.3.4) for different top and bottom adherends thicknesses. Furthermore, a brief evaluation of the model for different conditions is presented.

F.1. Evaluation of the model

The aim of this model was to assess the effect of changing the top and bottom adherends' thickness solely on wave propagation through the welding stack. Because comparing the model results with experimental ones is not possible due to the multiple assumptions that were made, then the validity of the numerical results will be evaluated by means of changing the conditions in the model and check if they are congruent with what the physics indicate.

Figure F.1 shows the displacement magnitude at the time in which the sonotrode is at its lowest point (1.25×10^{-5} s) for different material cases for equal adherend thicknesses of 1.83 mm and in the sliced workplane 1 from Figure 2.6. The original case is the same as described in Section 2.3.4, where the adherends are composites, the ED is LMPAEK, the sonotrode is steel, and the anvil is aluminum.

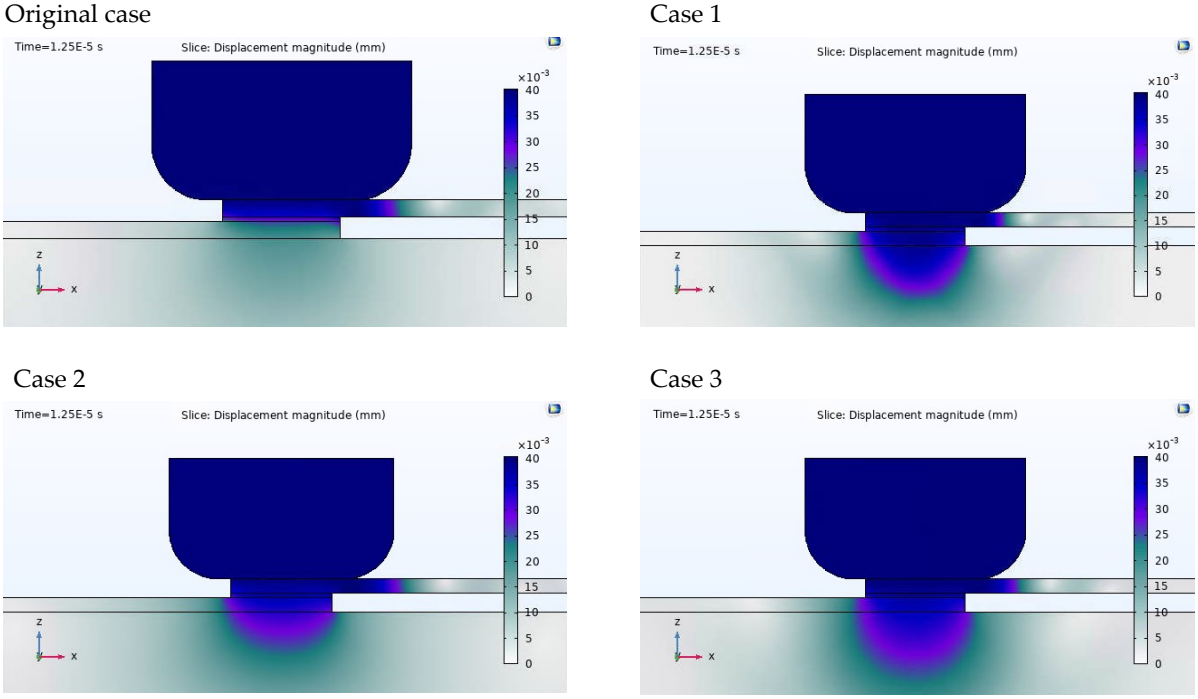

Figure F.1: COMSOL wave propagation results for different material cases at 1.25×10^{-5} s.

For cases 1 and 2 the material of the adherends, ED, and anvil were changed to LMPAEK and steel, respectively. Because all the domains were assumed as linear elastic isotropic materials, other effects such as attenuation in viscoelastic materials are not considered in the model. The acoustic impedance (Z) is defined as the resistance of a medium to acoustic motion, such as an ultrasonic vibration, and it can be defined with the following equation [59]:

$$Z = \rho c = \rho \sqrt{\frac{E}{\rho}} \tag{F.1}$$

Where ρ and c are the density and wavespeed of such medium. If the material is isotropic (such as in the model), then the wavespeed can be expressed as $\sqrt{E/\rho}$ [59]. Considering the material properties from Table 2.4, LMPAEK has an acoustic impedance of 2 MPa $\cdot$ s $\cdot$ m^{-1}, whereas steel has an acoustic impedance of 40 MPa $\cdot$ s $\cdot$ m^{-1}. The much higher impedance of steel therefore explains why the vibrations penetrate more for case 1 than for case 2, as there is more resistance to to motion on the second case.

Case 3 is for a configuration in which the adherends and anvil are composites, whereas the sonotrode is still made of steel and the ED of LMPAEK. The difference on the wave propagation can be explained by the impedance mismatch between two media. When an acoustic wave travelling in a medium encounters a medium with different properties (namely density and Young's modulus), then a portion of that wave will get reflected and the other one will get transmitted. The reflection coefficient is an indication of how much of the wave is reflected when travelling from a medium 1 to a medium 2, and is defined as [90]:

$$R = \frac{Z_2 - Z_1}{Z_2 + Z_1} \tag{F.2}$$

For the case in which $Z_1 = Z_2$, then there is no impedance mismatch and there will be no reflection since the wave continues travelling as if it were in the same medium [90]. This is therefore evidenced when comparing the original case and case 3, since the change in the properties of the anvil causes reflection of the wave that results in a change of direction and therefore a lower displacement magnitude.

Another case was evaluated, but for a different frequency (1 MHz rather than 20 kHz) while keeping the original material case. Figure F.2 shows a brief evolution of the wave at different times. For such frequency, the maximum displacement of the sonotrode will occur at 2.5 $\times 10^{-7}$ s, which corresponds to the first image presented.

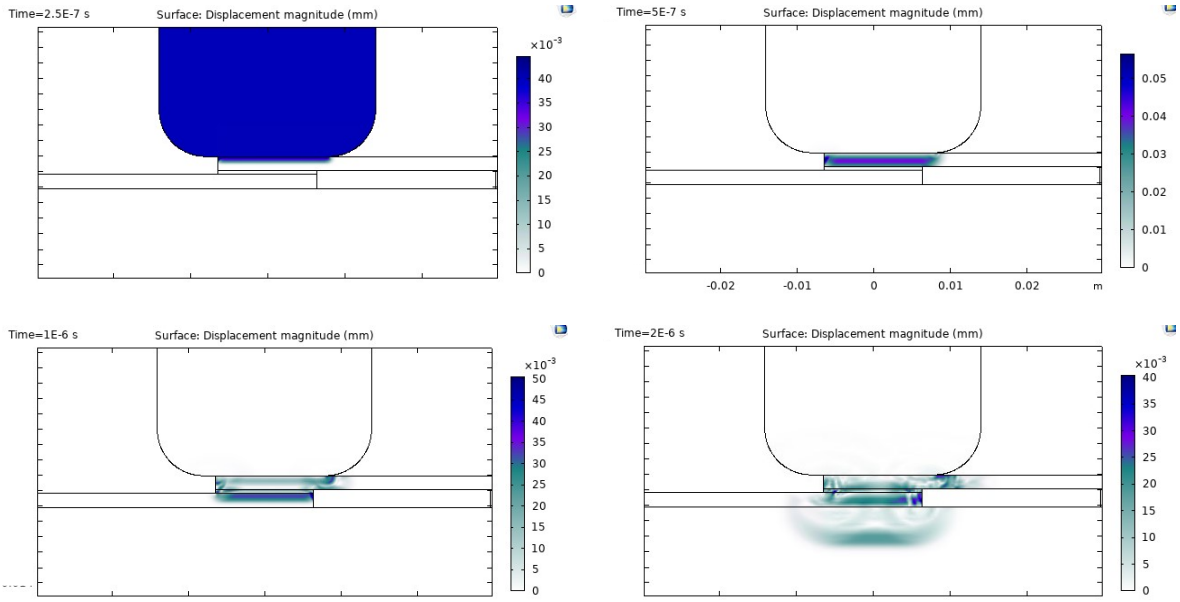

Figure F.2: COMSOL wave propagation results for a wave with frequency of 1 MHz.

The theory indicates that changing the frequency will result on a smaller wavelength as seen in Equation 1.6. Considering again the material properties form Table 2.4 and Equation F.1, then the wavelength at

20 kHz for the composite adherends in the model is 147 mm, whereas for 1 MHz is 2.94 mm. This therefore is in agreement with the results obtained for a higher frequency, where it is clear that there are now multiple waves propagating through the welding stack rather than one standing wave for the 20 kHz case.

Finally, certain similarities were noticed between the obtained welds and the points of maximum amplitude in the wave propagation model. Figure F.3 shows damage in the top adherend right under the edge of the sonotrode where the the overlap ends (circled in red). From the model results, it is noticed that this edge also presents the higher displacement magnitude. This can be explained by the fact that the vibrations at this edge are not transmitted to the rest of the welding stack, but rather concentrated at the top adherend. Figure F.4 also shows damage at different positions of the top adherend. This occurs because the waves generated by the sonotrode also travel in the length direction of the top adherend, as is also shown in the model results. These however are no longer longitudinal waves but shear waves, as the direction of propagation is perpendicular to the motion in the medium. The fact that this damage occurs periodically as seen in the images indicates that the distance between these red circles is most likely equal to half the shear wavelength. Unfortunately, this value was not measured experimentally as only the longitudinal wavelength was determined (see Appendix H).

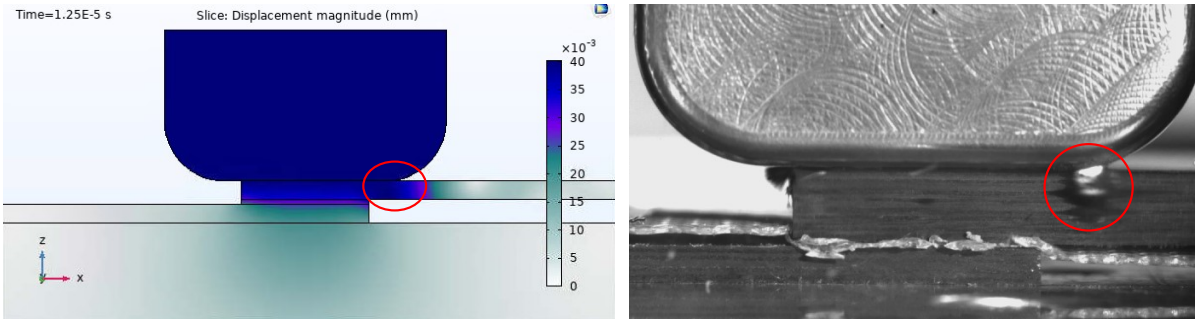

Figure F.3: Damage in the adherend at the right edge of the sonotrode.

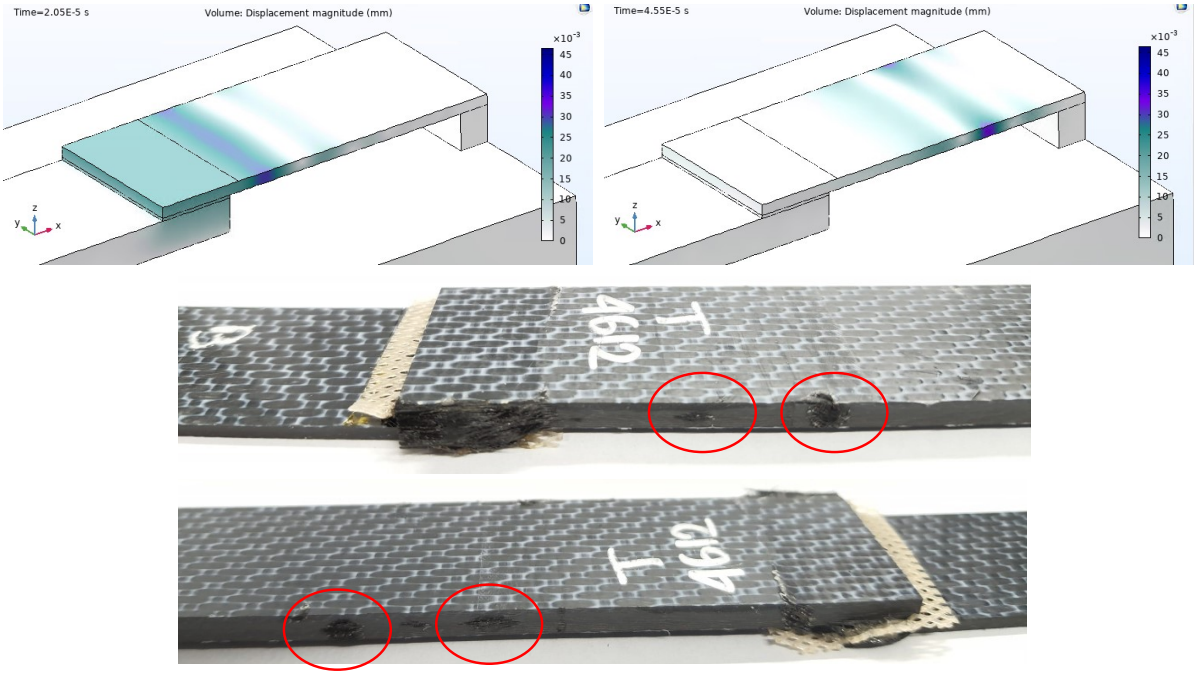

Figure F.4: Damage in the top adherend in different poisitions of the top adherend.

F.2. Effect of changing the top adherend's thickness

The figures shown in this section are a complement of the results shown in Section 3.1.6. Figure F.5 and Figure F.6 show the results from the wave propagation model when assuming the top adherend's thickness as 1.17 mm and 4.72 mm. The sonotrode was hidden for clarity. The propagation of the ultrasonic wave is visualized with the total displacement magnitude in the geometry. The time at which this displacement is maximum (see Figure 2.9) is 1.25 $\times 10^{-5}$ s. To emphasise on the wave propagation in the thickness direction, the results on a 2D plane (workplane 1 from Figure 2.6) are shown in Figure F.7 and Figure F.8. The top adherend's thickness is 1.83 mm.

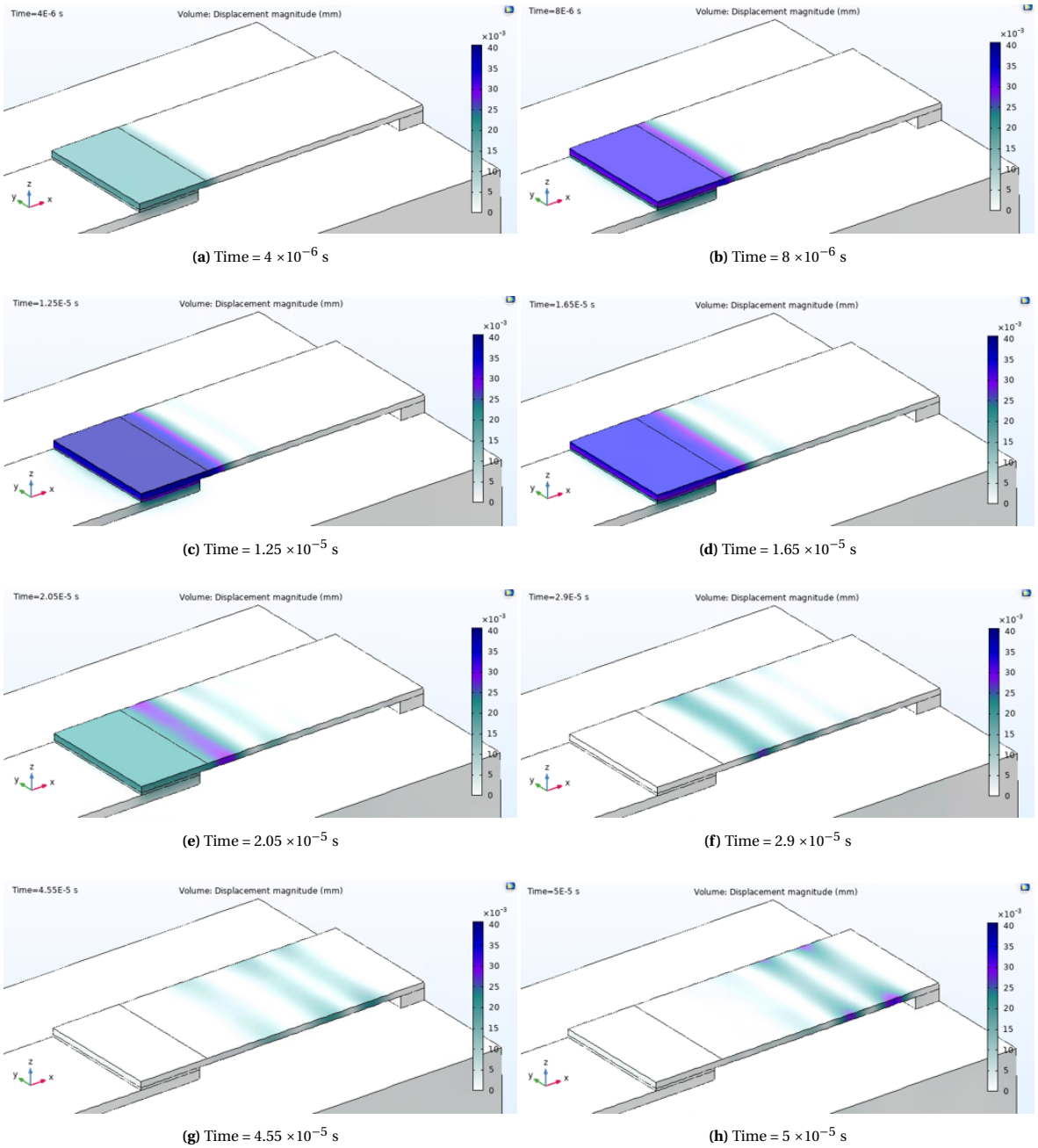

(a) Time = 4 $\times 10^{-6}$ s

(b) Time = 8 $\times 10^{-6}$ s

(c) Time = 1.25 $\times 10^{-5}$ s

(d) Time = 1.65 $\times 10^{-5}$ s

(e) Time = 2.05 $\times 10^{-5}$ s

(f) Time = 2.9 $\times 10^{-5}$ s

(g) Time = 4.55 $\times 10^{-5}$ s

(h) Time = 5 $\times 10^{-5}$ s

Figure F.5: COMSOL wave propagation model results (total displacement magnitude in mm]) for a top adherend's thickness of 1.17 mm.

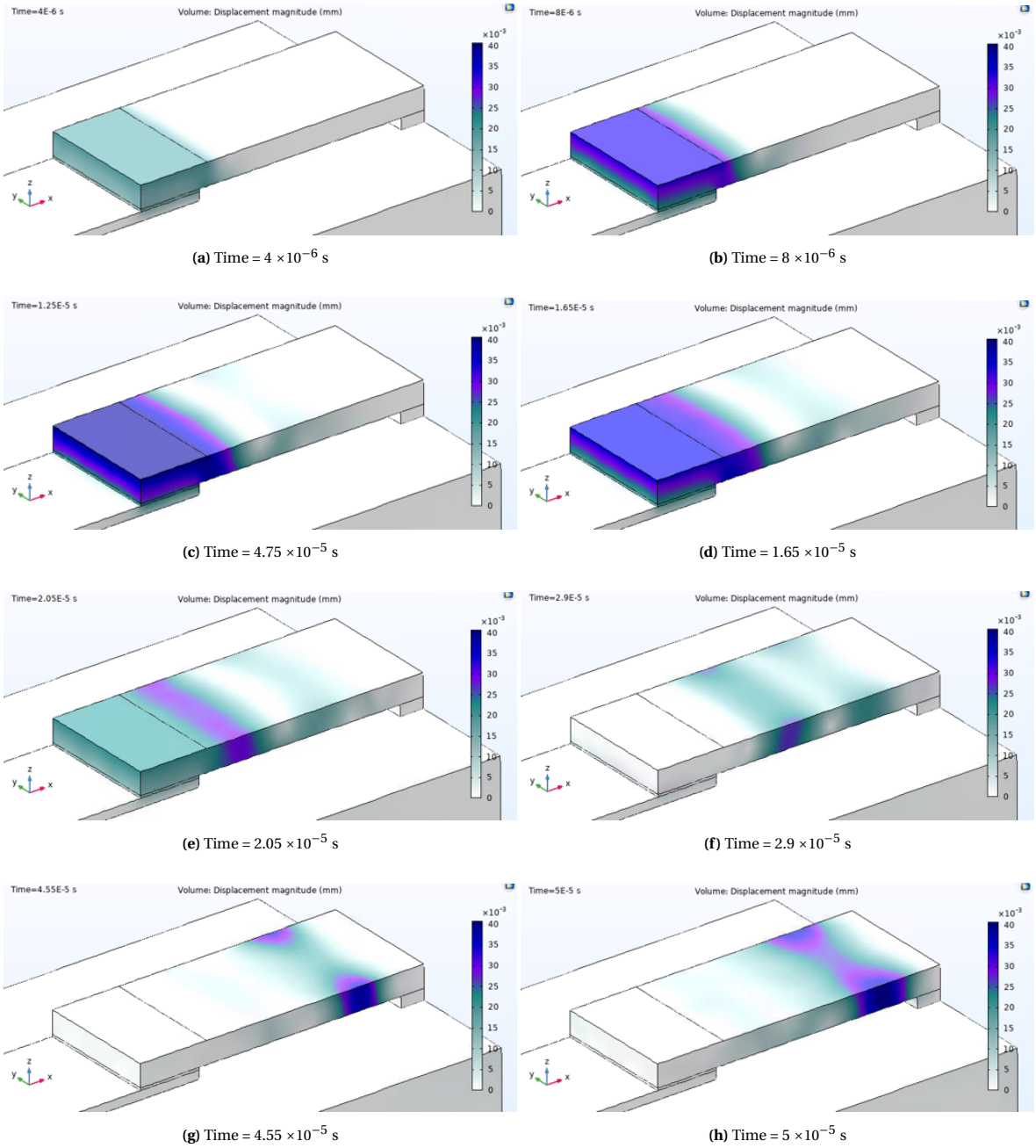

(a) Time = 4×10^{-6} s

(b) Time = 8×10^{-6} s

(c) Time = 4.75×10^{-5} s

(d) Time = 1.65×10^{-5} s

(e) Time = 2.05×10^{-5} s

(f) Time = 2.9×10^{-5} s

(g) Time = 4.55×10^{-5} s

(h) Time = 5×10^{-5} s

Figure F.6: COMSOL wave propagation model results (total displacement magnitude in mm]) for a top adherend's thickness of 4.72 mm.

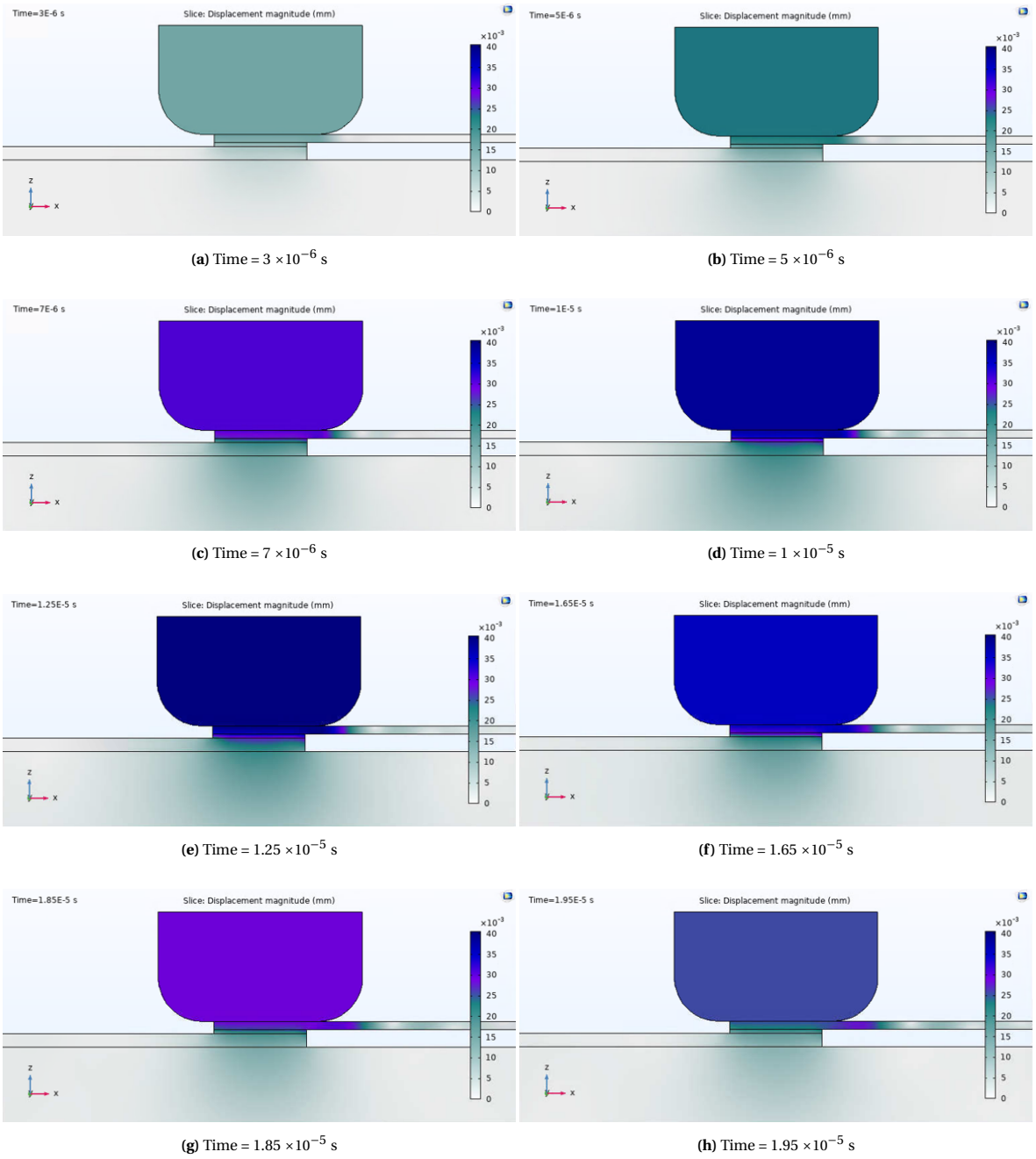

(a) Time = 3×10^{-6} s

(b) Time = 5×10^{-6} s

(c) Time = 7×10^{-6} s

(d) Time = 1×10^{-5} s

(e) Time = 1.25×10^{-5} s

(f) Time = 1.65×10^{-5} s

(g) Time = 1.85×10^{-5} s

(h) Time = 1.95×10^{-5} s

Figure F.7: COMSOL wave propagation model results (total displacement magnitude in mm) for a top adherend's thickness of 1.17 mm. Results in the sliced workplane 1 from Figure 2.6.

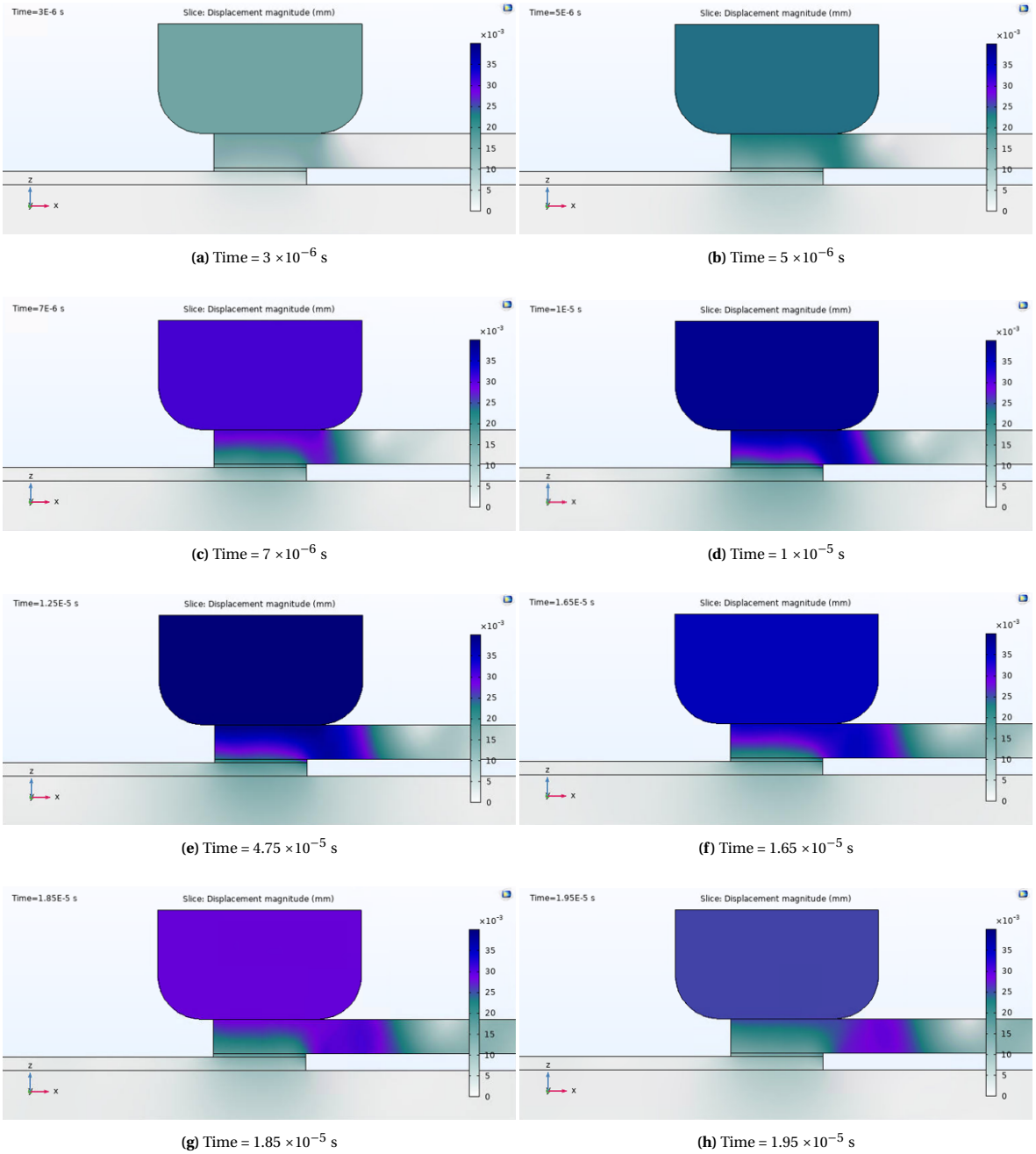

(a) Time = 3×10^{-6} s

(b) Time = 5×10^{-6} s

(c) Time = 7×10^{-6} s

(d) Time = 1×10^{-5} s

(e) Time = 4.75×10^{-5} s

(f) Time = 1.65×10^{-5} s

(g) Time = 1.85×10^{-5} s

(h) Time = 1.95×10^{-5} s

Figure F.8: COMSOL wave propagation model results (total displacement magnitude in mm) for a top adherend's thickness of 4.72 mm. Results in the sliced workplane 1 from Figure 2.6.

F.3. Effect of changing the bottom adherend's thickness

The figures shown in this section are a complement of the results shown in Section 3.2.6. Figure F.9 and Figure F.10 show the results from the wave propagation model when assuming the bottom adherend's thickness as 1.17 mm and 5.79 mm. The sonotrode was hidden for clarity. The propagation of the ultrasonic wave is visualized with the total displacement magnitude in the geometry. The time at which this displacement is maximum (see Figure 2.9) is 1.25 $\times 10^{-5}$ s. To emphasise on the wave propagation in the thickness direction, the results on a 2D plane (workplane 1 from Figure 2.6) are shown in Figure F.11 and Figure F.12. The bottom adherend's thickness is 1.83 mm.

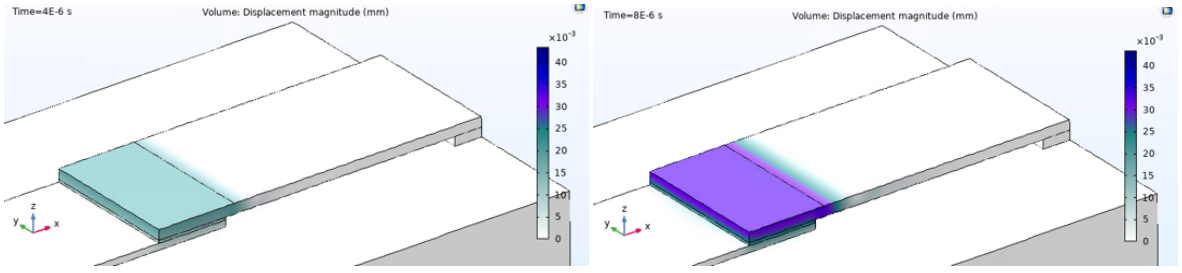

(a) Time = 4 $\times 10^{-6}$ s **(b)** Time = 8 $\times 10^{-6}$ s

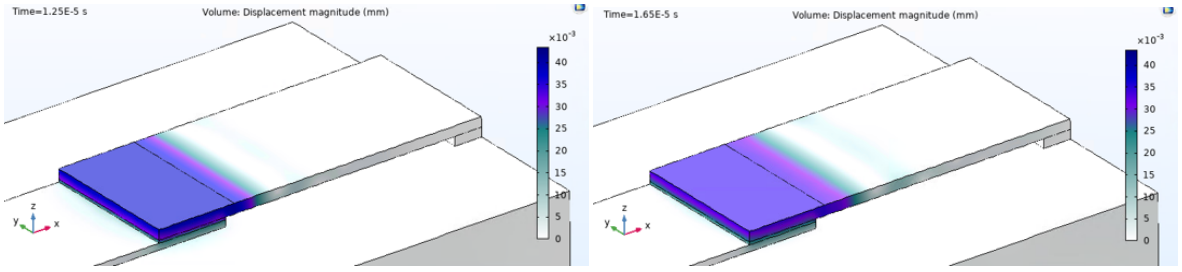

(c) Time = 1.25 $\times 10^{-5}$ s **(d)** Time = 1.65 $\times 10^{-5}$ s

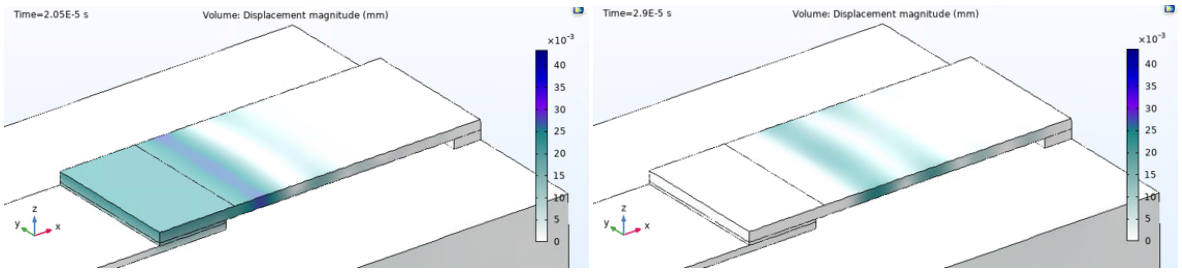

(e) Time = 2.05 $\times 10^{-5}$ s **(f)** Time = 2.9 $\times 10^{-5}$ s

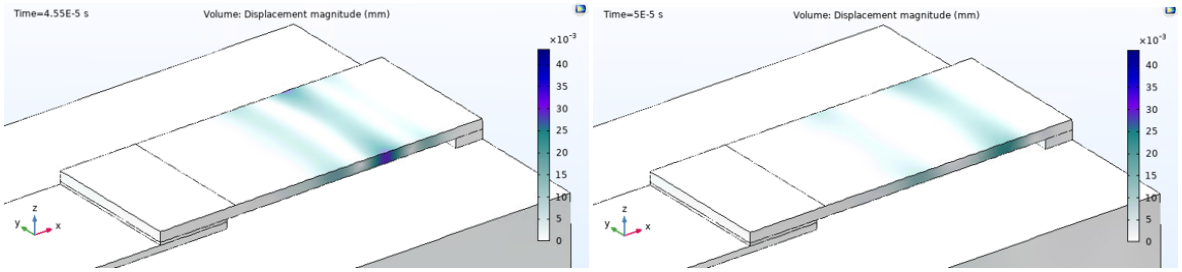

(g) Time = 4.55 $\times 10^{-5}$ s **(h)** Time = 5 $\times 10^{-5}$ s

Figure F.9: COMSOL wave propagation model results (total displacement magnitude in mm]) for a bottom adherend's thickness of 1.17 mm.

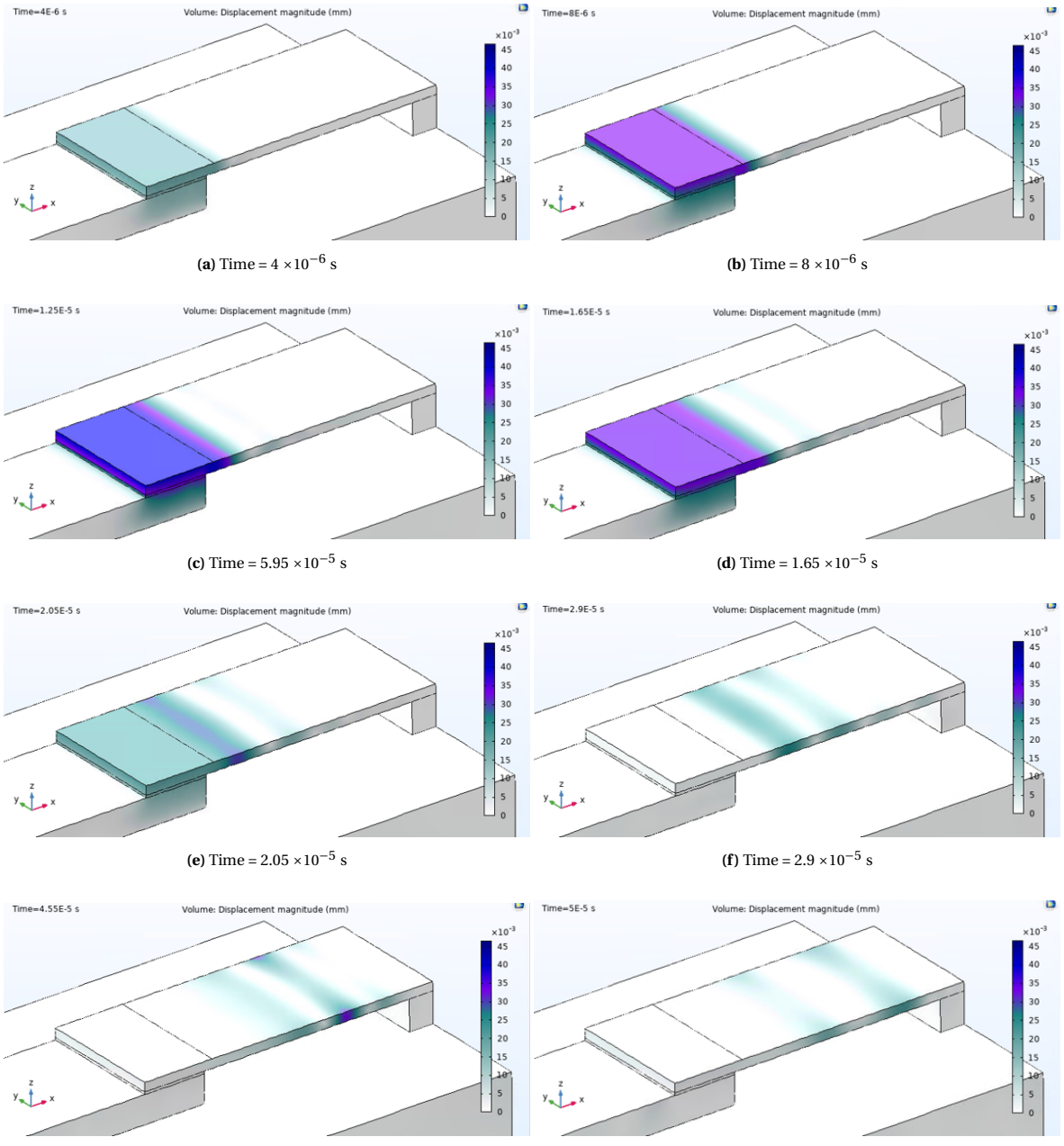

(a) Time = 4×10^{-6} s

(b) Time = 8×10^{-6} s

(c) Time = 5.95×10^{-5} s

(d) Time = 1.65×10^{-5} s

(e) Time = 2.05×10^{-5} s

(f) Time = 2.9×10^{-5} s

(g) Time = 4.55×10^{-5} s

(h) Time = 5×10^{-5} s

Figure F.10: COMSOL wave propagation model results (total displacement magnitude in mm]) for a bottom adherend's thickness of 5.79 mm.

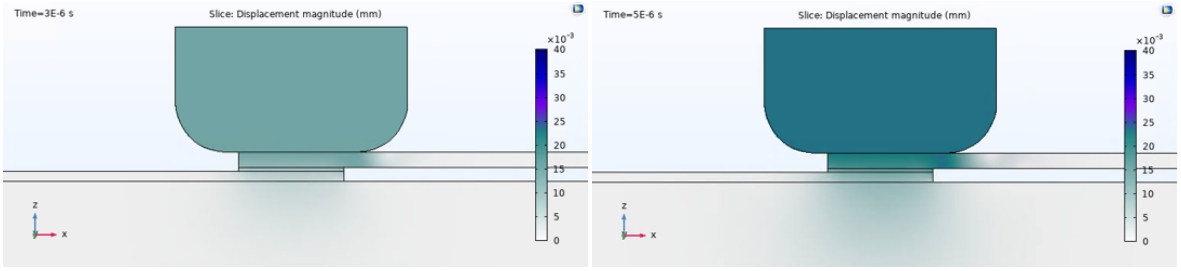

(a) Time = 4×10^{-6} s **(b)** Time = 8×10^{-6} s

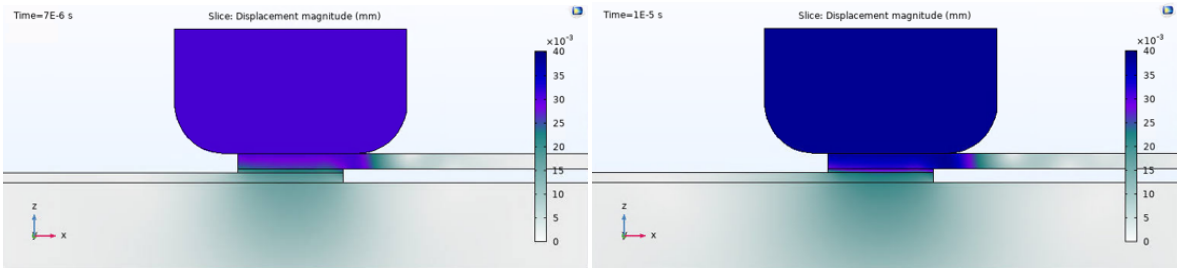

(c) Time = 1.25×10^{-5} s **(d)** Time = 1.65×10^{-5} s

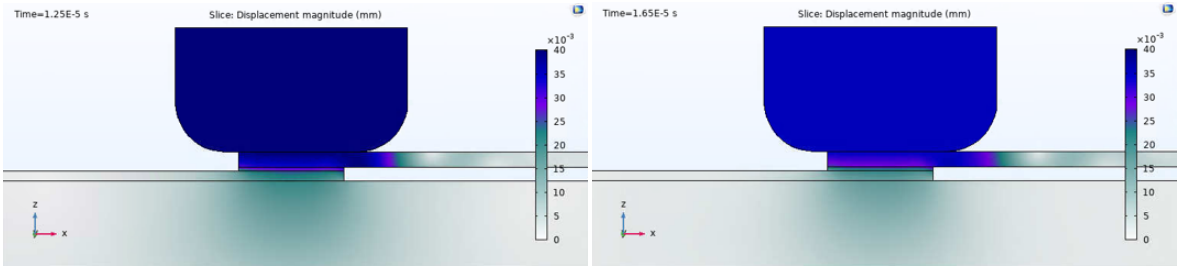

(e) Time = 2.05×10^{-5} s **(f)** Time = 2.9×10^{-5} s

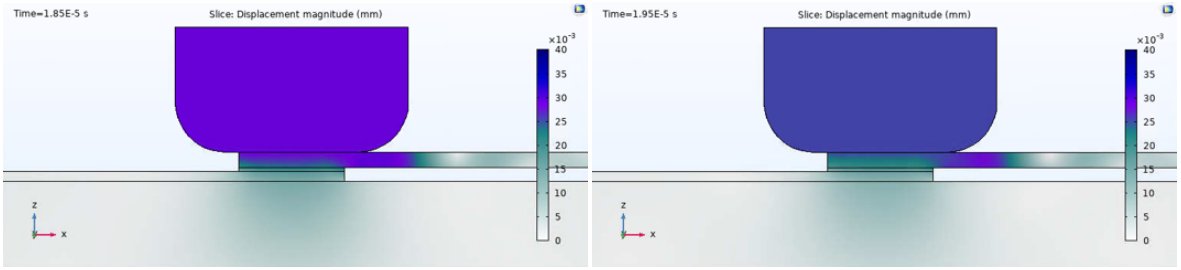

(g) Time = 4.55×10^{-5} s **(h)** Time = 5×10^{-5} s

Figure F.11: COMSOL wave propagation model results (total displacement magnitude in mm) for a bottom adherend's thickness of 1.17 mm. Results in the sliced workplane 1 from Figure 2.6.

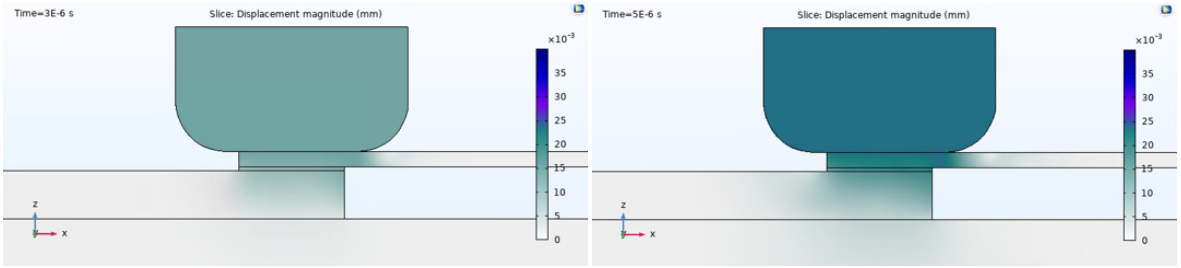

(a) Time = 4×10^{-6} s **(b)** Time = 8×10^{-6} s

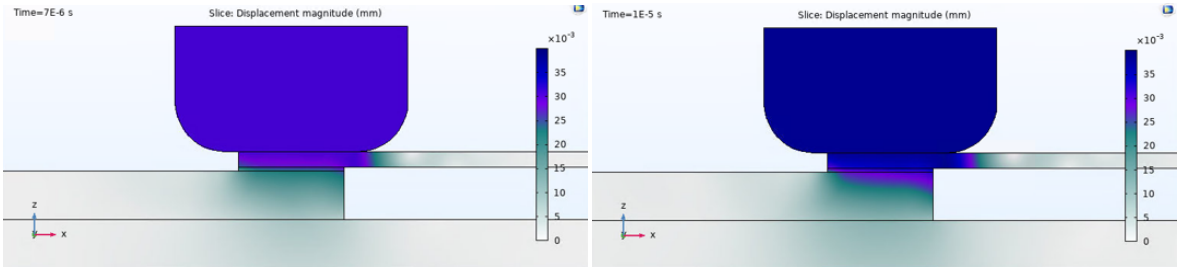

(c) Time = 5.95×10^{-5} s **(d)** Time = 1.65×10^{-5} s

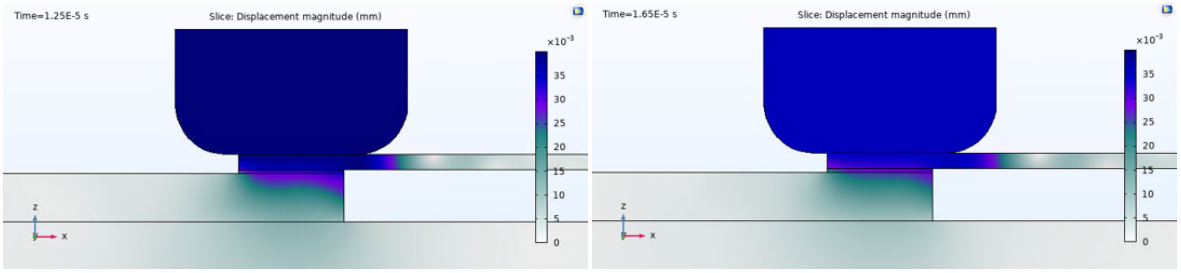

(e) Time = 2.05×10^{-5} s **(f)** Time = 2.9×10^{-5} s

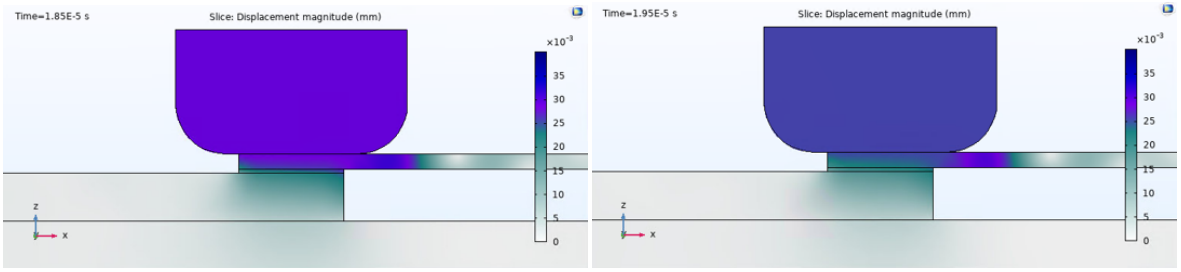

(g) Time = 4.55×10^{-5} s **(h)** Time = 5×10^{-5} s

Figure F.12: COMSOL wave propagation model results (total displacement magnitude in mm) for a bottom adherend's thickness of 5.79 mm. Results in the sliced workplane 1 from Figure 2.6.

G

COMSOL heat transfer model

This appendix shows some images from the COMSOL heat transfer model (see Section 2.3.4) results at different times (2500 ms, 5000 ms, 7500 ms, and 10000 ms) and for certain thicknesses of the bottom adherend: the extreme experimental thickness (1.17 mm and 5.79 mm), a thickness in the middle of these values (2.37 mm), and the added 10.00 mm thickness.

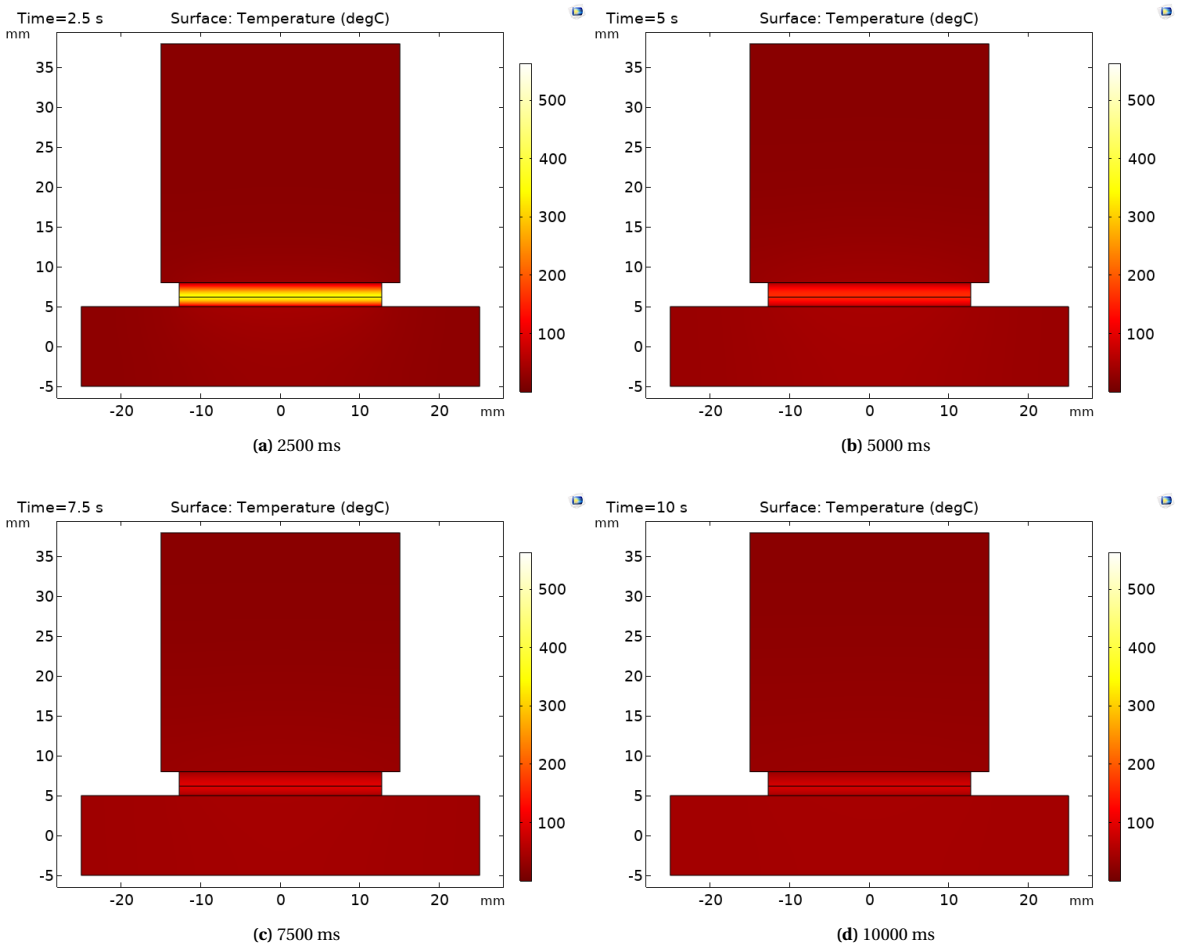

(a) 2500 ms **(b)** 5000 ms

(c) 7500 ms **(d)** 10000 ms

Figure G.1: Results of the COMSOL heat transfer model for B = 1.17 mm.

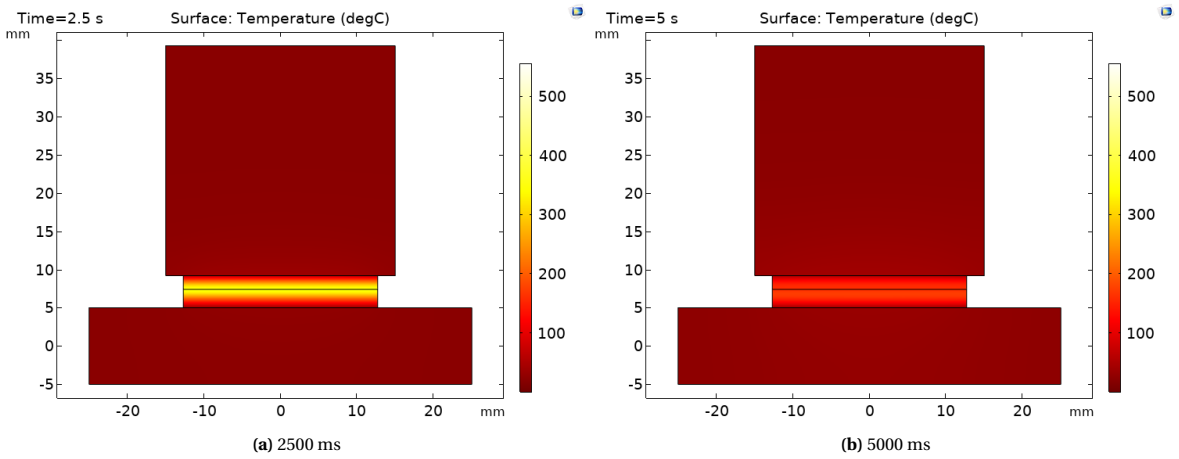

(a) 2500 ms

(b) 5000 ms

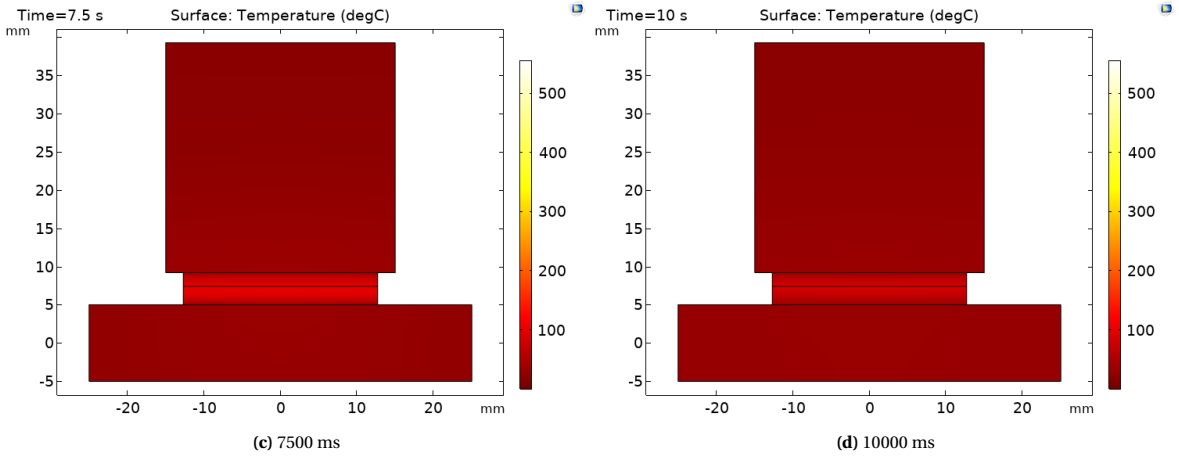

(c) 7500 ms

(d) 10000 ms

Figure G.2: Results of the COMSOL heat transfer model for B = 2.37 mm.

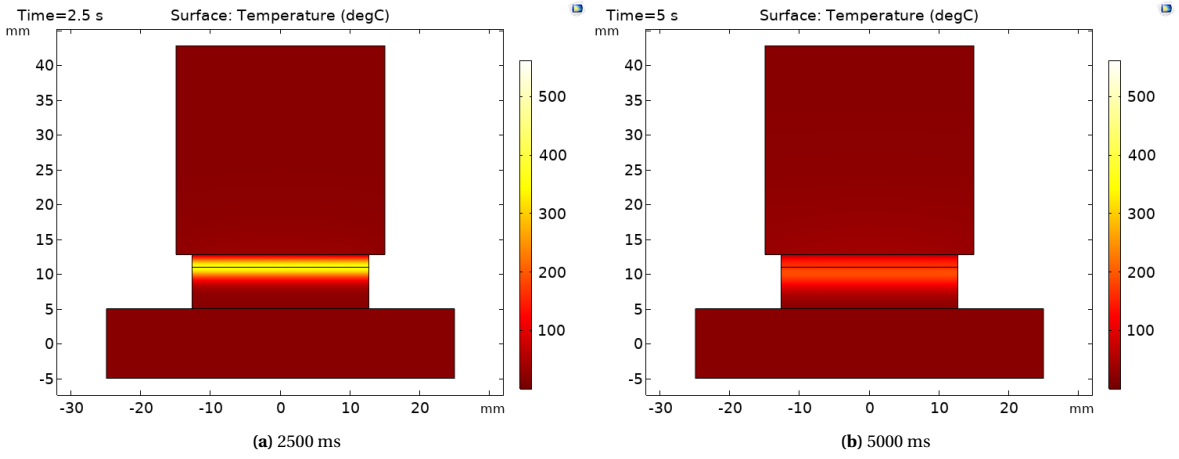

(a) 2500 ms

(b) 5000 ms

Figure G.3: Results of the COMSOL heat transfer model for B = 5.79 mm.

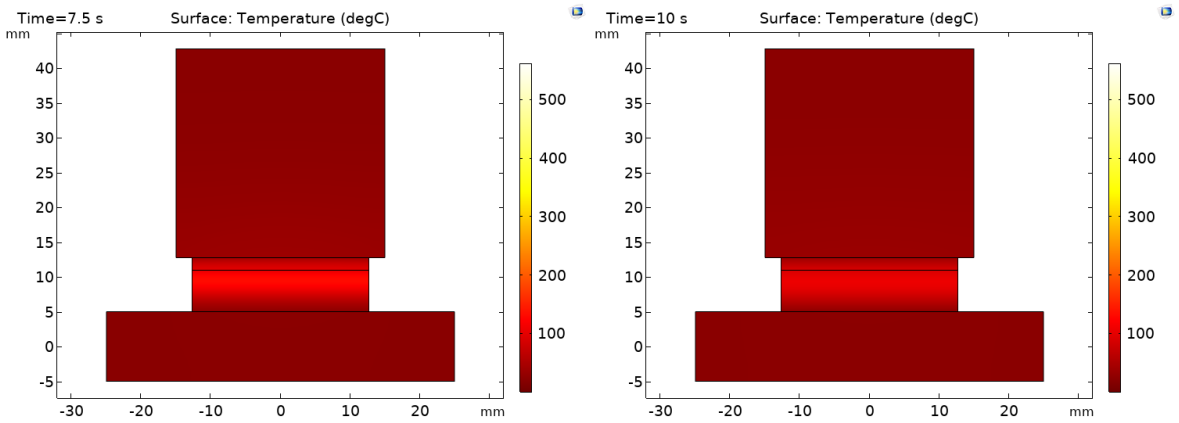

(c) 7500 ms **(d)** 10000 ms

Figure G.3: (continued) Results of the COMSOL heat transfer model for B = 5.79 mm.

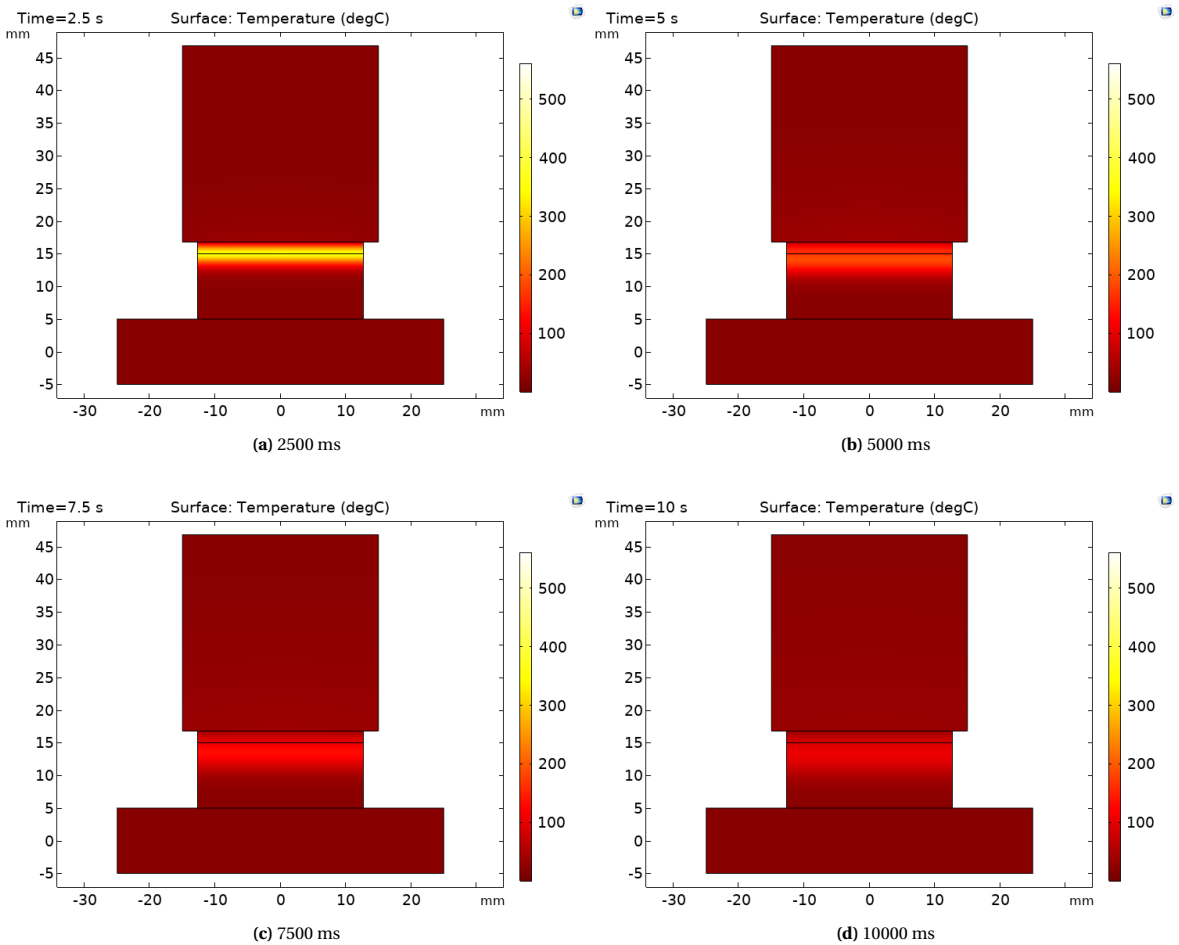

(a) 2500 ms **(b)** 5000 ms

(c) 7500 ms **(d)** 10000 ms

Figure G.4: Results of the COMSOL heat transfer model for B = 10.00 mm.

H

Speed of sound measurements

Following the methodology mentioned in Section 2.3.3, the speed of sound in the material was determined. The measurements were done in the samples with thicknesses of 1.83 mm and 4.72 mm. The equipment would show the wave intensity along the distance with an assumed speed of sound of 3000 m/s as shown in Figure H.1. The distance between the two peaks will then be the theoretical thickness of the sample. With this value, which was measured with Tracker, the time of flight of the wave (t_f) could be calculated and with the known thickness (T_s) of the sample the actual speed of sound (c) could be determined:

$$c = \frac{T_s}{t_f} \tag{H.1}$$

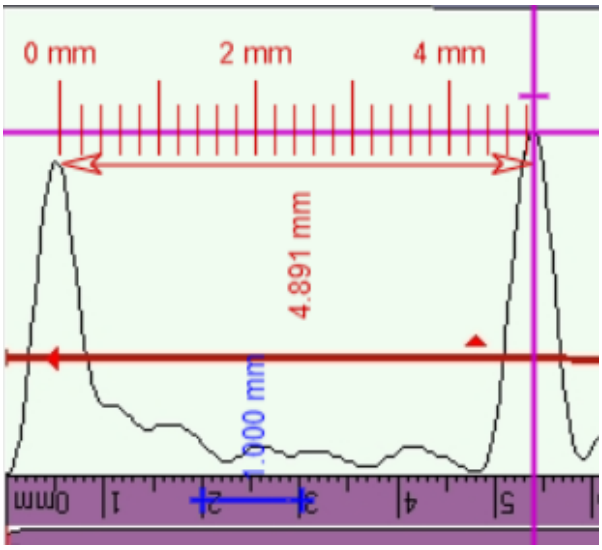

Figure H.1: Obtained output from the pulse-echo method.

With the known speed of sound, the wavelength (λ) at f = 20 kHz (the frequency of the equipment) can be calculated following Equation 1.6 from the literature study:

$$\lambda = \frac{c}{f}$$

This procedure was followed with 12 samples in total as can be seen in Table H.1. The speed of sound and wavelength with their corresponding standard deviation are:

$$c = 2918 \pm 38 \text{ m/s}$$

$$\lambda_{20\text{kHz}} = 146 \pm 2 \text{ mm}$$

Table H.1: Speed of sound and wavelength results.

Test #	Real thickness [mm]	Theoretical thickness [mm]	Time of flight [μs]	Speed [m/s]	Wavelength [m]
1	1.80	1.829	0.610	2952	0.148
2	1.79	1.849	0.616	2900	0.145
3	1.83	1.829	0.610	3002	0.150
4	1.82	1.847	0.616	2956	0.148
5	1.83	1.872	0.624	2933	0.147
6	1.81	1.865	0.622	2912	0.146
7	4.69	4.883	1.628	2881	0.144
8	4.71	4.891	1.630	2889	0.144
9	4.71	4.864	1.621	2905	0.145
10	4.70	4.920	1.640	2866	0.143
11	4.69	4.786	1.595	2940	0.147
12	4.68	4.883	1.628	2875	0.144

The thermocouples effect

It has already been established in literature that placing thermocouples (TCs) at the interface will have an effect on the heating [6, 84, 91], as they concentrate the vibrational energy and may not present the real temperature results. However, placing TCs at the adherends showed to also have a major effect in the process behaviour in particular cases, which is exhibited in the displacement. The curves comparing the displacement with and without TCs (all present or only interface TCs) when the top and bottom adherend change are shown in Figure I.1 and Figure I.2.

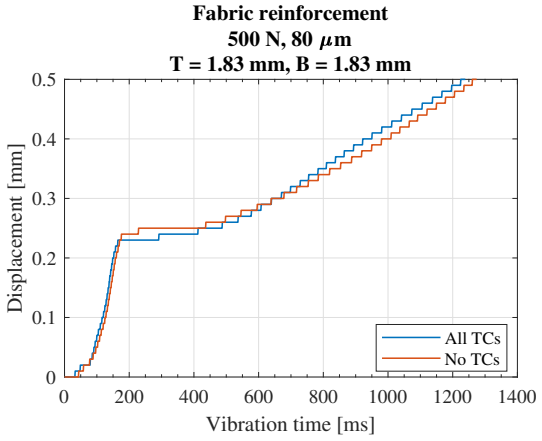

(a) T = 1.83 mm (all TCs present)

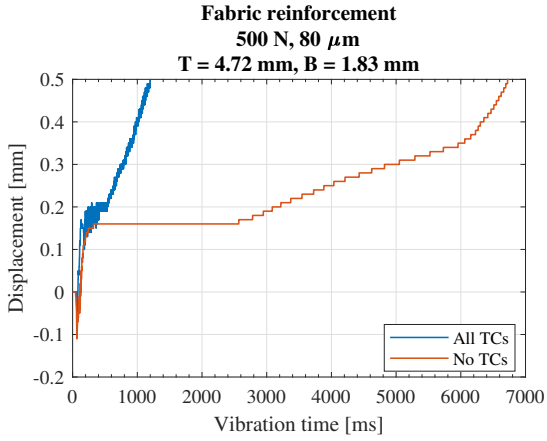

(b) T = 4.72 mm (all TCs present)

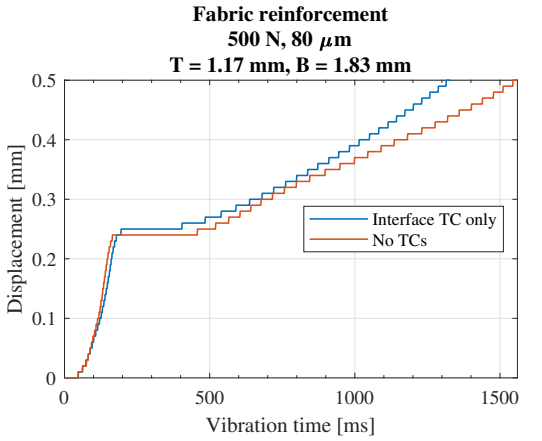

(c) T = 1.17 mm (only interface TC present)

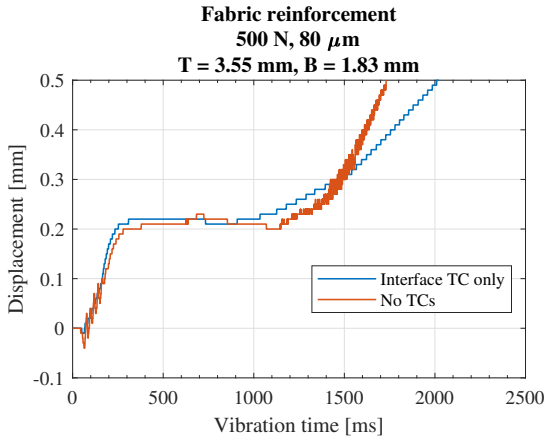

(d) T = 3.55 mm (only interface TC present)

Figure I.1: Comparison between displacement curves for different thicknesses of the top adherend when TCs are present.

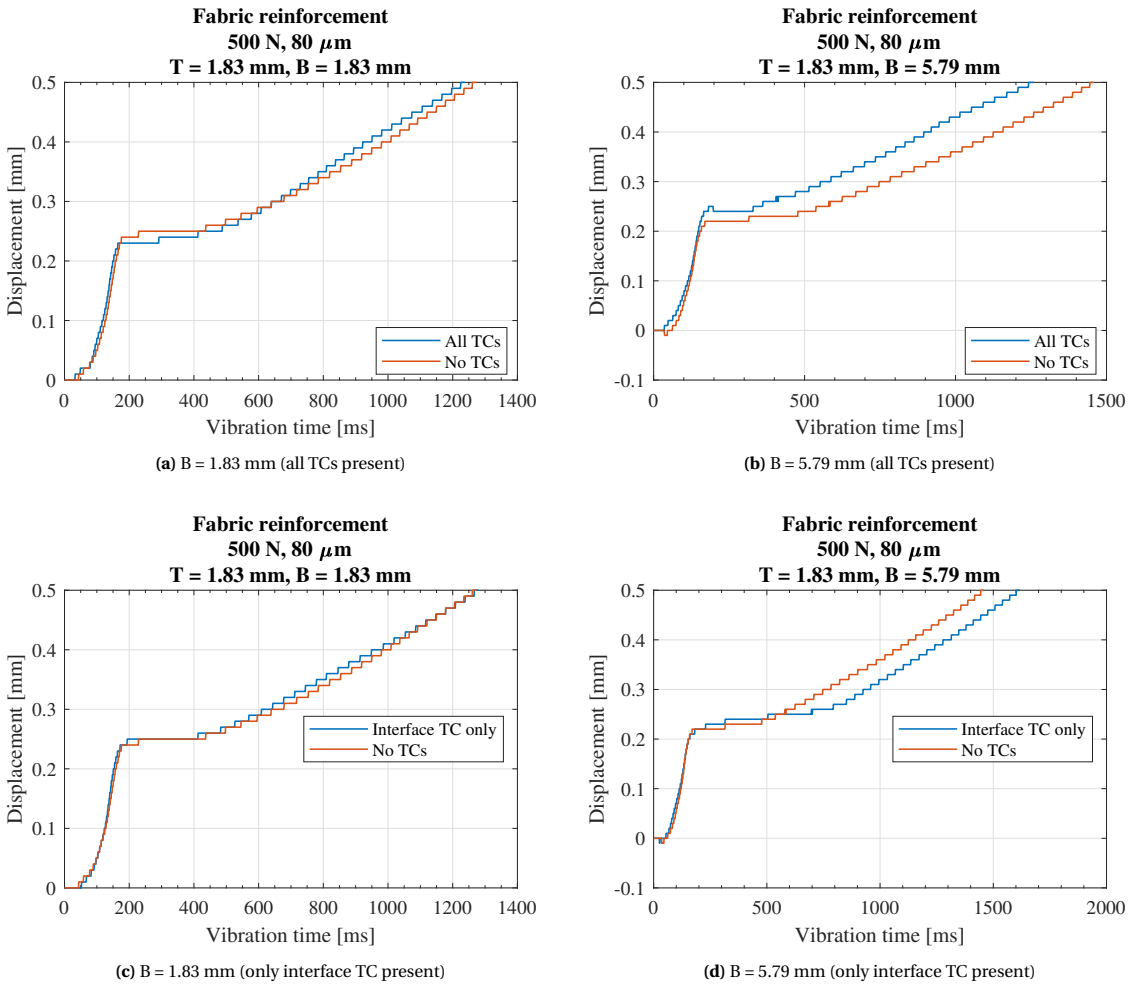

(a) B = 1.83 mm (all TCs present)

(b) B = 5.79 mm (all TCs present)

(c) B = 1.83 mm (only interface TC present)

(d) B = 5.79 mm (only interface TC present)

Figure I.2: Comparison between displacement curves for different thicknesses of the bottom adherend when TCs are present.

From these figures it is noticed that the TCs effect is considerably less prominent when changing the bottom adherend's thickness, which is in agreement with the discussion in Chapter 4. The change in where the displacement plateau occurs can be explained by the presence of the wire at the interface.

A different response is observed when changing the top adherend's thickness. For the thinner values (1.17 mm and 1.83 mm), the effect of placing TCs at either the interface or at the interface and adherends is similar as for the bottom adherend. However, when moving to thicker adherends (3.55 mm and 4.72 mm) there is a dramatic change in the displacement curves, particularly in Figure I.1b. This can be explained by the presence of the holes inside the adherends, which entirely changes the compliance of the adherend and was shown to significantly affect the process response. Although this effect was identified, a more in detail study of the effect was not executed. However, for future research, it would be of great importance to determine whether the implications of placing TCs in the adherends are relevant enough to reconsider this experimental setup.

Bibliography

[1] J. Dıaz and L. Rubio, "Developments to manufacture structural aeronautical parts in carbon fibre reinforced thermoplastic materials," Journal of Materials Processing Technology, vol. 143, pp. 342–346, 2003.

[2] S. Pantelakis and K. Tserpes, Revolutionizing Aircraft Materials and Processes. Springer, 2020.

[3] A. Benatar and T. G. Gutowski, "Ultrasonic welding of peek graphite APC-2 composites," Polymer Engineering & Science, vol. 29, no. 23, pp. 1705–1721, 1989.

[4] S. K. Bhudolia, G. Gohel, K. F. Leong, and A. Islam, "Advances in ultrasonic welding of thermoplastic composites: A review," Materials, vol. 13, no. 6, p. 1284, 2020.

[5] C. Ageorges and L. Ye, Fusion bonding of polymer composites. Springer Science & Business Media, 2002.

[6] I. F. Villegas, "In situ monitoring of ultrasonic welding of thermoplastic composites through power and displacement data," Journal of Thermoplastic Composite Materials, vol. 28, no. 1, pp. 66–85, 2015.

[7] G. Palardy and I. F. Villegas, "On the effect of flat energy directors thickness on heat generation during ultrasonic welding of thermoplastic composites," Composite Interfaces, vol. 24, no. 2, pp. 203–214, 2017.

[8] B. Jongbloed, J. Teuwen, G. Palardy, I. Fernandez Villegas, and R. Benedictus, "Continuous ultrasonic welding of thermoplastic composites: Enhancing the weld uniformity by changing the energy director," Journal of Composite Materials, vol. 54, no. 15, pp. 2023–2035, 2020.

[9] C. Brito, J. Teuwen, C. Dransfeld, and I. Villegas, "The effects of misaligned adherends on static ultrasonic welding of thermoplastic composites," Composites Part A: Applied Science and Manufacturing, p. 106810, 2022.

[10] R. J. Young and P. A. Lovell, Introduction to polymers. CRC press, 2011.

[11] H. Yeh, "Ultrasonic welding of medical plastics," in Joining and assembly of medical materials and devices, pp. 296–323e, Elsevier, 2013.

[12] K. P. Menard, "Dynamic mechanical analysis: a practical introduction," 1999.

[13] N. Saba, M. Jawaid, O. Y. Alothman, and M. Paridah, "A review on dynamic mechanical properties of natural fibre reinforced polymer composites," Construction and Building Materials, vol. 106, pp. 149–159, 2016.

[14] C. Ageorges, L. Ye, and M. Hou, "Advances in fusion bonding techniques for joining thermoplastic matrix composites: A review," Composites - Part A: Applied Science and Manufacturing, vol. 32, pp. 839–857, jun 2001.

[15] A. Yousefpour, M. Hojjati, and J. P. Immarigeon, "Fusion Bonding/Welding of Thermoplastic Composites," Journal of Thermoplastic Composite Materials, vol. 17, no. 4, pp. 303–341, 2004.

[16] A. Benatar and T. Gutowski, "Method for fusion bonding thermoplastic composites," SAMPE Q.;(United States), vol. 18, no. 1, 1986.

[17] I. F. Villegas, L. Moser, A. Yousefpour, P. Mitschang, and H. E. Bersee, "Process and performance evaluation of ultrasonic, induction and resistance welding of advanced thermoplastic composites," Journal of Thermoplastic Composite Materials, vol. 26, no. 8, pp. 1007–1024, 2013.

[18] M. Troughton, Handbook of Plastics Joining. William Andrew Inc., 2 ed., 2008.

[19] I. F. Villegas, "Ultrasonic welding of thermoplastic composites," Frontiers in Materials, vol. 6, p. 291, 2019.

[20] A. Levy, A. Poitou, S. Le Corre, and E. Soccard, "Ultrasonic welding of thermoplastic composites, modeling of the process.," International Journal of Material Forming, vol. 1, no. 1, pp. 887–890, 2008.

[21] I. F. Villegas and H. E. Bersee, "Ultrasonic welding of advanced thermoplastic composites: An investigation on energy-directing surfaces," Advances in Polymer Technology, vol. 29, no. 2, pp. 112–121, 2010.

[22] T. Zhao, C. Broek, G. Palardy, I. F. Villegas, and R. Benedictus, "Towards robust sequential ultrasonic spot welding of thermoplastic composites: Welding process control strategy for consistent weld quality," Composites Part A: Applied Science and Manufacturing, vol. 109, pp. 355–367, 2018.

[23] T. Zhao, G. Palardy, I. F. Villegas, C. Rans, M. Martinez, and R. Benedictus, "Mechanical behaviour of thermoplastic composites spot-welded and mechanically fastened joints: A preliminary comparison," Composites Part B: Engineering, vol. 112, pp. 224–234, 2017.

[24] S. Hassanifard, M. Zehsaz, and F. Esmaeili, "Spot weld arrangement effects on the fatigue behavior of multi-spot welded joints," Journal of mechanical science and technology, vol. 25, no. 3, p. 647, 2011.

[25] C. A. Meijerman, "Fatigue Behavior of Multi-Spot Welded Joints in Thermoplastic Composites: Effects of Spot Arrangement in a Four-Spot Joint," Master's thesis, Delft University of Technology, 01 2021.

[26] B. Jongbloed, J. Teuwen, G. Palardy, I. F. Villegas, and R. Benedictus, "Improving weld uniformity in continuous ultrasonic welding of thermoplastic composites," in Proceedings of the European Conference on Composite Materials–ECCM, vol. 18, 2018.

[27] B. Jongbloed, J. Teuwen, I. F. Villegas, R. Benedictus, et al., "Investigation on the melting of the weld interface in continuous ultrasonic welding of thermoplastic composites," in Proceedings of 22nd International Conference on Composite Materials (ICCM), Melbourne (Australia), 2019.

[28] B. Jongbloed, J. Teuwen, R. Benedictus, and I. F. Villegas, "On differences and similarities between static and continuous ultrasonic welding of thermoplastic composites," Composites Part B: Engineering, vol. 203, p. 108466, 2020.

[29] B. C. Jongbloed, J. J. Teuwen, R. Benedictus, and I. F. Villegas, "A study on through-the-thickness heating in continuous ultrasonic welding of thermoplastic composites," Materials, vol. 14, no. 21, p. 6620, 2021.

[30] G. Palardy, H. Shi, A. Levy, S. Le Corre, and I. F. Villegas, "A study on amplitude transmission in ultrasonic welding of thermoplastic composites," Composites Part A: Applied Science and Manufacturing, vol. 113, pp. 339–349, 2018.

[31] S. Tutunjian, O. Eroglu, M. Dannemann, N. Modler, and F. Fischer, "A numerical analysis of an energy directing method through friction heating during the ultrasonic welding of thermoplastic composites," Journal of Thermoplastic Composite Materials, vol. 33, no. 11, pp. 1569–1587, 2020.

[32] Z. Zhang, X. Wang, Y. Luo, Z. Zhang, and L. Wang, "Study on heating process of ultrasonic welding for thermoplastics," Journal of Thermoplastic Composite Materials, vol. 23, no. 5, pp. 647–664, 2010.

[33] J. A. Gallego-Juárez and K. F. Graff, Power ultrasonics: applications of high-intensity ultrasound. Elsevier, 2014.

[34] I. Fernandez Villegas, B. Valle Grande, H. Bersee, and R. Benedictus, "A comparative evaluation between flat and traditional energy directors for ultrasonic welding of CF/PPS thermoplastic composites," Composite Interfaces, vol. 22, no. 8, pp. 717–729, 2015.

[35] I. F. Villegas, "Strength development versus process data in ultrasonic welding of thermoplastic composites with flat energy directors and its application to the definition of optimum processing parameters," Composites Part A: Applied Science and Manufacturing, vol. 65, pp. 27–37, 2014.

[36] S.-I. Takeda, J. D. Tanks, S. Sugimoto, and Y. Iwahori, "Application of sheet-like energy directors to ultrasonic welding of carbon fibre-reinforced thermoplastics," Advanced Composite Materials, pp. 1–13, 2020.

[37] M. Kerssemakers, "Investigating the use of Fused Deposition Modeling as Energy Director application method for Ultrasonic Welding of Thermoplastic Composites," Master's thesis, Delft University of Technology, 01 2018.

[38] W. Tao, X. Su, H. Wang, Z. Zhang, H. Li, and J. Chen, "Influence mechanism of welding time and energy director to the thermoplastic composite joints by ultrasonic welding," Journal of Manufacturing Processes, vol. 37, pp. 196–202, 2019.

[39] K. Wang, D. Shriver, Y. Li, M. Banu, S. J. Hu, G. Xiao, J. Arinez, and H.-T. Fan, "Characterization of weld attributes in ultrasonic welding of short carbon fiber reinforced thermoplastic composites," Journal of Manufacturing Processes, vol. 29, pp. 124–132, 2017.

[40] A. Levy, I. F. Villegas, and S. Le Corre, "Ultrasonic welding of thermoplastic composites. modeling the heating phenomena," in The 19th International Conference on Composite Materials, Montreal, Canada, vol. 28, 2013.

[41] A. Benatar, R. V. Eswaran, and S. K. Nayar, "Ultrasonic welding of thermoplastics in the near-field," Polymer Engineering & Science, vol. 29, no. 23, pp. 1689–1698, 1989.

[42] B. C. P. Jongbloed, R. Vinod, J. J. E. Teuwen, R. Benedictus, and I. F. Villegas, "(de)consolidation in ultrasonic welding of thermoplastic composites," Under peer review at Composites Part A: Applied Science and Manufacturing, 2021.

[43] D. Grewell and A. Benatar, "Welding of plastics: fundamentals and new developments," International polymer processing, vol. 22, no. 1, pp. 43–60, 2007.

[44] N. Koutras, J. Amirdine, N. Boyard, I. F. Villegas, and R. Benedictus, "Characterisation of crystallinity at the interface of ultrasonically welded carbon fibre pps joints," Composites Part A: Applied Science and Manufacturing, vol. 125, p. 105574, 2019.

[45] F. Köhler, I. Villegas, C. Dransfeld, and A. Herrmann, "Static ultrasonic welding of carbon fibre unidirectional thermoplastic materials and the influence of heat generation and heat transfer," Journal of Composite Materials, vol. 55, no. 15, pp. 2087–2102, 2021.

[46] B. Jongbloed, J. Teuwen, G. Palardy, I. Fernandez Villegas, and R. Benedictus, "Continuous ultrasonic welding of thermoplastic composites: Enhancing the weld uniformity by changing the energy director," Journal of Composite Materials, vol. 54, no. 15, pp. 2023–2035, 2020.

[47] I. F. Villegas and C. Rans, "The dangers of single-lap shear testing in understanding polymer composite welded joints," Philosophical Transactions of the Royal Society A, vol. 379, no. 2203, p. 20200296, 2021.

[48] A. Benatar, "Ultrasonic welding of plastics and polymeric composites," in Power Ultrasonics, pp. 295–312, Elsevier, 2015.

[49] A. Benatar and Z. Cheng, "Ultrasonic welding of thermoplastics in the far-field," Polymer Engineering & Science, vol. 29, no. 23, pp. 1699–1704, 1989.

[50] S.-J. Liu, B.-C. Chang, L.-H. Chien, G.-M. Wu, and Y.-K. Chuah, "Weldability diagram for the ultrasonic welding of thermoplastics in far-field (913)," in TECHNICAL PAPERS OF THE ANNUAL TECHNICAL CONFERENCE-SOCIETY OF PLASTICS ENGINEERS INCORPORATED, vol. 1, pp. 1202–1206, 2000.

[51] M. Sinha and D. J. Buckley, "Acoustic properties of polymers," in Physical properties of polymers handbook, pp. 1021–1031, Springer, 2007.

[52] J. L. Jordan, R. L. Rowland, J. Greenhall, E. K. Moss, R. C. Huber, E. C. Willis, R. Hrubiak, C. Kenney-Benson, B. Bartram, and B. T. Sturtevant, "Elastic properties of polyethylene from high pressure sound speed measurements," Polymer, vol. 212, p. 123164, 2021.

[53] Y. Wang, Z. Rao, S. Liao, and F. Wang, "Ultrasonic welding of fiber reinforced thermoplastic composites: Current understanding and challenges," Composites Part A: Applied Science and Manufacturing, vol. 149, p. 106578, 2021.

[54] E. G. Obeda, "Ultrasonic assembly of thermoplasts," The Tool and Manufacturing Engineer, vol. 60, no. 3, pp. 60–63, 1968.

[55] D. J. Kolb, "Assembling thermoplastics by ultrasonic vibration," SPE JOURNAL, vol. 22, no. 11, p. 21, 1966.

[56] D. J. Kolb, "Ultrasonic welding," Modern Plastics Encyclopedia, pp. 989–994, 1967.

[57] H. Potente, "Ultrasonic welding—principles & theory," Materials & Design, vol. 5, no. 5, pp. 228–234, 1984.

[58] R. F. Gibson, Principles of composite material mechanics. CRC press, 2016.

[59] Y. Li, Z. Liu, J. Shen, T. H. Lee, M. Banu, and S. J. Hu, "Weld quality prediction in ultrasonic welding of carbon fiber composite based on an ultrasonic wave transmission model," Journal of Manufacturing Science and Engineering, vol. 141, no. 8, 2019.

[60] Q. Zhi, L. Lu, Z. Liu, and P. Wang, "Influence of horn misalignment on weld quality in ultrasonic welding of carbon fiber/polyamide 66 composite," Weld. J, vol. 97, no. 5, pp. 133s–143s, 2018.

[61] V. N. Khmelev, A. N. Slivin, and A. D. Abramov, "Model of process and calculation of energy for a heat generation of a welded joint at ultrasonic welding polymeric thermoplastic materials," in 2007 8th Siberian Russian Workshop and Tutorial on Electron Devices and Materials, pp. 316–322, IEEE, 2007.

[62] B. Zheng, X. Gao, M. Li, T. Deng, Z. Huang, H. Zhou, and D. Li, "Formability and failure mechanisms of woven cf/peek composite sheet in solid-state thermoforming," Polymers, vol. 11, no. 6, p. 966, 2019.

[63] B. M. Lempriere, Ultrasound and elastic waves: frequently asked questions. Elsevier, 2003.

[64] A. Sovetov, S. Voldov, Y. N. Orlov, and B. Y. Chernyak, "Choice of the size of hard plastic parts for ultrasonic welding," Russian Ultrasonics, vol. 6, pp. 137–143, 1976.

[65] A. Sovetov, B. Chernyak, A. Isaev, S. Volkov, and Y. Orlov, "Ultrasonic welding of rigid plastic articles with v-shaped edges," Russian Ultrasonics, vol. 9, 1976.

[66] G. Menges and H. Potente, "Studies on the weldability of thermoplastic materials by ultrasound," Welding in the World, vol. 9, no. 1, p. 2, 1971.

[67] C. Nonhof and G. Luiten, "Estimates for process conditions during the ultrasonic welding of thermoplastics," Polymer Engineering & Science, vol. 36, no. 9, pp. 1177–1183, 1996.

[68] S. Bolt, "Ultrasonic Plastic Welding of Carbon Fiber Reinforced Polyamide 6 to Aluminium and Steel," Master's thesis, Delft University of Technology, 12 2014.

[69] G. Wagner, F. Balle and D. Eifler, "Ultrasonic welding of hybrid joints," Jom, vol. 64, no. 3, pp. 401–406, 2012.

[70] C. Kassapoglou, Design and analysis of composite structures: with applications to aerospace structures. John Wiley & Sons, 1 ed., 2010.

[71] COMSOL, "Thermal Contact." `https://doc.comsol.com/5.5/doc/com.comsol.help.heat/heat_ug_ht_features.09.074.html`, 2022.

[72] COMSOL, "Theory for Thermal Contact." `https://doc.comsol.com/5.5/doc/com.comsol.help.heat/heat_ug_theory.07.66.html#645786`, 2022.

[73] Toray Advanced Composites & Victrex, "Processing guidelines for TC1225 PAEK composites," 2021.

[74] S. Delrue and V. Aleshin, "2D modeling of acoustic waves in solids with frictional cracks," in CFM 2017-23ème Congrès Français de Mécanique, AFM, Maison de la Mécanique, 39/41 rue Louis Blanc-92400 Courbevoie, 2017.

[75] B. Ghose, K. Balasubramaniam, C. Krishnamurthy, and A. S. Rao, "Two dimensional fem simulation of ultrasonic wave propagation in isotropic solid media using comsol," in COMSOL Conference, vol. 37, p. 38, 2010.

[76] S. Shridhara Bhat, "Tutorial on 2D Elastic wave propagation using COMSOL Multiphysics® (version 5.2)," 09 2017.

[77] COMSOL, "Structural mechanics module user's guide (version 5.6)." https://doc.comsol.com/5.6/doc/com.comsol.help.sme/StructuralMechanicsModuleUsersGuide.pdf, 2020.

[78] A. Levy, S. Le Corre, and I. F. Villegas, "Modeling of the heating phenomena in ultrasonic welding of thermoplastic composites with flat energy directors," Journal of Materials Processing Technology, vol. 214, no. 7, pp. 1361–1371, 2014.

[79] B. C. P. Jongbloed, "Sequential ultrasonic thermoplastic welding of thermoplastic composites," Master's thesis, Delft University of Technology, 10 2016.

[80] E. Jacquet, F. Trivaudey, and D. Varchon, "Calculation of the transverse modulus of a unidirectional composite material and of the modulus of an aggregate. application of the rule of mixtures," Composites science and technology, vol. 60, no. 3, pp. 345–350, 2000.

[81] TORAY, "Carbon fiber selector guide." https://www.toraycma.com/wp-content/uploads/Carbon-Fiber-Selector-Guide.pdf, 12 2021.

[82] COMSOL, "Meshing: Resolving the waves in space." https://doc.comsol.com/6.0/doc/com.comsol.help.aco/aco_ug_pressure.05.123.html#1396380, 2021.

[83] COMSOL, "Resolving time-dependent waves." https://www.comsol.com/support/knowledgebase/1118, 2022.

[84] R. Vinod, "Effect of consolidation parameters on (de)consolidation in ultrasonic welding of thermoplastic composites," Master's thesis, Delft University of Technology, 10 2020.

[85] N. Tateishi, T. North, and R. Woodhams, "Ultrasonic welding using tie-layer materials. Part I: Analysis of process operation," Polymer Engineering & Science, vol. 32, no. 9, pp. 600–611, 1992.

[86] A. Levy, S. Le Corre, and A. Poitou, "Ultrasonic welding of thermoplastic composites: a numerical analysis at the mesoscopic scale relating processing parameters, flow of polymer and quality of adhesion," International journal of material forming, vol. 7, no. 1, pp. 39–51, 2014.

[87] M. Tolunay, P. Dawson, and K. Wang, "Heating and bonding mechanisms in ultrasonic welding of thermoplastics," Polymer Engineering & Science, vol. 23, no. 13, pp. 726–733, 1983.

[88] H. Li, C. Chen, R. Yi, Y. Li, and J. Wu, "Ultrasonic welding of fiber-reinforced thermoplastic composites: a review," The International Journal of Advanced Manufacturing Technology, pp. 1–29, 2022.

[89] N. Koutras, I. Villegas, and R. Benedictus, "Effect of ultrasonic welding process on the crystallinity at the welding interface of cf/pps joints," in 18th European Conference on Composite Materials, ECCM 2018, Applied Mechanics Laboratory, 2020.

[90] J. David and N. Cheeke, Fundamentals and applications of ultrasonic waves. CRC press, 2012.

[91] A. Bruin, "Investigating the Degree of Crystallinity in Ultrasonically Welded Thermoplastic Composite Joints," Master's thesis, Delft University of Technology, 07 2020.